

Neutral Guest-Induced Assembly/Disassembly Approach for Concurrent Detection of Biologically Important Analytes under Physiological Condition

A Dissertation

Submitted in partial fulfillment for the degree of

Doctor of Philosophy



MEGHA BASAK

(Roll No. 176122022)

Thesis Supervisor: Prof. Gopal Das

Department of Chemistry

Indian Institute of Technology Guwahati

Assam -781039, India

Neutral Guest-Induced Assembly/Disassembly Approach for Concurrent Detection of Biologically Important Analytes under Physiological Condition

A Dissertation

Submitted in partial fulfillment for the degree of

Doctor of Philosophy



MEGHA BASAK

(Roll No. 176122022)

Thesis Supervisor: Prof. Gopal Das

Department of Chemistry

Indian Institute of Technology Guwahati

Assam-781039, India

The logo of Indian Institute of Technology Guwahati is a circular emblem. It features a central stylized figure with three rounded shapes, possibly representing a person or a symbol. The text "Indian Institute of Technology Guwahati" is written in English around the bottom half of the circle, and in Assamese at the top. The text in Assamese is "গুৱাহাটীৰ ভাৰতীয় প্ৰযুক্তিবিজ্ঞানীয়া প্ৰাচাৰ্যিকী সংস্থান".

*This thesis is dedicated to my
Mother for her endless love,
support and sacrifice*



INDIAN INSTITUTE OF TECHNOLOGY GUWAHATI

Department of Chemistry

STATEMENT

I do hereby declare that the matter embodied in this thesis is the result of investigations carried out by me in the Department of Chemistry, Indian Institute of Technology Guwahati, Assam – 781039, India, under the supervision of Prof. Gopal Das, Professor, Department of Chemistry, Indian Institute of Technology Guwahati, Assam – 781039, India.

In keeping with the general practice of reporting scientific observations, due acknowledgements have been made wherever this work is based on the findings of other investigators.

Date: April 2022

Place: IIT Guwahati

Megha Basak



INDIAN INSTITUTE OF TECHNOLOGY GUWAHATI

Department of Chemistry

CERTIFICATE

This is to certify that **Miss Megha Basak** (Roll No. 176122022) has been working under my supervision since July, 2017 as a regular registered Ph. D. student. Her thesis entitled “**Neutral Guest-Induced Assembly/Disassembly Approach for Concurrent Detection of Biologically Important Analytes under Physiological Condition**” is an authentic record of the results obtained from the research work carried out under my supervision in the Department of Chemistry, Indian Institute of Technology Guwahati, Assam - 781039, India. I am forwarding her thesis to submit for the award of degree of Doctor of Philosophy, from this institute. I hereby certify that he has fulfilled all the requirements, according to the rules of this institute regarding the investigations embodied in his thesis and this work has not been submitted elsewhere for a degree.

Prof. Gopal Das

(Thesis Supervisor)

Professor

Department of Chemistry

IIT Guwahati

Assam - 781039, India

Acknowledgement

While writing this section after much exhausted period hoping to be refreshed, but practically I have become more mentally tired as I had to go through all the memories left throughout the journey where each acquaintances put a brick to make stairs to which I have climbed up to this level. At this final stage of truly memorable journey towards my intellectual destination, first of all I would like to mention my mother Suparna Basak who has been my source of encouragement, inspiration, unconditional support and unbreakable belief, being a single mother. Any words of gratitude will fall short for her dedication and sacrifice for my education started from my school days to till now. I also want to mention my father Late Barun Basak and grandfather Late Jatindra Mohan Basak, for their eternal blessing and unconditional love which had always been strength for me. Pursuing doctoral degree was a dream for them, fortunately by God's grace I am at the end of this accomplishment.

I wish to express my sincere gratitude to my PhD supervisor Prof. Gopal Das for not only his excellent research works but also for generosity, simplicity and for being a very good human being by heart. His constant guidance, wide experience, deep understanding and insightful advice throughout the years helped me to enrich myself. He has changed the stereotype idea of becoming a tough supervisor to publish good journals, instead he cherished us as his own children and let us work with freedom. His kind supervision and unique style in leading the group always reflected in the happy faces of our group members. I feel blessed to work under his supervision.

Besides my supervisor, I am highly indebted to my doctoral committee members, Prof. Sandip Paul, Prof. Lal Mohan Kundu and Dr. Dipankar Srimani, for their valuable suggestions and careful evaluation of my thesis work. I would also like to thank former (Prof. B. K. Patel and Prof. T. Punniyamurthy) and present (Prof. Gopal Das) HODs, all the faculty members, Scientific officers specially Dr. Babulal Das, technical and non-technical staffs of the Department of Chemistry, IIT Guwahati. I sincerely appreciate all the staffs and instrument operators of Central Instrument Facility, for providing necessary instrumental facilities required during my research tenure.

I take this wonderful opportunity to thank extraordinary lab seniors Nilotpal da, Utsab da, Rupinder da, Biswajit da, Arnab da, Santanu da, J. K da as well as the amazing Lab mates Senjuti, Aresh, Deepa, Debojit lovely juniors like Sagnik, Debolina, Pegu, Rubi, Pampi and Subhrajyoti, Abhijit, Srijan from S. P. Biswas lab for their co-operation and inspiration in my research work, without which it would not been easy to complete the PhD thesis. It will be

incomplete if I do not mention Asesh like mentor and friend who taught me the basics of lab techniques and contributed to the work in greater extent from many aspects. I also owe my obligations to my other seniors, batch mates and juniors of PhD fraternity of the chemistry department for their help and support during this few years.

In context to this thesis work, I had opportunity to mingle with seniors and friends of Biosciences and Bioengineering department, IIT Guwahati. I shall always be obliged to Prof. Aiyagari Ramesh and his group for admirable support throughout my research work. I would like to offer my thanks to Poulomi di, Priya di and Basu, Berlina for their unconditional support and all the help they extended from time to time through these years.

Now it is time to thank all my IIT Guwahati friends whose contribution is worth mentioning. Of course, nothing would function properly without the care and affection of my beloved friends Anwasha, Tanushree, Naseema and Meenali. No word would suffice to thank Oindrila, Araghi, Subhasis, Sourav, Manideepa for their unconditional support and love during the tough hurdle. I take this opportunity to thank my friend Saghir, for being a source of encouragement and constant support which will be cherished throughout my life. From gossiping in the hostel rooms overnight to hanging out in the weekend, I will surely miss all of them and cherish the memories of love and laughter we shared together. I sincerely wish them good luck for their future.

I extend my feelings for my teachers to whom I owe debt for their kindness and benevolence; Sukriti di, Mala di, Archana di, Soma di, Amala di, Sharmila di, Sanjita di, Late Gopa di, Sanjib sir, Tapas sir, Amrit sir, Abhijit sir, Arunabha sir, Jayati maam, Sanchita maam, Debasis sir, Mohanto sir and many others from my school, college and university who gave me the direction and positive motivation to march forward in this field. I am sorry that many names are missing whose contribution and help is worth mentioning.

I would like to acknowledge IIT Guwahati for the fellowship, the Microsoft Corporation for presenting the MS Word and Excel as well as Adobe Corporation for AI software.

Finally, I bow down to the Lord Almighty for his grace and blessings from the beginning of my academic life up to this doctoral level.



-Megha

The thesis entitled “**Neutral Guest-Induced Assembly/Disassembly Approach for Concurrent Detection of Biologically Important Analytes under Physiological Condition**” is arranged into seven chapters based on the outcomes of experimental effort accomplished during the research tenure.

Chapter 1: Introduction

The chemistry beyond molecules, i.e., supramolecular chemistry, has made eloquent advancement in the past few decades. Now we have plunged into a new phase in which the development of supramolecular chemistry makes notable inroads into materials science, medicine, biology, and engineering. Supramolecular chemistry is the subject of making macromolecules between two or more chemical constituents based on noncovalent intramolecular forces. These weaker interactions (2–250 kJ/mol) than covalent bonds (100–400 kJ/mol) embrace π - π interaction, H-bonding, electrostatic interaction, hydrophobic interaction, and Van der Waals forces, elucidating the mechanisms of some key interactions, such as host-guest, self-assembly, and molecular recognition in representative applications from material science to biological chemistry.

This chapter provides a brief introduction to the basics of Molecular self-assembly regarding the change in the characteristics properties of small molecules with the slight modification in molecular framework for providing particulars on the working principle of molecular aggregates for advanced applications. The term ‘Molecular self-assembly’ defines the process in which spontaneous organization of molecules arranges themselves into well-ordered structures. To mimic the properties of biological systems by non-living systems, many disciplines use the concept of self-assembly, which is a prevalent process in cells and a common phenomenon of nature. The beauty of self-assembly stems from the fact that it is one of the few practical strategies for fabricating various kinds of supramolecular architectures at micro- or nano-level as the prerequisite for functionalization of materials in countless areas such as optoelectronics, chemosensors, nanotechnology, biotechnology and biomedicines. Nature furnishes us with many inspiring examples of biological self-assembled nanostructures which are very essential in the emergence and maintenance of life, i.e. folding of polypeptide chain, construction of cell membranes by assembly of phospholipid bilayers, structured nucleic acids, metalloproteins, polymer, dendrimer etc. One of the most common examples is the DNA double helix structure; in which two polymeric entwined strands are held together through π - π stacking and H-bonding between its complementary base pairs.

Self-assembly and its reverse process i.e. disassembly are ubiquitous in nature. The self-assembly of biomolecules, driven by weak, noncovalent intermolecular interactions, brings

about multicomponent complexes with a high level of structural hierarchy. In contrast, disassembly or dissociation, the reverse process of assembly, plays an indispensable role in modulating and terminating the actions of these supramolecular complexes. To regulate sophisticated biological processes, the assembly and disassembly processes are firmly controlled in living organisms via multiple and interconnected mechanisms. A well-established example is the dynamics of cytoskeletons, such as constant assembling and disassembling of actin filaments. Such dynamics mediate multiple cell behaviours, including growth, motility and membrane internalization. In essence, the formation of assemblies from monomers and the dissipation of the assemblies are dynamic, reversible processes, which promise applications in molecular imaging, analyte detection, anticancer therapy, and treatment of neurodegenerative diseases. Herein, we specifically focus on the synthesis of different types of small aromatic molecular framework and aspects of their aggregation behaviour, morphological tunability, and consequent processibility or applicability. We try to give an account of the fluorene/quinoxaline core based scaffolds which have been designed to undergo spontaneous assembly/disassembly in response to environmental and chemical stimuli, including biologically important or harmful analytes, or even in presence of trace water. Further, we illustrate the potential of these sensors with applications reaching out to different fields.

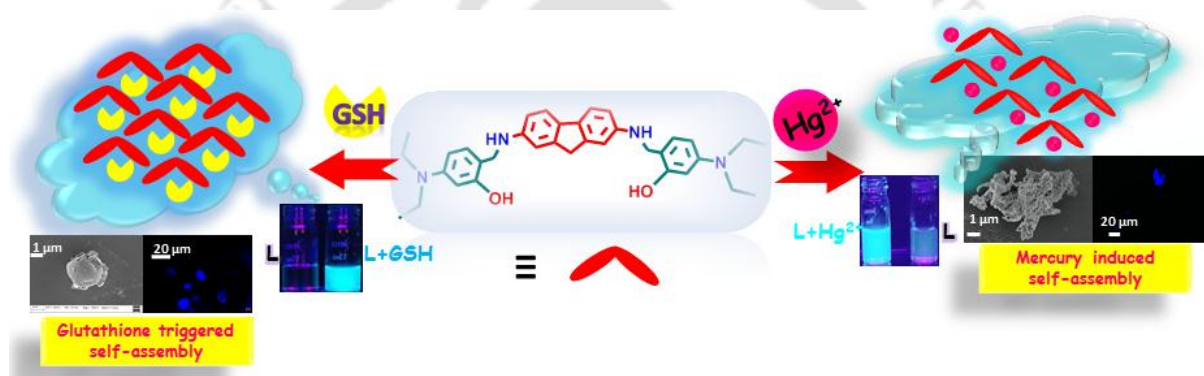
Chapter 2: Experimental methods and characterization

This chapter elaborates the comprehensive information about the various reagents and solvents used in the synthesis of the compounds along with synthetic procedures, specifications of analytical instruments employed as well as spectroscopic and microscopic experimental details followed for the characterization of the synthesized compounds and their assembled/disassembled form.

Chapter 3: Fluorene-salicylaldehyde probe: Mercury and glutathione recognition triggered self-assembly and simultaneous Turn-on chemosensing in water (Submitted)

In this chapter, three simple fluorene-salicylaldehyde/aldehyde conjugate probes (**L**₁, **L**₂ and **L**₃) were purposefully designed and synthesized by modifying the substituents in ortho and para positions respectively. Interestingly, we explored **L**₁ as a selective and sensitive multifunctional switch-on fluorescent probe towards Hg²⁺ (LOD ~ 17.35 ppb) and GSH (LOD ~ 25.83 ppb) independently over other coexisting analytes in the aqueous medium. The probe **L**₁ manifested rapid sensing exclusively toward Hg²⁺ (LOD = ~17.35 ppb) and GSH (LOD = ~25.83 ppb) with a significant “turn-on” fluorescence response along with red-shifted emission maxima at 414 nm and 420 nm, which could be ascribed to the analyte influenced aggregation induced emission

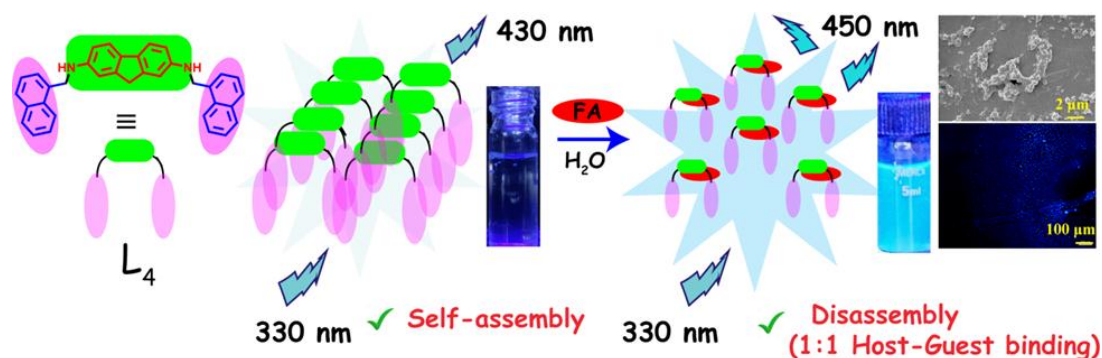
upon complexation. The recognition properties of L_1 towards Hg^{2+} and GSH were corroborated satisfactorily via fluorescence spectroscopic techniques, 1H -NMR, HRMS studies, FESEM experiments, fluorescence microscopy analyses, and theoretical calculations. Furthermore, scattered small rod-like particles of L_1 self-assembled into different morphology upon inclusion of Hg^{2+} and GSH respectively owing to analyte recognition triggered self-assembly of the sensor and hence emission enhancement. The result corroborated via DLS analysis also. The sensing strategy was successfully implemented to recognize Hg^{2+} and GSH in naturally contaminated water body samples, simulated physiological media, and real biological samples, including human serum specimens. More importantly, affordable test strips integrated with smartphone-assisted RGB analysis had been employed for the visual and quantitative detection of Hg^{2+} and GSH which may offer great potential in several fields of preliminary rapid environmental monitoring.



Scheme 1. A pictorial illustration of the research work covered in **Chapter 3**.

Chapter 4: Fluorene-naphthalene probe: Folic acid induced disassembly and simultaneous detection of folic acid in water (*J. Photochem. Photobiol. A* 113292, 414, 2021)

In this chapter we have focused on the synthesis of fluorene-based fluorophore adorned with dipodal naphthalene moiety, L_4 , using a straightforward method. The chemosensor formed stable electron donor-acceptor complexes with folic acid. DLS and FESEM studies showed that L_4 underwent self-aggregation to form aggregates by non-covalent interaction. Taking advantage of this property of L_4 , we further demonstrated the fluorescence sensing of various mono and dicarboxylic acids, where the selective 1:1 sensing ability of folic acid was demonstrated. The sensing ability of FA by L_4 led to the disassembly of the self-aggregated probe,



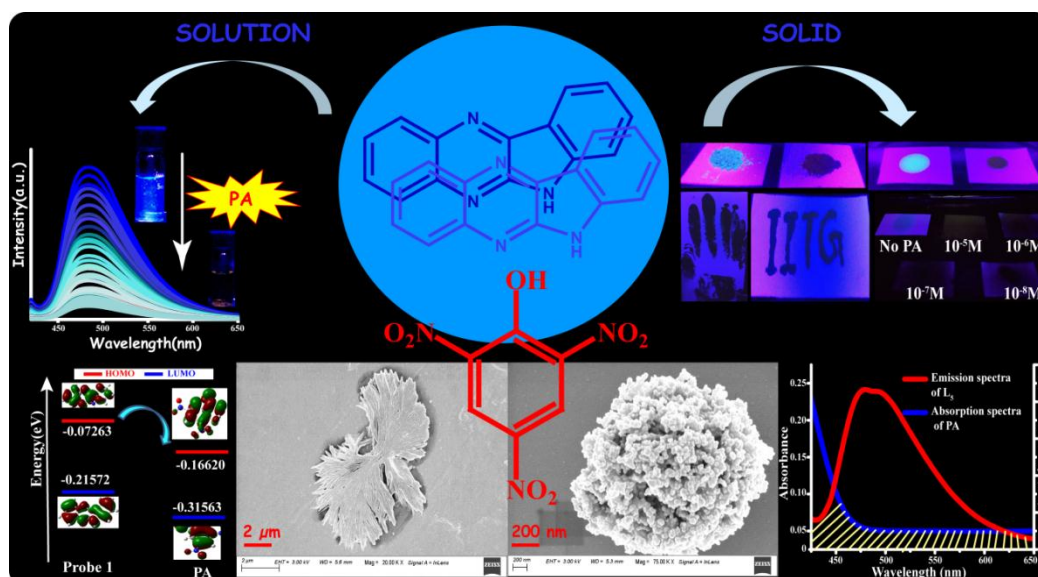
Scheme 2. A pictorial illustration of the research work covered in **Chapter 4.**

which was well established by FESEM study, DLS study, fluorescence microscope study, HRMS study, fluorescence Job's plot, and theoretical DFT calculation. The detection limit of L_4 for folic acid was as low as $0.38 \mu\text{M}$. The sensor for folic acid was applied successfully for practical detection in bio-fluidic samples and the actual samples' quantitative analysis, e.g., mung bean, orange, and spinach. Thus the observations indicated that the present inexpensive protocol could be used for rapid on-site estimation of folic acid without involving sophisticated instrumental facilities, lavish reagents, or trained technicians.

Chapter 5: Quinoxaline Based probe: Nitro-aromatics induced disassembly and selective Turn-off detection in water (Dyes. Pigm. 109779, 196, 2021)

In continuance of our interest in exploring the assembly/disassembly aptitude of neutral guest molecule, we report the synthesis of a small quinoxaline-based L_5 for effective and selective fluorescence-based detection of PA over other NACs in aqueous solution, natural water samples, solid and paper-based systems. Advancement in fluorescent chemosensor for discriminative and precise detection of picric acid (PA) in aqueous medium is highly desirable owing to its alarming

impact on the natural environment via soil and groundwater pollution. Due to π - π stacking interaction, L_5 spontaneously self-assembled in an aqueous solution to leaf-like aggregates, which was disrupted to smaller round-shaped aggregates in presence of PA. FESEM study, fluorescence microscopic analysis along with DLS investigation corroborated the aggregation-disaggregation process. Based on the experimental evidence, disaggregation of the self-assembled sensor, and PET, FRET is concomitantly responsible for the discriminative detection of PA in water with high selectivity and sensitivity. Self-aggregated L_5 manifested high selectivity and good sensitivity towards PA as the K_{SV} was $22.6 \times 10^6 \text{ M}^{-1}$ and LOD was ~ 56 ppb. Paper-based detection for PA was achieved at the picogram level, enabling rapid and real on-site detection. The developed probe could also be employed in imaging studies for

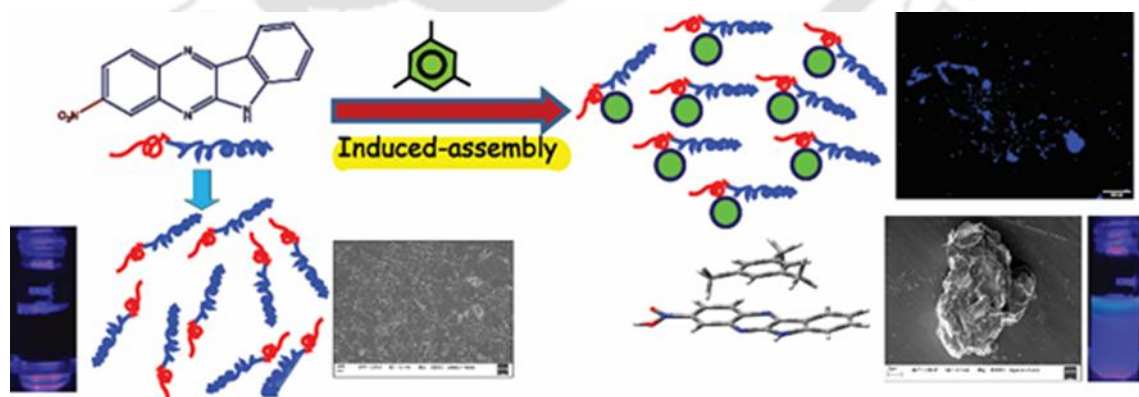


Scheme 3. A pictorial illustration of the research work covered in **Chapter 5**.

non-invasive fluorescence-based sensing of PA in live HeLa cells. Based on its non-toxic nature, it is envisaged that the probe can bear interesting prospect in future as a non-destructive imaging handle for PA detection in *in vivo* cellular system.

Chapter 6: Nitro substituted Quinoxaline framework: Benzene group of VOC triggered self-assembly and selective Turn-on detection in water (*Analyst*, 6239-6244, 146, 2021)

This chapter deals with design and fabrication of an electron withdrawing group appended (-NO₂) quinoxaline-based fluorophore, L₆, which was introduced as an effective chemosensor to detect benzene-derived VOCs in aqueous media. Hazardous volatile organic compounds (VOCs)



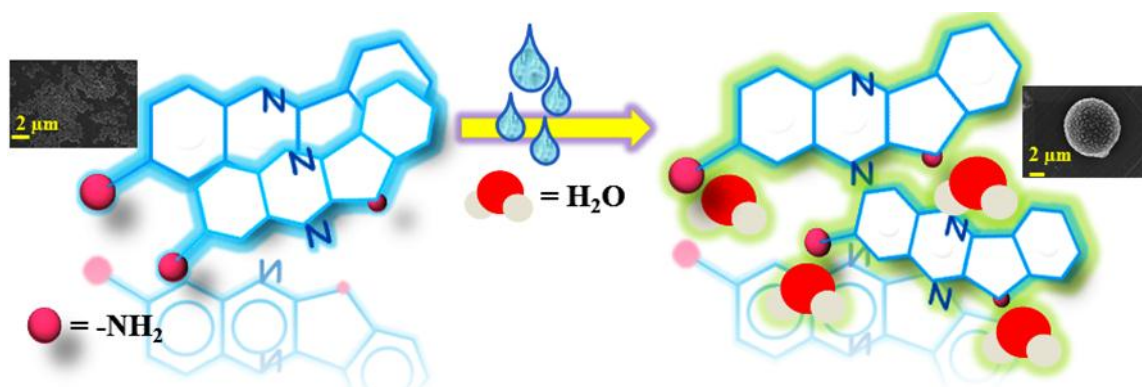
Scheme 4. A pictorial illustration of the research work covered in **Chapter 6**.

can significantly impact human health and the environment therefore, the detection of VOCs is of foremost importance. The probe displayed a differential “turn-on” fluorescence response

towards mesitylene (LOD = 2.66 ppm) uninfluenced by other VOCs. The sensing mechanism involved mesitylene detection induced assembly formation as the fibril network transformed into a stone-shaped morphology. The detection tunable morphological controllability was also justified by DLS study and fluorescence microscopic experiments. The probe possessed a notably high binding constant of $16.67 \times 10^8 \text{ M}^{-1}$ with mesitylene with a 1 : 1 stoichiometric binding ratio. The probe was employed ideally for practical detection in natural contaminated water sources, *i.e.*, lake water, river water, tap water and industrial wastewater, along with bio-fluidic samples, artificial urine as VOCs have become potential biomarkers of cancer. The current inexpensive strategy could be helpful for the rapid, efficient estimation of mesitylene in an aqueous medium without involving modern equipment facilities, costly chemicals, or professionally trained operators.

Chapter 7: Amine substituted Quinoxaline framework: Water induced self-assembly and simultaneous detection moisture(Submitted)

To sum up, in this chapter we have included three varieties of quinoxaline derivatives (**L₅**, **L₆** and **L₇**) containing electron-withdrawing, electron-donating groups, and only quinoxaline framework in excellent yields, and it was found that the fluorescence intensity of 6*H*-indolo[2,3-*b*]quinoxalin-3-amine (**L₇**) is strongly affected by solvent polarity, owing to excellent solvatochromism and large Stokes shift. Both experimental and theoretical analysis evinced that the incorporation of a strong electron-rich $-\text{NH}_2$ moiety to quinoxaline backbone notably enhanced the sensitivity of **L₇** towards solvent polarity. The highest polar sensitivity of probe **L₇** made it an effective water sensor towards frequently used organic solvents *i.e.* acetonitrile, THF, DMF, and methanol. The lowest limit of detection (LOD) for acetonitrile, THF, DMF, and methanol is 0.018%, 0.027%, 0.012%, and 0.420%, respectively, which provided an effective and suitable procedure for water/moisture detection in organic solvents. With an enhancement in water percentage, the fiber network-like morphology of probe **L₇** transformed into light emitting spherical aggregates presumably due to the increasing polarity index of the binary systems. Moisture content in commercial building materials and food products was also quantitatively estimated by the sensor **L₇** by switching ON-OFF emission intensities. However, after the probe stuff test strips were soaked, under 365 nm UV light the fluorescence color variations of dry common organic solvents in presence of different amounts of water could be noticed by the naked eye.



Scheme 5. A pictorial illustration of the research work covered in **Chapter 7**.

Conclusion and Future Perspective

So, it can be concluded that this report exemplifies the significant consequences in realization of aggregation/disaggregation prospective of certain fluorene and quinoxaline based derivatives and their response towards other biologically and environmentally relevant analytes. The progressive studies during the research period provides some interesting findings in aspect of neutral guest molecule induced assembly/disassembly and insightful route in morphological evolution regarding design, synthesis and characterization of chemosensor molecule with contrasting aggregation prospect in developing supramolecular organization for high-tech application in various fields. The results of our continuous effort manifest a systematic elaboration of structural alteration within molecular framework in the field of stimuli responsive molecule aggregation/disaggregation. In essence, we believe that this report would find meaningful contribution to both analytical chemistry and supramolecular chemistry community for enhancing cognizance and development in the particular field of research. Hopefully, this thesis may inspire further exploration of interesting photophysical characteristics along with morphological transformation and concurrent sensing endeavor with this type of molecular framework.

CHAPTER 1: Introduction

1.1 Supramolecular Self-assembly: A Brief Introduction	1
1.2 Detection of Analytes: Stimuli instructed assembly/disassembly approach	4
1.3 Importance of Sensing of small molecules	10
1.3.1 Background of Glutathione (GSH) detection	11
1.3.2 Background of Folic acid (FA) sensing	12
1.3.3 Background of Nitroaromatics (NACs) detection	13
1.3.4 Background of Volatile organic compounds (VOCs) sensing	14
1.4 Importance of moisture/trace water sensing	14
1.5 Concluding remarks and Objective of Thesis	15
References	17

CHAPTER 2: Experimental Details and Characterization

2.1 General Information and Materials	21
2.2 Synthetic procedure and characterization of the probes (L_1 - L_7)	21
2.2.1 Synthesis of L_1 [6,6'-(9H-fluorene-2,7-diyl)bis(azanediyl)bis(methylene) bis(3-(diethylamino)phenol]	21
2.2.2 Synthesis of L_2 [2,2'-(9H-fluorene-2,7-diyl)bis(azanediyl)bis (methylene) diphenol]	22
2.2.3 Synthesis of L_3 [N2,N7-bis(4-(dimethylamino)benzyl)-9H-fluorene-2,7-diamine]	22
2.2.4 Synthesis of L_4 [N2, N7-bis (naphthalene-1-yl) methyl-9H-fluorene-2, 7-diamine]	23
2.2.5 Synthesis of L_5 [6H-indolo[3,2-b]quinoxaline]	23
2.2.6 Synthesis of L_6 [3-nitro-6H-indolo[3,2-b]quinoxaline]	24
2.2.7 Synthesis of L_7 [6H-indolo[2,3-b]quinoxalin-3-amine]	24
2.3 UV-Vis and Fluorescence Spectral Studies	24
2.4 Estimation of the Apparent Binding Constant	25
2.5 Stern-Volmer Plot	26
2.6 Detection limit (LOD)	26

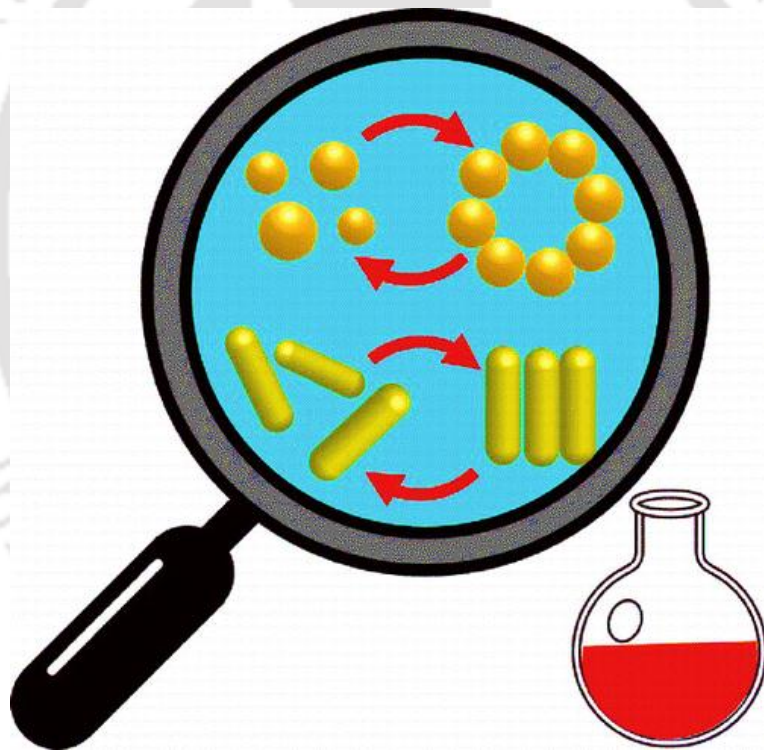
2.7 Field Emission Scanning Electron Microscope (FESEM) Studies	26
2.8 Dynamic light scattering measurement	26
2.9 Fluorescence Microscopy	26
2.10 Measurement of fluorescence lifetime	27
2.11 Photoluminescence Quantum Yield	27
2.12 Cytotoxic Effect on HeLa Cells	27
2.13 Cytotoxic Potential of L_5 and Live Cell Imaging for Detection of Picric Acid	28
2.14 Theoretical investigations (DFT study)	29
References	30
Appendix- Chapter 2	31
CHAPTER 3: Fluorene-salicylaldehyde probe: Mercury and glutathione recognition triggered self-assembly and simultaneous Turn-on chemosensing in water	
3.1 Background and focus of the chapter	47
3.2 Photophysical characterization	48
3.3 Fluorescence response of the Probe L_1 to Hg^{2+} in water	49
3.4 Spectral response of the Probe to GSH in water	51
3.5 Possible recognition mechanism of L_1 with Hg^{2+} /GSH	53
3.6 The practicability of L_1 towards Hg^{2+} in environmental and biological samples	56
3.7 Practical application of L_1 towards GSH in biological samples	57
3.8 Bioimaging application in live tissues	57
3.9 Solid state-based sensor for Hg^{2+} sensing	58
3.10 Paper-based sensor for GSH sensing	58
3.11 Conclusion	59
References	60
Appendix- Chapter 3	62
CHAPTER 4: Fluorene-naphthalene probe: Folic acid induced disassembly and simultaneous detection of folic acid in water	
4.1 Background and focus of the chapter	81
4.2 Self-Assembly of L_4	83
4.3 Photo physical Characterization of L_4	84

4.4 Sensing Behavior	84
4.5 UV-Visible Spectral Study	84
4.6 Fluorescence Spectral Study	85
4.7 Detection of FA in real samples and bio-fluids	86
4.8 Interference Experiment	87
4.9 Plausible Mechanism for Sensing FA	88
4.10 Theoretical Study	89
4.11 MTT Assay	90
4.12 Conclusion	90
References	91
Appendix- Chapter 4	94
CHAPTER 5: Quinoxaline Based probe: Nitro-aromatics induced disassembly and selective Turn-off detection in water	
5.1 Background and focus of the chapter	103
5.2 Photophysical Investigation	104
5.3 Sensing Performance toward PA	106
5.4 Quenching Mechanism of PA Sensing	110
5.5 Detection of PA in natural water samples, soil samples, and bio-fluid samples	111
5.6 Contact mode estimation of PA	112
5.7 Paper-based detection of PA	113
5.8 Live cell imaging for detection of PA	114
5.9 Conclusion	115
References	115
Appendix- Chapter 5	118
CHAPTER 6: Nitro substituted Quinoxaline framework: Benzene group of VOC triggered self-assembly and selective Turn-on detection in water	
6.1 Background and focus of the chapter	127
6.2 Photophysical studies	129
6.3 Sensing response towards VOCs in water	129
6.4 Plausible sensing mechanism	132

6.5 Detection of Mesitylene in natural samples	133
6.6 Paper-based analysis of mesitylene	134
6.7 Conclusion	136
References	136
Appendix- Chapter 6	138
CHAPTER 7: Amine substituted Quinoxaline framework: Water induced self-assembly and simultaneous detection moisture	
7.1 Background and focus of the chapter	145
7.2 Photophysical and Solvatochromic behavior of probe L ₇	146
7.3 Detection of trace Water content in common organic solvents	148
7.4 Water-directed self-assembly of probe L ₇ and Plausible sensing mechanism	150
7.5 Qualitative detection of moisture or water content in commercial materials and raw food Products	152
7.6 Paper-based sensor for moisture detection	153
7.7 Conclusion	154
References	154
Appendix- Chapter 7	157
Conclusion and Future Perspective	161
Curriculum Vitae	165

CHAPTER 1

Introduction



Chapter 1

1.1 Supramolecular Self-assembly: A Brief Introduction

The *chemistry beyond molecules*, i.e., supramolecular chemistry, has made eloquent advancement in the past few decades. Now we have plunged into a new phase in which the development of supramolecular chemistry makes notable inroads into materials science, medicine, biology, and engineering.^{1,1} Supramolecular chemistry is the subject of making macromolecules between two or more chemical constituents based on noncovalent intramolecular forces. These weaker interactions (2–250 kJ/mol) than covalent bonds (100–400 kJ/mol) embrace π - π interaction, H-bonding, electrostatic interaction, hydrophobic interaction, and Van der Waals forces, elucidating the mechanisms of some key interactions, such as host-guest, self-assembly, and molecular recognition in representative applications from material science to biological chemistry.^{1,2}

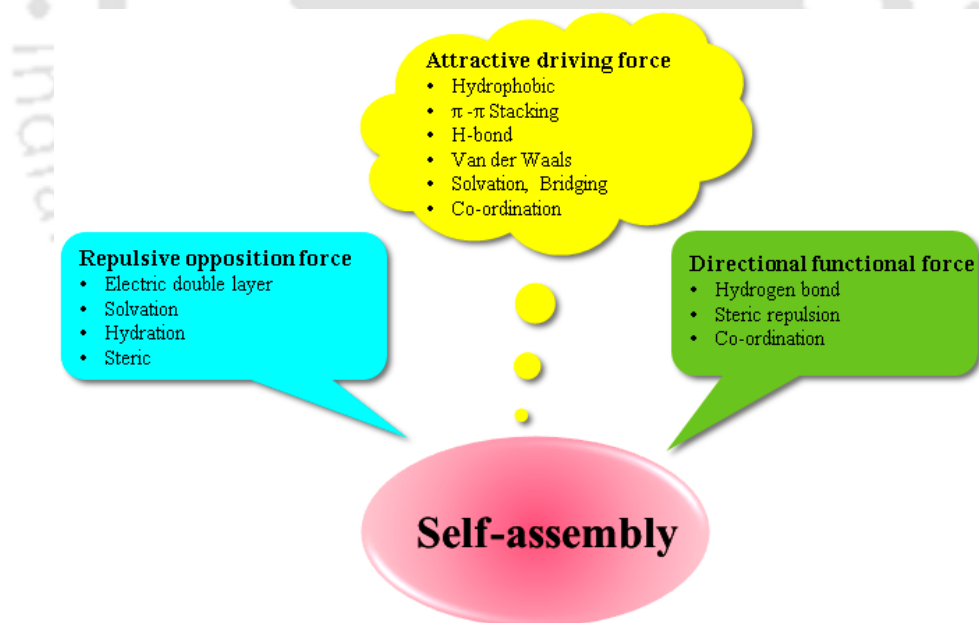


Figure 1.1: Three classes of distinctive forces involved in self-assembly.

These interactions execute an impressive role in the alignment of molecular units in an ordered structure facilitating self-assembly of the units. Besides, the directionality and functionality of self-organized structures are determined by other functional interactions or forces. All these distinctive non-covalent interactions important in molecular self-assembly are given below in Figure 1.1.^{1,3} A variety of approaches followed by chemists triggered the rapid expansion of

supramolecular self-assembly as an interdisciplinary area.^{1.4} The term “Self-assembly” describes spontaneous molecular arrangement of the disordered entities of molecules into ordered supramolecular structures resulting from specific local interactions among the components themselves.^{1.5} The interaction of a ligand with its receptor is also attributed to self-assembly (Figure 1.2). Nature furnishes us with many inspiring examples of biological self-assembled nanostructures which are very essential in the emergence and maintenance of life, i.e. folding of polypeptide chain (Figure 1.3), construction of cell membranes by assembly of phospholipid bilayers, structured nucleic acids, metalloproteins, polymer, dendrimer etc. One of the most common examples is the DNA double helix structure; in which two polymeric entwined strands are held together through π - π

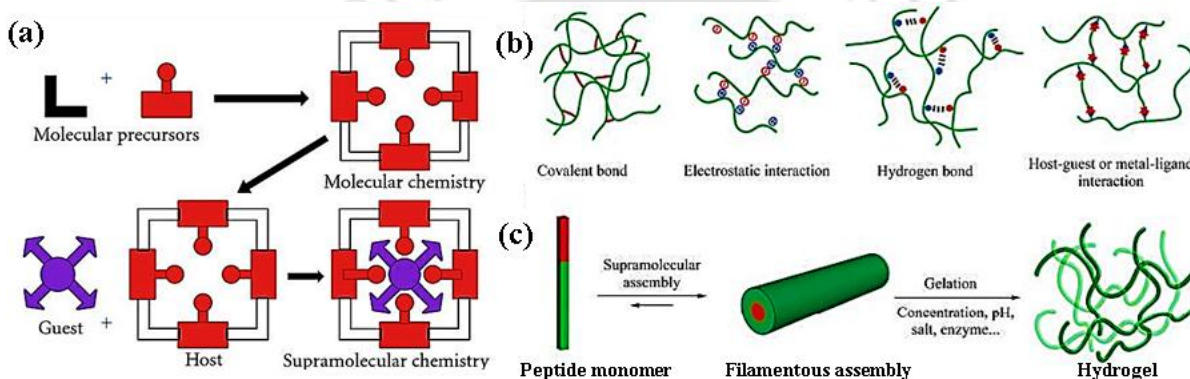


Figure 1.2:(a) : Comparison between the scope of molecular and supramolecular chemistry according to Lehn.^{1.6} (b) Schematic illustrations for interaction mechanisms i.e. covalent bond, electrostatic interaction, hydrogen bond, and host-guest or metal-ligand interaction.(c) assembly of peptidic monomers into filamentous assemblies that entangle further into supramolecular hydrogels.^{1.7}

stacking and H-bonding between its complementary base pairs.^{1.8} However, self-assembly of small molecules as building units is a useful strategy for the formation of structure controlled materials as well,^{1.9} DNA-based nanomaterials have shown their potential in diagnostics and therapeutic delivery. The large variety of potential supramolecular interactions of different specificities available offers endless possibilities for the construction of diverse non-covalent supramolecular structures with tunable properties and functionalities. Such systems have found applications in sensors, luminescent materials, gels and materials chemistry, light-emitting devices, biological and cell imaging probes.^{1.10-1.13} Recognition of this relatively new field of chemistry was first achieved when the 1987 Nobel Prize in Chemistry was awarded to Lehn, Pedersen, and Cram for the design and development of cryptands, crown ethers, and cavitands, respectively.^{1.14} Because of its boundless potential, supramolecular chemistry has achieved immense interest among chemists who wish to understand the intermolecular interactions involved in building supramolecular structures and hence this field has expanded toward the

construction of larger and more complex architectures such as macromolecules and multimetallic helicates, rotaxanes, metal-organic

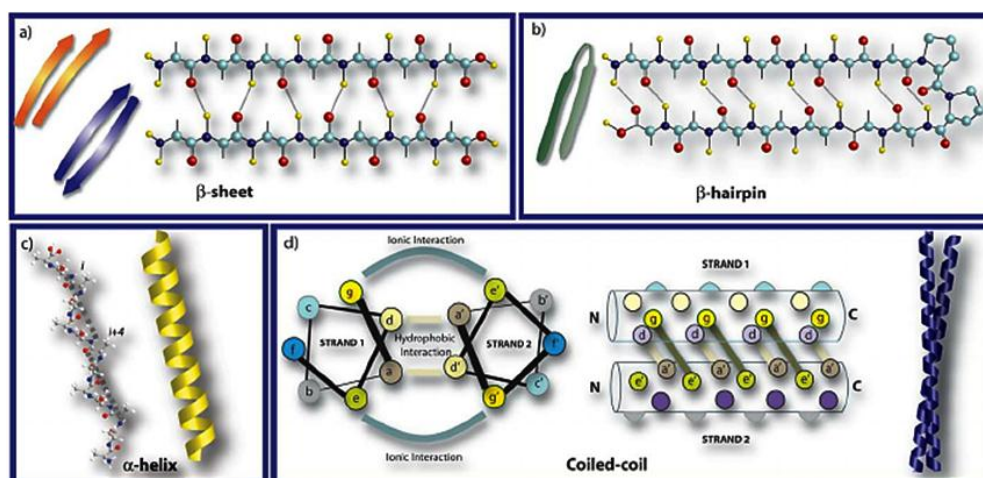


Figure 1.3: Schematic illustration of the molecular self-assembly involved in the formation of different secondary structures peptides: (a) β -sheet, (b) β -hairpin, (c) α -helix and (d) coiled-coil.

frameworks, coordination polymers, clusters, etc.^{1.15-1.16} Discovery of complex synthetic molecular machines led to the 2016 Nobel Prize in Chemistry, being awarded to Sauvage, Stoddart, and Feringa for their pioneering work.^{1.17}

Recently, the strategy has been shifted to synthesis of molecules which can be handled at the molecular level. Based on the size and nature of building blocks, self-assembly can be categorized into three main classes, i.e. atomic, molecular, and colloidal self-assemblies (Figure 1.4).^{1.18} The process of self-assembly not only covers bulk materials, but also it can apply to two-dimensional systems, i.e. surfaces and interfaces. Thus, on the basis of the systems and where it occurs, it can be classified as biological or interfacial. Further, based on its processing, it can be categorized as thermodynamic or kinetic self-assembly. Atomic, molecular, biological, and interfacial self-assemblies are covered under thermodynamic processes, while colloidal and some interfacial self-assemblies come under kinetic ones. Among these types of assemblies, atomic and biological self-assemblies are directional while others are random or nondirectional such as colloidal, molecular, and interfacial self-assemblies. Finally, as a result of self-assembly, spontaneous association can lead to generation of ordered structures in a range from angstrom to centimeter of diverse sizes and shapes. Herein, we specifically focus on the synthesis of different types of small aromatic molecular framework and aspects of their aggregation behaviour, morphological tunability, and consequent processibility or applicability. We try to give an account of the fluorene/quinoxaline core based scaffolds which have been designed to undergo spontaneous assembly/disassembly in response to environmental and chemical stimuli, including

biologically important or harmful analytes, or even in presence of trace water. Further, we illustrate the potential of these sensors with applications reaching out to different fields.

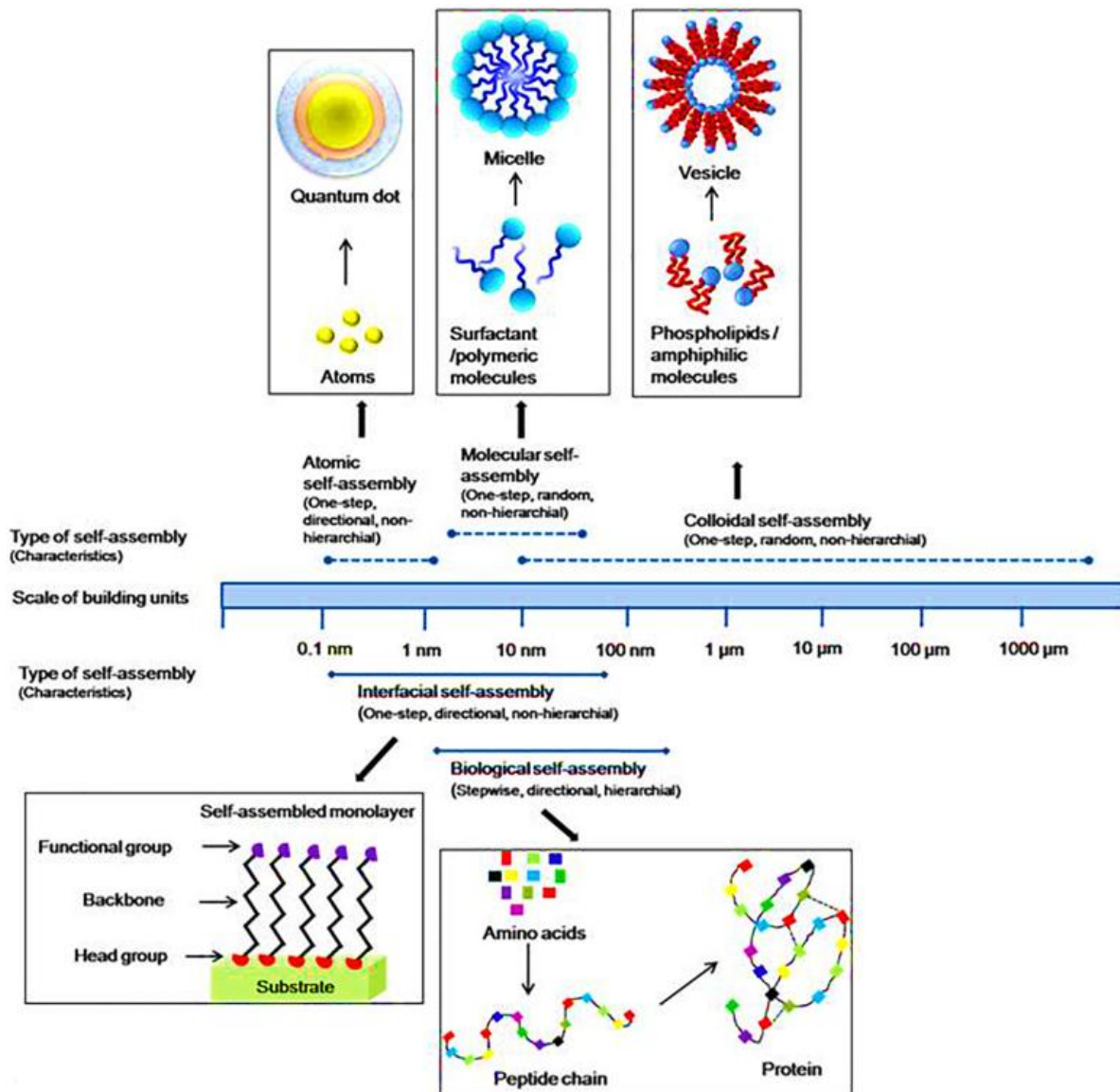


Figure 1.4: Schematic representation of atomic, molecular, colloidal self-assemblies based on size or nature of building units, and biological, interfacial on the basis of system where the self-assembly occurs.

1.2 Detection of Analytes: Stimuli instructed assembly/disassembly approach

Self-assembly and its reverse process i.e. disassembly are ubiquitous in nature. The self-assembly of biomolecules, driven by weak, noncovalent intermolecular interactions, brings about multicomponent complexes with a high level of structural hierarchy. In contrast, disassembly or dissociation, the reverse process of assembly, plays an indispensable role in modulating and terminating the actions of these supramolecular complexes. To regulate sophisticated biological processes, the assembly and disassembly processes are firmly controlled in living organisms via multiple and interconnected mechanisms. A well-established example is

the dynamics of cytoskeletons, such as constant assembling and disassembling of actin filaments. Such dynamics mediate multiple cell behaviours, including growth, motility and membrane internalization.^{1,19} Similarly, the tubulin assembly–disassembly cycle, being fueled by the hydrolysis of β -tubulin-bound GTP, enacts multifaceted roles in cell division and intracellular transport,^{1,20} and is modulated by microtubule polymerases (i.e., XMAP215) and depolymerases (i.e., MCAK). Besides microtubules and actin filaments, emerging evidence reveals that inflammasomes, as a class of supramolecular organizational centers,^{1,21} form upon danger signals and disassemble when the inflammation phase ends. The rapid assembly of inflammasomes indicates that, besides enzymatic reactions, ligand–receptor interactions (or molecular recognition) are able to catalyze molecular self-assembly. These fundamental facts in cell biology reveal that assembling to form multicomponent complexes is the forward process to initiate many biological events, and disassembly or dissociation is the reverse process to modulate or to terminate the actions of these complexes. Over the last few decade, considerable progress has been made in the field, which promises a fundamentally new approach for developing therapeutics for ameliorating human illness. Thus, it is worthwhile to review these studies for the future development of supramolecular medicine. Hence in this section we have highlighted the recent progress towards designing and controlling the assembly and disassembly of small molecules, both under cell free conditions and in the cellular environment. The dynamic consequences of the interplay between assembly and disassembly

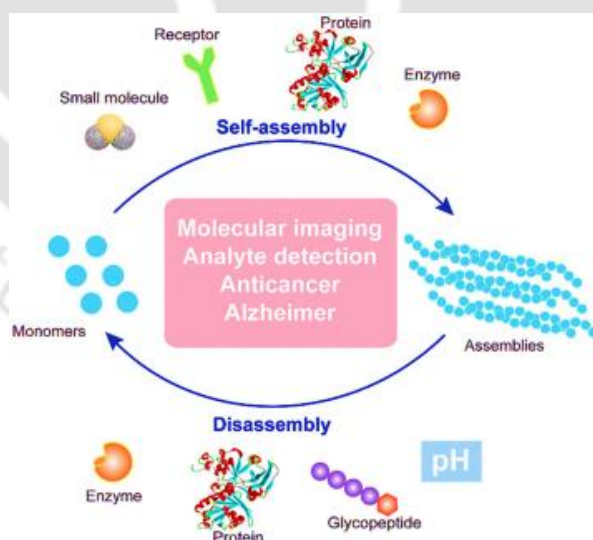


Figure 1.5: Schematic illustration of regulating dynamic assemblies via self assembly and disassembly processes for therapeutics and diagnostics.

play crucial roles in many complex physiological processes. In essence, the formation of assemblies from monomers and the dissipation of the assemblies are dynamic, reversible

processes, which promise applications in molecular imaging, analyte detection, anticancer therapy, and treatment of neurodegenerative diseases.

Hamachi et al. reported the combination of enzymatic reactions with a H_2O_2 -responsive hydrogel for the detection of variety of biomarkers through the naked eye.^{1,22} As shown in Figure 1.6, peptide precursor **1**, with a p-boronophenylmethoxycarbonyl (BPmoc) group at the N-terminus, reacts with H_2O_2 to generate unmodified peptide **2** and p-quinonemethide. The decomposition of the BPmoc group diminishes the intermolecular interactions and disassembles the nanofiber network of **1**, resulting in a gel–sol transition that is capable of sensing analytes.

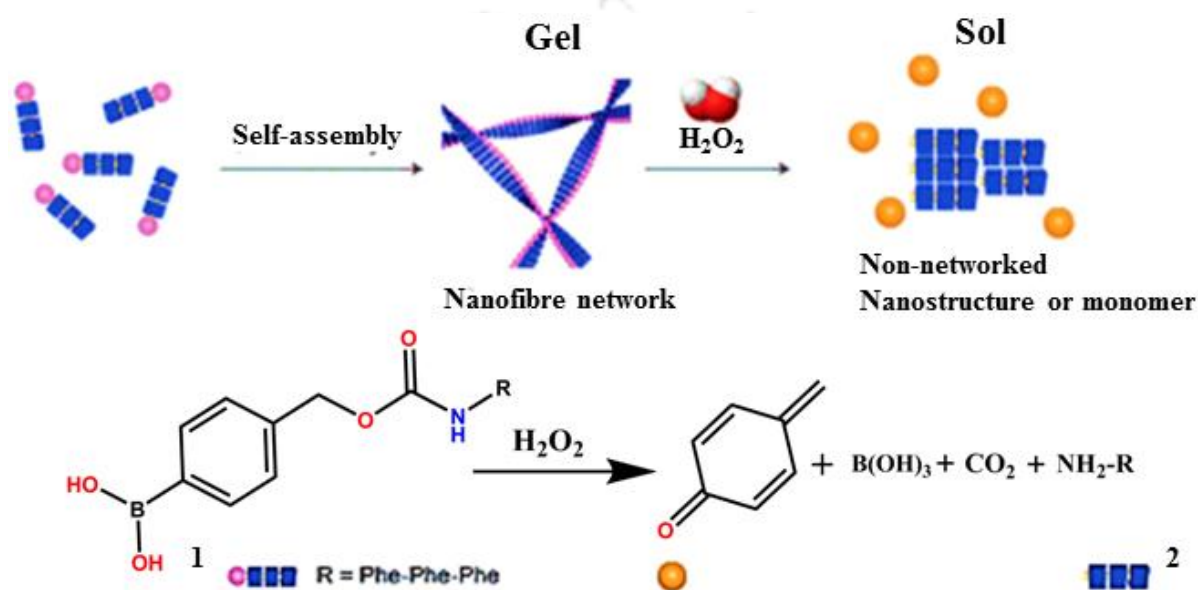


Figure 1.6: Schematic diagram of the self-assembly of **1** to form a nanofiber network (gel) and its degradation to **2** upon H_2O_2 oxidation.

As shown in Figure 1.7, probe molecule consists^{1,23} of a ligand (i.e., methotrexate) for targeting dihydrofolate reductase (eDHFR), a fluorophore (i.e., tetramethylrhodamine) for imaging, a hydrophobic module (i.e., phenylalanine) for tuning the self-assembling ability, and a linker. In aqueous solution, probe spontaneously forms spherical or oval aggregates, suppressing its fluorescence. The specific ligand–protein recognition causes the disassembly of the aggregates to light up the fluorescence, while a competitive inhibitor exchanges the probe to result in aggregates and a decrease of the fluorescence. Incubating with HeLa cells overexpressing GFP-fused eDHFR (HeLa-DG cell), strong intracellular fluorescence co-localizes with GFP fluorescence, suggesting that the binding between eDHFR and the ligand induces the disassembly of aggregates. Moreover, the release of probe, driven by the ligand exchange by a competitive inhibitor, significantly decreases the fluorescence inside the cells.

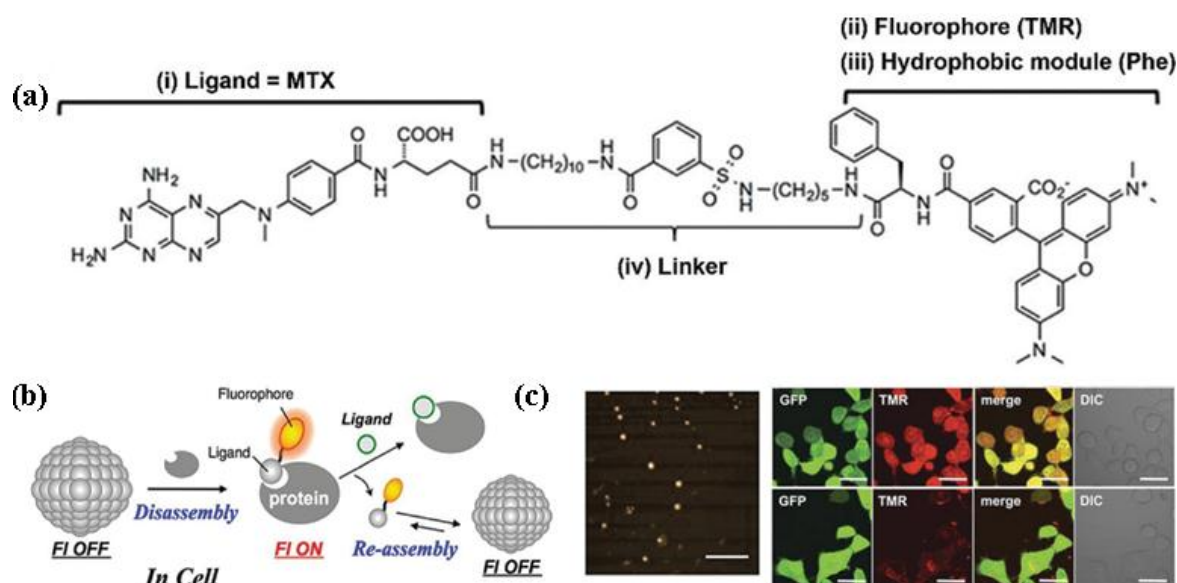


Figure 1.7: (a) Chemical structure of ligand-tethered probe for intracellular eDHFR imaging. (b) Schematic illustration of protein-responsive nanoaggregates for specific and reversible intracellular protein sensing. (c) Atomic force microscopy (AFM) image of the self-assembled probe (10 mM) (scale bar 500 nm) and CLSM images of the HeLa cell line stably overexpressing GFP-fused eDHFR (HeLa-DG cell) treated with probe (2 mM) for 12 h at 37 °C or with probe (2 mM) for 12 h at 37 °C, and then treated with TMP (10 mM) (scale bars, 20 μm).

π - π stacking as the non-covalent interaction usually occurs between the electron rich aromatic rings and the electron-deficient aromatic rings in assembling systems. The stacking can be classified into four patterns, including face-to-face stacking, wavelike stacking, crossing stacking, and mixing stacking, with increasing difficulty in shear sliding. The photophysical properties of luminophores are usually altered due to the electron distribution and energy transfer of the stacked aromatic rings in different stacking patterns.^{1.24-1.25} As a result, the fluorescence produced by π - π stacking in supramolecular assemblies is easily controlled, which greatly expands the application of such supramolecular luminescent materials.

Qi Lin and co-workers reported self-assembly of pillar[5]arene derivatives **1** and tripodal compound **2** via π - π stacking interactions turned on blue emission for both networks.^{1.26-1.27} The addition of Hg^{2+} to supramolecular network of **1**, and picric acid to that of **2** disrupted the self-assembly resulting in the quenching of blue fluorescence. Interestingly, the blue fluorescence can be recovered via the introduction of cyanide, which selectively interacted with Hg^{2+} (to form $\text{Hg}(\text{CN})_2$) and picric acid (deprotonating it to form HCN) thereby reinstating the self-assembly of **1** and **2**. **1** and **2** sensed Hg^{2+} and picric acid with a detection limit of 25.3 nM and 11.9 nM, respectively, and the subsequent compositions sensed cyanide with a detection limit of 77.1 nM and 0.745 μM, respectively (Figure 1.8).

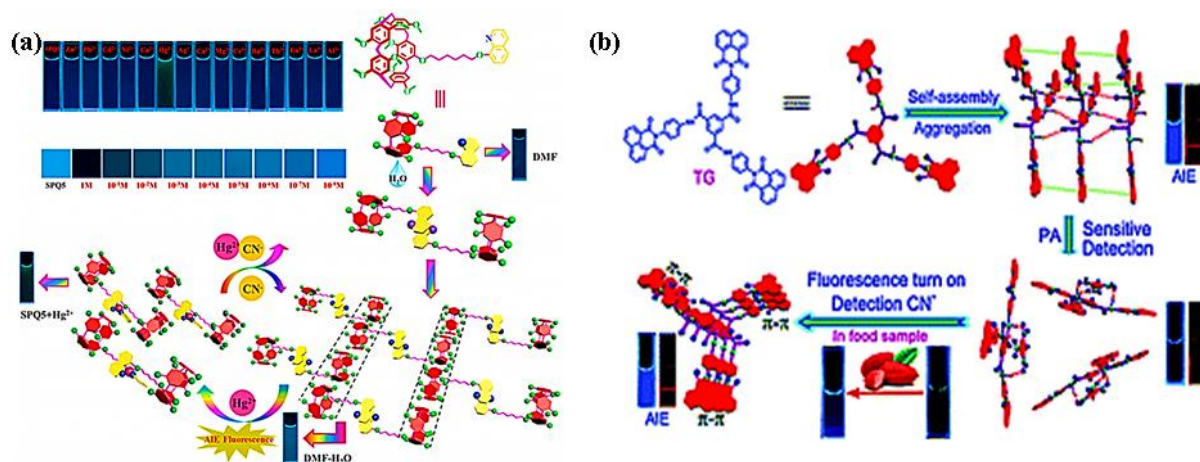


Figure 1.8: Illustrations of supramolecular self-assemblies of **1** (a) and **2** (b), the subsequent disruption to supramolecular network in the presence of Hg^{2+} and picric acid.

New strategies that can simultaneously detect and remove highly toxic environmental pollutants such as heavy metal ions are still in urgent need. Herein, Yang et al.^{1,28} successfully developed a fluorescent supramolecular polymer from a newly designed [2]biphenyl-extended pillar[6]arene equipped with two thymine sites as arms (**H**) and a tetraphenylethylene (TPE)-bridged bis(quaternary ammonium) guest (**G**). Interestingly, supramolecular assembly-induced emission enhancement (SAIEE) could be switched on upon addition of Hg^{2+} into the above-mentioned supramolecular polymer system to generate spherical-like supramolecular nanoparticles, due to the restriction of intramolecular rotation (RIR)-related AIE feature of **G**. Significantly, this supramolecular polymer with integrated modalities has been successfully used for real-time detection and removal of toxic heavy metal Hg^{2+} ions from water with quick response, high selectivity, and rapid adsorption rates, which could be efficiently regenerated and recycled without any loss via a simple treatment with Na_2S (Figure 1.9). The newly developed supramolecular polymer system combines the inherent rigid and spacious cavity of novel extended-pillarene host with the AIE characteristics of TPE-based guest, suggesting a great potential in the treatment of heavy metal pollution and environmental sustainability.

Yuan Xu reported a novel hydrazone Schiff base fluorescent probe $N'-(7-(\text{diethylamino})-2\text{-oxo-}2\text{H-chromen-}3\text{-yl)methylene)pyrazine-2-carbohydrazone}$ (**NPC**) (Figure 1.10),^{1,29} which self-assembled into nanoparticles in aqueous solution. Based on disassembly-induced emission and the site-specific recognition mechanism, the binding of **NPC** with HSA resulted in a fluorescence “turn-on” response. Probe **NPC** exhibited superior selectivity and sensitivity toward HSA with a detection limit of 0.59 mg L^{-1} in PBS and 0.56 mg L^{-1} in the urine sample

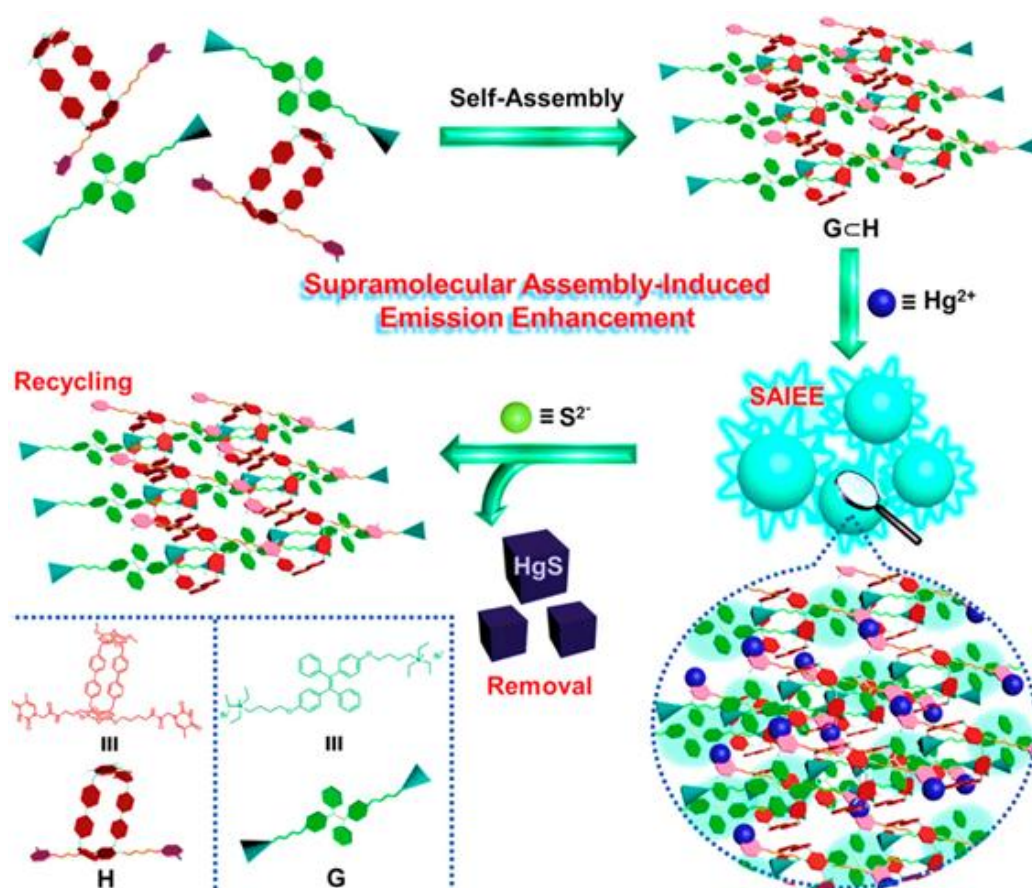


Figure 1.9: Schematic illustration of the sensing and removal of Hg²⁺ from water based on the “switch-on” fluorescence of the supramolecular polymers (GCH) and the regeneration–recycling process.

0.59 mg L⁻¹ in PBS and 0.56 mg L⁻¹ in the urine sample. The site-binding mechanism of NPC with HSA was explored by fluorescence quenching study, Job's plot analysis, HSA destruction, site marker displacement and molecular docking. Fluorescence imaging of HSA in MCF-7 cells was achieved by using a non-toxic NPC probe, suggesting that NPC could be applied to visualize the level of HSA in vivo. Using a simple test paper, the over expression of HSA in urine could be easily picked up for household measurement. In addition, this efficient platform combining site-binding and the disassembly-induced detection strategy will provide a new avenue to develop excellent biosensors for clinical diagnosis. The strategy of assembling-induced emission is efficiently applicable in the numbers of luminescent assembling systems, the molecular structure and function of which can be controlled precisely through assembly. Based on the intrinsic dynamic and reversible property of non-covalent interactions, assembly endows luminophores with controllable conformations or configuration switching and response to internal factors or external environment stimuli either chemically or physically. Supramolecular materials with well-organized structures can regulate the intermolecular

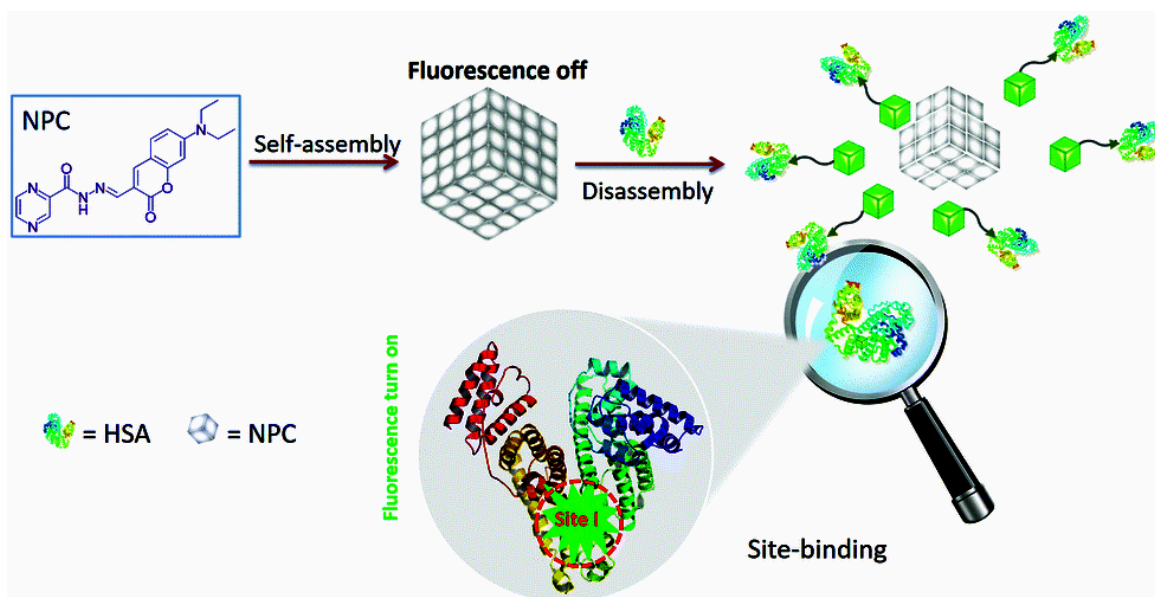


Figure 1.10: Schematic illustration for fluorescence detection mechanism of nanoprobe NPC toward HAS via assembly-disassembly pathway.

interactions and energy transfer processes effectively by the assembly or disassembly process hence can induce some unexpected luminescent properties that the independent component does not have. We provide a recap and discussion according to the types of building blocks and non-covalent driving forces between different components, including hydrogen bonding, host-guest interaction, π - π interaction and metal coordination interaction responsible for assembly/disassembly mechanism.

1.3 Importance of Sensing of small molecules

Fluorescent sensors have been widely applied in diverse fields, such as biology, physiology, medicine, and pharmacology. They have also been the subject of intense research interest on the part of many chemists and biologists. Compounds incorporating a binding site, a fluorophore, and a mechanism for communication between the two sites are called fluorescent chemosensors. The field of fluorescent chemosensors has been in existence for about 150 years. In this time, a large range of fluorescent chemosensors have been established for the detection of biologically and/or environmentally important/harmful neutral small species. Despite the progress made in this field, several problems and challenges still exist. Fluorescent sensor-based detection methods possess many advantageous features, such as simplicity, low cost, high sensitivity, facile adaptation to automated analysis, an ability to support spatially resolved imaging, and provide for diverse signal output modes. More broadly, fluorescent sensors offer an unique route for detecting biologically and/or environmentally important/harmful neutral analytes and can

help to uncover physiological and pathological functions of these analytes. Analyte detection by a fluorescent chemosensor is usually achieved through one or more common photophysical mechanisms, including chelation induced enhanced fluorescence (CHEF), intramolecular charge transfer (ICT), photoinduced electron transfer (PET), aggregation induced emission (AIE)^{1.30-1.32} and the number of approaches is still expanding. The early fluorescent chemosensors, concentrated mainly on the detection of metal ions rather than the detection of anions or neutral species due to the selective binding of metal ions in water being significantly easier than that of neutral species. However, more recently and since around 1980, we have witnessed a massive growth and development of the area catalyzed by the inspirational and pioneering work by the two fathers of modern chemosensors: de Silva and Czarnik.^{1.33} Since those pioneering days, different kind of fluorescent chemosensors and the scope of applicability is accelerating to include numerous relevant neutral analytes.

Small neutral molecules such as glutathione, folic acids are essential for our survival since they play a vital role in a range of physiological and pathological processes. Conversely, some small neutral molecules like nitroaromatics (explosives), and benzene group VOCs are a threat to public health and safety. For these important reasons we have tried to stimulate the development of fluorescent chemosensors, specially fluorene and quinoxaline based newly synthesized probes for the following neutral molecules detection over the research tenure.

1.3.1 Background of Glutathione (GSH) detection

Many life-threatening diseases start out with no obvious symptoms and are not easy to be diagnosed at an early stage but accompanying some abnormal biochemical indexes of molecules. It is necessary and significant to accomplish visual quantitative detection of biomolecules quickly and conveniently.^{1.34-1.36} Glutathione (GSH), a most abundant nonprotein thiol compound in mammalian and eukaryotic cells, plays a pivotal role in kinds of cellular functions like gene expression and signal transduction.^{1.37} Glutathione composed of glutamic acid, cysteine and glycine (Figure 1.11), can prevent free radicals and peroxides from damaging important intracellular components. Abnormal levels of these molecules have been linked to a number of diseases, such as liver damage, leucocyte loss, psoriasis, cancer and AIDS.^{1.38} When cells are under oxidative stress, there exists an imbalance between GSH and its oxidized form, glutathione disulfide (GSSG). The latter then rapidly converts into GSH under the action of GSH reductase, increasing of the ratio of GSH to GSSG and relieving the oxidative stress of cells. The alteration of the intracellular redox status (ratio of GSH to GSSG) is associated with numerous clinical diseases, suggesting that intracellular GSH could be used as an important clinical biomarker. Accordingly, the detection of these thiol

containing biomolecules in biological samples is very important. The aberrant GSH level can indicate the possibility of suffering disease and act as an important index for monitoring human health conditions. Therefore, the detection and quantification of GSH are necessary and significant, due to its vital biological and clinical importance.

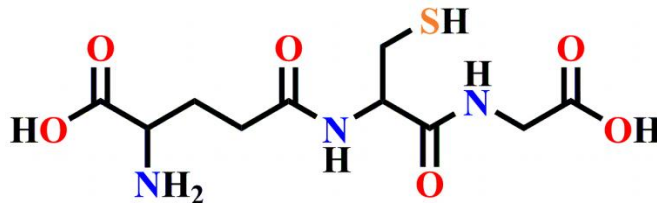


Figure 1.11: Chemical structure of Glutathione(GSH).

1.3.2 Background of Folic acid (FA) sensing

Folic acid (FA), a water soluble vitamin also known as vitamin M is responsible for synthesis of red blood cells. The common name of FA is vitamin B9.^{1.39} Its natural form is known as folate. FA molecule consists of bicyclic pterin moiety joined by a methylene bridge C(9)-N(10) to p-amino benzoic acid, which in turn is connected to L-glutamic acid with the help of peptide bond (Figure 1.12). FA is essential for various human metabolic activities. It is a major factor in the nucleic acid synthesis. It accelerates the cell division and therefore helps in growth and development of foetus.^{1.40} In human beings, folate level is found about 10 mg–30 mg. The normal level of folate in serum is about 5–15 ng/mL, while in cerebrospinal fluid it is about 16–21 ng/mL.^{1.41}

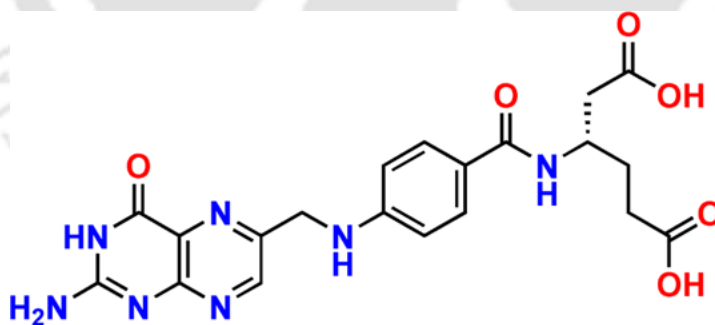


Figure 1.12: Chemical structure of Folic acid (FA).

In erythrocytes it is found in the range from 175 to 316 ng/mL.^{1.42} Liver consists of abundant amount of folate as compared to the blood and various tissues. The range below 5 ng/mL of serum folate indicate the symptoms of its deficiency, which causes a large number of disorders. Folate is also used in repairing and synthesis of methylate DNA especially during pregnancy. Its deficiency can lead various health problems.^{1.43} Hyperhomocysteinemia and cancer development

due to impaired DNA synthesis and repair could be the long-term complications of folate deficiencies.^{1.44} These concerns along with drawbacks of traditional analytical techniques, fluorimetric biosensing methods are designed for FA monitoring.

1.3.3 Background of Nitroaromatics (NACs) detection

One pressing concern in anti-terrorism and homeland security is explosive detection. Explosive bombs have been by far the most common form of terrorism, due to their ease of producing and deploying, and consequently killed tens of thousands of people as well as caused enormous property damage. The recent rise in global terrorism has stimulated the necessity of standoff/remote, sensitive and low-cost detection of explosives. In addition, given the widespread use of explosive formulations, the analysis of explosives has been of importance in forensic research, landmine detection, and environmental problems associated with explosive residues.^{1.45} The extensive use of explosives for military purpose has also raised concerns about environmental contaminations where they are produced and stored.^{1.46} Great public health threat, including anemia, carcinogenicity, abnormal liver function, cataract development and skin irritation, etc., could also be posed to both animals and human beings through short-term or long-term exposure of nitroaromatic explosives(NACs). Nitro aromatic compounds (NACs) such as 2,4,6-trinitrotoluene (TNT), 2,4-dinitrotoluene (DNT), 1,3,5-trinitro-perhydro-1,3,5-triazine (RDX), and picric acid (PA) (Figure 1.13), the main ingredients in explosives.

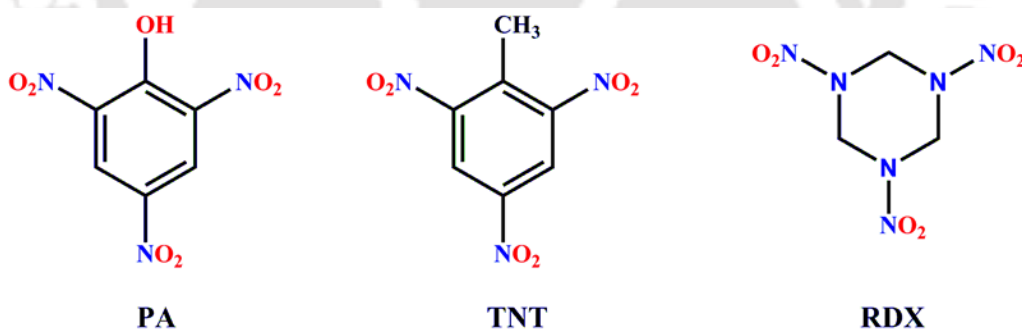


Figure 1.13: Chemical structure of main nitroaromatics(NACs).

These NACs are also continuously being released into the environment during their commercial production or leaching from military waste sites, mining activity, and space experiments. Degradation of these NACs leads to the generation of reactive nitrogen oxide species, which readily react with biological macromolecules and cause the formation of potent genotoxic and mutagenic metabolites.^{1.47-1.48} Thus, being able to detect NACs at ultra low levels has become an urgent issue in the interest of both national security and environmental protection. The analysis of fluorescence signals for the detection of NACs has emerged as a prominent technique by

virtue of its high detection sensitivity, selectivity, and applicability in both solution and solid phase.

1.3.4 Background of Volatile organic compounds (VOCs) sensing

Volatile organic compounds (VOCs) are one of the chief issues in the environment and their wide distribution has raised major concerns, in particular with environmental sciences. VOCs correspond to a class of organics that are characterized by their highly volatile nature under existing environmental conditions. The chemical characteristics (e.g., low water solubility, high lipid solubility, semi-volatility and ability to pass through biological membranes and accumulate in the fatty tissues) make them of great concern in the environment. The main subgroups of VOCs include halogenated organics, monocyclic aromatic hydrocarbons, organic sulfides and sulfoxides, BTEXs, THMs, acetone, and esters. VOCs may be of biogenic or anthropogenic origin. Anthropogenic sources raise more concern than natural sources. Major anthropogenic sources of VOCs to the aquatic environment are paints and coatings, gasoline, solvents, industrial and urban wastewaters, urban and rural run-offs, and atmospheric depositions. The analysis of VOCs is of growing interest due to their impact on global environmental conditions and human health. Apart from accumulating and persisting in the environment, VOCs contribute to the increased greenhouse effects and associated ozone depletion. Of total dissolved organic carbon, 10% is VOCs in relatively unpolluted waters and the concentrations are much higher in raw waters from different anthropogenic sources.^{1.49} Hence, to get deep insight into the behavior of VOCs, analytical techniques at environmental background levels ($\mu\text{g/L}$ and ng/L) become crucial. Despite a number of emerging VOC sensors and related analytical methods in recent years, this area still needs to be advanced due possible technical difficulties related to portability, sensitivity or sample processing. In fact, from the viewpoint of users, it would be better to get the testing result whenever and wherever possible, and that requires a portable device capable of both on-site detection and real-time monitoring.

1.4 Importance of moisture/trace water sensing

Water is one of the most important and essential substance not only in daily human life but also in chemistry. It is an important impurity that needs to be removed to perform many chemical and industrial production processes specially in manufacturing oils and petroleum product. Organic solvents are indispensable in the fields of materials, pharmaceuticals and chemical industries, and they participate in the synthesis, purification and analysis of compounds and materials.^{1.50} Small amounts of water can also induce corrosion and substantial damage on production lines or equipment. In particular, jet fuel must be free of water contamination for the safe operation of

aircrafts.^{1.51} Moisture in the air and surroundings plays a substantial role in industrial processes, chemical reactions and biological processes, hence controls the yield and selectivity of the final product for many sensitive chemical reactions. Furthermore, the water content in food products also affects their quality and stability during storage. Therefore, the detection of trace H₂O content is important and challenging in the food and food-related industries. Accordingly, efficient methods for the timely detection of amounts of water are highly valuable not only in synthetic laboratories but also for industrial applications. In addition, the accurate determination of water content in ethanol is also of great significance to fuels, alcoholic beverages, and their related industries.^{1.52} The most commonly used water content determination techniques are Karl Fischer titration and gas chromatography, which are time-consuming, and require special equipment and well-trained personnel. In contrast, fluorescence sensors have promising application potential in trace water assay, not only because of their simple operation and low cost, but also because of their rapid response and high sensitivity. Luminescent water sensors have attracted great interest because of their significant advantages over electrochemical sensors involving their capability for remote and in situ monitoring as well as the ease of their fabrication.^{1.53}

1.5 Concluding remarks and Objective of Thesis

The huge popularity and importance of the chemosensors, especially the optical (fluorogenic and chromogenic) chemosensors have attracted the attention of analytical chemists at large all over the world. However, the high demand of developing newer sensing probes are laid in their wide spread advantages and applications. All the above examples of the optical chemosensors and the related discussions clearly indicate that the field of chemosensing has entered an advanced phase in recent years. It is not enough anymore to just develop a system that is only selective to a specific target analyte. Several other factors like stability of the probe, water solubility, switch-on or ratiometric response, large stokes shift and extinction coefficient, non-cytotoxicity, cell permeability etc. have become equally important to be looked into. A number of mechanisms, including photoinduced electron transfer (PET), intramolecular charge transfer (ICT), metal–ligand charge transfer (MLCT), twisted intramolecular charge transfer (TICT), electronic energy transfer (EET), and fluorescence resonance energy transfer (FRET), and excimer/exciple formation have been used extensively to design fluorescent sensors. However fluorescent probes designed by these strategies often encounter drawbacks like aggregation-caused quenching effect, which bars them from being used at high concentrations and hence result in reduced fluorescence and compromised sensitivity. Recent development of a novel class of fluorogenic

molecules with aggregation-induced emission (AIE) characteristics based on conformational restriction has come to the limelight and the design and synthesis of AIE probes for biosensing and imaging applications has become a hot research subject. As, unlike the conventional fluorophores, AIE fluorogens (AIEgens) emit strongly in the aggregated state, it conveniently offers the solution to overcome the aggregation-caused quenching effect. However, even though these AIE active compounds are very interesting in nature, similarly addition of stimulus-responsive groups to self-assembled systems can enable a biological stimulus-driven assembly–disassembly mutual switch or structural composition/morphological transformation, thereby amplifying the imaging signal and/or enhancing the therapeutic effect. Metal ions and common biologically as well as environmentally important anions remain to be the central targets of the mostly developed optical probes for past decades. However, with the rapid advances in the chemical science, biology, health science and environmental science several new neutral guest species come to the forefront which needs to be detected using newer sensing probes. On the other hand, in general designing an effective sensing system that can selectively sense a neutral species is itself a difficult task due to the relatively weaker binding affinity as well as reactivity of the neutral guests. Hence, this thesis encompasses different environmentally important/harmful stimuli, sensor fabrication approaches, and outstanding selective detection applications based on the dis-assembly/disaggregation triggered fluorescence responses or the self-assembly/aggregation induced fluorescence performances. Stimulus-responsive self-assemblies with discriminative fluorescence performance have emerged as powerful tools for efficient biological processes, hence could alter the characteristics of probe moieties, particularly the size and shape, for a desired effect in imaging. Our prime concern was to introduce sensing systems that can rapidly sense target analytes by some form of optical responses which is conspicuous by naked eye; so that even an uneducated person could identify the sensing outcomes. Hence, all of the reported probes in this thesis are purposely designed to have the inherent feature of naked eye sensing ability. As summarized, objective of my thesis work is,

- ✚ To design, synthesis and characterization of small biocompatible fluorogenic and/or chromogenic probes, for the optical detection of target analytes via simple steps.
- ✚ To study the aggregation behavior of small biocompatible molecules in aqueous/mixed aqueous medium.
- ✚ Exploring the scope of introducing new sensing mechanisms involving stimuli triggered assembly/dis-assembly based luminescence responses other than AIE phenomenon.
- ✚ Application of the developed sensing probes in aqueous medium including environmental or biological samples.

References

- 1.1 J. F. Stoddart, *Supramol. Chem.*, 2015, **27**, 567–570.
- 1.2 J. W. Steed, D. R. Turner and K. Wallace, John Wiley & Sons, 2007
- 1.3 A. C. Mendes, E. T. Baran, R. L. Reis, and H. S. Azevedo, *Wiley Interdiscip. Rev. Nanomed. Nanobiotechnol.*, 2013, **5**, 582–612.
- 1.4 M. J. Webber, E. A. Appel, E. W. Meijer, and R. Langer, *Nat. Mater.*, 2016, **15**, 13–26.
- 1.5 C. Stoffelen, and J. Huskens, *Small*, 2016, **12**, 96–119.
- 1.6 K. Dinesh, S. Deepak, S. Gurmeet, S. Mankaran, and R.S. Mahendra, *ISRN Pharmaceutics*, 2012, **14**, 474830.
- 1.7 H. Su, Y. Wang, C. F. Anderson, J. M. Koo, H. Wang and H. Cui. *Chinese J. Polym. Sci.*, 2017, **35(10)**, 1194–1211.
- 1.8 J.-M. Lehn, *Science*, 2002, **295**, 2400.
- 1.9 K. Ariga, M. Nishikawa, T. Mori, J. Takeya, L. K. Shrestha, and J. P. Hill, *Sci. Technol. Adv. Mater.* 2019, **20**, 51–95.
- 1.10 R. Laishram, S. Bhowmik, and U. Maitra, *J. Mater. Chem. C*, 2015, **3**, 5885–5889.
- 1.11 P. Sutar, and T.K. Maji, *Chem. Commun.*, 2016, **52**, 8055–8074.
- 1.12 J.-C.G. Bunzli, S. Comby, A.-S. Chauvin, and C.D.B. Vandevyver, *J. Rare Earths.*, 2007, **25**, 257–274.
- 1.13 E.M. Surender, S. Comby, B.L. Cavanagh, O. Brennan, T.C. Lee and T. Gunnlaugsson, *Chem.*, 2016, **1**, 438–455.
- 1.14 The Nobel Prize in Chemistry 1987, Nobelprize.org. Nobel Media AB 2014. Web. 23 May 2017. http://www.nobelprize.org/nobel_prizes/chemistry/laureates/1987/
- 1.15 D.E. Barry, D.F. Caffrey and T. Gunnlaugsson, *Chem. Soc. Rev.*, 2016, **45**, 3244–3274.
- 1.16 D.J. Tranchemontagne, J.L. Mendoza-Cortes, M. O’Keeffe, and O.M. Yaghi, *Chem. Soc. Rev.*, 2009, **38**, 1257–1283.
- 1.17 The 2016 Nobel Prize in Chemistry. Press Release. Nobelprize.org. Nobel Media AB 2014. Web. 23 May 2017. http://www.nobelprize.org/nobel_prizes/chemistry/laureates/2016/press.html.
- 1.18 S. Yadav, A. Kumar Sharma and P. Kuma, *Front. Bioeng. Biotechnol.*, **8**, 127.
- 1.19 T. D. Pollard and J. A. Cooper, *Science*, 2009, **326**, 1208–1212.
- 1.20 A. Akhmanova and M. O. Steinmetz, *Nat. Rev. Mol. Cell Biol.*, 2015, **16**, 711–726.
- 1.21 A. Lu and H. Wu, *FEBS J.*, 2015, **282**, 435–444.
- 1.22 M. Ikeda, T. Tanida, T. Yoshii, K. Kurotani, S. Onogi, K. Urayama and I. Hamachi, *Nat. Chem.*, 2014, **6**, 511–518.

- 1.23 T. Yoshii, K. Mizusawa, Y. Takaoka and I. Hamachi, *J. Am. Chem. Soc.*, 2014, **136**, 16635–16642.
- 1.24 S. Burattini, B.W. Greenland, W. Hayes, M.E. Mackay, S.J. Rowan and H.M. Colquhoun, *Chem. Mater.*, 2011, **23**, 6–8.
- 1.25 D. Li, J. Wang, and X. Ma, *Adv. Optical Mater.*, 2018, **6**, 1800273.
- 1.26 X.-Q. Ma, Y. Wang, T.-B. Wei, L.-H. Qi, X.-M. Jiang, J.-D. Ding, W.-B. Zhu, H. Yao, Y.-M. Zhang and Q. Lin, *Dye. Pigment.* 2019, **164**, 279–286.
- 1.27 Q. Lin, X.-W. Guan, Y.-Q. Fan, J. Wang, L. Liu, J. Liu, H. Yao, Y.-M. Zhang and T.-B. Wei, *New J. Chem.*, 2019, **43**, 2030–2036.
- 1.28 D. Dai, Z. Li, J. Yang, C. Wang, J. R. Wu, Y. Wang, D. Zhang, and Y. W. Yang., *J. Am. Chem. Soc.*, 2019, **141**, 4756–4763.
- 1.29 Z. G. Wang, X. J. Yan, H. B. Liu, D. L. Zhang, W. Liu, C. Z. Xie, Q. Z. Li and J. Y. Xu, *J. Mater. Chem. B*, 2020, **8**, 8346–8355.
- 1.30 A. W. Czarnik, American Chemical Society, Washington, DC, 1993.
- 1.31 B. Daly, J. Ling and A. P. de Silva, *Chem. Soc. Rev.*, 2015, **44**, 4203–4211
- 1.32 R. T. K. Kwok, C. W. T. Leung, J. W. Y. Lam and B. Z. Tang, *Chem. Soc. Rev.*, 2015, **44**, 4228–4238.
- 1.33 A. P. de Silva, H. Q. N. Gunaratne, T. Gunnlaugsson, A. J. M. Huxley, C. P. McCoy, J. T. Rademacher and T. E. Rice, *Chem. Rev.*, 1997, **97**, 1515–1566.
- 1.34 G. Fu, Y. Zhu, K. Xu, W. Wang, R. Hou, X. Li, *Anal. Chem.* 2019, **91** (20), 13290–13296.
- 1.35 X. Wei, W. Zhou, S. T. Sanjay, J. Zhang, Q. Jin, F. Xu, D. C. Dominguez and X. Li, *Anal. Chem.*, 2018, **90** (16), 9888–9896.
- 1.36 G. Fu, S. T. Sanjay, W. Zhou, R. A. Brekken, R. A. Kirken, X. Li, *Anal. Chem.* 2018, **90** (9), 5930–5937.
- 1.37 H. Ma, X. Li, X. Liu, M. Deng, X. Wang, A. Iqbal, W. Liu and W. Qin, *Sens. Actuators, B*, 2018, **255**, 1687–1693.
- 1.38 G. Yin, T. Niu, T. Yu, Y. Gan, X. Sun, P. Yin, H. Chen, Y. Zhang, H. Li and S. Yao, *Angew. Chem., Int. Ed.*, 2019, **58**, 4557–4561.
- 1.39 Y. Amitai and G. Koren, *JAMA Pediatr.*, 2015, **169**, 1083.
- 1.40 A.E. Czeizel, *Prev. Nutr. Food Sci.*, 2009, **25**, 643–672.
- 1.41 E.H. Reynolds, B.B. Gallagher, R.H. Mattson, M. Bowers and A.L. Johnson, *Nature.*, 1972, **240**, 155–157.

- 1.42 L. Haandel, M.L. Becker, T.D. Williams, J.F. Stobaugh, J.S. Leeder, *Rapid Commun. Mass Spectrom.*, 2012, **26**, 1617–1630.
- 1.43 A. Hurdle, *Pathology.*, 1970, **2**, 193–198.
- 1.44 J. Mcguire, 2005, (<https://doi.org/10.1201/9781420026399.ch8>)
- 1.45 Y. Salinas, R. Martinez-Manez, M. D. Marcos, F. Sancenon, A. M. Costero, M. Parra and S. Gil, *Chem. Soc. Rev.*, 2012, **41**, 1261–1296.
- 1.46 N. P. Saravanan, S. Venugopalan, N. Senthilkumar, P. Santhosh, B. Kavita and H. G. Prabu, *Talanta*, 2006, **69**, 656–662.
- 1.47 D. Ownby, J. Belden, G. Lotufo and M. Lydy, *Chemosphere.*, 2005, **58**, 1153–1159.
- 1.48 B. Lachance, P. Robidoux, J. Hawari, G. Ampleman, S. Thiboutot and G. Sunahara, *Mutat. Res., Genet. Toxicol. Environ. Mutagen.* 1999, **444**, 25–39.
- 1.49 T. Huybrechts, J. Dewulf, H. Van Langenhove, *J. Chromatogr, A*, 2003, 1000, 283.
- 1.50 H.S. Jung, P. Verwilst, W.Y. Kim and J.S. Kim, *Chem. Soc. Rev.*, 2016, 45, 1242-1256.
- 1.51 Bitten, *J. Anal. Chem.*, 1968, **40**, 960–962.
- 1.52 W.-E. Lee, Y.-J. Jin, L.-S. Park, G. Kwak, *Adv. Mater.*, 2012, **24**, 5604-5609.
- 1.53 Q. Deng, Y. Li, J. Wu, Y. Liu, G. Fang, S. Wang and Y. Zhang, *Chem. Commun.*, 2012, **48**, 3009.



CHAPTER 2

Experimental Details & Characterization



Chapter 2

This chapter illustrates comprehensive information about the various materials and methodology followed for the synthesis and characterization of the probes (**L₁–L₇**) involved. It also describes the specification of analytical instruments used along with different experimental conditions and calculations followed to study their assembled/disassembled form and interaction with other neutral analytes.

2.1 General Information and Materials

All the reagents, solvents, starting materials, different metal salts and amino acids were procured from commercial purveyors and were used as received. All were of reagent grade. The solvents used were HPLC grade. For NMR analyses, deuterated solvent [(CD₃)₂SO] was purchased from Sigma-Aldrich. The UV-Visible absorption spectra were archived on a Perkin-Elmer Lambda-750 UV-Vis spectrophotometer using 10 mm path length quartz cuvettes in 250-700 nm wavelengths. Baseline correction was applied for all spectra. Fluorescence emission spectra were documented on a Horiba Fluoromax-4 spectrofluorometer using a 1 cm path length of quartz cuvettes having a slit width of 3 nm at 298 K. High-resolution mass spectrometry of all probes were carried out on a Waters Q-ToF Premier mass spectrometer. The solution-phase ¹H and ¹³C Nuclear Magnetic Resonance spectra were recorded using Bruker Advances 600 MHz, 500 MHz and 400 MHz NMR instruments. The chemical shifts were reported in parts per million (ppm) with the deuterated solvents. The following abbreviations are used to delineate spin multiplicities in ¹H NMR spectra: s = singlet; d = doublet; t = triplet; q = quartet, m = multiplet.

2.2 Synthetic procedure and characterization of the probes

2.2.1 Synthesis of **L₁** [6,6'-(9*H*-fluorene-2,7-diyl)bis(azanediyl)bis(methylene) bis(3(diethylamino)phenol

To a stirring solution (10mmol, 1.96g) of 2,7diaminofluorene in methanol (10 mL), 4-diethylamino salicaldehyde (25mmol, 4.8g) in 10 mL methanol was added and refluxed overnight. Condensation of these two reactants resulted a Schiff base product, filtered and

collected after frequent washing with cold methanol. The gradual addition of NaBH₄ in ice-cold condition reduced the Schiff base in its methanolic solution. After the reaction, water was added dropwise to the reaction mixture and extracted with CH₂Cl₂. The organic phase was separated and concentrated under reduced pressure to procure the dark brown product **L₁** (**Scheme 3.1, Chapter 3**). **L₁** was well characterized by ESI-MS, ¹H NMR, ¹³C NMR, FT-IR analysis. Calculated Yield =75%. ESI-MS (positive mode, m/z) calculated for C₃₅H₄₂N₄O₂ [M+H]⁺: 551.3580. Found: 551.3582. ¹H NMR of **L₁** (500 MHz, DMSO-d₆, δ ppm): 8.75 (s, 1H), 7.23-7.25 (d, 1H), 6.76-6.79 (d, 1H), 6.68 (s, 1H), 6.47-6.49(d, 1H), 6.15 (s, 2H), 6.02-6.04 (d, 1H), 4.89 (s, 2H), 3.57 (s, 1H), 3.18-3.24 (m, 4H), 1.02-1.06(t, 6H). ¹³C NMR (150 MHz, DMSO-d₆, δ ppm): 156.12, 147.15, 146.44, 143.17, 131.28, 131.21, 130.99, 118.58, 112.73, 111.05, 110.72, 103.46, 99.48, 43.99, 36.29, 15.17, 12.68. FT-IR (KBr pellets, cm⁻¹): 3367 (O-H), 3307 (N-H), 2963 (Aromatic C-H), 1619 (N-H bending), 1466 (Aromatic ring C=C stretching), 1256 (C-N stretch), 804 (N-H wagging).

2.2.2 Synthesis of **L₂** [2,2'-(9H-fluorene-2,7-diyl)bis(azanediy)bis (methylene)diphenol]

Similarly condensation of 2,7 diaminofluorene (10mmol, 1.96g) in 10 mL methanol with salicaldehyde (25mmol, 2.6g) followed by gradual addition of NaBH₄ yielded brown colored **L₂** (**Scheme 3.1, Chapter 3**), subsequently characterised by ESI-MS, ¹H NMR, ¹³C NMR, FT-IR analysis. Calculated Yield =73%.ESI-MS (positive mode, m/z) calculated for C₂₇H₂₄N₂O₂ [M+H]⁺: 409.1916. Found: 409.1957. ¹H NMR of **L₂** (500 MHz, DMSO-d₆, δ ppm): 9.46 (s, 1H), 7.26-7.28 (d, 1H), 7.19-7.21 (d, 1H), 7.01-7.04 (t, 1H), 6.80-6.81(d, 1H), 6.73 (s, 1H), 6.70-6.71 (d, 1H), 6.50 (s, 1H), 5.80 (s, 1H), 4.20 (s, 2H), 3.57(s, 1H). ¹³C NMR (150 MHz, DMSO-d₆, δ ppm): 155.44, 143.53, 132.83, 128.67, 127.87, 120.01, 119.53, 119.21, 118.95, 111.80, 116.98, 115.26, 31.74, 29.47. FT-IR (KBr pellets, cm⁻¹): 3283 (O-H), 2920 (N-H), 2851 (Aromatic C-H), 1614 (N-H bending), 1461 (Aromatic ring C=C stretching), 1245(C-N stretch), 813 (N-H wagging).

2.2.3 Synthesis of **L₃** [N²,N⁷-bis(4-(dimethylamino)benzyl)-9H-fluorene-2,7-diamine]

Synthesis of **L₃** is similar to that of **L₁** and **L₂**. 4-dimethylamino benzaldehyde (25mmol, 3.72g) was refluxed with 2,7 diaminofluorene (10mmol, 1.96g) in 10 mL methanol followed by reduction with NaBH₄ resulted **L₃** (**Scheme 3.1, Chapter 3**), subsequently characterised by ESI-MS, ¹H NMR, ¹³C NMR, FT-IR techniques. Calculated Yield =75%. ESI-MS (positive mode, m/z) calculated for C₃₁H₃₄N₄ [M]⁺: 462.2874 Found: 462.2880. ¹H NMR of **L₃** (500 MHz, DMSO-d₆, δ ppm): 7.62-7.65 (d, 1H), 7.21-7.22 (d, 1H), 7.13 (s, 1H), 6.73-6.75 (d, 1H), 6.66(s, 1H), 6.62-6.64 (d, 1H), 6.46 (s, 1H), 4.09 (s, 1H), 2.98 (s, 3H). ¹³C NMR (150 MHz, DMSO-d₆, δ

ppm): 154.68, 142.92, 143.48, 128.55, 124.88, 118.92, 112.91, 111.50, 109.63, 46.95, 40.70, 36.54. FT-IR (KBr pellets, cm^{-1}): 2920 (N-H), 2850 (Aromatic C-H), 1607 (N-H bending), 1464 (Aromatic ring C=C stretching), 1226 (C-N stretch), 805 (N-H wagging).

2.2.4 Synthesis of L_4 [N^2, N^7 -bis (naphthalene-1-yl) methyl-9H-fluorene-2, 7-diamine]

The mixture of 10mmol (2g) of 2,7diaminofluorene and 25mmol (3.9g) of 1-naphthaldehyde were stirred and refluxed in 50 mL of methanol overnight. Condensation of these two reactants produced a deep yellow color solid Schiff base product, filtered and collected after frequent washing with cold methanol. The gradual addition of NaBH_4 reduced the Schiff base in its methanolic solution. After the reaction, water was added drop by drop to the reaction mixture and extracted with CH_2Cl_2 . The organic phase was separated and concentrated under reduced pressure to procure the crude product L_4 (Scheme 4.1, Chapter 4). L_4 was well characterized by ESI-MS, ^1H NMR, ^{13}C NMR, FT-IR analysis. Calculated Yield =74%. ESI-MS (positive mode, m/z) calculated for $\text{C}_{35}\text{H}_{28}\text{N}_2$: 476.2252. Found: 476.2330. ^1H NMR of L_4 (400 MHz, DMSO-d_6 , δ ppm): 8.16 (d, 1H), 7.95-7.97 (m, 1H), 7.83 (d, 1H), 7.46-7.58 (m, 3H), 7.31 (d, 1H), 6.78 (s, 1H), 6.58-6.61 (dd, 1H), 6.11-6.14 (t, 1H), 4.72 (d, 2H), 3.60 (s, 1H). ^{13}C NMR (150 MHz, DMSO-d_6 , δ ppm): 147.35, 143.56, 135.70, 133.79, 131.60, 131.51, 128.90, 127.66, 126.48, 126.12, 125.89, 125.44, 124.07, 119.00, 111.39, 109.33, 45.47, 36.82. FT-IR (KBr pellets, cm^{-1}): 3370 (N-H), 3050 (Aromatic C-H), 1621(N-H bending), 1474 (Aromatic ring C=C stretching), 1323 (C-N-C asymmetric stretch), 1264 (C-N stretch), 735 (N-H wagging).

2.2.5 Synthesis of L_5 [6H-indolo[3,2-b]quinoxaline]

To a suspension of ortho-phenylene diamine (108.14 mg, 1 mmol) in 30 ml glacial acetic acid, isatin (176.55 mg, 1mmol) was added portionwise at room temperature. The reaction mixture was allowed to reflux overnight. After cooling to room temperature, ice cold water was added to get the precipitate. The precipitate was then filtered off and washed several times with methanol/acetic acid followed by ether to obtain the pure yellow solid product L_5 (Scheme 5.1, Chapter 5). L_5 was well characterized by ESI-MS, ^1H NMR, ^{13}C NMR, FT-IR analysis. Calculated yield =90%. ESI-MS (positive mode, m/z) calculated for $\text{C}_{14}\text{H}_9\text{N}_3$ [$\text{M}+\text{H}$] $^+$: 220.0876; found: 220.0894; ^1H NMR (600 MHz, DMSO-d_6 , δ ppm): 12.03 (s, 1H), 8.35 (d, 1H), 8.309 (d,1H), 8.079 (d,1H), 7.86(d, 1H), 7.656 (t, 1H), 7.711 (t, 1H), 7.581 (d, 1H), 7.37-7.408 (m, 1H); ^{13}C NMR (150 MHz, DMSO-d_6 , δ ppm):146.36, 143.74, 140.68, 132.67, 131.11, 129.37, 127.94, 125.19, 124.46, 122.59, 119.26, 115.21, 112.63; FT-IR (KBr pellets, cm^{-1}): 3092(N-H stretching), 2925(C-H stretching), 1719(C-H bending), 1615(C=N), 1340(C-N), 753(N-H wagging).

2.2.6 Synthesis of **L₆** [3-nitro-6H-indolo[3,2-b]quinoxaline]

Similarly, to a suspension of 4-nitro ortho-phenylene diamine (153.14 mg, 1 mmol) in 25 mL glacial acetic acid, isatin (176.41 mg, 1 mmol) was added portion-wise at room temperature. The reaction mixture was allowed to reflux overnight. After stirring for 24 hours, it was cooled to room temperature, and crushed ice was added slowly to get the precipitate. The precipitate was then filtered off and washed several times with methanol/acetic acid followed by ether to obtain the pure brown solid product **L₆** (**Scheme 6.1, Chapter 6**). **L₆** was well characterized by ESI-MS, ¹H NMR, ¹³C NMR, FT-IR analysis. Calculated yield = 85%. ESI-MS (positive mode, m/z) calculated for C₁₄H₈N₄O₂ [M+H]⁺: 265.0726; found: 265.0723; ¹H NMR (600 MHz, DMSO-d₆, δ ppm): 9.045 (s, 1H), 8.578 (s, 1H), 8.444 (d, 1H), 8.306 (d, 1H), 8.257 (d, 1H), 7.9561 (d, 1H), 7.698-7.660 (m, 1H), 7.382-7.349 (m, 1H); ¹³C NMR (150 MHz, DMSO-d₆, δ ppm): 148.61, 146.39, 145.00, 143.22, 138.16, 135.48, 133.76, 130.41, 125.21, 124.10, 116.63, 114.92, 111.91, 111.11; FT-IR (KBr pellets, cm⁻¹): 3091(N-H stretching), 2924(C-H stretching), 1719(C-H bending), 1618(C=N), 1521(N-O asymmetric stretch), 1337(N-O symmetric stretch), 750(N-H wagging).

2.2.7 Synthesis of **L₇** [6H-indolo[2,3-b]quinoxalin-3-amine]

Hydrazine monohydrate (4.0 mL) was added drop wise to the mixture of compound **L₆** (2.0 g) and Pd/C 10 % (.15g, cat) in methanol (50 ml). After refluxing for 24 hours, the solution was filtered through celite to remove Pd/C. Evaporation of the solvent gave **L₇** as a yellow powdery solid, dried under vacuum (**Scheme 7.1, Chapter 7**). **L₇** was well characterized by ESI-MS, ¹H NMR, ¹³C NMR, FT-IR analysis. Calculated yield = 90%. ESI-MS (positive mode, m/z) calculated for C₁₄H₁₀N₄ [M+H]⁺: 235.0984; found: 235.0932; ¹H NMR (500 MHz, DMSO-d₆, δ ppm): 11.689 (s, 1H), 8.251-8.238 (d, 1H), 8.186-8.173 (d, 1H), 7.994-7.979 (d, 1H), 7.618-7.605 (d, 1H), 7.593-7.7.482 (t, 1H), 7.379-7.346 (t, 1H), 6.936 (s, 2H), 6.777- 6.769 (d, 1H); ¹³C NMR (150 MHz, DMSO-d₆, δ ppm): 146.32, 145.21, 144.72, 136.94, 136.56, 135.24, 132.10, 131.30, 124.32, 123.43, 119.40, 115.86, 114.87, 112.89; FT-IR (KBr pellets, cm⁻¹): 3214(N-H stretching), 2923(C-H stretching), 1706(C-H bending), 1595(C=N), 1391(C-N stretch), 746(N-H wagging).

2.3 UV-Vis and Fluorescence Spectral Studies

Stock solutions of different analytes (metals, amino acid, carboxylic acids; 50 × 10⁻³ mol L⁻¹) were prepared in water, whereas stock solutions of different NACS and VOCs (50 × 10⁻³ mol L⁻¹) were prepared in methanol and DMSO respectively. Stock solution of probes **L₁₋₆** (1 × 10⁻³ mol

L^{-1}) were prepared in DMSO. For fluorescence selectivity experiments, the solution of probes was then diluted to 2×10^{-6} mol L^{-1} with Millipore water by taking only 4 μ L of stock solution and making the final volume 2 mL except L_5 . For L_5 , the solution of probe was diluted to 5×10^{-6} mol L^{-1} with Millipore water by taking the only 10 μ L of stock solution and making the final volume 2 mL. In fluorescence titration experiments, a quartz optical cell of 10mm pathlength was filled with a 2.0 mL solution of respective probes to which various analytes were gradually added using a micropipette. For the competitive selectivity experiment, fluorescence emission of the 'chemosensor-sensed guest' ensemble was collected in the absence and presence of the excess (50 equiv.) competitive analytes. For fluorescence measurements, $L_{1,3}$ was excited at 315 nm, and emission was procured from 335 nm to 650 nm whereas L_4 was excited at 330nm, and emission was procured from 350 nm to 650 nm. $L_{5,6}$ was excited at 400 nm, and emission was recorded from 420 nm to 650nm.

Stock solution of L_7 (1×10^{-3} mol L^{-1}) was prepared in DMSO. For fluorescence selectivity experiments, the solution of L_7 was further diluted to 2×10^{-6} mol L^{-1} with different organic solvents like, millipore water, methanol, acetonitrile, dimethylformamide, dimethylsulfoxide, tetrahydrofuran, ethylacetate, acetic acid and hexane by taking only 4 μ L of stock solution and making the final volume 2 mL. In fluorescence titration experiments, a quartz optical cell of 10mm pathlength was filled with a 2.0 mL solution of L_7 in water-other solvent systems, with a v:v ratio in the range of 0-100% with an increment of 10%. For fluorescence measurements, L_7 was excited at 410 nm, and emission was procured from 420 nm to 650 nm.

2.4 Estimation of the Apparent Binding Constant

Probes L_1 , L_4 and L_6 with a sufficient concentration of 2 μ M in water was titrated with varying analyte concentrations. Thus the apparent binding constant for forming the **Probe-analyte** complex was assessed utilizing the Benesi–Hildebrand (B–H) plot (**Equation 1**).

$$1/(I-I_0) = 1/\{K(I_{\max}-I_0) C\} + 1/(I_{\max}-I_0) \quad (1)$$

I_0 is the emission intensity of probes at maximum (λ_{\max}), and I is the recorded emission intensity at that particular wavelength in the presence of a specific concentration of the analyte (C). I_{\max} is the maximum emission intensity value obtained at λ_{\max} during titration with varying analyte concentrations. K is the apparent binding constant (M^{-1}) and was determined from the linear plot's slope.

2.5 Stern-Volmer Plot

The quenching behaviour of **L₅** and **L₇** were studied by Stern-Volmer equation,

$$I_0 / I = 1 + K_{sv} [Q], \quad (2)$$

where I_0 , I are the fluorescence intensities before and after addition of the quencher, K_{sv} is the Stern- Volmer quenching rate constant and $[Q]$ is the concentration of the quencher.

Detection Limit

2.6 Detection limit (LOD)

The detection limit (**L₁₋₇**) was evaluated based on the fluorescence titration changes. The fluorescence emission spectrum of respective probe was computed ten times, and the standard deviation of the blank measurement was obtained. The fluorescence emission at λ_{max} was plotted as a concentration of added analyte to gain the slope. The detection limits were calculated using the following equation:

$$\text{Detection limit} = 3\sigma/k \quad (3)$$

where σ is the standard deviation of blank measurement, and k is the slope between the fluorescence emission intensity versus [analyte]. The conversion to ppm/ppb unit was done considering molecular weight of analytes.

2.7 Field Emission Scanning Electron Microscope (FESEM) Studies

Morphology of **L₁**, **L₁-Hg²⁺**, **L₄**, **L₄-FA**, **L₅**, **L₅-PA**, **L₆**, **L₆-mesitylene** complexes were imaged separately using Gemini 300 FESEM (Carl Zeiss) instrument. Images of **L₇** in different solvents were acquired using same instrument. The samples were prepared by drop-casting (2 μ M), the DMSO/Water mixture on Al-foil wrapped coverslip, then coated with Au and dried under vacuum before the imaging.

2.8 Dynamic light scattering measurement

Dynamic light scattering (DLS) experiments were performed on Malvern Zetasizer Nano ZS instrument equipped with a 4.0 mW He-Ne laser running at a wavelength of 633 nm. The samples and the background were measured at room temperature (25 °C) at a scattering angle of 173°. DLS experiments were executed with optically clear solutions of respective probes (**L₁₋₆**) (2 μ M) in water with 50 equivalents of analytes and **L₇** (2 μ M) in different solvents. The solution was equilibrated for 60 minutes before taking the measurements.

2.9 Fluorescence Microscopy

The freshly prepared samples of L_{1-6} (2 μ M), L_{1-6} -analyte complexes (probes mixed with 50 equivalents of analytes), and only analytes were drop-casted (5 μ l) on a glass slide and were entirely dried at room temperature followed by image acquisition using a Fluorescence microscope (Eclipse Ti-U, Nikon, USA) with a blue filter. For L_7 , probe (2 μ M) in different solvents were drop-casted in similar manner and allowed for image acquisition.

2.10 Measurement of fluorescence lifetime

Fluorescence lifetimes were evaluated utilizing the time-correlated single-photon counting (TCSPC) method in the Edinburgh Instrument Life-Spec II spectrometer. The samples (L_{1-6} , L_{1-6} -analytes, L_7 in different solvents) were excited at respective excitation wavelengths keeping the emission wavelength fixed as mentioned earlier using a pulsed diode laser. The fluorescence decays were surveyed by the re-convolution method using the FAST software provided by Edinburgh Instruments.

2.11 Photoluminescence Quantum Yield

The quantum yield is defined as the ratio of photon emitted and the ratio of photon absorbed. We had pursued the Petite Integrating Sphere method to determine the quantum yield by Horiba Jobin Yvon Fluoromax-4 Spectrofluorometer. It was determined in 100% aqueous medium for L_{1-6} (2 μ M), L_{1-6} -analyte complex (L mixed with 50 equivalents of analytes) keeping respective excitation wavelengths fixed as mentioned earlier. To determine the quantum yield, the equation we employed was (as per the instruction written on the official website of Horiba),

$$\Phi = [(E_c - E_a) / (L_a - L_c)] \quad (4)$$

Where E_c = Emission of the sample, E_a = Emission of the blank, L_c = Scatter of the sample & L_a = Scatter of the blank.

We have calculated the quantum yield of probe L_7 in different organic solvents by Parker-Rees method^{2,1} using quinine sulphate as reference (0.1 M H_2SO_4). The formula for quantum yield calculation by Parker-Rees method is as follows.

$$\Phi_s = (A_r F_s n_s^2 / A_s n_r^2 F_r) \Phi_r \quad (5)$$

where Φ_r is the quantum yield of reference 0.1 M quinine sulphate solution and Φ_s is the quantum yield of sample. A_r and A_s are the absorbance of reference and samples respectively. F_r and F_s are the integrated area of fluorescence intensity for reference and samples respectively and n_r and n_s are the refractive indices of reference and samples respectively.

2.12 Cytotoxic Effect on HeLa Cells

An MTT assay determined the cytotoxic effect of the **L₄** and **L₄-FA** complex on cultured HeLa cells as per the manufacturer's instruction (Sigma-Aldrich, MO, USA). HeLa cells were initially cultivated in a 25 cm² tissue culture flask in DMEM medium boosted with 10% (v/v) FBS, streptomycin (100 µg/mL), and penicillin (100 µg/mL) under a humidified atmosphere of 5% CO₂ in an incubator until the cells were approximately 90% convergent. Before MTT assay, cells were trypsinized and seeded into 96 well tissue culture plates at a cell density of 10⁴ cells per well and incubated with varying concentrations (0, 2, 4, and 8 µM) of the **L₄** and folic acid (0, 6.25, 12.5, 25, 50 and 100 µM) prepared in methanol solvent (0.1% v/v) and incubated for a period of 24 h under 5% CO₂. Solvent control samples (cells incubated in 0.1% methanol) were also included in parallel sets. Following incubation, the growth media was carefully aspirated, and fresh DMEM containing MTT solution was included in the wells. The plate was incubated for 4 h at 37° C. Following incubation, the supernatant was collected, and the insoluble colored formazan product was solubilized in DMSO, and its absorbance was determined in a microtiter plate reader (Infinite M200, TECAN, Switzerland) at 570 nm. The assay was accomplished for each combined concentration of the test samples. Data analysis and determination of standard deviation was executed with Microsoft Excel 2010 (Microsoft Corporation). In the MTT assay, the absorbance for the solvent control cells was considered 100% cell viability. The absorbance for the treated cells was compared to determine % cell viability concerning the solvent control.

2.13 Cytotoxic Potential of **L₅** and Live Cell Imaging for Detection of Picric Acid

An in vitro MTT assay was conducted to ascertain the cytotoxic effect of **L₅** on HeLa cells (human cervical carcinoma cells). MTT (3-(4,5-Dimethylthiazol-2-yl)-2,5-Diphenyltetrazolium Bromide) solution was procured from Sigma-Aldrich, USA. HeLa cells were initially grown in 25 cm² tissue culture flask in Dulbecco's modified Eagle medium (DMEM) supplemented with 10% (v/v) fetal bovine serum (FBS), penicillin (100 µg/mL) and streptomycin (100 µg/mL) at 37 °C in a CO₂ incubator. HeLa cells were then seeded onto 96-well tissue culture plates (approximately 10⁴ cells per well) and incubated in separate sets with various concentrations of **L₅**, **L₅-picric acid** complex and picric alone (2.5 µM, 5.0 µM, 7.5 µM and 10 µM each) made in DMEM for a period of 24 h at 37 °C in a CO₂ incubator. Untreated HeLa cells were also incubated in parallel sets under the same conditions. Following 24 h incubation, the media was carefully removed and fresh DMEM containing MTT solution was added to the cells and incubated for 4 h at 37 °C in a CO₂ incubator. Following incubation, the MTT solution was

gently aspirated and the insoluble and coloured formazan product was solubilized in DMSO. The absorbance of the solution was subsequently measured in a microtiter plate reader (Tecan, Austria GmbH) at 570 nm against a reference of 640 nm. MTT assay for every sample was performed in six sets. The absorbance obtained for the untreated cells (control samples) represented 100% cell viability. The absorbance obtained for the treated cells was compared to the control to ascertain the % cell viability. HeLa cells were grown in 25 cm² tissue culture flask in Dulbecco's modified Eagle medium (DMEM) supplemented with 10% (v/v) fetal bovine serum (FBS), penicillin (100 µg/mL) and streptomycin (100 µg/mL) at 37 °C in a CO₂ incubator. Subsequently, HeLa cells were seeded into confocal dish (20 mm diameter) and grown in DMEM medium at 37 °C in a CO₂ incubator to obtain around 80% confluency. The cells were then washed thrice with sterile phosphate buffered saline (PBS) and incubated with 10 µM L₅ in DMEM at 37 °C for 1 h in a CO₂ incubator. The cells were then washed with sterile PBS in order to remove excess L₅ and their images were acquired using a confocal microscope (Zeiss LSM 880, Germany). The excitation wavelength used for the laser was 405 nm for blue emission. In a separate set, 10 µM picric acid made in DMEM was added to HeLa cells pre-treated with L₅ for 1 h. Following addition of picric acid, the cells were further incubated for 1 h. The cells were then washed with sterile PBS and their images were acquired with a confocal microscope as mentioned earlier.

2.14 Theoretical investigations (DFT study)

DFT optimizations of L₁, L₁-GSH and L₁-Hg²⁺ complex were accomplished with the exchange correlation function B3LYP and the basis set 6-31G (d,p) for C,H, N and O atoms and LANL2DZ for Hg atoms incorporating in the Gaussian 09 package.^{2,2}

DFT optimizations of L_{4,6} and L_{4,6}-analytes (FA/PA/mesitylene) complexes were accomplished with the B3LYP/ 6-31G (d,p) method basis set using the Gaussian 09 program.^{2,3}

The ground state geometry was carried out to optimize by using DFT at B3LYP/6-311G (d, p) level. TDDFT computations were then carried out based on the optimized ground state geometries. In addition, probe L₇ in vacuo, water, methanol, tetrahydrofuran and acetonitrile solvents were done using the Time dependent Self-Consistent Field (TD-SCF) method and Integral equation formalism Polarizable Continuum Model (IEF-PCM).^{2,4-2.5} The corresponding calculations were obtained by the methods of Gaussian 09 package.

References

- 2.1 C. A. Parker and W. T. Rees, *Analyst*, 1960, **80**, 587-600.
- 2.2 J. P. Nandre, S. R. Patil, S. K. Sahoo, C. P. Pradeep, A. Churakov, F. Yu, L. Chen, C. Redshaw, A. A. Patil and U. D. Patil, *Dalton Trans.*, 2017, **46**, 14201–14209.
- 2.3 M. Fisch, G. Trucks, H. Schlegel, G. Scuseria, M. Robb, J. Cheeseman, G. Scalmani, V. Barone, B. Mennucci and G. Petersson, *Gaussian 09 (Revision A. 02)*, Wallingford, CT, 2009.
- 2.4 J. Tomasi, B. Mennucci and E. Cance, *THEOCHEM*, 1999, **464**, 211.
- 2.5 A. D. Becke, *J Chem Phys* 1993, **98**, 5648-5652.



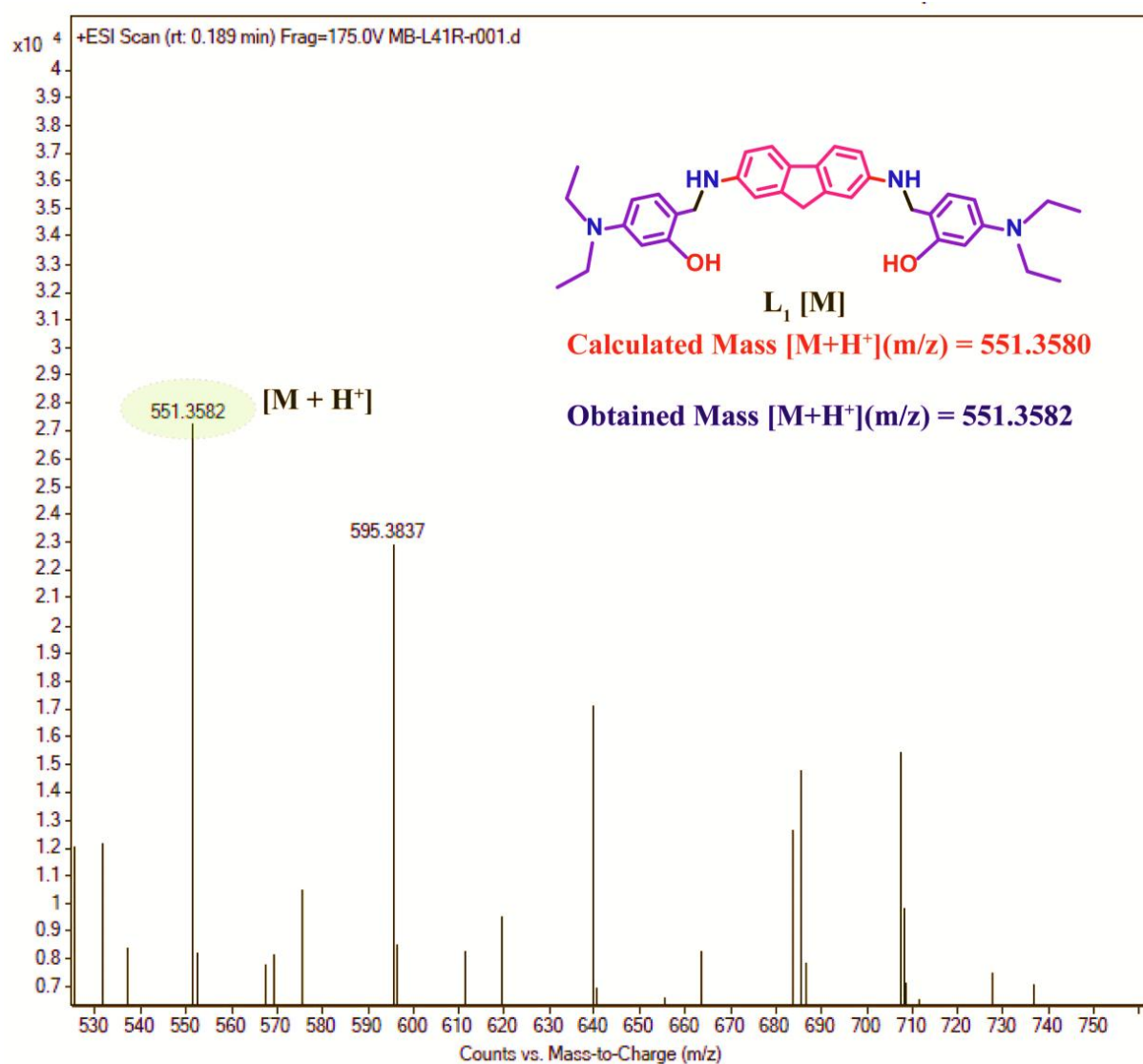
Appendix - Chapter 2

Figure A2.1: ESI-MS spectra of L₁ in 1:1 water-acetonitrile in positive ionization mode.

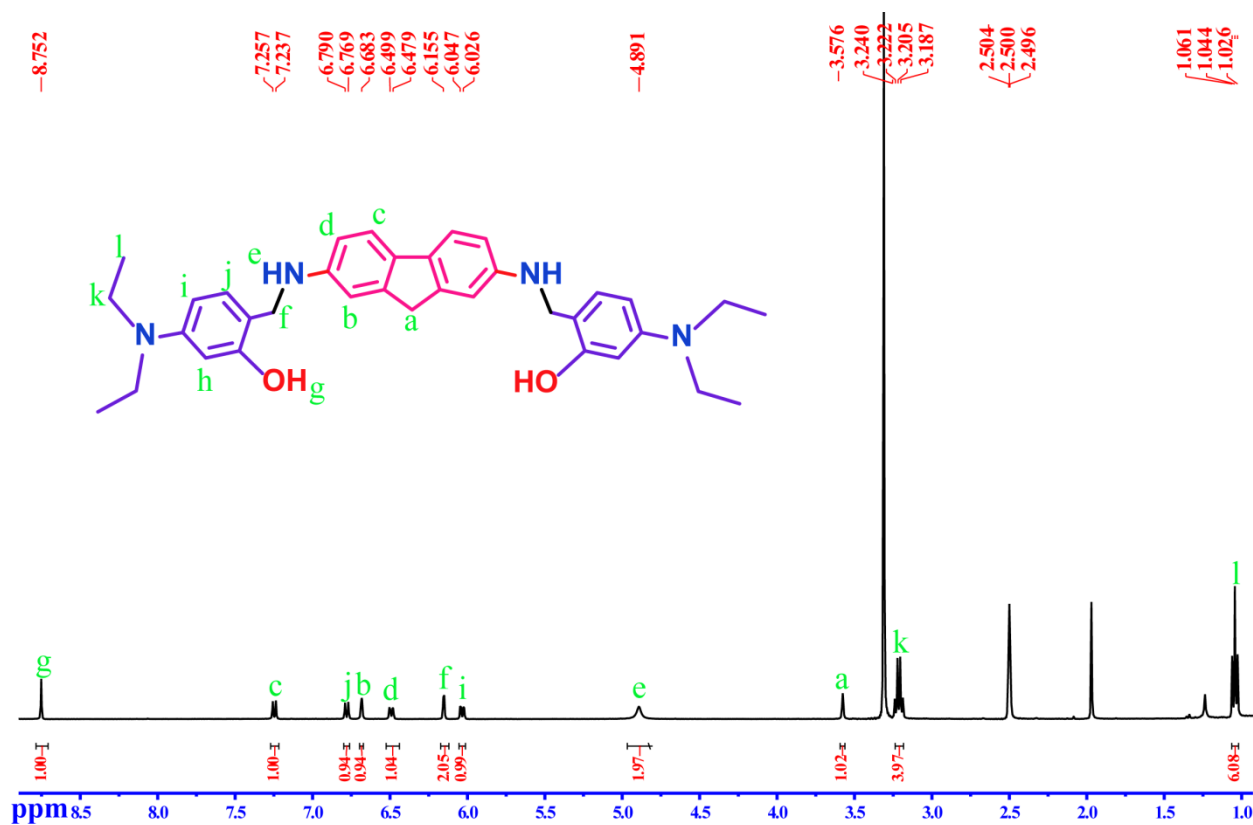


Figure A2.2: ^1H NMR of L_1 in DMSO-d_6 at room temperature.

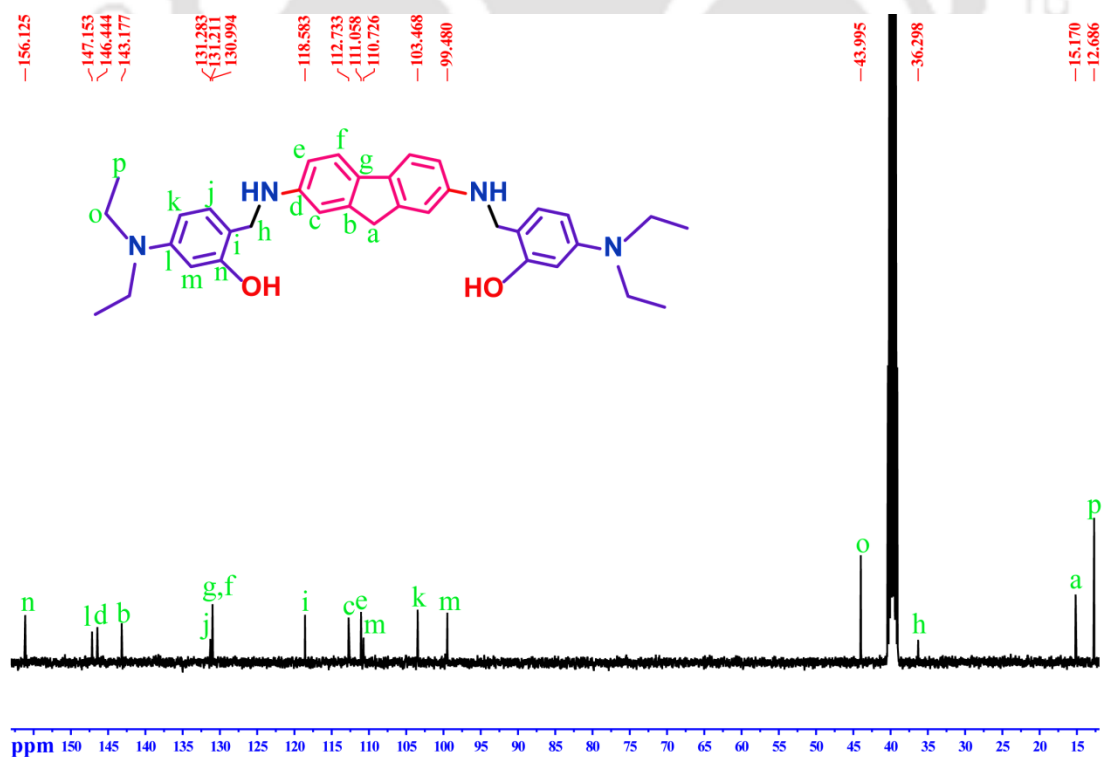


Figure A2.3: ^{13}C NMR of L_1 in DMSO-d_6 at room temperature.

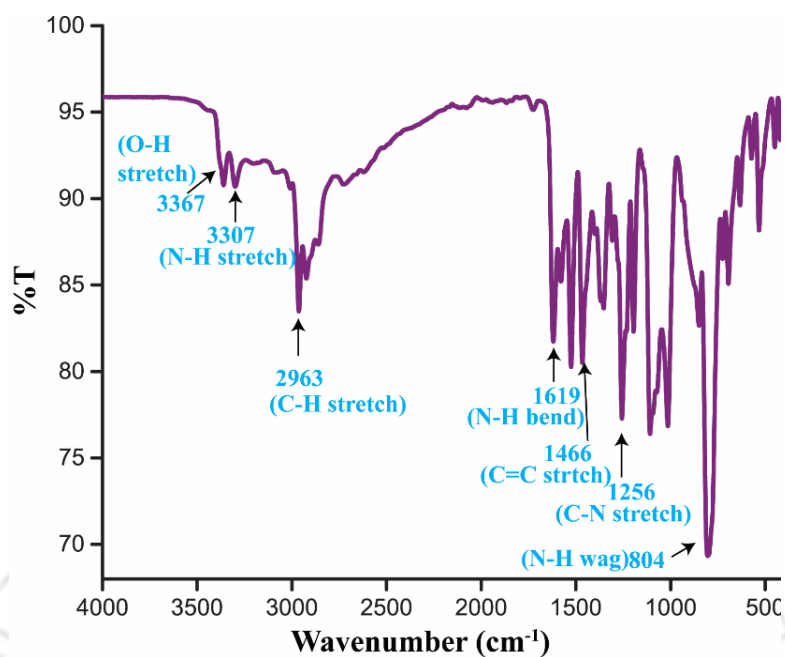


Figure A2.4: FTIR spectrum of L_1 recorded in KBr pellet at room temperature.

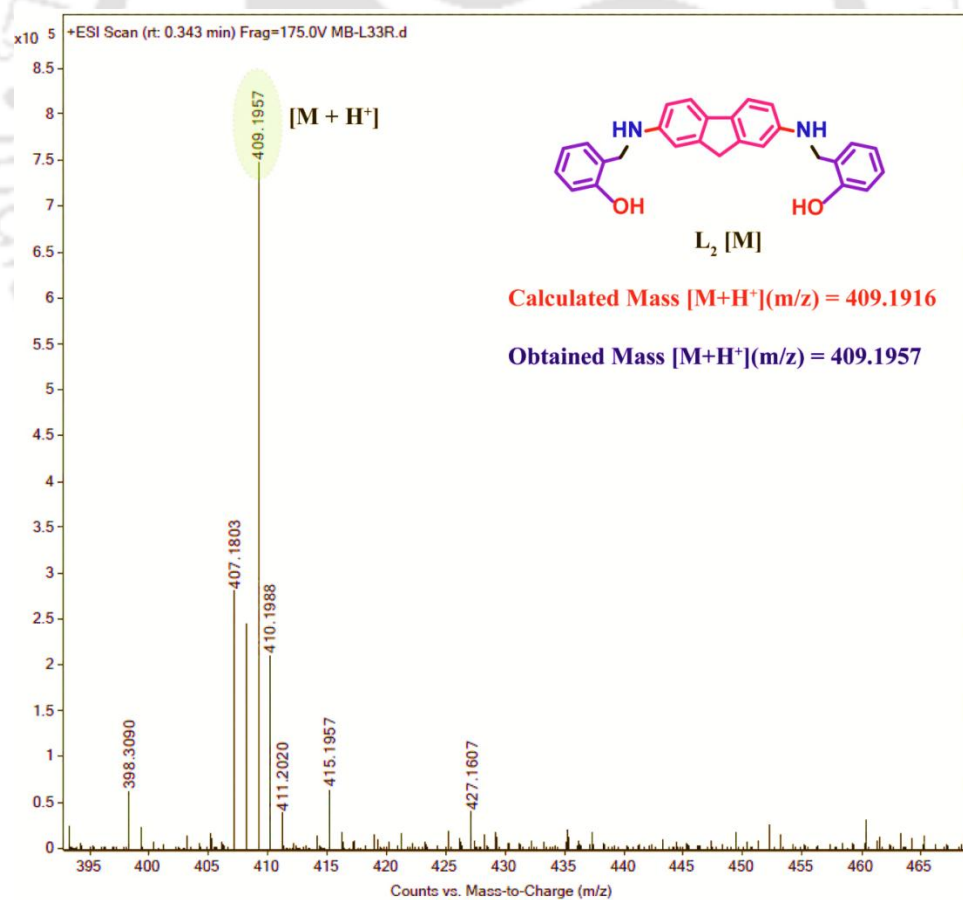


Figure A2.5: ESI-MS spectra of L_2 in 1:1 water-acetonitrile in positive ionization mode.

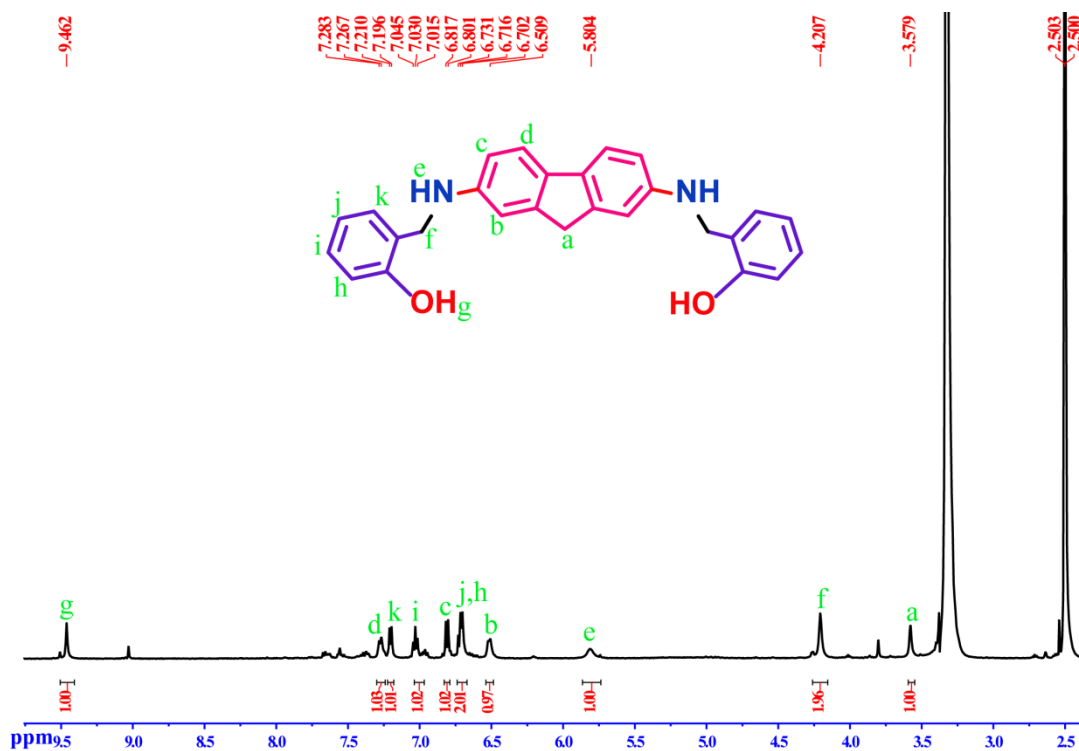


Figure A2.6: ¹H NMR of L₂ in DMSO-d₆ at room temperature.

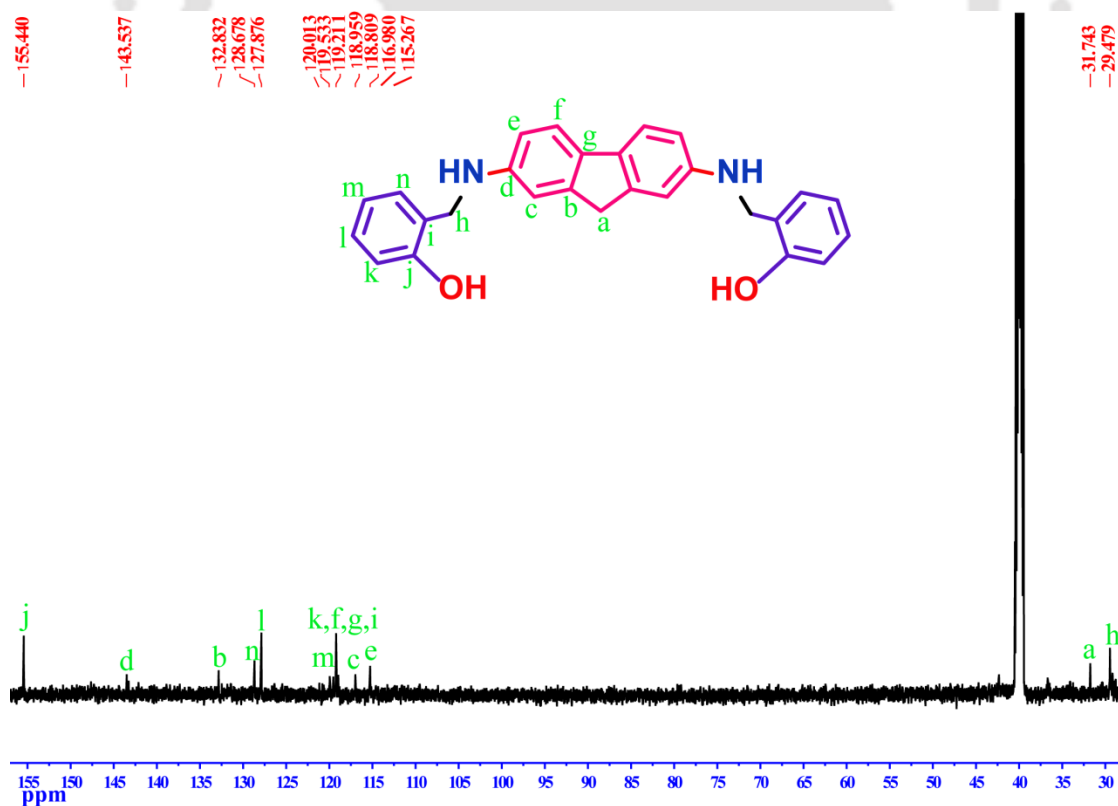


Figure A2.7: ¹³C NMR of L₂ in DMSO-d₆ at room temperature.

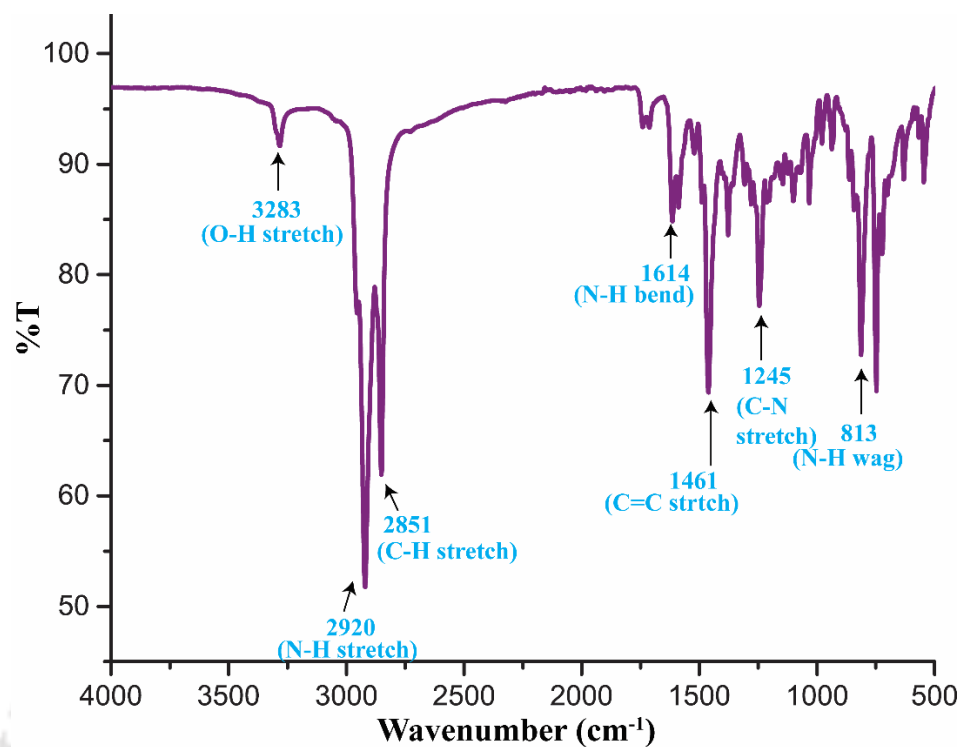


Figure A2.8: FTIR spectrum of L_2 recorded in KBr pellet at room temperature.

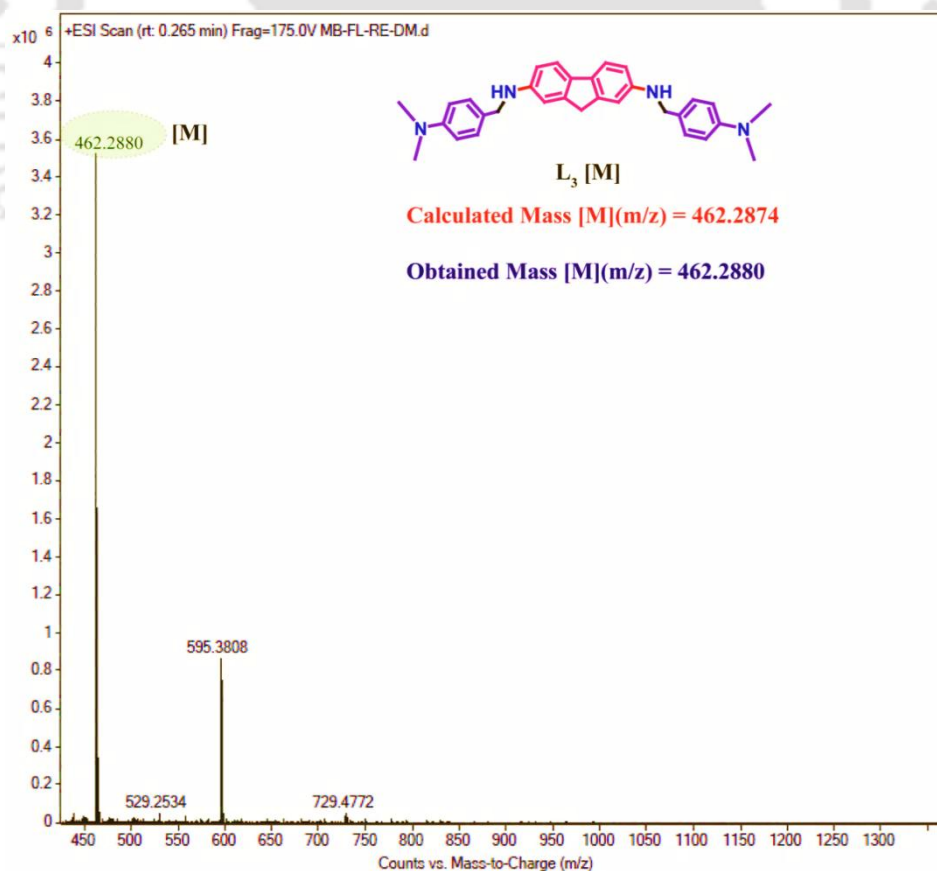


Figure A2.9: ESI-MS spectra of L_3 in 1:1 water-acetonitrile in positive ionization mode.

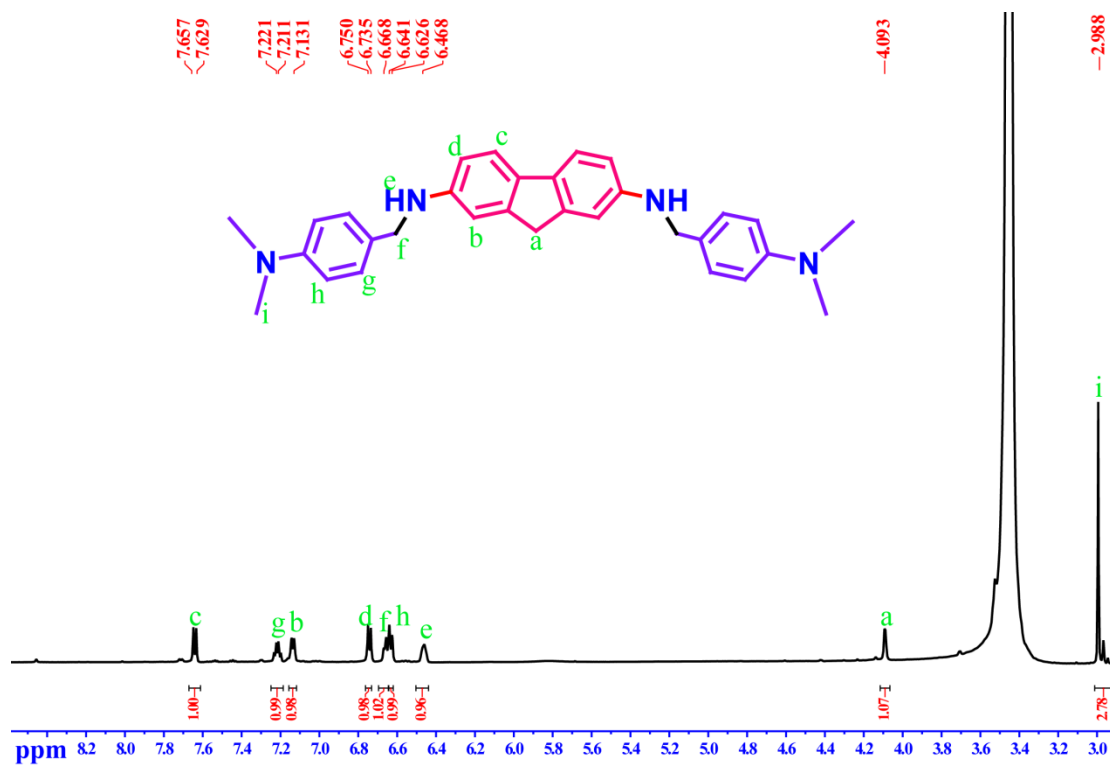


Figure A2.10: ¹H NMR of L₃ in DMSO-d₆ at room temperature.

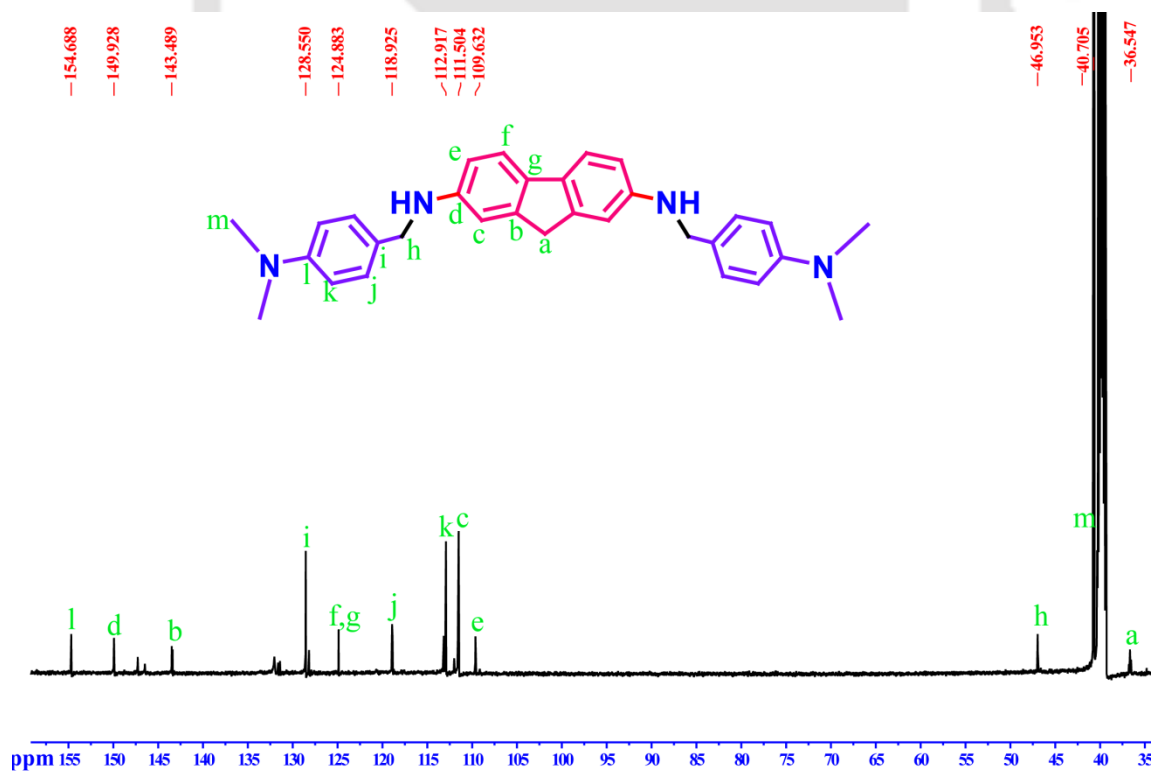


Figure A2.11: ¹³C NMR of L₃ in DMSO-d₆ at room temperature.

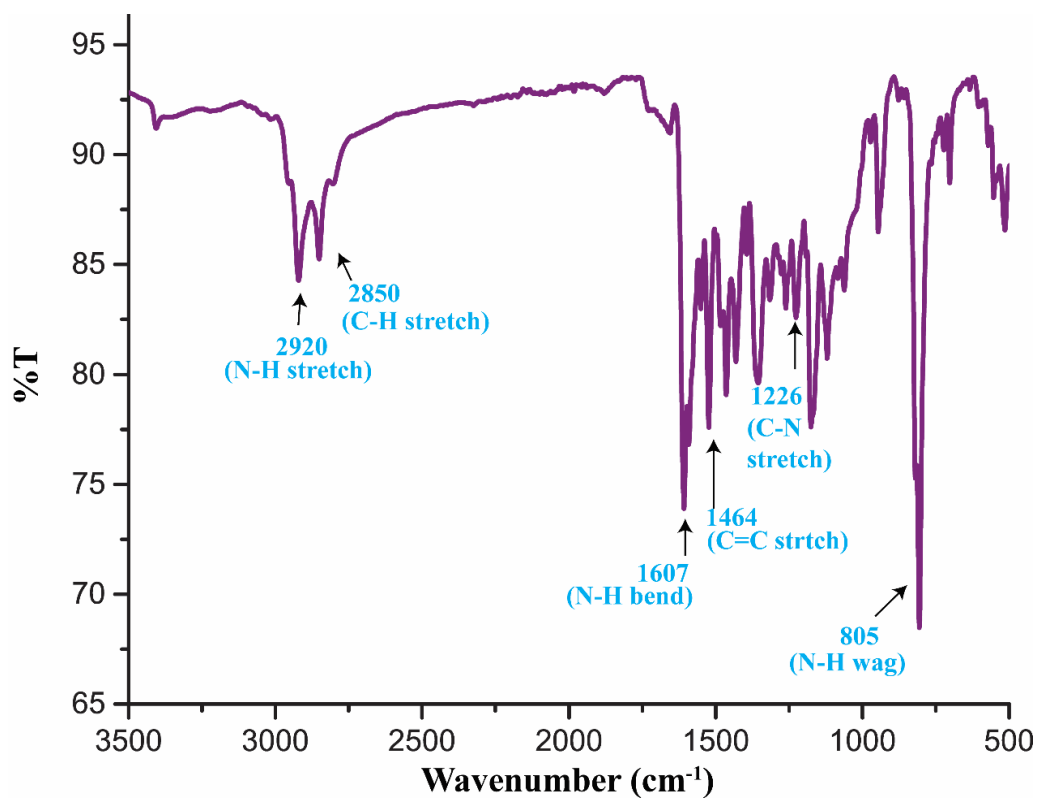


Figure A2.12: FTIR spectrum of L_3 recorded in KBr pellet at room temperature.

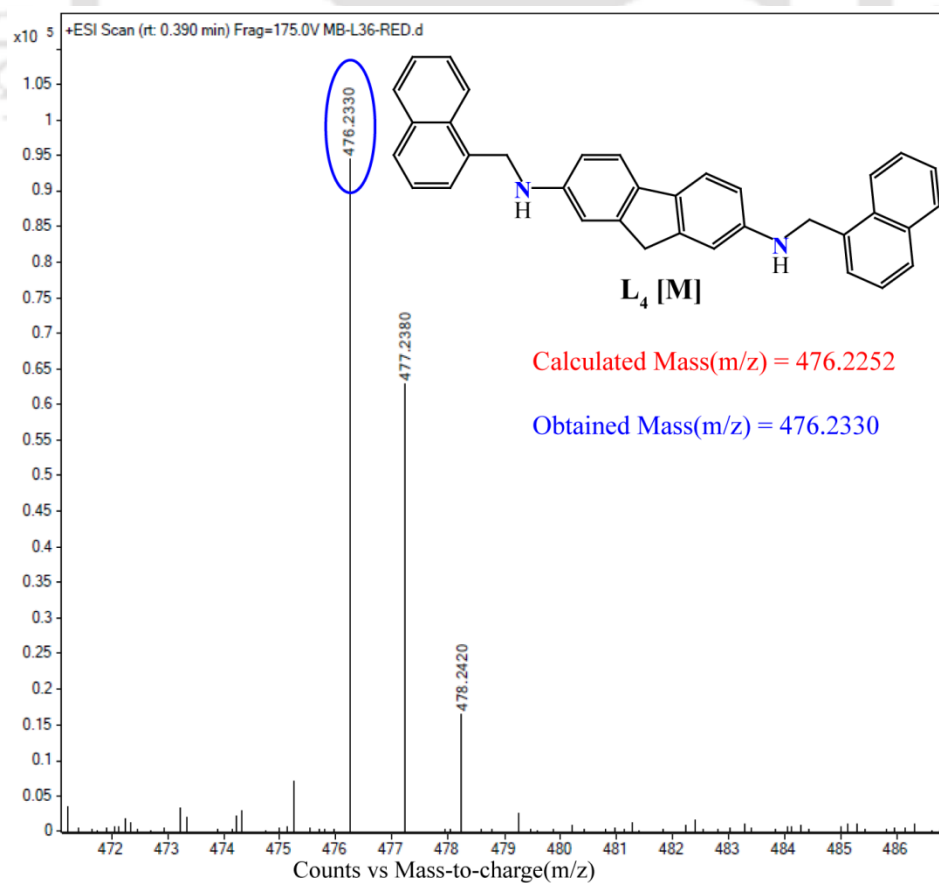


Figure A2.13: ESI-MS spectra of L_4 in 1:1 water-acetonitrile in positive ionization mode.

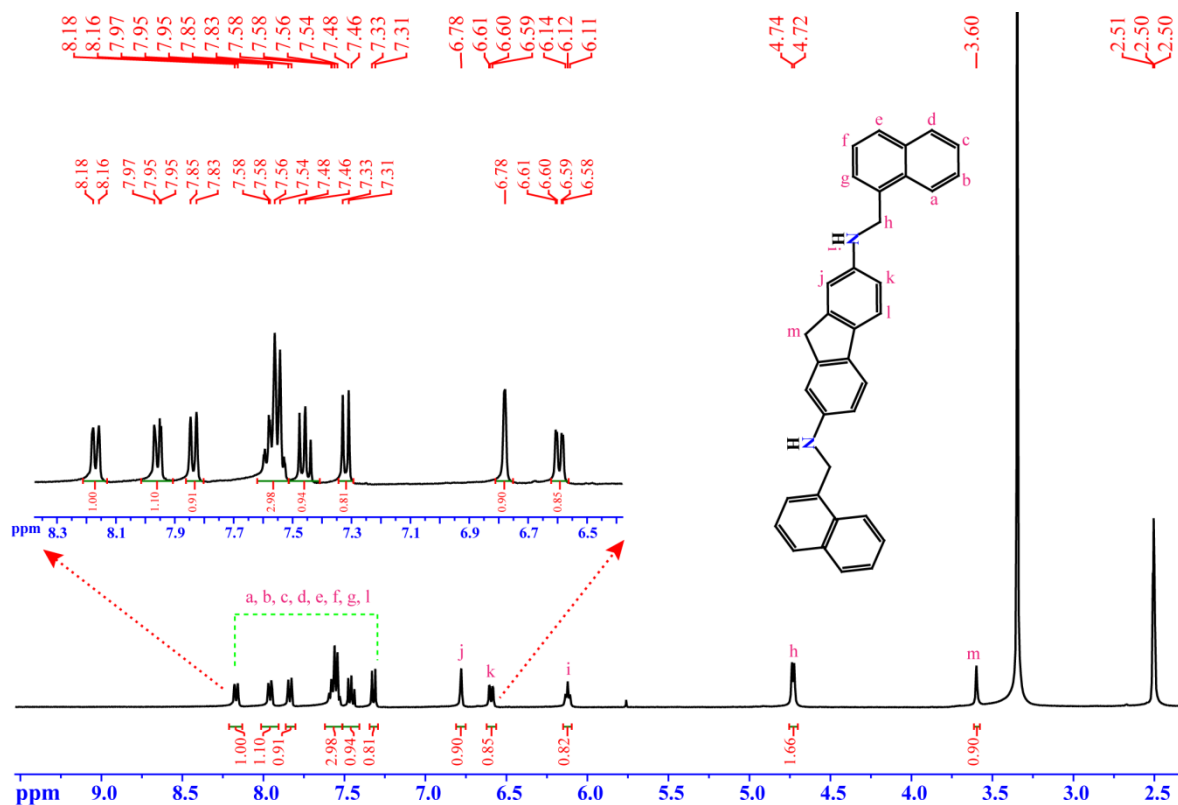


Figure A2.14: ¹H NMR of L₄ in DMSO-d₆ at room temperature.

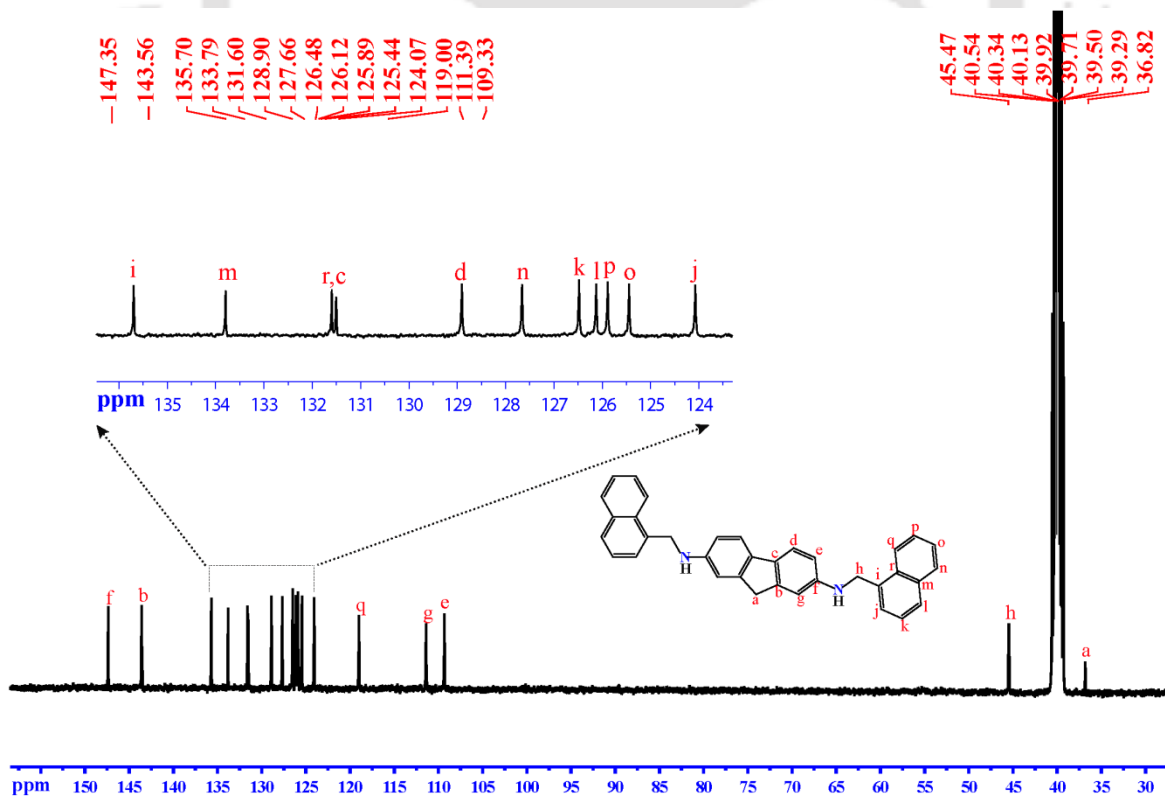


Figure A2.15: ¹³C NMR of L₄ in DMSO-d₆ at room temperature.

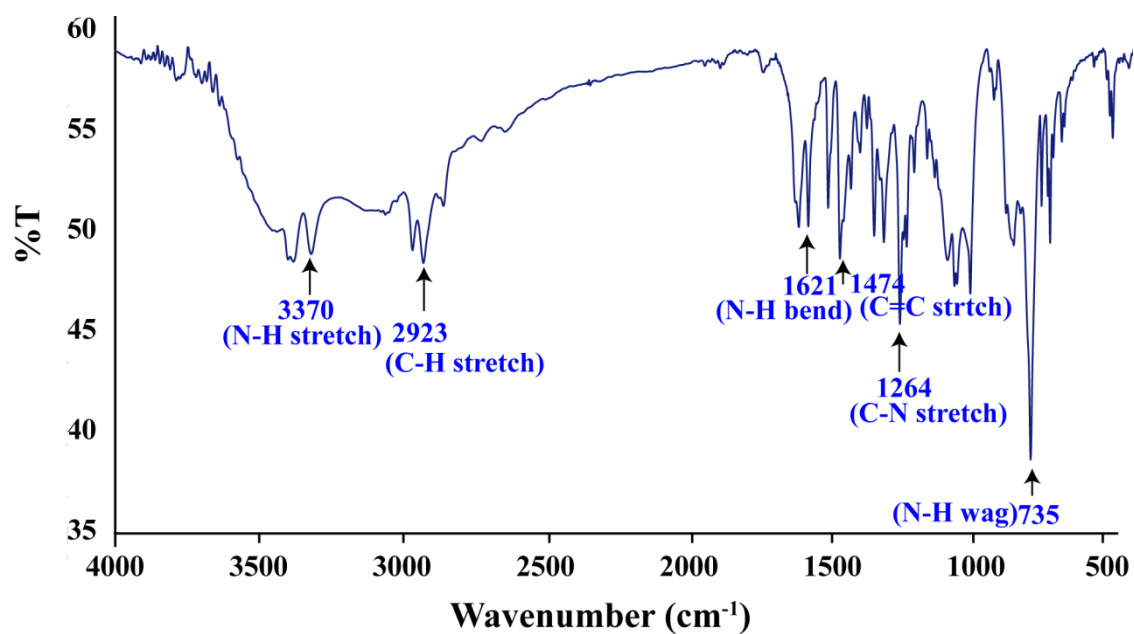


Figure A2.16: FTIR spectrum of **L₄** recorded in KBr pellet at room temperature.

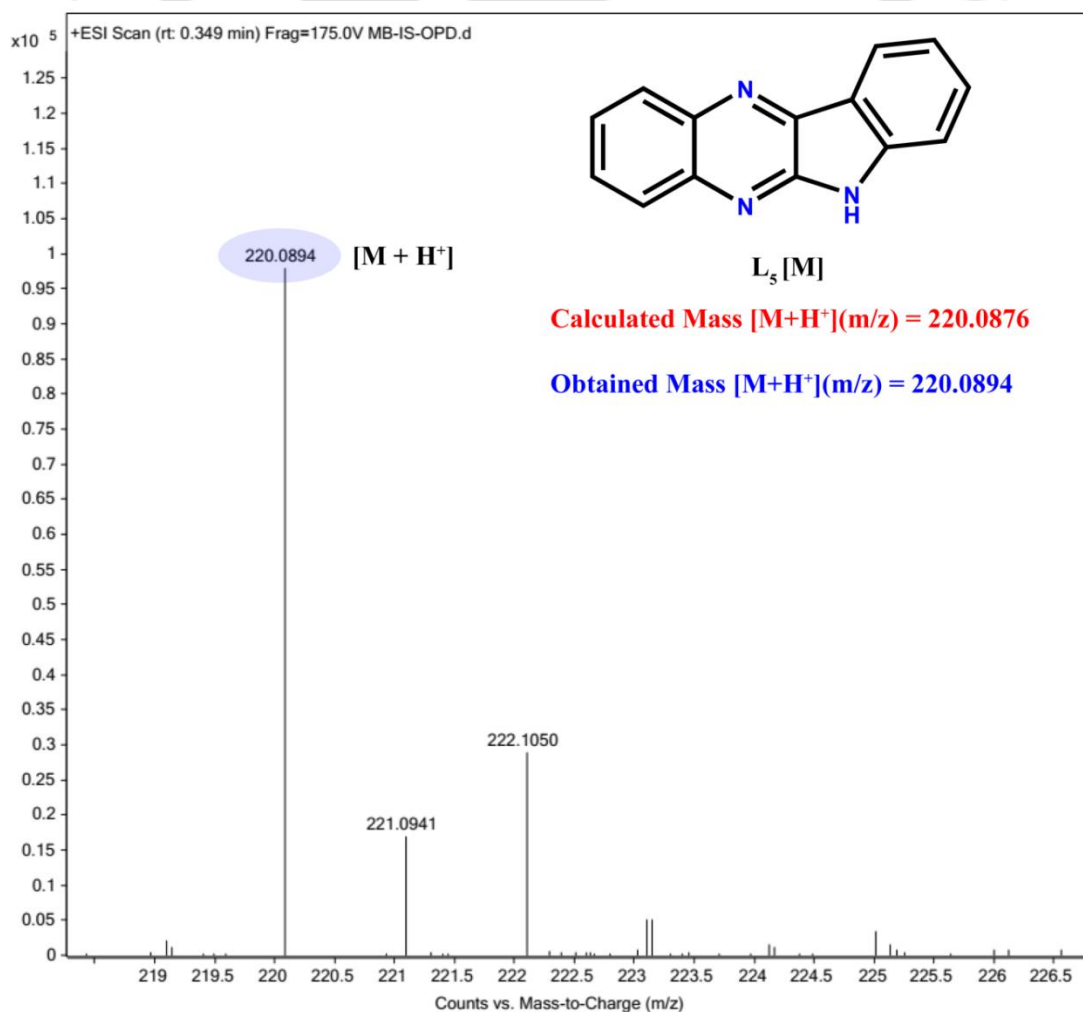


Figure A2.17: ESI-MS spectra of **L₅** in 1:1 water-acetonitrile in positive ionization mode.

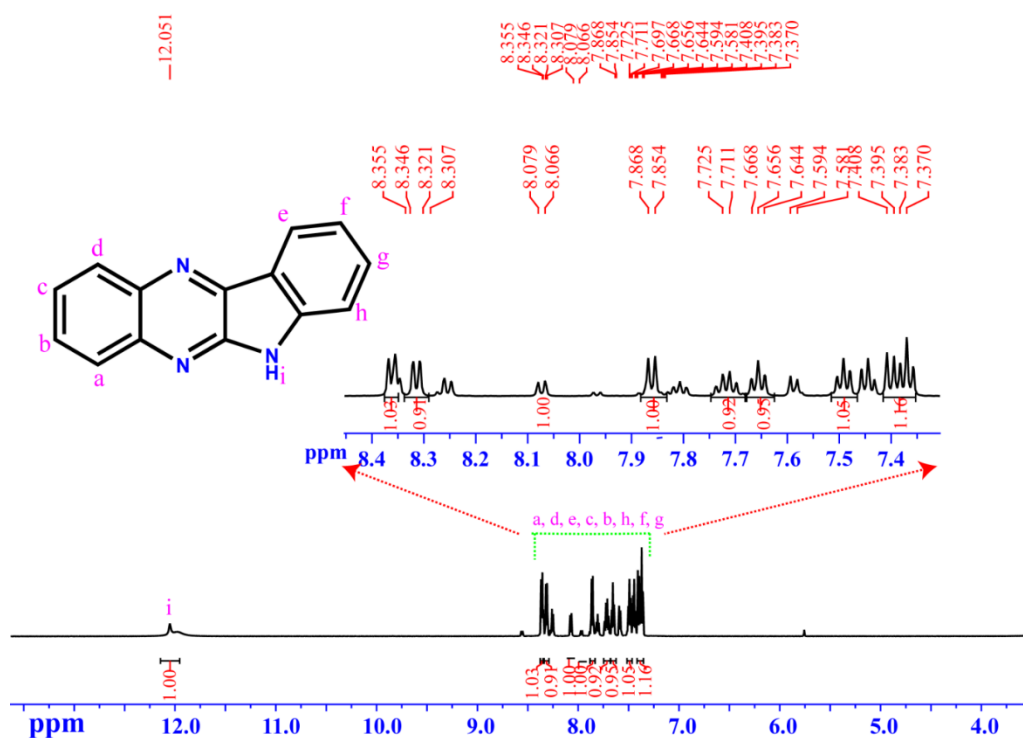


Figure A2.18: ^1H NMR of L_5 in DMSO-d_6 at room temperature.

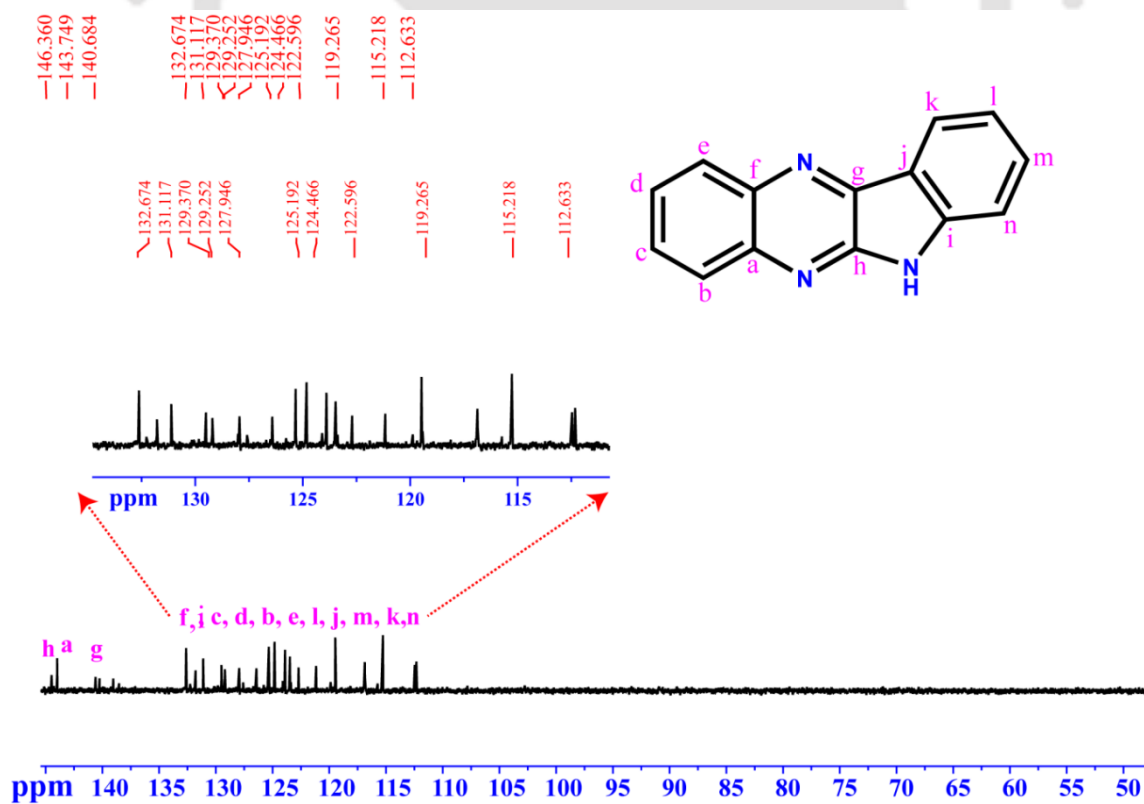


Figure A2.19: ^{13}C NMR of L_5 in DMSO-d_6 at room temperature.

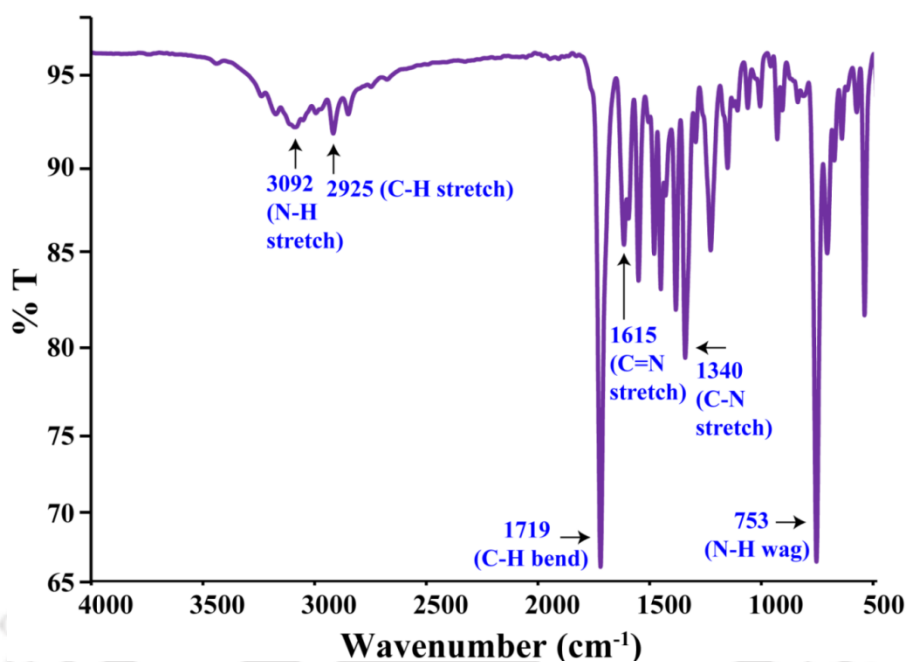


Figure A2.20: FTIR spectrum of L_5 recorded in KBr pellet at room temperature.

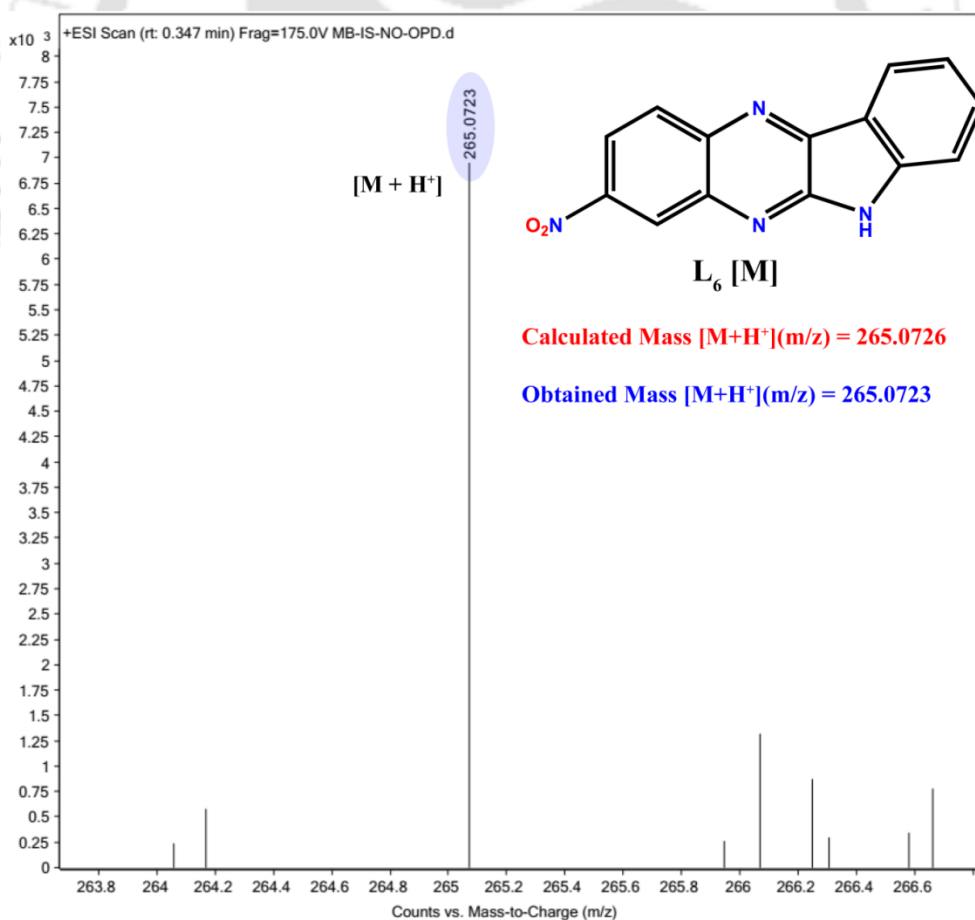


Figure A2.21: ESI-MS spectra of L_6 in 1:1 water-acetonitrile in positive ionization mode.

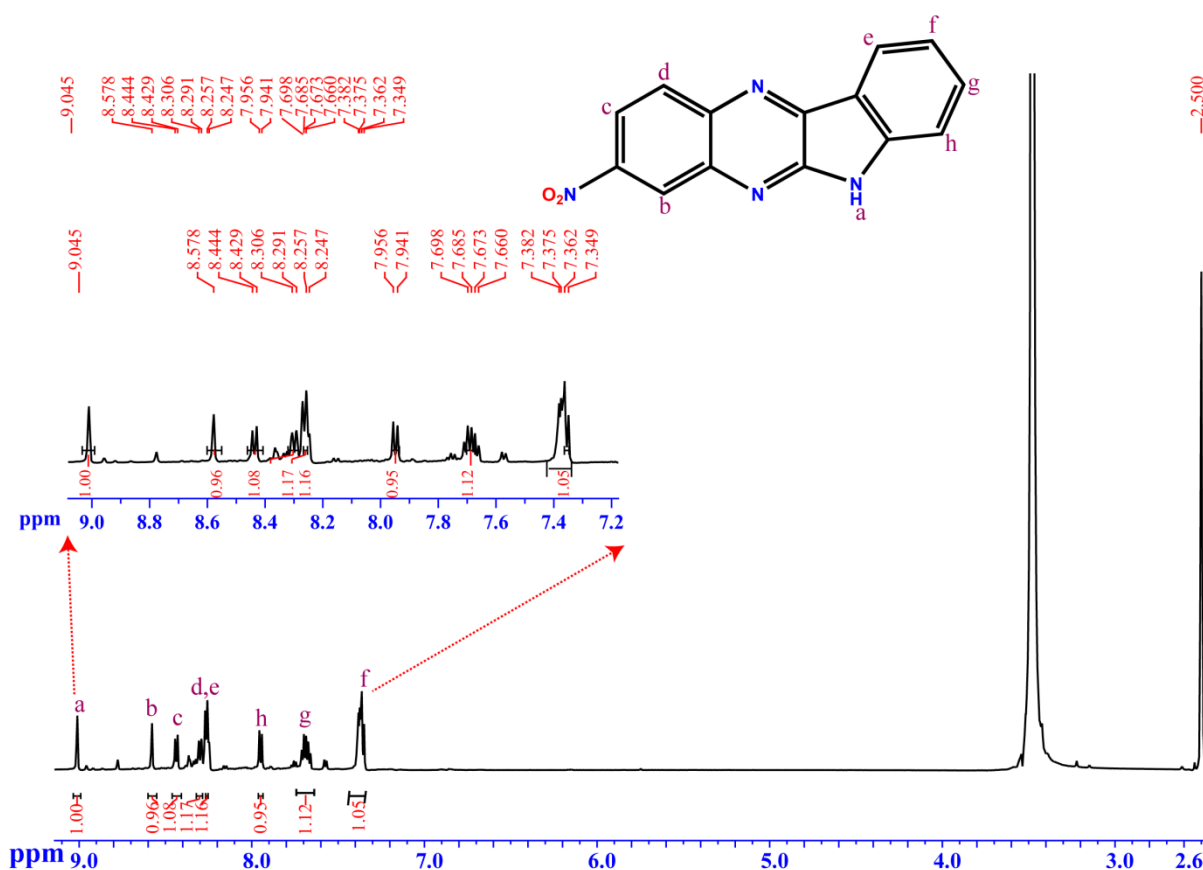


Figure A2.22: ^1H NMR of L_6 in DMSO-d_6 at room temperature.

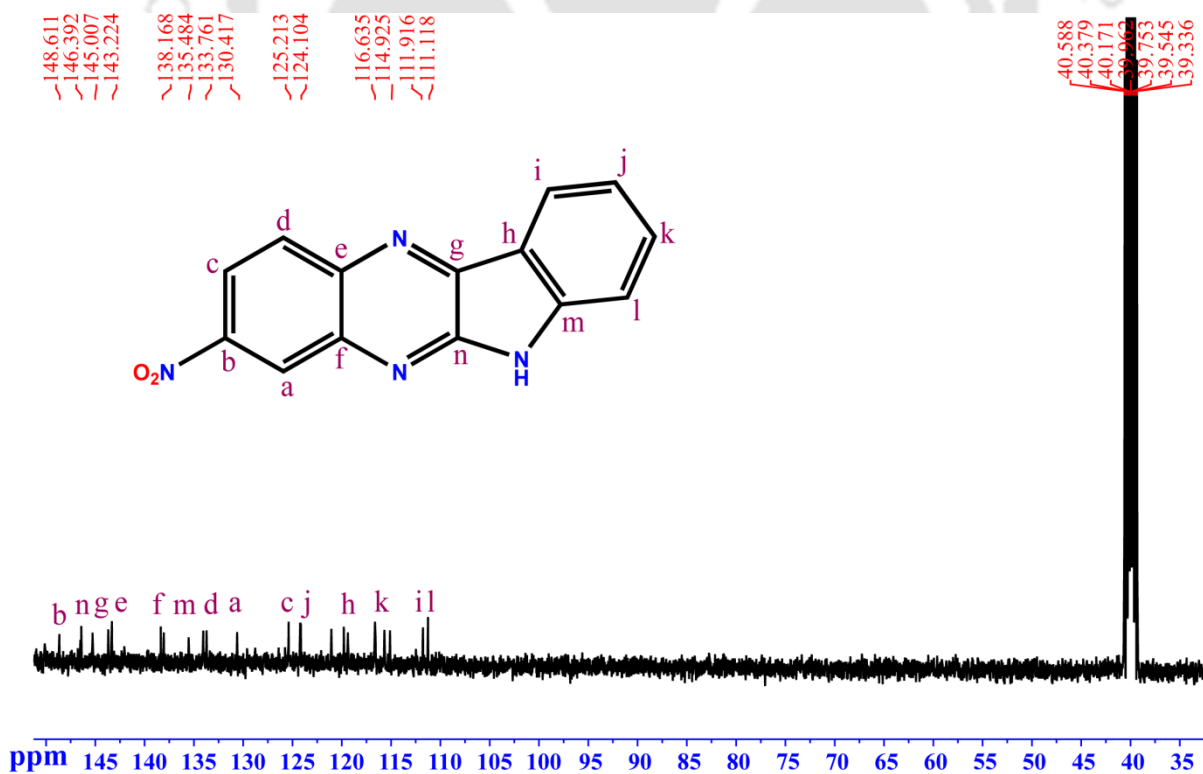


Figure A2.23: ^{13}C NMR of L_6 in DMSO-d_6 at room temperature.

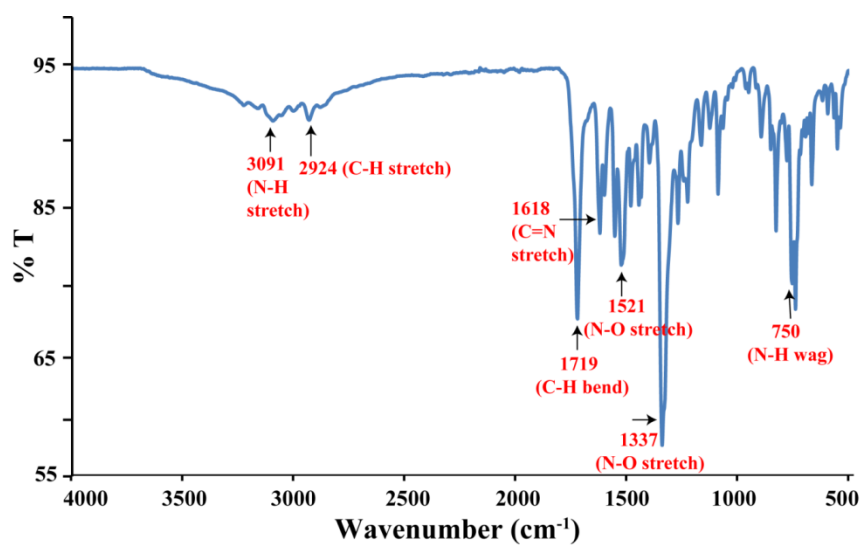


Figure A2.24: FTIR spectrum of L₆ recorded in KBr pellet at room temperature.

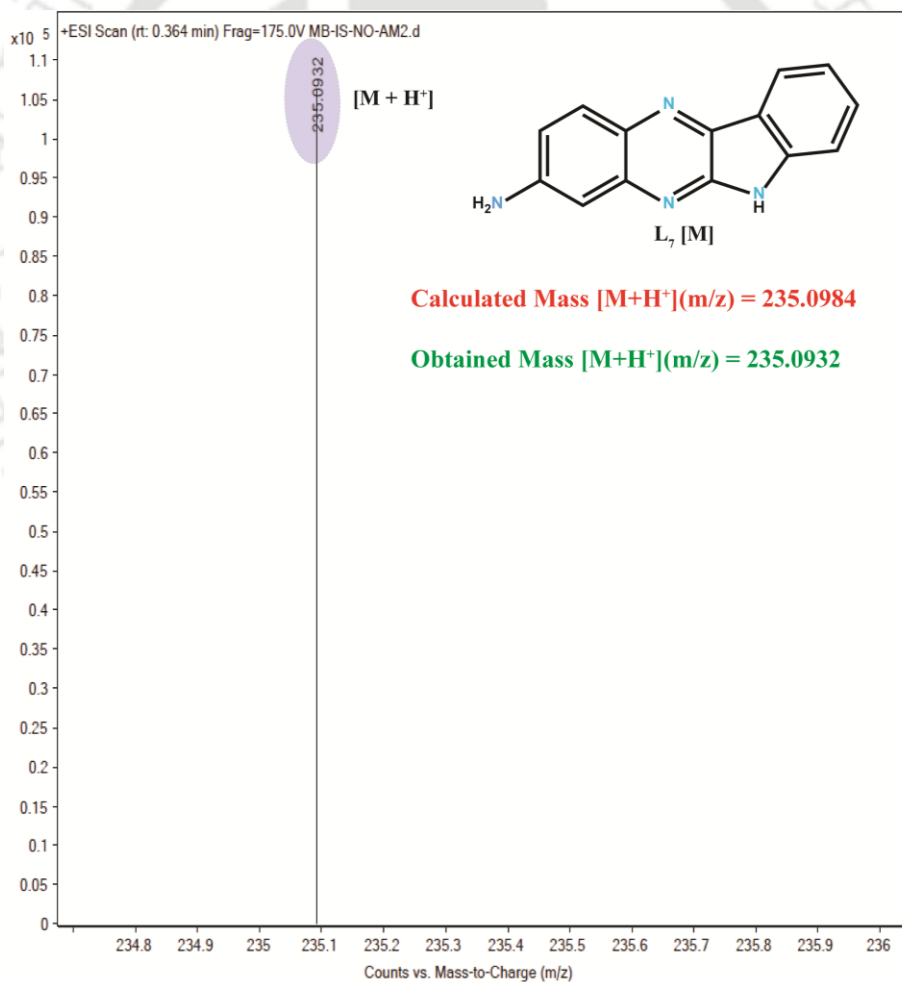


Figure A2.25: ESI-MS spectra of L₇ in 1:1 water-acetonitrile in positive ionization mode.

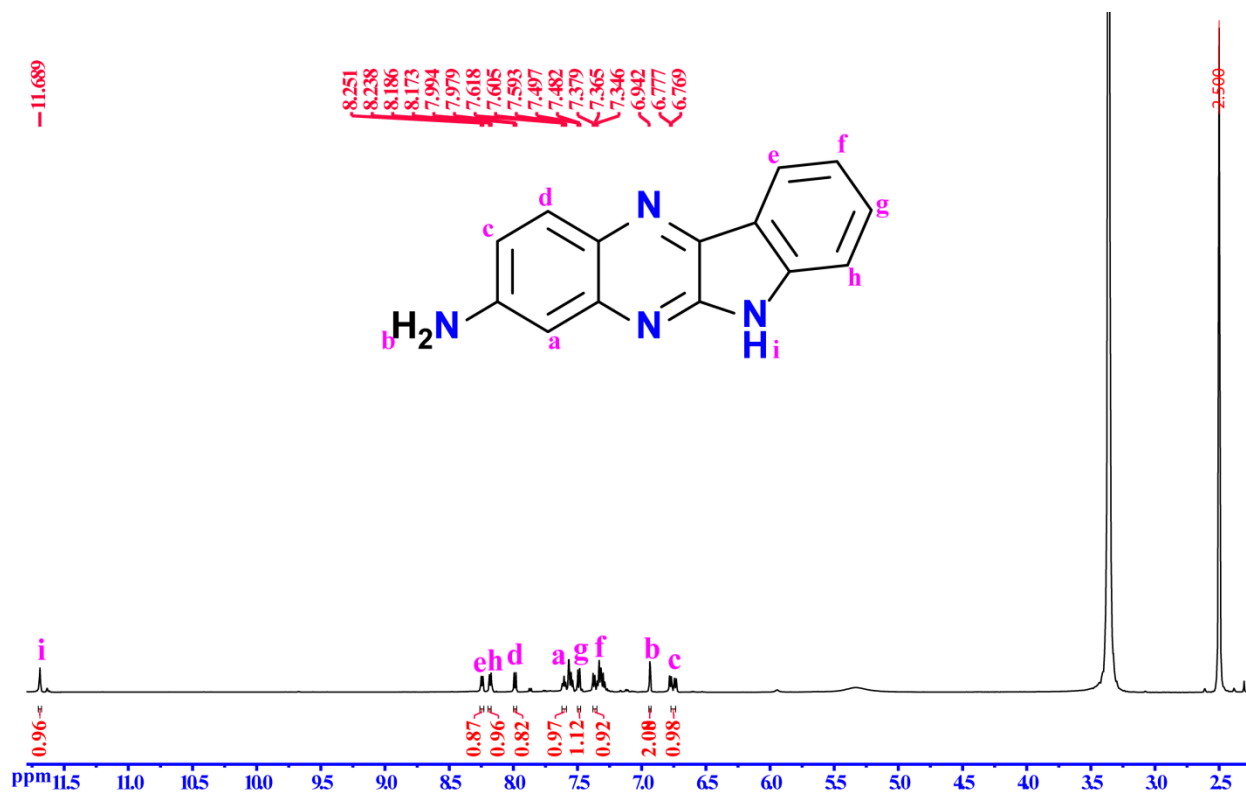


Figure A2.26: ¹H NMR of **L₇** in DMSO-d₆ at room temperature.

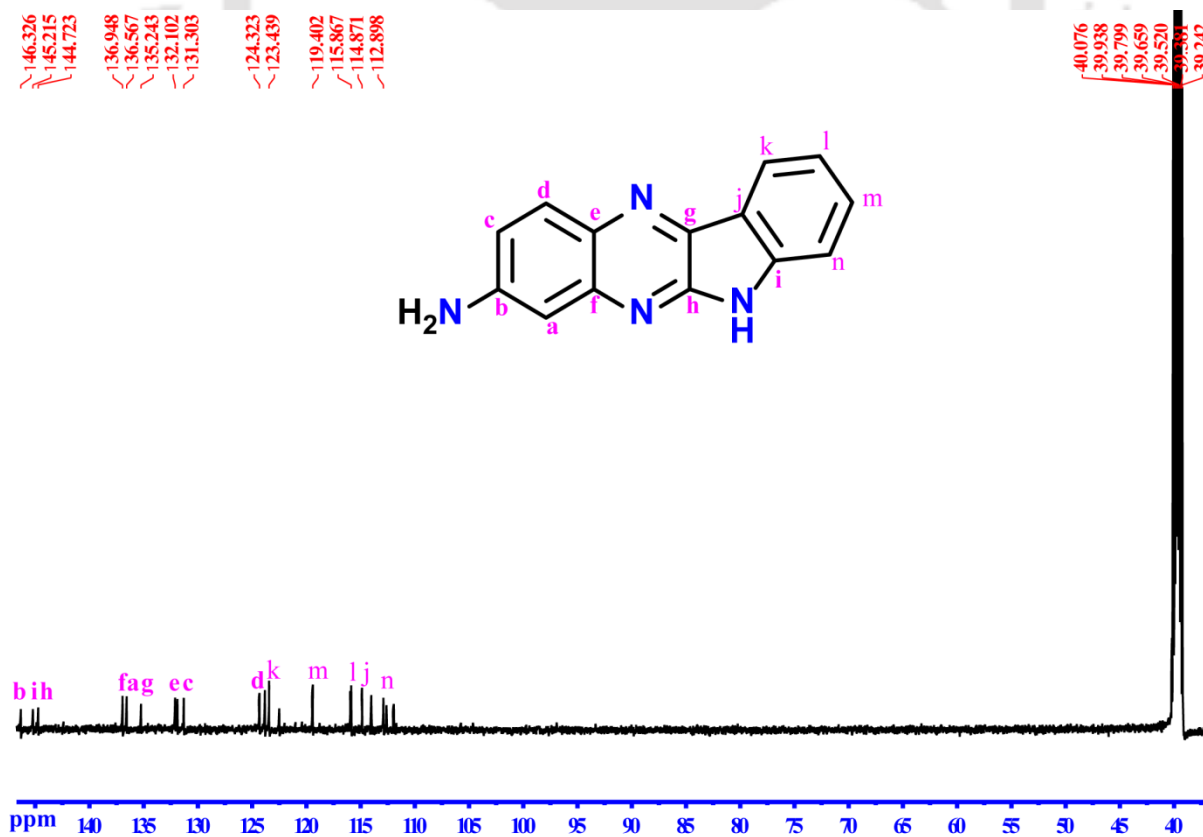


Figure A2.27: ¹³C NMR of **L₇** in DMSO-d₆ at room temperature.

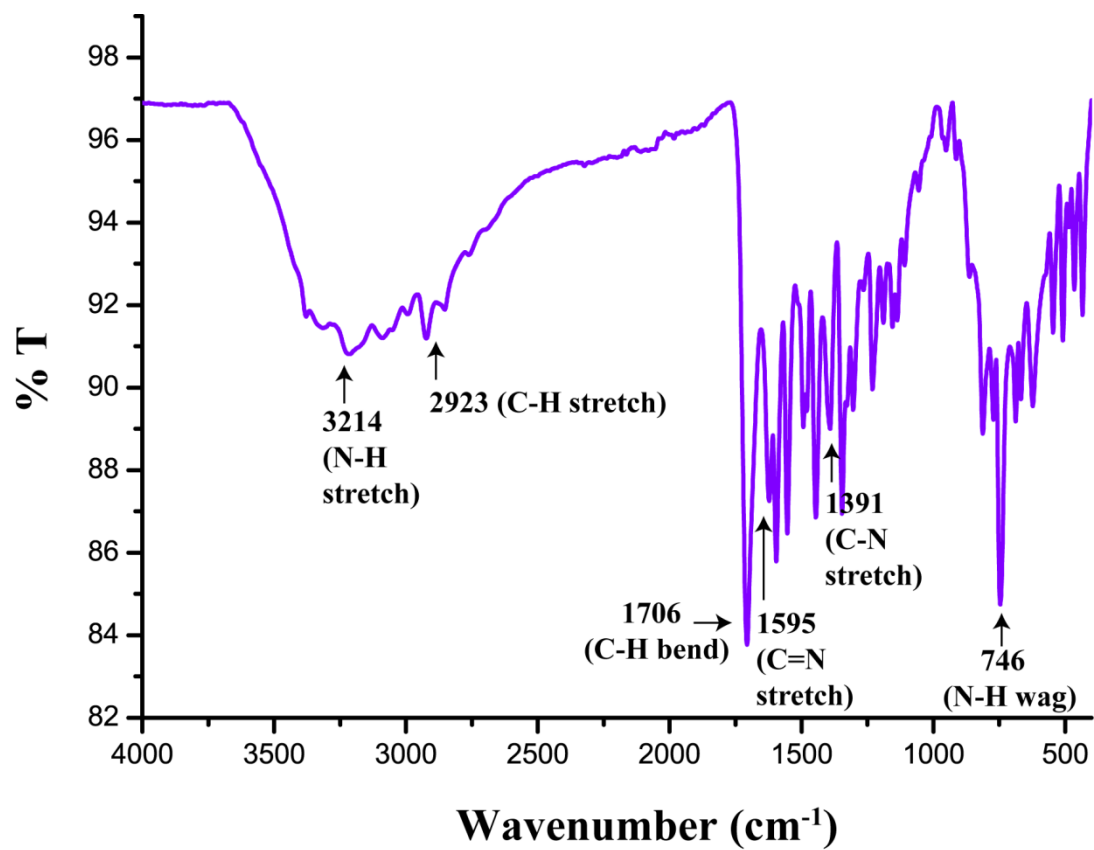
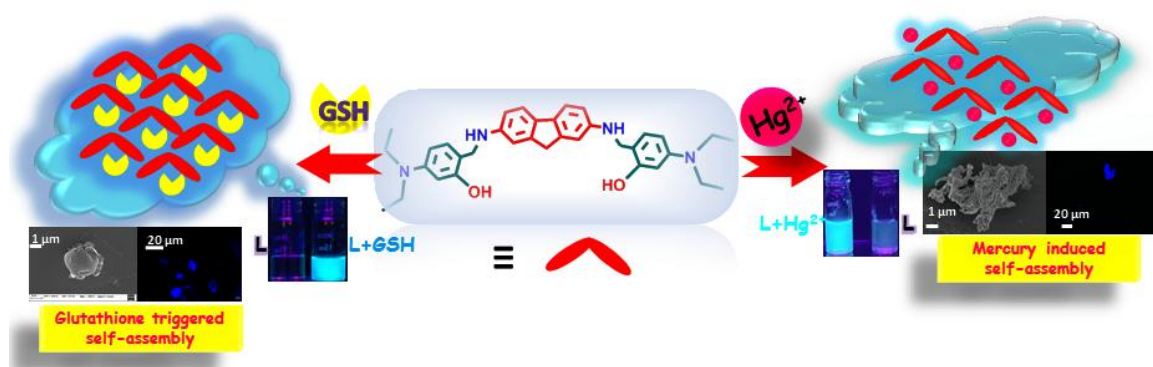


Figure A2.28: FTIR spectrum of L₇ recorded in KBr pellet at room temperature.



CHAPTER 3

Fluorene-salicylaldehyde probe: Mercury and glutathione recognition triggered self-assembly and simultaneous Turn-on chemosensing in water



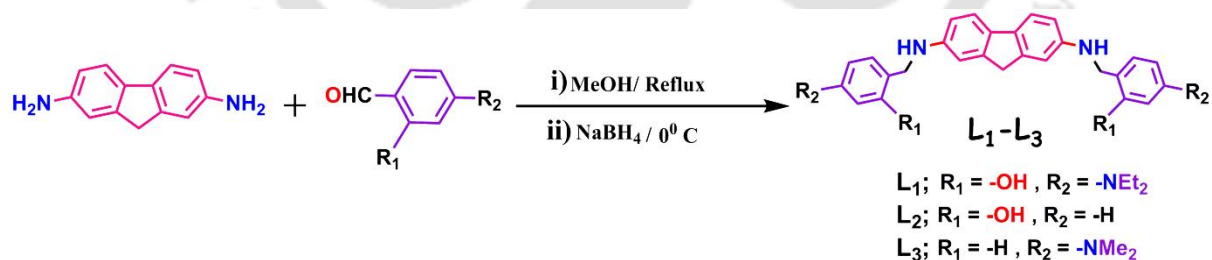
Chapter 3

3.1 Background and focus of the chapter

Modern industrialization and globalization ensure a highly polluted atmosphere for humankind and animals worldwide, where water sources being the principal and most essential ingredient of all living organisms, are significantly affected part of the earth.^{3.1} Heavy metal is among those topmost candidates in the context of toxicity.^{3.2-3.4} Among the various heavy metals, mercury(Hg), a ubiquitous and bioaccumulative toxicant mainly introduced by volcanic emissions and several industrial anthropogenic operations, critically warning human health and natural aquatic ecology.^{3.5-3.7} In the mid-1950s, one Japanese doctor, announced an "epidemic of an unknown disease of the central nervous system," indicating the official discovery of Minamata disease. The fish-based diets of the local people and cats of Minamata were affected mostly due to dumping mercury in Minamata Bay that got bioaccumulated and biomagnified in the muscle of fish.^{3.8} Similar catastrophes provoked in Iraq during the 1970s where people consumed mercury-based fungicide-treated seed grains.^{3.9} Mercury can easily penetrate through the biological membranes, tissues and even at very low concentrations, mercury exposure can cause tragic consequences on human health, including prenatal brain injury, vision loss, severe damage to the heart, stomach, kidney, and central nervous system.^{3.10-3.14} U.S. Environmental Protection Agency (EPA) has also set the maximum allowable level of mercury at 2.0 ppb in drinking water to avoid the harmful effects of mercury.^{3.15} Consequently, the extent of toxicity for mercury makes it highly desirable to probe them in drinking water, different environmental sources, and natural aquatic systems. Although there are various well-established techniques such as high-performance liquid chromatography(HPLC), atomic absorption spectroscopy (AAS), electrochemical analysis, surface-enhanced Raman scattering for the detection of mercury ions,^{3.16-3.19} optical detection based on fluorometric changes is the most advantageous method for a low limit of detection and easy facile detection of analyte without any expensive prior set-up.

On the other hand, from a metabolic point of view, biological thiols (Cys, Hcy, GSH) play crucial roles in several physiological processes and are associated with each other for redox regulation.^{3.20-3.21} These biological thiols also serve as biomarkers of cancer, liver damage, and

osteoporosis.^{3.22-3.23} Amidst these, Glutathione (GSH, γ -glutamyl-cysteinyl-glycine), the most abundant cellular biothiol, provides redox homeostasis, maintains biochemical, metabolic reactions,^{3.24} and supports cellular defense against free radicals and toxins.^{3.25} However, abnormal levels of GSH have been involved with various fatal human diseases such as cancer, AIDS, Alzheimer's disease, and neurodegenerative diseases.^{3.26} Therefore, selective and sensitive discrimination of these biothiols amidst other amino acids has attracted significant interest and considerable studies in the field of chemical and biological sciences. So far, although numerous fluorescent sensors have been evolved, fluorene-based single-molecule probes for detecting GSH and mercury independently seldom have been exploited. It is encouraging and challenging to discriminate between Cys/GSH/Hcy due to their similar structure and reactivity. Therefore, from the practical point of view, a single-molecule cost-effective dual-sensor-based probe with a fast response for mercury as well as GSH with high selectivity and sensitivity in environmental and biological systems would be highly inspiring. Owing to these importances, amidst various classes of fluorophores herein, we report a new bifunctional fluorene-*N,N*-diethyl amine salicylaldehyde scaffold (**L**₁) (Scheme 3.1) for sensing and detection of Hg²⁺ and GSH discretely in an aqueous matrix based on fluorescence "off-on" response. For the practical utility of the probe (**L**₁), smartphone-assisted paper-based sensors, which are easy to store and carry, successfully enabled simple, rapid, real-time detection of analytes without using other sophisticated instruments and may contribute great significance for early disease diagnosis. Meanwhile, the chemosensor showed selective and sensitive sensing exclusively towards Hg²⁺ and GSH in several environmental and biological samples.



Scheme 3.1: Synthetic route of the probes **L**₁, **L**₂, and **L**₃.

3.2 Photophysical characterization

The photophysical studies of **L**₁, **L**₂, and **L**₃ were attained at room temperature in certain polar protic and polar aprotic solvents using UV-Visible and fluorescence spectroscopy experiments. Initially, 1.0 mM stock solutions of **L**₁, **L**₂, and **L**₃ were prepared in dimethylsulfoxide (DMSO) and diluted accordingly for spectral analyses (Figure A3.1). The electronic absorption spectrum of **L**₁ exhibited an absorption band at 292 nm and a

broad peak at 434 nm in an aqueous matrix which may be ascribed to the intraligand $\pi-\pi^*$ and $n-\pi^*$ electronic transitions,^{3,27} followed by leveling off the tails beyond 450 nm, probably due to generation of nano-aggregates in the solution.^{3,28} The photoluminescence spectral data were recorded after the addition of varying water fraction content (f_w) to a solution of L_1 in acetonitrile (Figure A3.2). The luminescence spectrum of L_1 in acetonitrile manifested emission maxima at 386 nm while raising the percentage of water up to 100; the intense emission maxima significantly quenched with the appearance of a slight red-shift peak at 392 nm.

3.3 Fluorescence response of the Probe L_1 to Hg^{2+} in water

The fluorescence behavior of receptor L_1 (2.0 μM) was explored after optimization at several wavelengths from 292 nm to 434 nm, and the appropriate excitation wavelength (λ_{ex}) opted at 315 nm. Upon excitation at 315 nm in an aqueous solution, probe L_1 (2.0 μM) manifested a very weak emission maximum centered about 384 nm with a very low quantum yield ($\phi = 0.001$) (Figure 3.1), which can be attributed to an efficient PET mechanism operating via donor fluorene motif.^{3,29} The pH is a great major parameter, for that reason to explore the appropriate pH for L_1 (2.0 μM), the pH effect on the sensing performance of L_1 (2.0 μM) was examined in the range of pH 4.0–12.0. We then executed fluorescence spectroscopic analyses in 100% aqueous matrix (pH 7.4) to explore sensing ability of L_1 towards a series of metal ions (50 equiv.; Hg^{2+} , Zn^{2+} , Cd^{2+} , Cu^{2+} , Co^{2+} , Ni^{2+} , Pb^{2+} , Ca^{2+} , Mg^{2+} , Mn^{2+} , Fe^{3+} , Al^{3+} and Cr^{3+}). As displayed in Figure 3.1a, for Hg^{2+} , a notable (~ 7 fold) "turn-on" fluorescence intensity with a red-shift (30 nm) was identified while the other metal ions did not influence the fluorescence response of L_1 . A prominent emission enhancement (Quantum yield = 0.048) was observed upon excess addition of Hg^{2+} , which may be ascribed to chelation-enhanced fluorescence upon coordination to Hg^{2+} , whereas in L_2 and L_3 , no such significant fluorescence changes were observed. Under 365 nm U.V. light, distinct naked-eye color change of aqueous solution of L_1 upon excess addition of Hg^{2+} further supported selective discrimination of L_1 over other metal ions (Figure 3.1a Inset). Furthermore, to gain insight and look into the sensing ability of L_1 towards Hg^{2+} , fluorescence titration experiments were carried out in a 100% aqueous medium with various equiv. of Hg^{2+} solution. Upon incremental addition of Hg^{2+} solution (0–100 μM), the luminescence intensity of L_1 raised gradually and attained a plateau with 30 nm wavelength red-shift (Figure 3.1b). Job's plot analysis was performed to gain insight into the sensing mechanism, which revealed that L_1 - Hg^{2+} formed a 1:2 stoichiometric complex (Figure A3.3). On the other hand, the determination of the association constant for L_1 - Hg^{2+} was quite

unprecedented because of the complex equilibria. The detection limit for Hg^{2+} was evaluated to be ~ 17.35 ppb (Figure A3.4a) employing definition by IUPAC ($3\sigma/k$).^{3,30} The limit of quantification (LOQ) for Hg^{2+} was estimated to be 57.88 ppb.

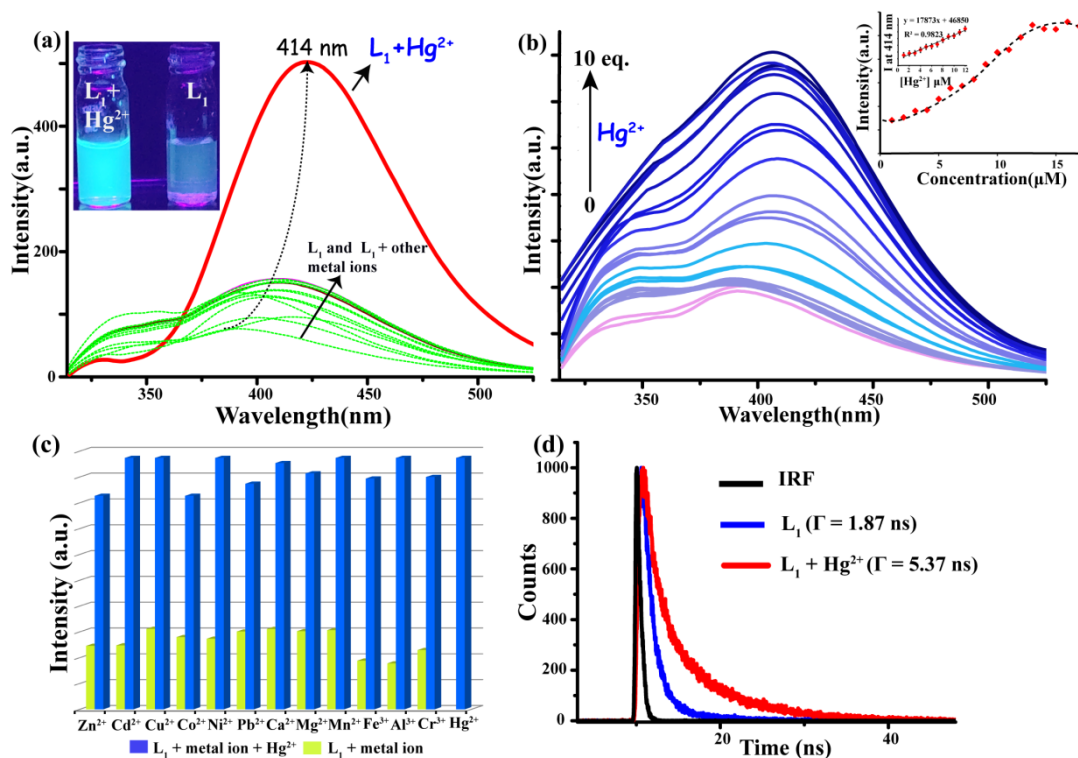


Figure 3.1: (a) Fluorescence spectra of probe L_1 (2 μM ; $\lambda_{\text{ex}} = 315$ nm) observed upon the addition of 50 equivalents of metal ions (nitrate or chloride salts of Hg^{2+} , Zn^{2+} , Cd^{2+} , Cu^{2+} , Co^{2+} , Ni^{2+} , Pb^{2+} , Ca^{2+} , Mg^{2+} , Mn^{2+} , Fe^{3+} , Al^{3+} and Cr^{3+}) in a aqueous medium. Inset: Under 365 nm UV lamp, visual color change of the solution after the addition of excess Hg^{2+} salt. (b) Fluorescence titration spectra of L_1 (2 μM) upon incremental addition of Hg^{2+} in aqueous matrix. Inset: changes in the emission intensity at 414 nm upon gradual addition of Hg^{2+} (0-20 μM). (c) Comparison of fluorescence emission intensity of L_1 (2 μM) at 414 nm on interaction with various metal ions before (green bars) and after (blue bars) addition of Hg^{2+} (d) Time-resolved fluorescence emission spectra of L_1 (2 μM) in absence and presence of Hg^{2+} in water.

Sensitivity towards analyte is prime characteristic to assess the property of the probe. Hence competitive experiments were accomplished by adding Hg^{2+} (50 equiv) solution to the L_1 solution (2.0 μM) in presence of other common cations (Zn^{2+} , Cd^{2+} , Cu^{2+} , Co^{2+} , Ni^{2+} , Pb^{2+} , Ca^{2+} , Mg^{2+} , Mn^{2+} , Fe^{3+} , Al^{3+} , Cr^{3+} and Hg^{2+} ; Figure 3.1c), anions and biological thiols (Cl^- , Br^- , I^- , F^- , OH^- , H_2PO_4^- , SO_4^{2-} , HSO_4^- , cysteine, homocysteine, glutathione, S^{2-} , HSO_3^- and NO_3^- ; Figure A3.4b). This result demonstrated that probe L_1 could detect Hg^{2+} with high sensitivity and selectivity in a sulfide-rich environment, including common biological interferant thiols such as cysteine, homocysteine, etc. Nevertheless, only the presence of S^{2-} quenched emission intensity which may be an important prerequisite for reuse of the probe L_1 . Upon complexation with L_1 , Hg^{2+} probably drew the electron cloud from the 4-dialkyl amine fragment

via the conjugated aromatic system. Hence, the possibility of internal charge transfer (ICT) is enhanced, resulting in the generation of new, red-shifted spectra. To study the mechanistic aspect of fluorescence enhancement, time-resolved fluorescence decay of **L**₁ (2.0 μM; λ_{ex}=315nm) was performed (Figure 3.1d) before and after the addition of Hg²⁺ (50 equiv) solution in water. Both the time-resolved decay plots were fitted to bi-exponential decay along with a remarkably enhanced lifetime from 1.87 ns to 5.37 ns after the addition of Hg²⁺ (Table A3.1). Radiative (k_r) and non-radiative (k_{nr}) rate constants were calculated using the following relations (Table A3.2):

$$k_r = \Phi_f / T_f$$

$$1 / T_f = k_r + k_{nr}$$

where Φ_f and T_f are the fluorescence quantum yield and average fluorescence lifetime, respectively. The stronger the binding, the lesser the probability of deactivation via non-radiative pathways as is observed in case of aqueous solution hence, radiative rate constant increases and non-radiative rate constant decreases with increase of analyte concentration. These results demonstrated that increased luminescence lifetime could attribute to restricted rotation around the C-N bond of **L**₁-Hg²⁺, consequently enhancing fluorescence.

3.4 Spectral response of the Probe to GSH in water

The responses of **L**₁ (2.0 μM) to several amino acids also were investigated in an aqueous medium through fluorescence spectroscopy techniques. After adding 50 equiv. of copious amino acids (Glutathione, cysteine, homocysteine, alanine, serine, glutamic acid, glycine, phenylalanine, lysine, tyrosine, leucine, arginine, proline and histidine; Figure A3.5) into the aqueous liquor of **L**₁, fluorescence spectra (λ_{ex} = 315nm) was recorded. Surprisingly, as depicted in Figure 3.2a, only Glutathione (GSH) rendered a substantial (~10 fold) fluorescence enhancement with 36nm bathochromic shift (Quantum yield =0.001 and 0.44) while the luminescence spectra of **L**₁ remained unaffected by other coexisting amino acids except for serine and glutamic acid where to some extent red shift was observed. For quantitative analysis, fluorescence titration experiments were executed between **L**₁ and GSH (0-20 equiv.) in the aqueous medium (pH 7.4)(Figure 3.2b). Incremental addition of GSH solution caused progressive enhancement of luminescence intensity of probe **L**₁ and attained maximum intensity with a red-shifted fluorescence maximum at 420 nm. The color changes were also noticeable by naked-eye under 365 nm UV-illumination (Figure 3.2a, Inset). Job's plot analysis applying fluorescence titration results disclosed that binding stoichiometry between **L**₁ and GSH was

found to be 1:1. Based on the 1:1 stoichiometric binding mode, the binding constant (K_a) was determined to be $3.2 \times 10^4 \text{ M}^{-1}$ (Figure A3.6). The limit of detection (LOD) was evaluated

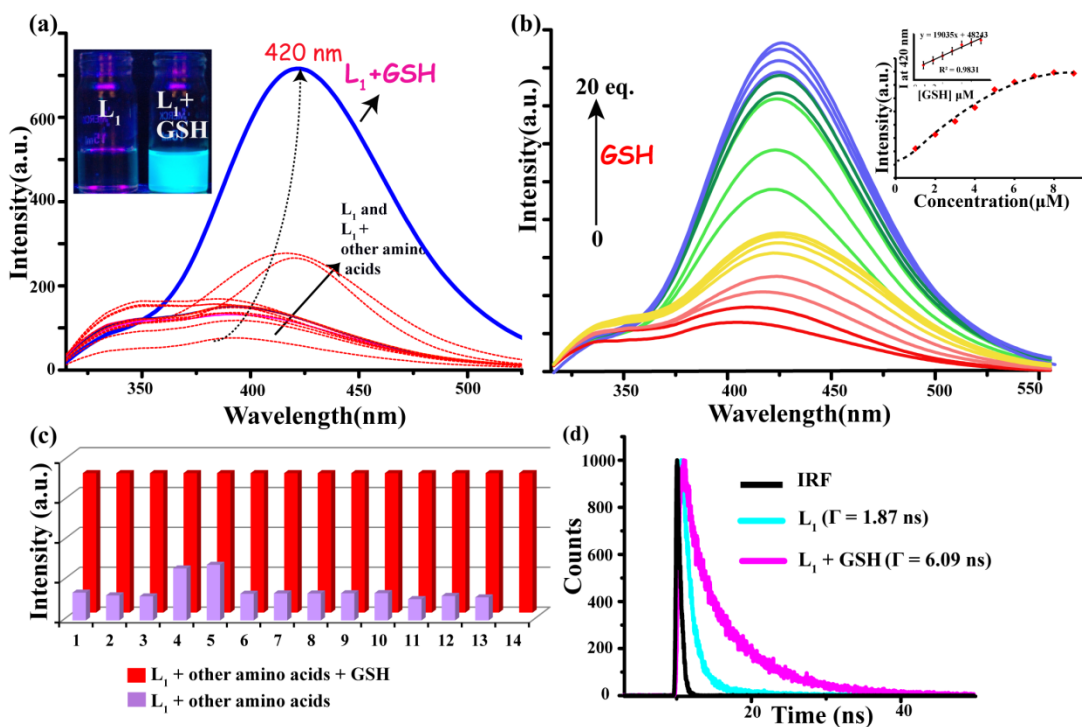


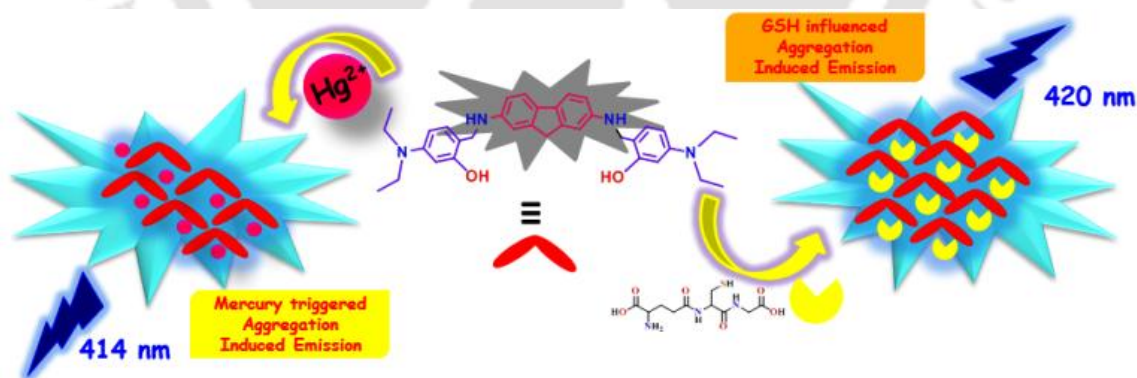
Figure 3.2: (a) Changes in the fluorescence emission of probe L_1 ($2 \mu\text{M}$; $\lambda_{\text{ex}} = 315 \text{ nm}$) were observed upon adding 50 equivalents of several amino acids in an aqueous medium. Inset: visual fluorescence color change in the presence of excess GSH. (b) Fluorescence titration of L_1 ($2 \mu\text{M}$) upon incremental addition of GSH in water. (c) Bar diagram showing the observed emission intensity changes of L_1 with various amino acids (1= cysteine, 2= homocysteine, 3= alanine, 4= serine, 5= glutamic acid, 6= glycine, 7= phenylalanine, 8= lysine, 9= tyrosine, 10= leucine, 11= arginine, 12= proline, 13= histidine and 14= glutathione) before (violet bars) and after (red bars) addition of GSH. (d) Time-resolved decay profile of L_1 ($2 \mu\text{M}$) in the absence and presence of GSH in the aqueous matrix.

to be $\sim 25.83 \text{ ppb}$ based on $3\sigma/k$ (Figure A3.7a) and the limit of quantification (LOQ) for GSH was estimated to be 86.05 ppb . The selectivity and competitive experiments were also accomplished to judge the practicality of L_1 as a GSH selective chemosensor. As demonstrated in Figure 3.2c, the enhanced emission intensity of $L_1\text{-Hg}^{2+}$ in an aqueous medium revealed a negligible change of fluorescence in the presence of common amino acids and common anions (Figure A3.7b). These results designated excellent selectivity of probe L_1 towards Glutathione. To explore the mechanistic aspect of fluorescence enhancement, time-resolved fluorescence decay of L_1 ($2.0 \mu\text{M}$; $\lambda_{\text{ex}}=315\text{nm}$) were performed (Figure 3.2d) in the absence and presence of GSH (50 equiv) solution in water where decay plots were fitted to bi-exponential decay followed by elevation of fluorescence lifetime from 1.87 ns to 6.09 ns (Table A3.3). The radiative rate constant increases and the non-radiative rate constant decreases with an increase in GSH concentration due to stronger binding, hence lesser is the probability of deactivation via

non-radiative pathways (Table A3.4). This outcome signified that probe **L**₁ had high sensitivity and selectivity towards GSH in the biological environment, including interferants such as cysteine, homocysteine, S²⁻ etc.

3.5 Possible recognition mechanism of **L**₁ with Hg²⁺/GSH

In the cause of exploring the recognition phenomenon (Scheme 3.2) of probe **L**₁ for Hg²⁺ and GSH, Job's plot analysis was executed, which had been further backed up by ESI-MS spectrometric studies (Figure A3.8-A3.9). The stoichiometric ratios 1:2 and 1:1 between **L**₁-Hg²⁺ and **L**₁-GSH are denoted by the utmost emission at mole fractions 0.7 and 0.5, respectively. Furthermore, to clarify the probable binding modes of **L**₁, ¹H NMR experiments in the presence of Hg²⁺ and GSH were performed in a DMSO-d₆ medium. As depicted in Figure A3.10, the broadening of both the -NH (δ 5.01) and -OH (δ 8.89) proton signals after the addition of 2 equiv. of Hg²⁺ along with a slight downfield shift in the neighboring aromatic protons (Δδ, 0.11, 0.058, 0.14, 0.087, 0.082 ppm) designating the oxygen atom of hydroxyl group and the nitrogen atom of amine group might be the probable coordination sites for Hg²⁺.^{3.31-3.32} From Figure A3.11, in the presence of GSH, weaker signals of hydroxyl and amine protons of **L**₁ indicated probable intermolecular hydrogen-bond interaction.^{3.33} Furthermore, the 2D NOESY spectra of **L**₁ with GSH in DMSO-d₆ medium unveiled additional cross-peaks due to possible proton interactions in between them (Figure A3.12). However, **L**₂ and **L**₃ did not respond towards Hg²⁺/GSH (Figure A3.13).



Scheme 3.2: Schematic illustration of the sensing mechanism of chemosensor **L**₁ towards Hg²⁺ and GSH.

FESEM measurements and fluorescence microscopic analyses were carried out to figure out any kind of variation in surface morphology of probe **L**₁ before and after the addition of Hg²⁺ and GSH solutions, respectively. As evident from Figure 3.3, **L**₁ displayed smaller scattered particles, which transformed into a massive heterostructure upon treatment with Hg²⁺ and GSH

both(1:50 equivalent, strongly indicating the analyte mediated aggregation of the L_1 -analyte ensemble.

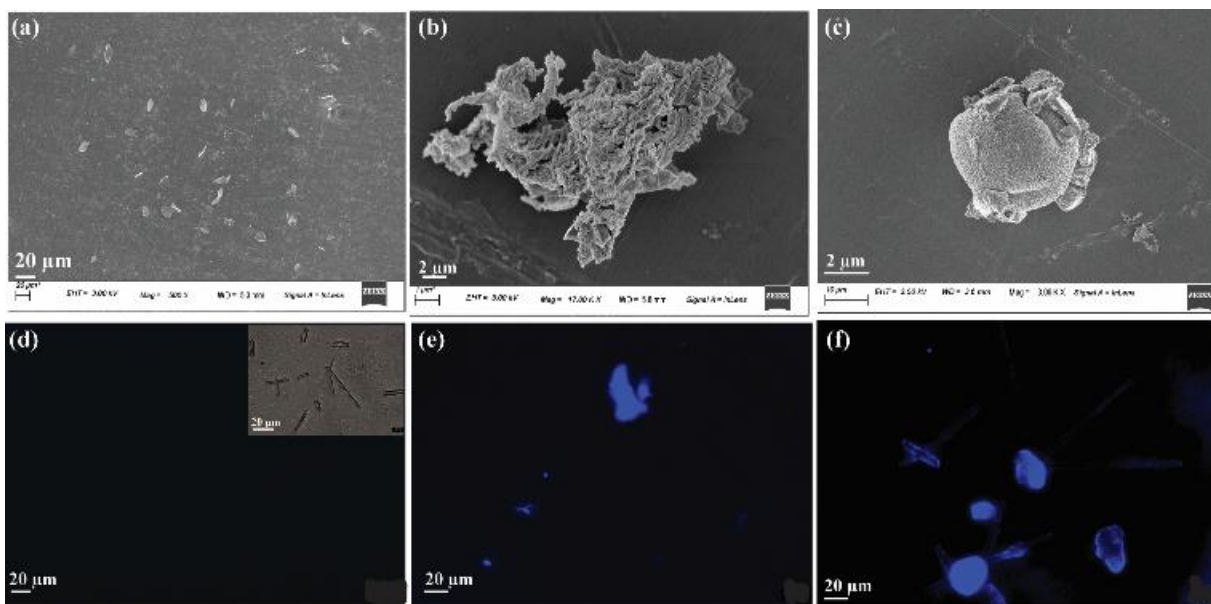


Figure 3.3: FESEM and Fluorescence microscope images(Inset:Bright field images) of L_1 (2.0 μM) (a and d), $L_1 + \text{Hg}^{2+}$ (b and e), $L_1 + \text{GSH}$ (c and f) in water.

Interestingly, fluorescence microscopic images clearly illustrated the intense blue fluorescence emitted by L_1 -mercury and L_1 -glutathione ensembles compared to only the probe (Figure 3.3c-3.3f). To gain more information on the supramolecular self-assembled structure of the probe L_1 , especially the size variation of their aggregates in the aqueous medium, DLS experiments were executed. As anticipated, it was observed that the addition of 50 equivalent Hg^{2+} and GSH independently resulted in higher average particle size of 402.6 nm and 312.2 nm as compared to only L_1 (214.5 nm) (Figure A3.14), strongly corroborating the SEM result. Thus it can be stated that the presence of Hg^{2+} and GSH introduced the aggregation induced emission (AIE) behavior to the system to enable the turn-on fluorescence response facilitating the aggregation phenomenon by lowering the solubility of L_1 . For a better understanding of the mechanism of fluorescence enhancement and photophysical characteristics of probe L_1 , $L_1 + \text{GSH}$, and $L_1 + \text{Hg}^{2+}$, their structures were optimized by DFT calculations. The structural optimizations were performed at the B3LYP functional combined with 6-31G(d, p) for C, H, O, N, and LANL2DZ basis sets for Hg atoms using Gaussian 09 package.^{3.34-3.35} The comparative energy analysis revealed that upon complexation of L_1 with Hg^{2+} and GSH independently resulted in a smaller energy gap to the free probe. TDDFT computations were then carried out based on the optimized ground state geometries using the Time-dependent Self-Consistent Field (TD-SCF) method. Furthermore, the estimated frontier orbital energy of $L_1 + \text{Hg}^{2+}$ (1.2265 eV) and $L_1 +$

GSH (2.9284 eV) were decreased in comparison to chemosensor L_1 (3.7373 eV), hence undoubtedly establishing the theoretical aspect of observed bathochromic shift. However, the Hg-O (2.63 Å) and Hg-N (2.48 Å) bond distances in the optimized structure (Figure 3.4b) suited well within the sum of van der Waals radii of the respective atoms (O 1.52 Å, N 1.54 Å, Hg 1.55-2.23 Å).^{3.36-3.37} Metal coordination contributed the system more planarity, which in turn enhanced the rigidity of the aromatic system^{3.38-3.39} and as a result increased the internal charge transfer from the 4-dialkyl amine moiety to the metal coordination sites. In the absence of metal ions, there is no electronic charge transfer over the 4-dialkyl amine substituted salicylaldehyde ring, and hence the quenched fluorescence owing to the lack of internal charge transfer all over the system.

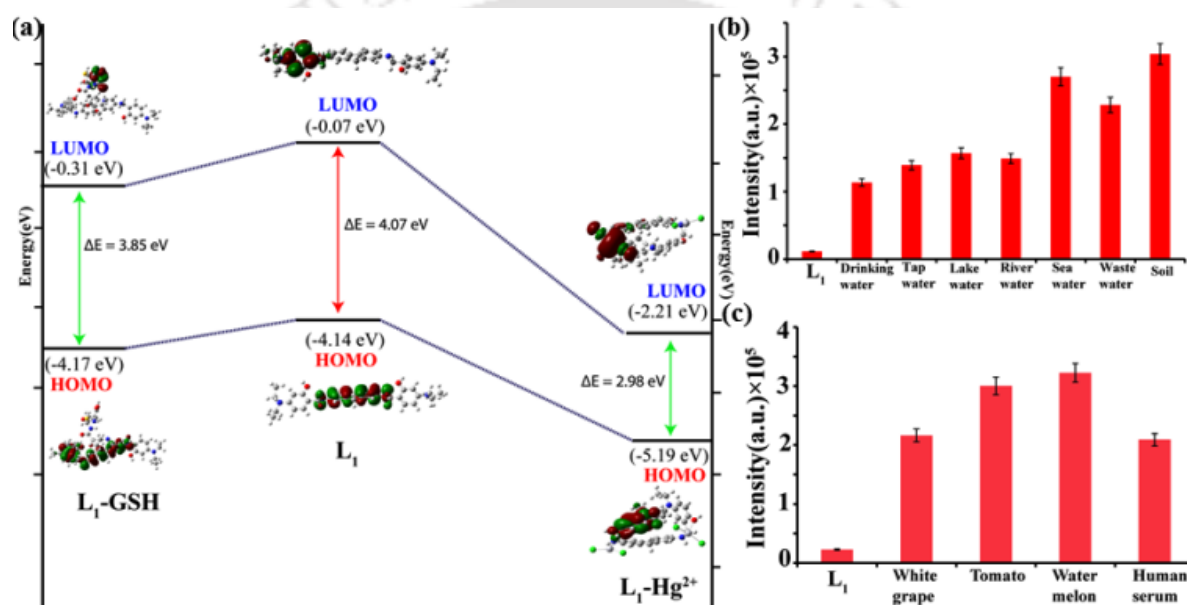


Figure 3.4: (a) Energy level diagrams along with HOMO and LUMO distributions of L_1 , L_1 + GSH, and L_1 + Hg^{2+} complexes. (b) Fluorescence spectral intensity changes for L_1 (2 μ M) at 414 nm upon addition of Hg^{2+} in real water samples (Drinking water, Tap water, Lake water, River water, Seawater, Industrial wastewater, and in soil). (c) Variation in emission intensity of L_1 for real samples (white grapes, tomato, watermelon, and diluted human serum) to recognize GSH.

Therefore metal ion triggered electron pull, and the 4-dialkyl amine assisted electron push, the possibility of internal charge transfer throughout the aromatic π -system elevated; this led to a highly conjugated π -system and consequently enhancement of the luminescence intensity. Furthermore, it has been depicted that the hydrogen bonding interactions (C=O--H-N; 2.59 Å, C=O--H-O; 2.79 Å) (Figure 3.4b) played prime roles for L_1 -GSH 1:1 binding. Although it is well-explored that structures of cysteine, homocysteine are analogous. Still, the existence of a multidentate anchor along with the specific steric structure prevailing in GSH reflected the significant selectivity and sensitivity of the chemosensor (Figure A3.15).^{3.40} It is presumed that

GSH molecules can anchor on the surface and bring the adjacent probe molecules closer through hydrogen bonds between the carboxyl groups and amino groups, leading to compact packing and aggregation of the probe-analyte ensemble. These interactions resulted in the formation of stable complexes triggering fluorescence enhancement and hence are in good agreement with the generation of red-shifted emission maxima. Interestingly, the change in emission spectral behavior of **L**₂ and **L**₃ remained unchanged with the tested analytes since the presence of both the 4-dialkyl amine moiety and the hydroxyl group are significant prerequisites for discriminative sensing ability of **L**₁ towards Hg²⁺/GSH.

3.6 The practicability of **L**₁ towards Hg²⁺ in environmental and biological samples

The toxic effect of Hg²⁺ ions has been well-established that it can be highly notorious to environmental ecology and the living beings on this planet. In the light of spectral characteristics of the chemosensor **L**₁, we examined its potential capabilities for analysis for Hg²⁺ in environmental and biological specimens. Furthermore, to assess the potential outlook of probe **L**₁ recognizing Hg²⁺ in the presence of common interferant analytes, copious natural water samples were arranged. River water, seawater, and lake water samples were brought from the Brahmaputra river (near IITG Campus), the Bay of Bengal, and Serpentine lake (IITG Campus), respectively. Industrial wastewater was arranged by the Chemical Engineering department of IITG. Drinking water and tap water were readily available in the laboratory. At first, these water specimens were centrifuged at 12000 rpm for 10 min, filtered using a 0.2 μm membrane filter to segregate any particulate matter, followed by spiking with mercury solution before the addition of **L**₁. Soil samples were collected from the IITG campus garden, and a 2.0 g sample of soil was crushed in a petri dish. Next, 5.0 mg Hg²⁺ salt was mixed with the soil sample, combined thoroughly, and from the mixture, 50 mg soil sample was added to the aqueous solution of **L**₁ (2.0 μM), each solution was filtered, and fluorescence was recorded.^{3,41} Ultimately, the emission maximum of **L**₁ (2 μM) in the presence of Hg²⁺ at 414 nm with akin fluorescence enhancement was achieved (Figure 3.4d). The quantitative recovery amounts carried out by spiked samples of analyte are shown in Table A3.3. Another practical application of the sensor for Hg²⁺ in biological samples i.e., simulated physiological media, artificial urine,^{3,42} and milk samples^{3,43} were also explored. Interestingly, the experiment unveiled that **L**₁(2.0 μM) was able to recognize Hg²⁺ in the simulated gastric fluid (pH ~2.0), intestinal fluid (pH ~8.0), body fluid (pH~7.4), artificial urine and milk samples by manifesting similar distinguishable "turn-on" luminescence enhancement (Figure A3.16).

3.7 Practical application of L_1 towards GSH in biological samples

To examine the analytical performance of the proposed chemosensor for complicated biological environments, the detection of GSH concentrations in several food samples was explored. All the raw food samples, i.e., tomatoes, watermelon, and white grapes (excellent GSH rich foods), were purchased from the local market (Guwahati, Assam). The food samples were cleaned with distilled water, then air-dried, diced into smaller cubes followed by centrifugation in a refrigerated centrifuge at 3000 rpm for 20 minutes. After filtration, the supernatant was collected through a 0.45 μm membrane filter and diluted to appropriate concentrations.^{3.44} These resulting solutions were kept in a refrigerator at 4°C for future use. Each sample extract was taken in an appropriate amount and subjected to fluorimetric analysis. Satisfactory results were achieved based on the robust "turn-on" fluorescence enhancement of L_1 (Figure 3.4e). Furthermore, using the chemosensor, L_1 fluorescence spectroscopic experiments were accomplished to recognize GSH content in 1:10 diluted human blood serum also.^{3.45} Moreover, the obtained fluorimetric results suggested that L_1 could reliably and feasibly detect GSH content in human serum without any expensive instrumentation. Recoveries of the known spiked quantity of GSH in real food samples and human serum are summarized in Table A3.4. Interestingly, the developed chemosensor L_1 (2.0 μM) showed a significant advantage of recognizing GSH in the simulated gastric fluid (pH ~2.0), intestinal fluid (pH ~8.0), body fluid (pH~7.4), and artificial urine specimens by emitting similar distinguishable strong blue fluorescence (Figure A3.16b).

3.8 Bioimaging application in live tissues

To explore the practical applicability of L_1 (2.0 μM) to sense mercury in live tissues, we examined its potentiality via bioimaging utilizing confocal fluorescence microscopy.^{3.46} An extensive investigation was further accomplished to ensure whether the chemosensor L_1 could recognize the presence of in vivo Hg^{2+} in living plant tissues since Hg^{2+} can readily penetrate and flow through the plant tissues' cell membrane, causing dreadful phytotoxicity.^{3.46} For this, the Indian holy basil plant was selected as a model plant and pre-incubated with L_1 and $L_1 + \text{Hg}^{2+}$. After several hours, the plant sample was dried, dissected, and placed on a coverslip to take images in fluorescence microscopy. Consequently, bright blue fluorescence was observed, whereas only L_1 incubated tissue did not release any detectable fluorescence. Seedlings of gram seed were incubated with L_1 and $L_1 + \text{Hg}^{2+}$ separately and kept for one day. The next day, L_1 -loaded seedlings were get dried, and fluorescence microscopic images were obtained. Gram seeds with $L_1 + \text{Hg}^{2+}$ resulted in strong bluish emission (Figure 3.5a). The abovementioned results indicated that L_1 could be potentially utilized to detect enrichment of Hg^{2+} in live tissues.

3.9 Solid state-based sensor for Hg^{2+} sensing

For convenient use of L_1 in on-site analysis, i.e., for contact mode detection of Hg^{2+} , other than the fluorescent paper sensor, L_1 impregnated fabric-based wearable sensor was able to detect

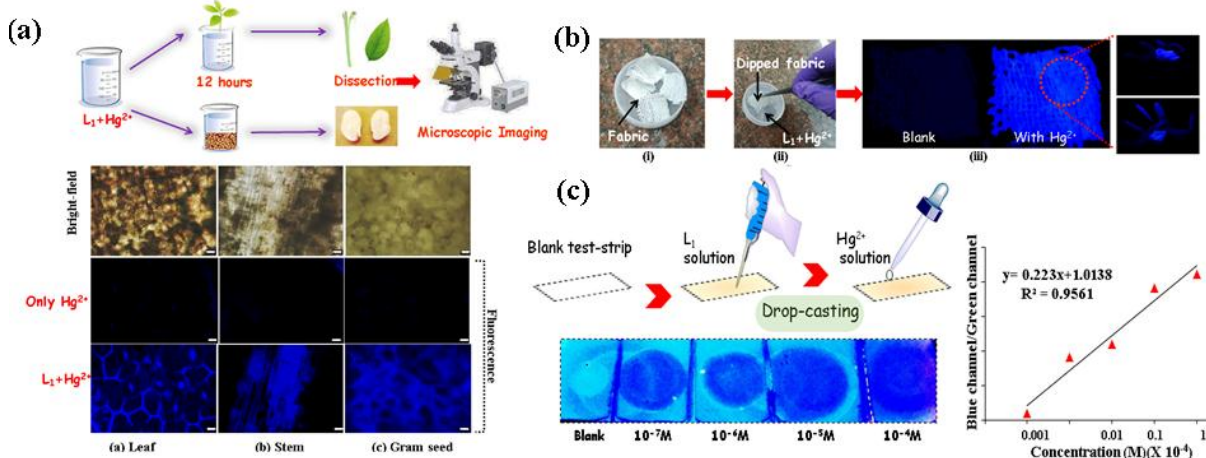


Figure 3.5: (a) Schematic pictorial representation of loading of $\text{L}_1 + \text{Hg}^{2+}$ in plant tissue and gram seed; Fluorescence images of plant tissues and gram seed treated with probe L_1 , only Hg^{2+} and $\text{L}_1 + \text{Hg}^{2+}$ (Scale bar= 20 μm). (b) Graphical illustration for coating of non-woven fabric with $\text{L}_1 + \text{Hg}^{2+}$ mixture (i and ii); Photograph of only fabric and $\text{L}_1 + \text{Hg}^{2+}$ coated fabric under 365 nm light, Inset: fabric in contact with gloves. (c) Fluorescence response of L_1 stuffed test strips towards several concentrations of Hg^{2+} (10^{-4} - 10^{-7} M) under 365nm UV illumination.

mercury in work environment exhibiting remarkable discriminative emission enhancement (Figure 3.5b).^{3,47} Whatman 42 filter paper was soaked into the solution of L_1 (5×10^{-6} M) in DMSO and dried at room temperature for several hours. When the solvent evaporated completely, the L_1 coated filter paper was cut into small portable test strips (2.0 cm \times 2.0 cm) and then used to rapidly analyze respective analytes. As shown in Figure 3.5c, to facilitate the visual recognition of Hg^{2+} , the above-prepared low-cost paper test strips moistened with L_1 were subjected to visualize under a 365 nm hand-held UV lamp after spraying freshly prepared Hg^{2+} (10^{-4} - 10^{-7} M) solutions. To our delight, naked-eye discernible color enhancement was observed with increasing concentrations of Hg^{2+} (Figure 3.5c). Hence wearable sensors encapsulated into gloves, clothes, and inexpensive, portable paper strip-based sensors are likely to be exploited to field detection without resorting to sophisticated equipment.

3.10 Paper-based sensor for GSH sensing

In cooperation with the fluorescence color change in the aqueous phase, the fluorescent paper strip could simplify the detection process and recognize the quantitative analysis of convenient, on-site GSH detection (Figure 3.6). After adding different concentrations of GSH solutions in pre-treated L_1 coated paper strips under 365 nm U.V. illumination, photographs were taken by a

smartphone, which resulted in specific RGB values through a smartphone application (Color recognizer) (Figure A3.17).^{3,48} Therefore, paper strips along with RGB analysis via smartphone sensing platform could be reliable for visual, on-site, and quantitative recognition of GSH since the human eye might not detect the minute color variation. Hence smartphone-assisted

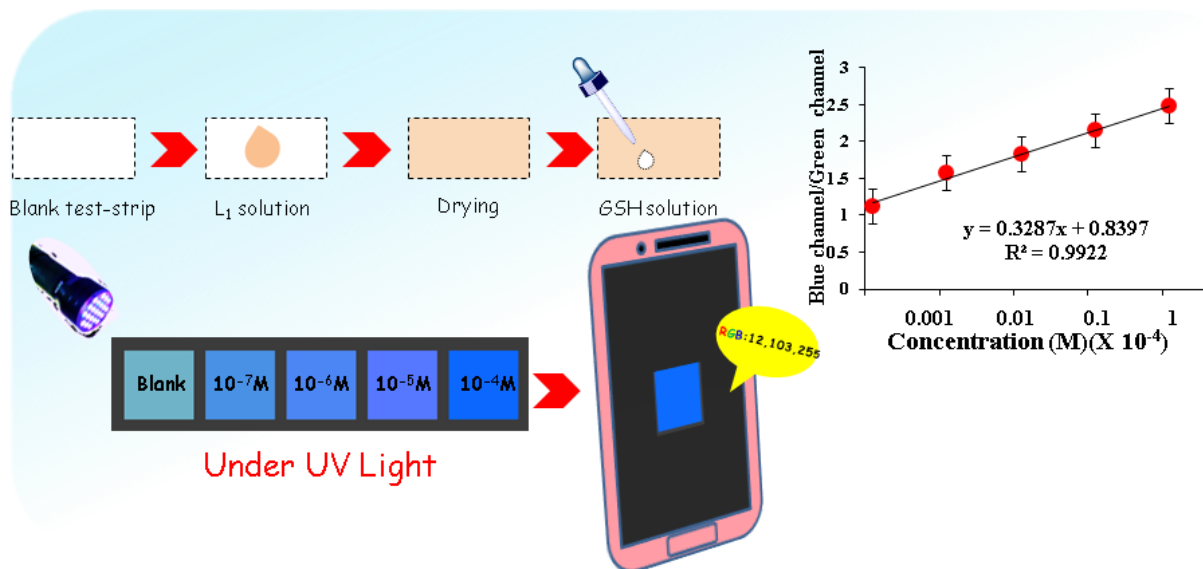


Figure 3.6: Illustration of the paper strip making procedure; Photograph of L_1 pre-treated test strips dropped with different concentrations of GSH solution (10^{-4} - 10^{-7} M) captured by a smartphone camera for naked-eye detection under a hand-held UV light; Linear relationship between the B/G values versus concentration of GSH solution.

paper-based sensors, due to their design simplicity and excellent performance, might have huge potential in bioanalysis and bio-detection for diagnosing tumor biomarker GSH levels soon.

3.11 Conclusions

In summary, we have successfully designed, synthesized, and characterized three simple fluorene-salicylaldehyde /aldehyde conjugate probes L_1 , L_2 , and L_3 . Surprisingly, we explored L_1 as a selective and sensitive multifunctional switch-on fluorescent probe towards Hg^{2+} (LOD ~ 17.35 ppb) and GSH (LOD ~ 25.83 ppb) respectively over other coexisting analytes in the aqueous medium. The recognition events of chemosensor L_1 towards Hg^{2+} /GSH were unveiled satisfactorily via fluorescence spectroscopic techniques, 1H -NMR, HRMS studies, FESEM experiments, fluorescence microscopy analyses, and theoretical calculations. The sensing mechanism of L_1 towards Hg^{2+} and GSH additionally involved analyte recognition triggered self-assembly formation, attributed to aggregation induced emission phenomenon. The sensing strategy was successfully implemented to recognize Hg^{2+} /GSH in naturally contaminated water body samples, simulated physiological media, and in real biological samples, including human serum specimens. Apart from the visual color changes in the solution state, in-field device

application was further established by sensing Hg^{2+} and GSH in L_1 coated portable, economical paper strips along with a smartphone sensing platform (RGB analysis), showing significant potential in biomedical domain applications for disease diagnosis soon.

References

- 3.1 A. Alsbaiee, B. J. Smith, L. Xiao, Y. Ling, D. E. Helbling and W. R. Dichtel, *Nature*, 2016, **529**, 190.
- 3.2 G. Banfalvi, *Springer*, 2011, 3-28.
- 3.3 N. Herawati, S. Suzuki, K. Hayashi, I. F. Rivai and H. Koyoma, *Bull. Environ. Contam. Toxicol.*, 2000, **64**, 33–39.
- 3.4 S. Sarkar and R. Shunmugam, *ACS Appl. Mater. Interfaces.*, 2013, **5**, 7379–7383.
- 3.5 H. S. So, B. A. Rao, J. Hwang, K. Yesudas and Y. A. Son, *Sens. Actuators B: Chemical.*, 2014, **202**, 779–787.
- 3.6 R. Verma and B. D. Gupta, *Food Chem.*, 2015, **166**, 568–575.
- 3.7 H. Ozay, R. Kagit, M. Yildirim, S. Yesilot and O. Ozay, *J. Fluoresc.*, 2014, **24**, 1593–1601.
- 3.8 B. Weiss, *Toxicol. Sci.*, 2007, **97**, 223–225.
- 3.9 L. Amin-Zaki, S. Elhassani, M. A. Majeed, T. W. Clarkson, R. A. Doherty and M. Greenwood, *Springer. Dordrecht*. 1974, 233–241.
- 3.10 G. L. Wang, K. L. Liu, Y. M. Dong, Z. J. Li and C. Zhang, *Anal. Chim. Acta.*, 2014, **827**, 34–39.
- 3.11 G. V. Guerreiro, A. J. Zaitouna and R. Y. Lai, *Anal. Chim. Acta.*, 2014, **810**, 79–85.
- 3.12 S. H. Gao, M. S. Xie, H. X. Wang, H. Y. Niu, G. R. Qu and H. M. Guo, *Tetrahedron*, 2014, **70**, 4929–4933.
- 3.13 A. Han, X. Liu, G. D. Prestwich and L. Zang, *Sens. Actuators B: Chemical.*, 2014, **198**, 274–277.
- 3.14 L. Shi, Z. Chu, Y. Liu, W. Jin and X. Chen, *Biosens. Bioelectron.*, 2014, **54**, 165–170.
- 3.15 J. Chen, J. Pan and S. Chen, *Chem. Commun.*, 2017, **53**, 10224–10227.
- 3.16 X. C. Le, M. Ma and N. A. Wong, *Anal. Chem.*, 1996, **68**, 4501–4506.
- 3.17 H. M. Anawar, *Talanta*, 2012, **88**, 30–42.
- 3.18 H. N. Kim, W. X. Ren, J. S. Kim and J. Yoon, *Chem. Soc. Rev.*, 2012, **41**, 3210–3244.
- 3.19 M. Mulvihill, A. Tao, K. Benjauthrit, J. Arnold and P. Yang, *Angew. Chem.*, 2008, **120**, 6556–6560.
- 3.20 T.P. Akerboom, M. Bilzer and H. Sies, *J. Biol. Chem.*, 1982, **257**, 4248–4252.
- 3.21 H. Kimura, Y. Nagai, K. Umemura and Y. Kimura, *Antioxid. Redox Signal.*, 2005, **7**, 795–803.
- 3.22 W.A. Kleinman and J.P. Richie, *Biochem. Pharmacol.*, 2000, **60**, 19–29.
- 3.23 P.K. Pullela, T. Chiku, M.J. Carvan and D.S. Sem, *Anal. Biochem.*, 2006, **352**, 265–273.
- 3.24 X. Chen, Y. Zhou, X. Peng and J. Yoon, *Chem. Soc. Rev.*, 2010, **39**, 2120–2135.
- 3.25 A. Pastore, F. Piemonte, M. Locatelli, A. L. Russo, L. M. Gaeta, G. Tozzi and G. Federici, *Clin. Chem.*, 2001, **47**, 1467–1469.
- 3.26 H. Tapiero, D. Townsend and K. Tew, *Biomed. Pharmacother.*, 2003, **57**, 134–144.
- 3.27 Y. Deng, W. Yuan and G. Liu, *J. Phys. Chem. B.*, 2014, **118**, 14536–545.

- 3.28 J. Zhao, S. Ji, Y. Chen, H. Guo and P. Yang, *Physical Chemistry Chemical Physics.*, 2012, **14**, 8803–8817.
- 3.29 S. Fernández-Alonso, T. Corrales, J.L. Pablos and F. Catalina, *Sens. Actuators B Chem.*, 2018, **270**, 256–262.
- 3.30 M. A. Wani, N. Thakur, M. D. Pandey and R. Pandey, *New J. Chem.*, 2017, **41**, 10000–10008.
- 3.31 C. Guiqiu, G. Zhi, Z. Guangming and T. Lin, *Analyst*, 2015, **140**, 5400.
- 3.32 Y. Xueying, W. Kangnan, C. Duxia, L. Zhiqiang, G. Ruifang, W. Qianqian, X. Yongxiao, S. Yatong and Z. Xun, *Sensors and Actuators B.*, 2017, **250**, 132–138.
- 3.33 S.R. Patil, J.P. Nandre, D. Jadhav, S. Bothra, S.K. Sahoo, M. Devi, C.P. Pradeep, P.P. Mahulikar and U.D. Patil, *Dalton Trans.*, 2015, **43**, 13299-13306.
- 3.34 M. Fisch, G. Trucks, H. Schlegel, G. Scuseria, M. Robb, J. Cheeseman, G. Scalmani, V. Barone, B. Mennucci and G. Petersson, *Gaussian 09 (Revision A. 02)*, Wallingford, CT, 2009.
- 3.35 S.Z. Hu, Z.H. Zhou and B. E. Robertson, *Z. kristallogr.*, 2009, **224**, 375-383.
- 3.36 S. C. Nyburg and C. H. Faerman, *Acta Crystallogr., Sect. B: Struct. Sci.*, 1985, **41**, 274-279.
- 3.37 W. A. E. Omar, *J. Adv. Res.*, 2013, **4**, 525.
- 3.38 F. Suzuki, T. Fukushima, M. Fukuchi and H. Kaji, *J. Phys. Chem. C.*, 2013, **117**, 18809.
- 3.39 Y. P. Shi, Y. Pan, H. Zhang, Z. M. Zhang, J. M. Li, Q. C. Yi, M. S. Yang, *Biosens. Bioelectron.*, 2014, **56**, 39–45.
- 3.40 V.K. Gupta, A.K. Singh, M. Al. Khayat and B. Gupta, *Analytica Chimica Acta.*, 2007, **590**, 81–90.
- 3.41 T. Brooks and C.W. Keevil, *Letters in Applied Microbiology.*, 1997, **24**, 203–206.
- 3.42 S. Yupeng, P. Yi, Z. Heng, Z. Zhaomin, L. Mei-Jin, Y. Changqing and Y. Mengsu, *Biosensors and Bioelectronics.*, 2014, **56**, 39–45.
- 3.43 T. Hongliang, L. Qian, M. Chanjiao, S. Yonghai, X. Fugang, C. Shouhui and W. Li, *Biosensors and Bioelectronics*, 2015, **63**, 566–571.
- 3.44 N. Yan, Z. F. Zhu, N. Ding, L. Zhou, Y. L. Dong and X. G. Chen, *J. Chromatogr. A.*, 2009, **1216**, 8665–8670.
- 3.45 Y. Yang, S. Rong, W. Ying-Zhe, Q. Fang-Zhou, F. Yan, T. Xiao-Liang, B. De-cheng, Z. Guo-Lin and L. Wei-Sheng, *Sensors and Actuators B.*, 2018, **255**, 3479–3487.
- 3.46 C. Xue, F. Jie, L. Sijie, M. Rony, L. Wenjin, G. Chao, T. Di and Li. Wei, *Sensors & Actuators: B. Chemical.*, 2021, **342**, 130064.
- 3.47 J. Chen and Z.M. Yang, *BioMetals.*, 2012, **25**, 847–857.
- 3.48 C. Suyun, W. Haiqian, D. Yuanxin, Y. Fan, Y. Liang and J. Changlong, *ACS Sustainable Chem. Eng.*, 2020, **8**, 8175–8183.

Appendix - Chapter 3

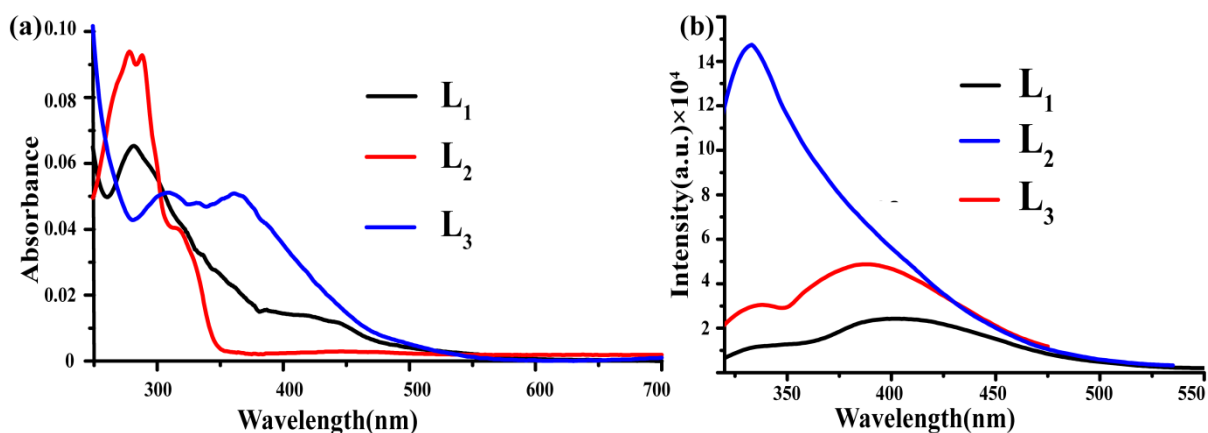


Figure A3.1: (a) UV-visible spectra of L₁, L₂ and L₃ in aqueous medium at room temperature. (b) Fluorescence emission spectra of L₁, L₂ and L₃ in aqueous medium at room temperature ($\lambda_{\text{ex}} = 315$ nm, slit = 3nm / 3nm).

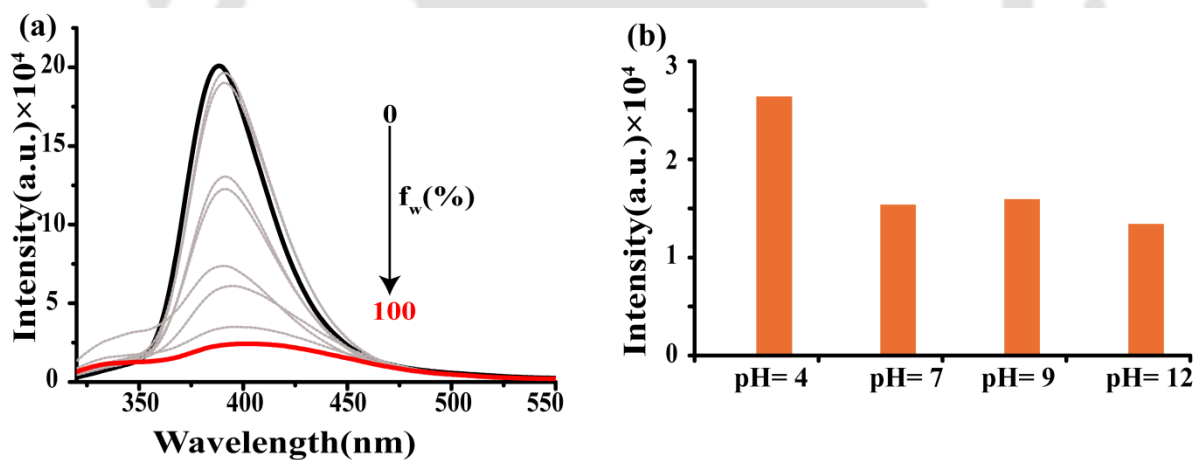


Figure A3.2: Fluorescence spectral changes of L₁ with increasing water content in acetonitrile solution ($\lambda_{\text{ex}} = 315$ nm, slit = 3nm / 3nm). (b) Fluorescence spectral changes of L₁ with increasing pH in aqueous solution ($\lambda_{\text{ex}} = 315$ nm, slit = 3nm / 3nm).

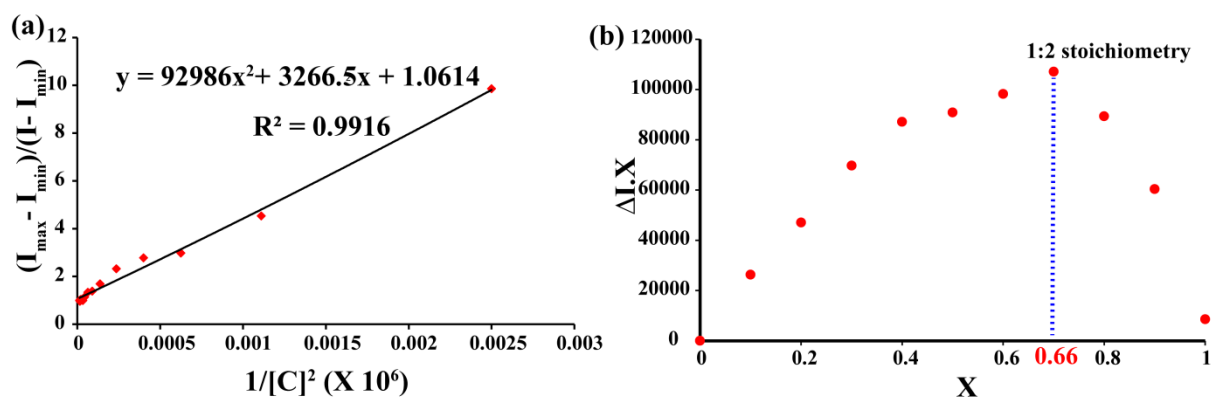


Figure A3.3: (a) Determination of affinity constant of L_1 for Hg^{2+} in aqueous medium using the Benesi-Hildebrand method. (b) Job's plot for determining L_1 's stoichiometry with Hg^{2+} (1:2 host-guest complex).

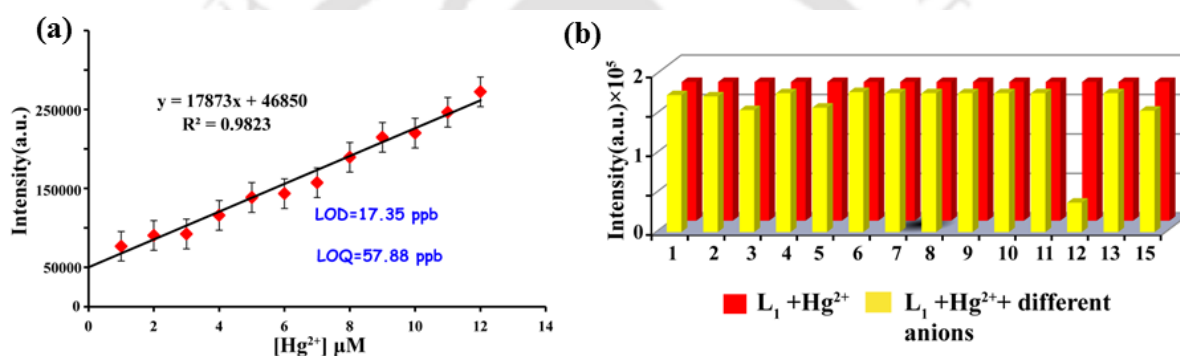


Figure A3.4: (a) Fluorescence emission intensity of L_1 at 414 nm vs. Hg^{2+} concentration to calculate the limit of detection (LOD). (b) Fluorescence response of L_1 (2.0 μM) to various analytes (1= Cl^- , 2= Br^- , 3= I^- , 4= F^- , 5= OH^- , 6= $H_2PO_4^-$, 7= SO_4^{2-} , 8= HSO_4^- , 9= cysteine, 10= homocysteine, 11= glutathione, 12= S^{2-} , 13= HSO_3^- and 14= NO_3^-).

Table A3.1: Fluorescence lifetime values of L_1 (2.0 μM) and L_1-Hg^{2+} in aqueous medium.

Sample	B_1	ΔB_1	B_2	ΔB_2	a_1	Δa_1	a_2	Δa_2	τ_1	$\Delta \tau_1$	τ_2	$\Delta \tau_2$	$\langle \tau \rangle$ (ns)	χ^2
L_1	0.05	0.0005	0.02	0.0001	0.82	0.01	0.17	0.01	1.14	0.01	5.28	0.006	1.87	1.0
L_1+Hg^{2+}	0.03	0.0004	0.01	0.0002	0.27	0.07	0.73	0.07	1.42	0.02	6.85	0.008	5.37	1.0

Table A3.2: Rate constants for radiative and non-radiative decays, average lifetimes of L_1 (2.0 μM) and $L_1\text{-Hg}^{2+}$ in aqueous medium.

Sample	K_r (S^{-1})	K_{nr} (S^{-1})	Slower decay component	Faster decay component	Average lifetime(ns)
L_1	0.00069×10^9	0.53×10^9	1.14	5.28	1.87
$L_1 + \text{Hg}^{2+}$	0.009×10^9	0.18×10^9	1.42	6.85	5.37

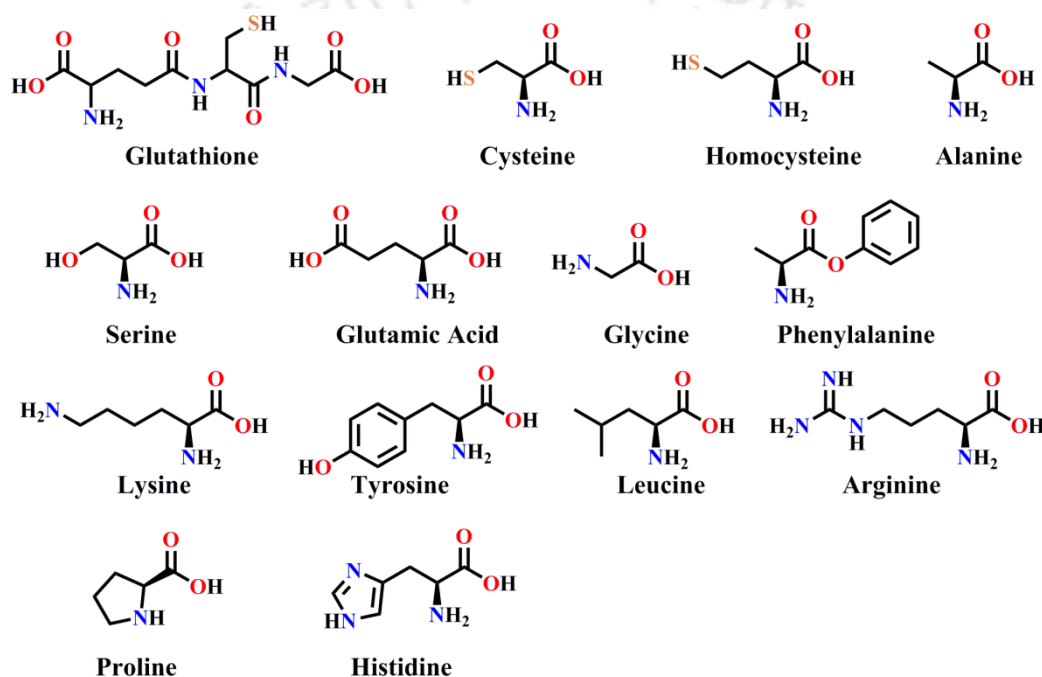


Figure A3.5: Chemical structures of different amino acids used in our study.

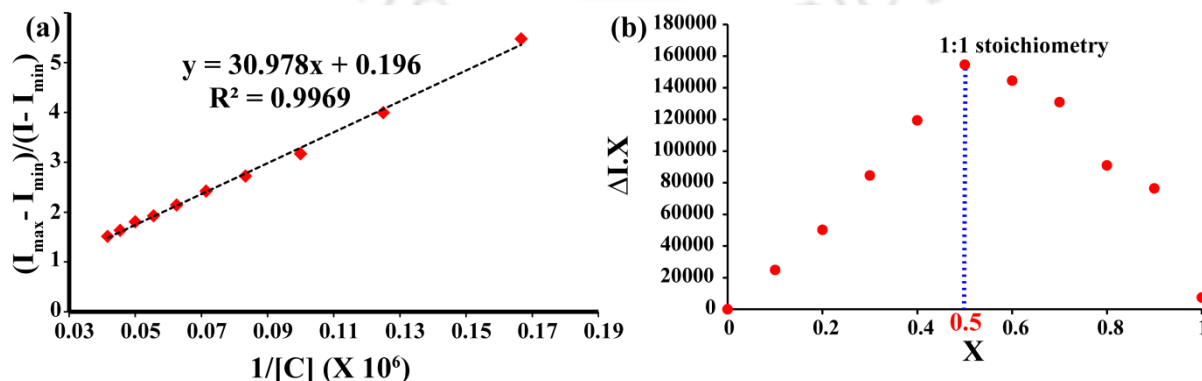


Figure A3.6: (a) Determination of affinity constant of L_1 for GSH in aqueous medium using the Benesi-Hildebrand method. (b) Job's plot for determining L_1 's stoichiometry with GSH (1:1 host-guest complex).

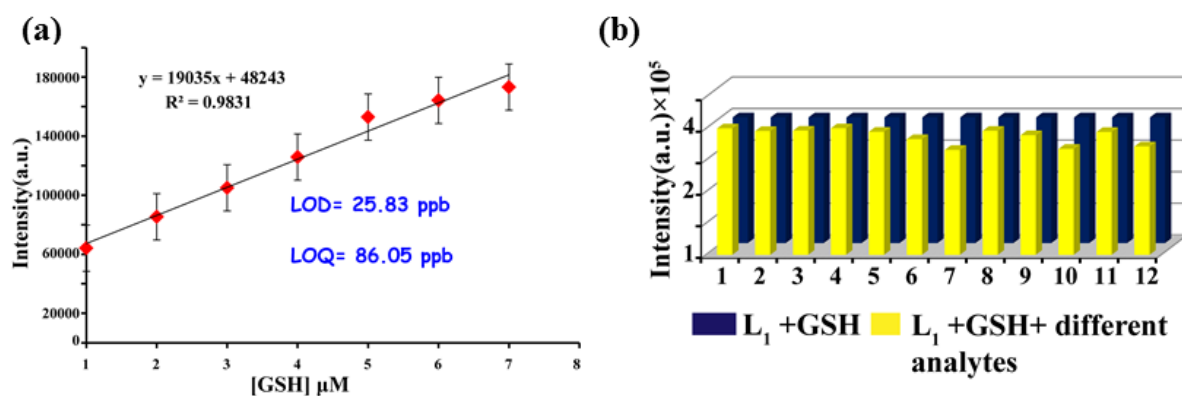


Figure A3.7: (a) Fluorescence emission intensity of L_1 at 420 nm vs. GSH concentration to calculate the limit of detection (LOD). (b) Fluorescence response of L_1 (2.0 μM) to various analytes (1= Cl^- , 2= Br^- , 3= I^- , 4= F^- , 5= NO_3^- , 6= H_2PO_4^- , 7= HCO_3^- , 8= HSO_4^- , 9= NO_2^- , 10= Hg^{2+} , 11= Cu^{2+} and 12= Zn^{2+})

Table A3.3: Fluorescence lifetime values of L_1 (2.0 μM) and L_1 -GSH in aqueous medium.

Sample	B_1	ΔB_1	B_2	ΔB_2	a_1	Δa_1	a_2	Δa_2	τ_1	$\Delta \tau_1$	τ_2	$\Delta \tau_2$	$\langle \tau \rangle$ (ns)	χ^2
L_1	0.05	0.0005	0.02	0.0001	0.82	0.01	0.17	0.01	1.14	0.01	5.28	0.006	1.87	1.0
L_1 +GSH	0.02	0.0017	0.02	0.0006	0.17	0.02	0.83	0.02	1.62	0.03	7.00	0.007	6.09	1.0

Table A3.4: Rate constants for radiative and non-radiative decays, average lifetimes of L_1 (2.0 μM) and L_1 -GSH in aqueous medium.

Sample	K_r (S^{-1})	K_{nr} (S^{-1})	Slower decay component	Faster decay component	Average lifetime(ns)
L_1	0.00069×10^9	0.53×10^9	1.14	5.28	1.87
L_1 + GSH	0.07×10^9	0.09×10^9	1.62	7.0	6.09

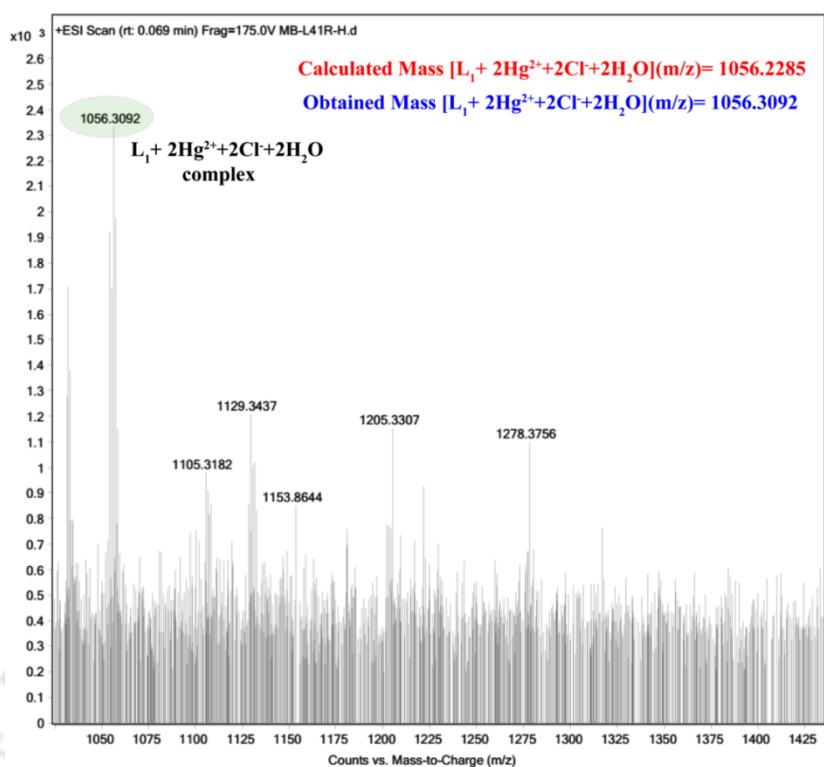


Figure A3.8: ESI-MS spectra of L_1 in 1:1 water-acetonitrile in the presence of Hg^{2+} in positive ionization mode.

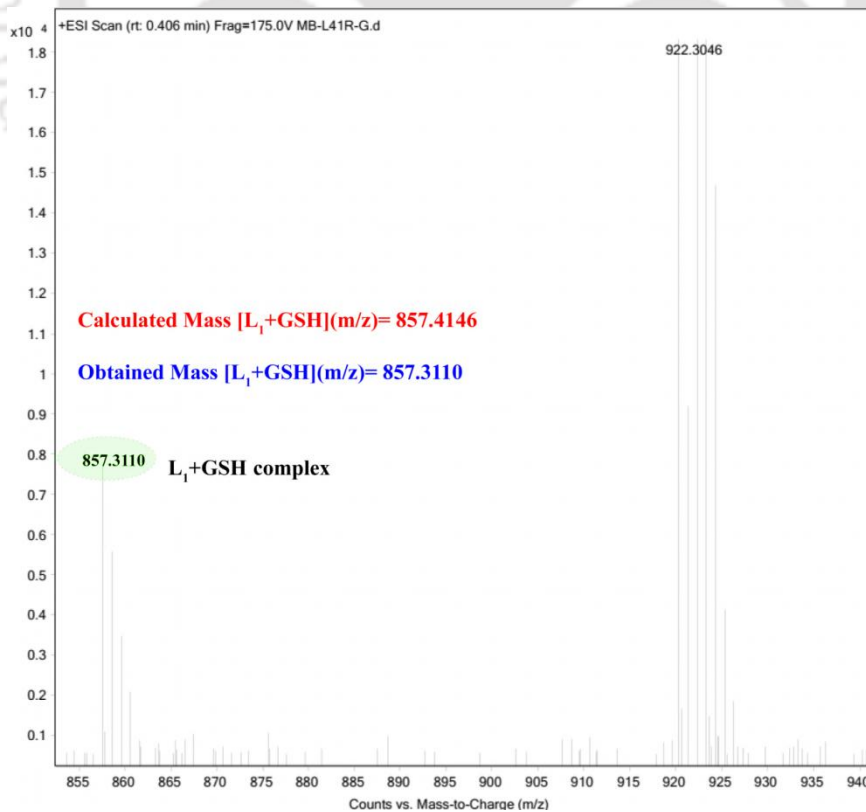


Figure A3.9: ESI-MS spectra of L_1 in 1:1 water-acetonitrile in the presence of GSH in positive ionization mode.

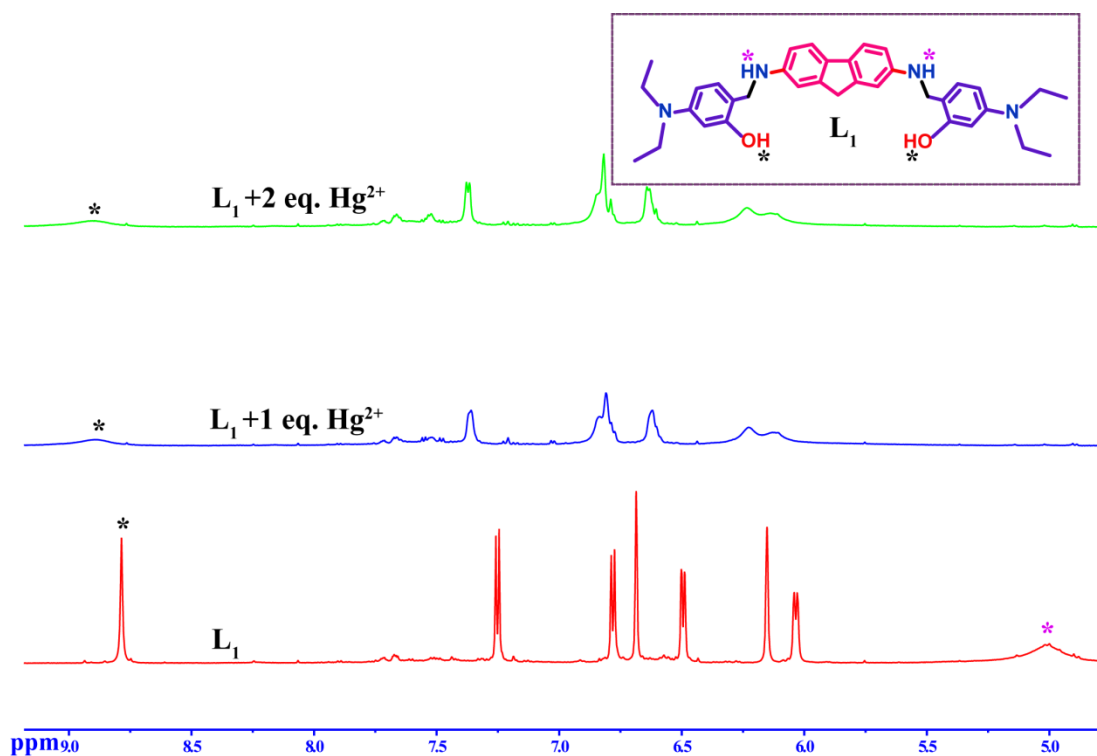


Figure A3.10: ^1H NMR spectral changes of L_1 in DMSO-d_6 upon addition of 2 equiv. Hg^{2+} .

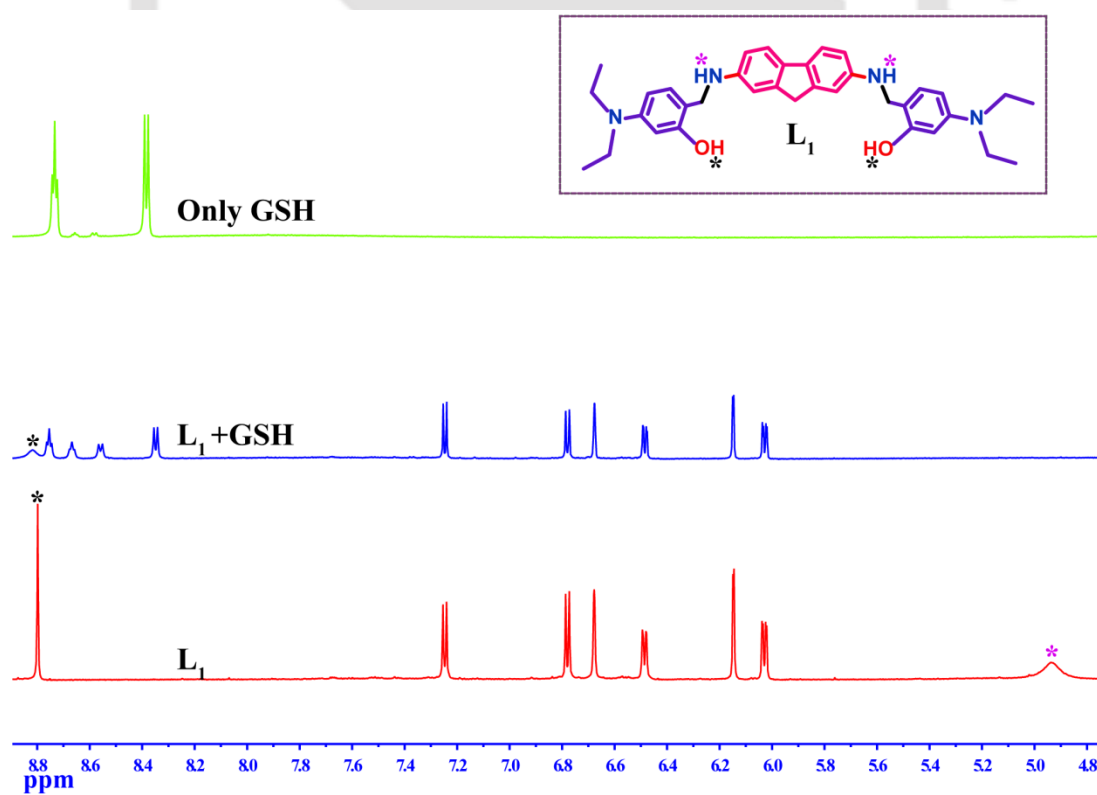


Figure A3.11: ^1H NMR spectral changes of L_1 in DMSO-d_6 upon addition of 1 equiv. GSH .

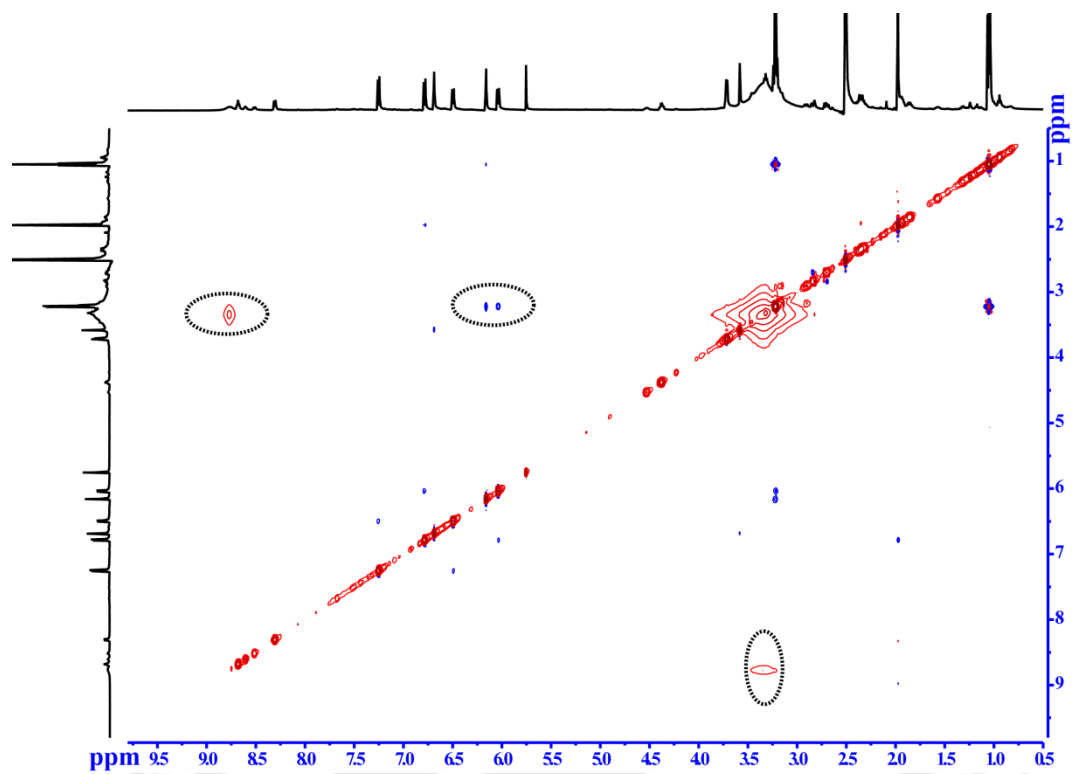


Figure A3.12: NOESY NMR spectra of L_1 - GSH.

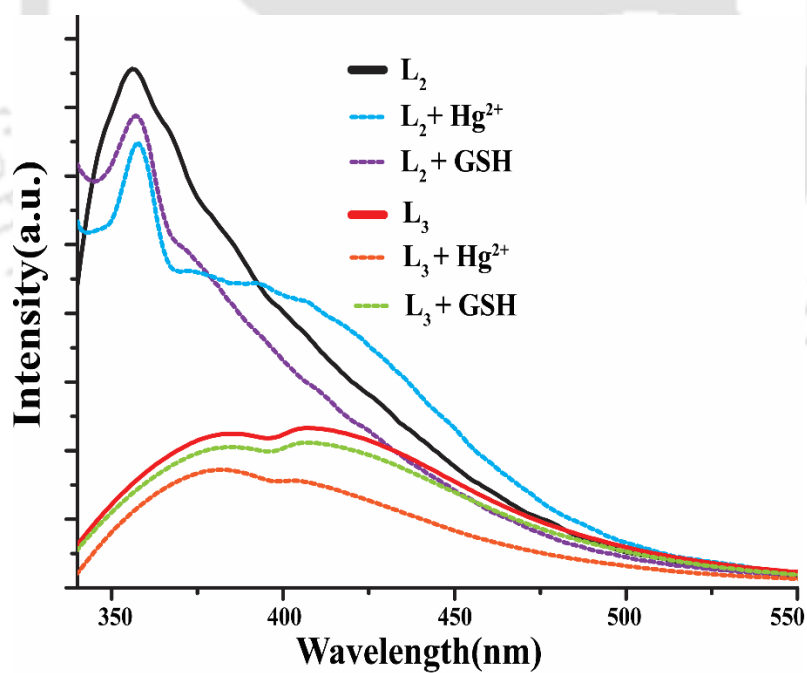


Figure A3.13: Fluorescence response of L_2 and L_3 towards Hg^{2+} /GSH.

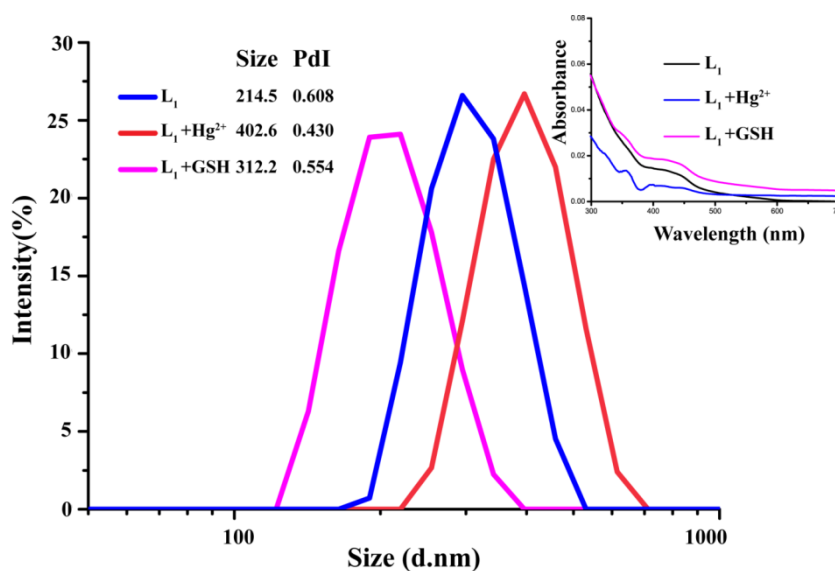


Figure A3.14: DLS analysis of L_1 (2.0 μ M), $L_1 + Hg^{2+}$ and $L_1 + GSH$ in aqueous medium. (Inset: UV spectra of $L_1 + Hg^{2+}$ and $L_1 + GSH$ showing upliftment of baseline indication aggregation nature).

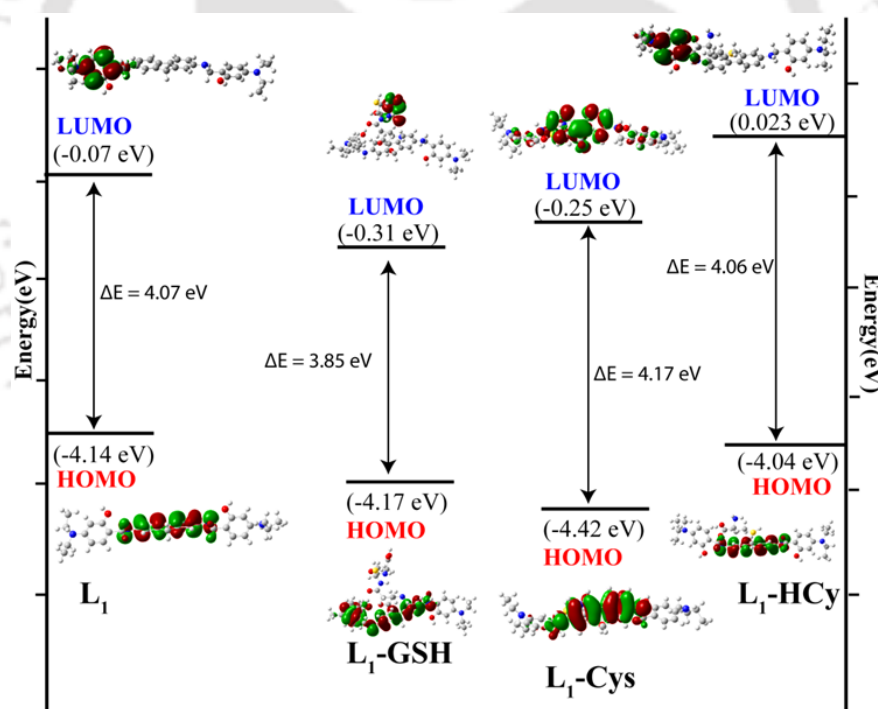


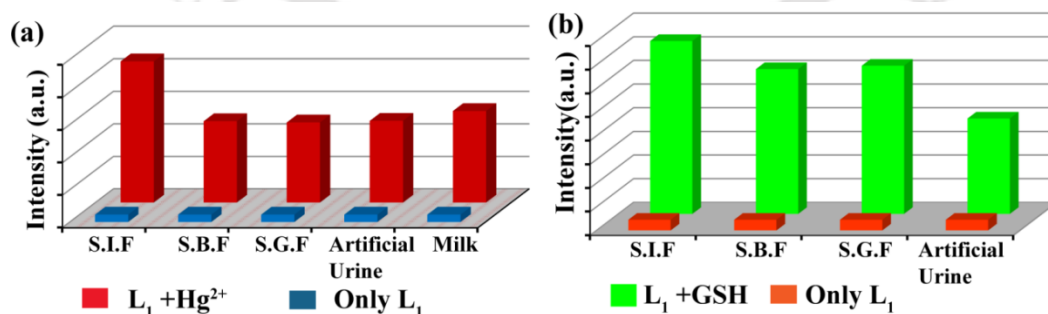
Figure A3.15: Comparative energy level diagrams of L_1 -cysteine ensemble; L_1 -homocysteine ensemble; L_1 -glutathione ensemble.

Table A3.5: Comparative analysis of Hg^{2+} in different real environmental samples by using fluorimetric method and AAS technique.

Sample	Fluorescence Spectroscopy				Atomic Absorption Spectroscopy(AAS)			
	Added (μM)	Detected (μM)	Recovery (%)	RSD(%)n=3	Added (μM)	Detected (μM)	Recovery (%)	RSD(%)n=3
Drinking water	2.0	1.8	90	0.4	2.0	2.0	100	0.38
Tap water	2.0	1.9	94	1.35	2.0	1.95	97.5	1.4
Lake water	2.0	2.1	101	0.36	2.0	2.13	106	0.4
River water	2.0	1.85	93	2.35	2.0	1.8	90	2.20
Sea water	2.0	2.1	105	0.45	2.0	2.15	107	0.37
Industrial wastewater	2.0	2.25	110	3.26	2.0	2.24	112	3.00

Table A3.6: Determination of GSH in different real biological samples.

Sample	Added (μM)	Detected (μM)	Recovery (%)	RSD(%)n=3
White grape	2.0	1.85	92.5	0.28
Tomato	2.0	2.1	105	3.52
Watermelon	2.0	2.2	110	1.95
1:10 Diluted Human serum	2.0	2.1	104	0.32

**Figure A3.16:** (a) Changes in the emission intensity of L_1 (2.0 μM) at 414 nm in the presence of excess Hg^{2+} in simulated fluid samples [S.B.F- Simulated Body Fluid (pH~7.4), S.G.F- Simulated Gastric Fluid (pH~2.0) and S.I.F- Simulated Intestinal Fluid (pH~8.0)], artificial urine sample and milk sample. (b) Fluorescence response of L_1 (2.0 μM) at 420 nm in the presence of excess GSH in simulated fluid samples [S.B.F- Simulated Body Fluid (pH~7.4), S.G.F-

Simulated Gastric Fluid (pH~2.0) and S.I.F- Simulated Intestinal Fluid (pH~8.0)] and artificial urine sample.

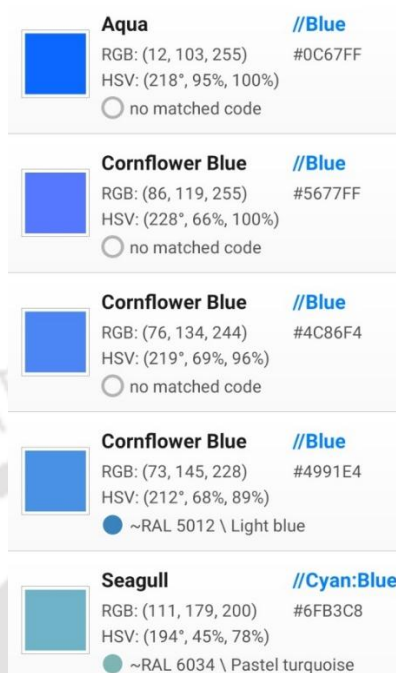


Figure A3.17: RGB analysis by the color recogniser app.

Table A3.7: Coordinates for optimized geometry of probe L_1

Center Number	Atomic Number	Atomic Type	Coordinates (Angstroms)		
			X	Y	Z
1	1	0	0.004941	1.376113	0.981315
2	6	0	-2.998745	-2.362238	0.303569
3	6	0	-3.481488	-1.034487	0.298160
4	6	0	-2.551594	0.024104	0.234648
5	6	0	-1.194182	-0.263495	0.188618
6	6	0	-0.719946	-1.588840	0.195180
7	6	0	-1.637487	-2.641792	0.251856
8	1	0	-3.716066	-3.178982	0.356312
9	1	0	-2.887777	1.055950	0.218958
10	1	0	-1.297957	-3.674914	0.254218
11	6	0	-0.023550	0.699079	0.116223
12	1	0	-0.071752	1.337462	-0.776888
13	6	0	1.176223	-0.229073	0.083408
14	6	0	2.523775	0.098033	0.023347
15	6	0	3.485000	-0.934377	0.000879
16	6	0	3.044201	-2.275710	0.049112
17	6	0	1.691728	-2.593628	0.114115
18	6	0	0.742655	-1.567802	0.130825
19	1	0	2.830379	1.138683	-0.009558

20	1	0	3.785642	-3.072258	0.028757
21	1	0	1.383794	-3.635853	0.152880
22	7	0	4.849704	-0.670822	-0.101463
23	1	0	5.443091	-1.423347	0.224551
24	7	0	-4.858157	-0.816469	0.398387
25	1	0	-5.401180	-1.586939	0.026821
26	6	0	5.388672	0.652651	0.198152
27	1	0	5.043380	1.017723	1.181174
28	1	0	5.023466	1.357593	-0.556514
29	6	0	-5.425347	0.475733	0.015098
30	1	0	-5.096064	0.770637	-0.996730
31	1	0	-5.055682	1.240176	0.707927
32	6	0	6.896435	0.618949	0.173612
33	6	0	7.636206	0.426087	1.342355
34	6	0	7.601480	0.726612	-1.038517
35	6	0	9.029678	0.354334	1.333353
36	1	0	7.101451	0.343307	2.286334
37	6	0	8.995265	0.642596	-1.061454
38	6	0	9.723011	0.460225	0.120172
39	1	0	9.574755	0.222044	2.262574
40	1	0	9.538519	0.702407	-2.001313
41	6	0	-6.933597	0.456302	0.075600
42	6	0	-7.678124	-0.309491	-0.837204
43	6	0	-7.652418	1.180183	1.025772
44	6	0	-9.069698	-0.337783	-0.798912
45	6	0	-9.047552	1.188636	1.060166
46	1	0	-7.102527	1.771534	1.754137
47	6	0	-9.786796	0.433362	0.134813
48	1	0	-9.612011	-0.999661	-1.466835
49	1	0	-9.552189	1.787809	1.807435
50	8	0	6.867728	0.909902	-2.177544
51	1	0	7.470639	0.978169	-2.933654
52	8	0	-6.962157	-1.064017	-1.737413
53	1	0	-7.579186	-1.522181	-2.328617
54	7	0	11.154041	0.397826	0.035471
55	7	0	-11.205819	0.361382	0.138500
56	6	0	11.758775	-0.660254	0.861336
57	1	0	11.930830	-0.324750	1.901164
58	1	0	11.042515	-1.486152	0.913045
59	6	0	11.798678	1.707664	0.247220
60	1	0	12.879819	1.536571	0.261413
61	1	0	11.529329	2.118204	1.239036
62	6	0	11.481084	2.733660	-0.838622
63	1	0	11.756502	2.344459	-1.824968

64	1	0	10.417174	2.988109	-0.855296
65	1	0	12.046176	3.654994	-0.657427
66	6	0	13.067920	-1.177618	0.261051
67	1	0	13.837154	-0.399278	0.213811
68	1	0	13.465974	-1.997608	0.870140
69	1	0	12.896762	-1.545297	-0.755719
70	6	0	-11.884452	0.470257	1.436070
71	1	0	-12.786649	-0.156165	1.379660
72	1	0	-11.232362	0.008284	2.183868
73	6	0	-11.936962	1.025655	-0.952670
74	1	0	-13.001384	0.862081	-0.744709
75	1	0	-11.778234	2.118058	-0.929505
76	6	0	-12.309266	1.873851	-1.906305
77	1	0	-12.782115	1.802928	2.892844
78	1	0	-11.463545	2.563450	1.985807
79	1	0	-13.037869	2.323161	1.223439
80	6	0	-11.645987	0.516773	-2.364688
81	1	0	-10.625622	0.749182	-2.681259
82	1	0	-11.795016	-0.566763	-2.429632
83	1	0	-12.331636	1.001631	-3.069295

Table A3.8: Coordinates for optimized geometry of probe L_1 -Hg²⁺ complex

Center Number	Atomic Number	Atomic Type	Coordinates (Angstroms)		
			X	Y	Z
1	1	0	0.767408	-1.408611	-0.138473
2	6	0	-2.610736	0.620029	2.710627
3	6	0	-2.873748	-0.536381	1.943305
4	6	0	-1.802498	-1.241929	1.350420
5	6	0	-0.498859	-0.781536	1.523244
6	6	0	-0.236572	0.398885	2.270775
7	6	0	-1.295633	1.097939	2.869028
8	1	0	-3.424732	1.145328	3.198058
9	1	0	-1.990409	-2.115855	0.733480
10	1	0	-1.113441	1.997183	3.452262
11	6	0	0.792161	-1.345307	0.957504
12	1	0	1.002261	-2.357169	1.330075
13	6	0	1.821991	-0.331951	1.421576
14	6	0	3.170104	-0.251188	1.080029
15	6	0	3.900138	0.890967	1.466215
16	6	0	3.314517	1.872880	2.295354
17	6	0	1.963711	1.765794	2.680971
18	6	0	1.205948	0.683610	2.199269

19	1	0	3.628118	-1.006192	0.448209
20	1	0	3.899814	2.740845	2.593454
21	1	0	1.510866	2.536013	3.300481
22	6	0	-5.396422	-0.118679	1.818983
23	1	0	-6.276992	-0.766926	1.753126
24	1	0	-5.430693	0.395892	2.789178
25	6	0	5.029876	1.979060	-0.471169
26	1	0	6.008383	1.975604	-0.959687
27	1	0	4.774627	3.008904	-0.187967
28	7	0	-4.222804	-1.057995	1.748045
29	1	0	-4.407721	-1.863954	2.357374
30	7	0	5.181655	1.135526	0.810359
31	1	0	5.866569	1.589386	1.425319
32	6	0	3.940248	1.388074	-1.337203
33	6	0	4.175677	0.245263	-2.119058
34	6	0	2.620772	1.845467	-1.187424
35	6	0	3.107703	-0.425123	-2.729968
36	6	0	1.501587	1.143347	-1.716731
37	1	0	2.468174	2.709462	-0.552032
38	6	0	1.787539	0.006692	-2.529943
39	1	0	3.293445	-1.308973	-3.336684
40	1	0	0.989173	-0.560555	-2.992232
41	6	0	-5.420549	0.901413	0.694088
42	6	0	-5.879561	0.554007	-0.589738
43	6	0	-5.015960	2.228693	0.912844
44	6	0	-5.917063	1.495013	-1.623936
45	6	0	-5.046072	3.221709	-0.108144
46	1	0	-4.677168	2.491142	1.906505
47	6	0	-5.511491	2.814549	-1.391971
48	1	0	-6.245214	1.198663	-2.617871
49	1	0	-5.546027	3.512967	-2.218957
50	8	0	-6.254061	-0.804769	-0.818826
51	1	0	-7.024860	-0.905948	-1.409370
52	8	0	5.514828	-0.227429	-2.215522
53	1	0	5.541657	-1.142502	-2.571201
54	7	0	0.188231	1.506840	-1.398450
55	7	0	-4.651523	4.539986	0.145537
56	6	0	-0.927722	0.734891	-2.000977
57	1	0	-0.808745	-0.328561	-1.748725
58	1	0	-0.870626	0.805093	-3.100610
59	6	0	-2.331898	1.156476	-1.553195
60	1	0	-2.567554	2.193240	-1.819864
61	1	0	-3.053976	0.502829	-2.051791
62	1	0	-2.473384	1.032317	-0.474100

63	6	0	-4.645535	5.544734	-0.933862
64	1	0	-5.577571	5.468327	-1.509399
65	1	0	-4.659884	6.536963	-0.467372
66	6	0	-3.427395	5.447066	-1.882087
67	1	0	-3.509968	6.185008	-2.690938
68	1	0	-2.495218	5.635820	-1.339431
69	1	0	-3.356157	4.450344	-2.332403
70	6	0	-0.066347	2.719833	-0.608099
71	1	0	0.615868	2.742759	0.251587
72	1	0	-1.066537	2.654768	-0.181522
73	6	0	0.059106	4.024999	-1.427337
74	1	0	-0.092592	4.904517	-0.785560
75	1	0	1.049051	4.106220	-1.890415
76	1	0	-0.690159	4.047435	-2.227580
77	6	0	-4.053895	4.914833	1.440350
78	1	0	-4.679175	4.535189	2.260750
79	1	0	-4.087662	6.007768	1.516723
80	6	0	-2.594204	4.437087	1.628180
81	1	0	-2.516546	3.349385	1.535895
82	1	0	-1.938722	4.888105	0.875092
83	1	0	-2.225206	4.723838	2.622523
84	80	0	-4.589320	-2.558053	-0.290580
85	80	0	6.571946	-0.801699	0.127122
86	17	0	8.536086	0.639149	0.791915
87	17	0	5.460282	-2.981197	-0.518008
88	17	0	-6.064913	-3.854160	1.315272
89	17	0	-2.861282	-2.435919	-2.109438

Table A3.9: Coordinates for optimized geometry of probe **L₁**-GSH complex

Center Number	Atomic Number	Atomic Type	Coordinates (Angstroms)		
			X	Y	Z
1	1	0	-1.493394	-3.740123	0.655408
2	6	0	-3.155242	-1.085488	-3.095032
3	6	0	-3.771583	-1.024085	-1.827961
4	6	0	-3.133504	-1.647030	-0.731842
5	6	0	-1.911225	-2.273627	-0.923873
6	6	0	-1.293908	-2.323583	-2.192674
7	6	0	-1.935598	-1.733785	-3.283520
8	1	0	-3.642711	-0.603607	-3.940605
9	1	0	-3.627833	-1.669809	0.235042
10	1	0	-1.481945	-1.754149	-4.271503
11	6	0	-1.008600	-2.920690	0.109484

12	1	0	-0.697458	-2.174145	0.851822
13	6	0	0.186537	-3.364276	-0.713350
14	6	0	1.354251	-3.980020	-0.291767
15	6	0	2.380694	-4.261035	-1.220116
16	6	0	2.193590	-3.870071	-2.565109
17	6	0	1.027240	-3.234920	-2.980089
18	6	0	0.005013	-2.986214	-2.059835
19	1	0	1.490878	-4.251150	0.754277
20	1	0	2.970182	-4.080417	-3.292632
21	1	0	0.915839	-2.948033	-4.023295
22	7	0	3.502792	-4.994548	-0.825392
23	1	0	3.512714	-5.165857	0.175787
24	7	0	-5.017543	-0.410342	-1.677501
25	1	0	-5.397275	-0.057417	-2.547574
26	6	0	4.876749	-4.644922	-1.261656
27	1	0	5.451722	-5.577383	-1.316857
28	1	0	4.816460	-4.237790	-2.270337
29	6	0	-5.312823	0.478652	-0.545107
30	1	0	-5.145160	1.531250	-0.823019
31	1	0	-4.602301	0.250566	0.251410
32	6	0	5.571619	-3.684722	-0.325747
33	6	0	6.346607	-4.144140	0.739225
34	6	0	5.368519	-2.295819	-0.412125
35	6	0	6.907607	-3.294670	1.691154
36	1	0	6.532579	-5.214474	0.825228
37	6	0	5.915428	-1.425102	0.533405
38	6	0	6.699449	-1.899736	1.608017
39	1	0	7.502397	-3.729448	2.484197
40	1	0	5.723167	-0.368838	0.400669
41	6	0	-6.723807	0.308169	-0.045555
42	6	0	-7.747791	1.204676	-0.348596
43	6	0	-7.079868	-0.807422	0.725674
44	6	0	-9.063024	1.021349	0.067070
45	1	0	-7.507275	2.089524	-0.935264
46	6	0	-8.387861	-1.020355	1.157060
47	6	0	-9.423835	-0.114842	0.830231
48	1	0	-9.799057	1.770369	-0.195219
49	1	0	-8.584482	-1.899038	1.761953
50	8	0	4.628879	-1.839090	-1.456714
51	1	0	4.560849	-0.857479	-1.399313
52	8	0	-6.072031	-1.678989	1.052375
53	1	0	-6.445446	-2.430390	1.536659
54	7	0	7.272140	-1.013574	2.531427
55	7	0	-10.729823	-0.325736	1.246417

56	6	0	6.701996	0.330487	2.697817
57	1	0	7.415169	0.911541	3.292886
58	1	0	6.653474	0.841730	1.729590
59	6	0	5.318651	0.329048	3.367558
60	1	0	4.945785	1.355088	3.494000
61	1	0	4.596036	-0.212472	2.752506
62	1	0	5.367140	-0.151470	4.355593
63	6	0	7.984948	-1.550387	3.692491
64	1	0	7.979727	-0.774955	4.464628
65	1	0	7.450444	-2.407757	4.130770
66	6	0	9.441689	-1.917900	3.374950
67	1	0	9.934542	-2.352170	4.254415
68	1	0	9.500864	-2.641222	2.556610
69	1	0	9.996784	-1.025159	3.068483
70	6	0	-11.800382	0.588993	0.867423
71	1	0	-12.739889	0.027913	0.902323
72	1	0	-11.680404	0.893354	-0.178055
73	6	0	-11.094951	-1.491816	2.036959
74	1	0	-10.350598	-1.654110	2.826870
75	1	0	-12.026630	-1.252997	2.559692
76	6	0	-11.888487	1.812965	1.787260
77	1	0	-10.947546	2.371034	1.771865
78	1	0	-12.695242	2.485451	1.473098
79	1	0	-12.080280	1.501657	2.819721
80	6	0	-11.288918	-2.765395	1.202362
81	1	0	-11.523125	-3.618129	1.849922
82	1	0	-12.113136	-2.637026	0.492280
83	1	0	-10.387997	-3.001042	0.629569
84	6	0	0.257769	0.956954	0.578427
85	1	0	0.789447	1.908702	0.706137
86	6	0	0.566703	0.377405	-0.828033
87	1	0	-0.030157	-0.525381	-0.958934
88	1	0	0.153796	1.087654	-1.557087
89	6	0	2.014965	0.008217	-1.166212
90	1	0	2.397771	-0.753438	-0.482902
91	1	0	2.030508	-0.470179	-2.152860
92	6	0	3.050349	1.119398	-1.186334
93	8	0	4.263626	0.884428	-1.174720
94	7	0	2.580247	2.396681	-1.188837
95	1	0	1.591593	2.525980	-1.337449
96	6	0	3.438890	3.565016	-1.144459
97	1	0	4.461526	3.192096	-1.065955
98	6	0	3.297599	4.450641	-2.394467
99	1	0	3.966802	5.308786	-2.288892

100	1	0	2.273967	4.833268	-2.485242
101	16	0	3.737151	3.468404	-3.897900
102	1	0	3.427758	4.438697	-4.784173
103	6	0	3.201898	4.430438	0.106558
104	8	0	4.124916	4.965375	0.695041
105	7	0	1.875785	4.613892	0.474668
106	1	0	1.186164	4.448251	-0.250617
107	6	0	1.563581	5.743959	1.324062
108	1	0	0.614056	5.584451	1.849469
109	1	0	2.351426	5.848659	2.074979
110	6	0	1.474756	7.030459	0.507399
111	8	0	1.539471	7.086821	-0.702298
112	8	0	1.236576	8.094699	1.299899
113	1	0	1.168600	8.875386	0.716170
114	7	0	-1.174512	1.217424	0.657641
115	1	0	-1.697749	0.393284	0.360236
116	1	0	-1.449879	1.402260	1.620000
117	6	0	0.871347	0.074558	1.663114
118	8	0	2.066114	-0.023458	1.849687
119	8	0	-0.038457	-0.592954	2.424102
120	1	0	0.483814	-1.111595	3.066540

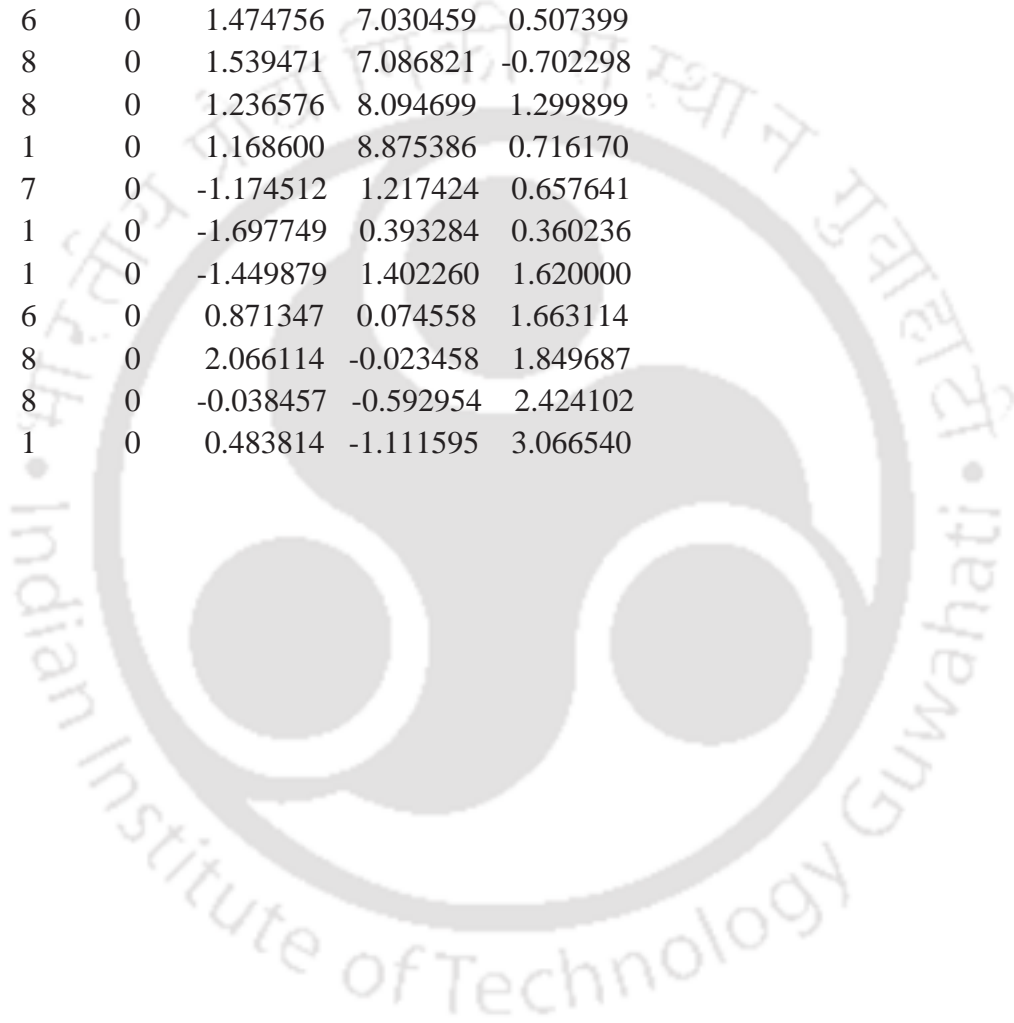


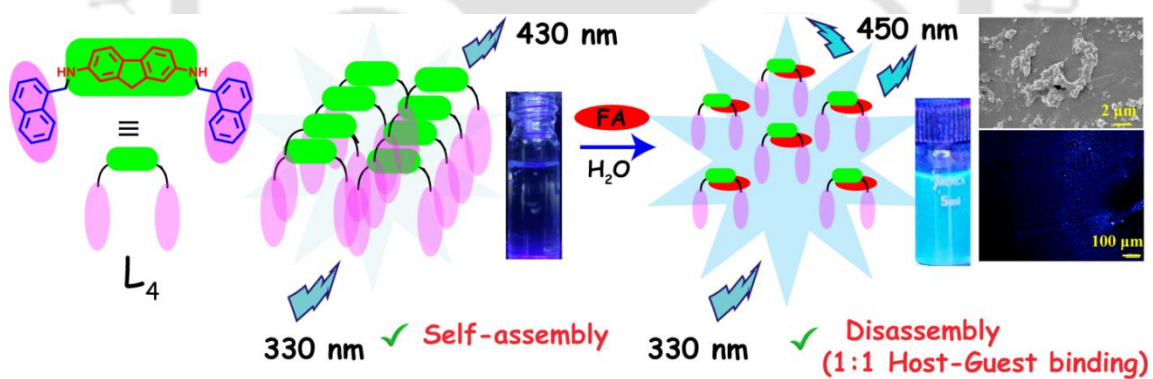
Table A3.10: A comparative study of the proposed receptor with some previously reported ones.

Sl No.	References	Receptor (Operation mode)	Solvent System	LOD(ppb)	Sensing analyte
1.	Present work (Bifunctional receptor i.e. both for mercury(II) and GSH)	Fluorene derivative (Off-on)	100% Aqueous medium	17.35 (0.0865 μM) 25.83 (0.0840 μM)	Hg²⁺ and GSH discretely
2.	Spectrochimica Acta Part A: Molecular and Biomolecular Spectroscopy, 2021, 257, 119316	Naphthoquinone probe (Off-on)	DMSO-H ₂ O (9:1, v/v) solution	90.46 (0.451 μ M)	Hg ²⁺
3.	Spectrochimica Acta Part A: Molecular and Biomolecular Spectroscopy, 2021, 250, 119776	Cytidine-Au nanoclusters (Colorimetric color change)	-	3073.2 (10 μ M)	GSH, GSSH, GR
4.	Sensors and Actuators: B. Chemical., 2018, 255(Part1), 657-665	Au/N-CQDs (On-off)	Aqueous medium	23.66 (0.118 μ M)	Hg ²⁺
5.	Microchemical Journal, 2019, 150, 104123	Quinazoline derivative (Off-on)	DMSO	1271 (6.34 μ M)	Hg ²⁺
6.	Inorganic Chemistry Communications, 2018, 89, 46-50	Fluorescein based probe (Off-on)	MeOH:HEPES (5:95 v/v, 20 mM, pH 7.4)	22 (0.11 μ M)	Hg ²⁺
7.	Anal. Methods, 2019, 11, 227-231	Terpyridine based probe (On-off)	Aqueous solution	138 (0.68 μ M)	Hg ²⁺
8.	ACS Appl. Mater. Inter., 2017, 9, 13554-13563.	Eu(DPA) ₃ @Lap-Tris/Cu ²⁺ (Off-on)	hydrogel	49.78 (0.162 μ M)	GSH
9.	Rsc Adv., 2016, 6, 79526-79532.	MnO ₂ -Cu nanocomposites (Off-on)	-	30.73 (0.1 μ M)	GSH
10.	Sensors and Actuators: B. Chemical., 2017, 251, 753-762	Bromoacetyl bromide-functionalized CDs (Off-on)	PBS buffer (0.01 mol/L, pH = 8.0)	43 (0.14 μ M)	GSH



CHAPTER 4

Fluorene-naphthalene probe: Folic acid induced disassembly and simultaneous detection of folic acid in water



Chapter 4

4.1 Background and focus of the chapter

Folic acid (FA), (2S)-2-[(4-[[[(2-amino-4-hydroxypteridin-6-yl)methyl]amino}phenyl]formamido]pentanedioic acid (Figure 4.1), conversant as vitamin B₉, plays an essential role in copious biological activities like new cell formation, synthesis of DNA, RNA, reparation of DNA and blood production.^{4.1} Lack of folic acid has been linked to megaloblastic anemia, leukopenia, cardiovascular diseases, Alzheimer's disease, tumorigenesis, paralysis, spinal and neurological congenital anomaly, infertility in both genders.^{4.2-4.4} FA supplementation is recommended in pregnancy and, even before pregnancy, is thought to be necessary for the mother to have a healthy pregnancy and prevent problems that may arise during the baby's growth.^{4.5} However, excess FA intake causes zinc deficiency, anorexia, nausea, and numerous gastrointestinal syndrome.^{4.6} Therefore, quantitative analysis of FA in biological samples for clinical viewpoint is highly demanded. Natural folates exist extensively in green leafy vegetables, citrus fruit, nuts, beans, egg yolk, individual berries, chickpeas, kidney beans, liver, cereals, wheat flour and, yeast.^{4.7} Folic acid is included in grain products in many countries^{4.8} because this can easily be broken down and lost during food preparation (cooking, steaming, frying, and baking).^{4.9} In these countries, fortified products fulfill a vital source of the population's folic acid.

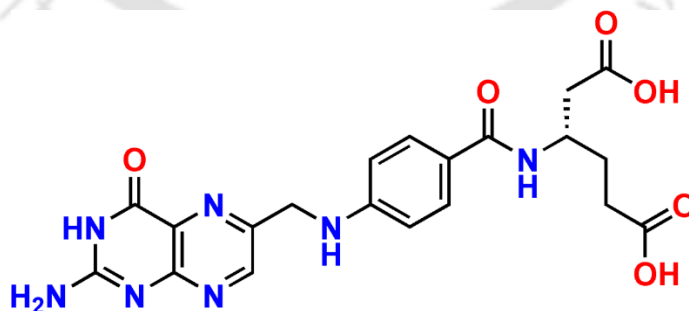
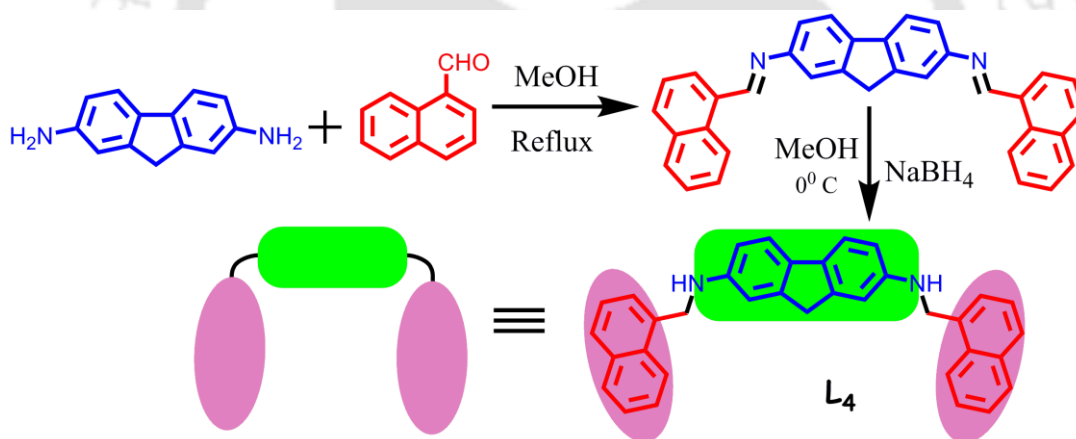


Figure 4.1: Chemical Structure of Folic Acid (FA).

Numerous analytical methods with high sensitivity and accuracy have been prospered to date for the separation and quantification of FA.^{4.10-4.16} Some fluorescent sensors based on Quantum dots (QDs), semiconductor nanocrystals have been reported with their high optical quantum yields

and photo-stability.^{4.17-4.18} Nevertheless, due to their biotoxicity and environmental concerns, the development of a novel approach for FA analysis is still far from completion. Fluorescent chemosensors, flaunting switch ‘on-off’ and ‘off-on’ responses have allured appreciable attention for the quantitative analysis of bioanalytes^{4.19-4.21} due to their versatility, ease of use, high sensitivity, selectivity, and fast response time. Among these two types of switches, ‘off-on’ is superior over ‘on-off’ in fluorescence sensing due to its lower background signal. In comparison with the appearance of the individual-molecule form, the molecular self-assembly of a molecule nourishes distinctive physicochemical properties that make self-assembly alluring for sensing purposes.^{4.22} Assembly disassembly are most two prevailing processes and have been employed recently to develop fluorescent sensors for bio-analytes since disassembly of the sensor retrieves the embedded fluorescence again.^{4.23} Therefore, ‘off-on’ switch probes based on the assembly disassembly approach for the detection of FA are very rarely documented.^{4.24} In this context, herein, we construct a simple and easy-to-operate organic luminophore based on fluorene bridged dipodal naphthalene moiety (Scheme 4.1), that can preferentially self-assemble to form aggregates in aqueous medium.



Scheme 4.1: Synthetic Scheme of the probe L_4 .

The probe shows selective and sensitive 1:1 binding ability towards FA among various carboxylic acids through an enhanced "turn-on" fluorescence emission in totally aqueous solution leading to the disaggregation of the self-assembled L_4 . To the best of our knowledge, this is the first report of using a “turn-on” fluorene-naphthalene based self-assembled probe for sensing FA in 100% aqueous media. The excellent sensitivity was ascribed to the combination of a Photoinduced Electron Transfer (PET) process and Fluorescence Resonance Energy Transfer (FRET) in the probe-folic acid interaction.^{4.25-4.26} The proposed sensor can recognize and determine FA in fruits, vegetables, and human fluids.

4.2 Self-Assembly of L₄

To recognize the self-aggregation behavior of L₄ in aqueous solution and solid state, we have carried out field-emission scanning electron microscopy (FESEM) and dynamic-light-scattering (DLS) studies in various concentrations (0.2 μM, 1 μM, 2 μM) of L₄. It is well documented in the literature that aromatic rings of the adjoining fluorophores in solution form aggregate through intermolecular π - π interaction.^{4.27-4.30} The FESEM analysis clearly revealed the transformation of scattered unsymmetrical shaped particles into rod-shaped aggregate upon varying the concentration from 0.2 μM to 2 μM (Figure 4.2). The DLS experiment also corroborated that L₄ can self-assemble to form aggregates in 100% aqueous medium (Figure A4.1). This variation in size was ascribed to an increment in the number of molecules participating in π - π stacking in the solution. Unitedly, these results suggest aggregation of the probe molecule in water with an increase in concentration.

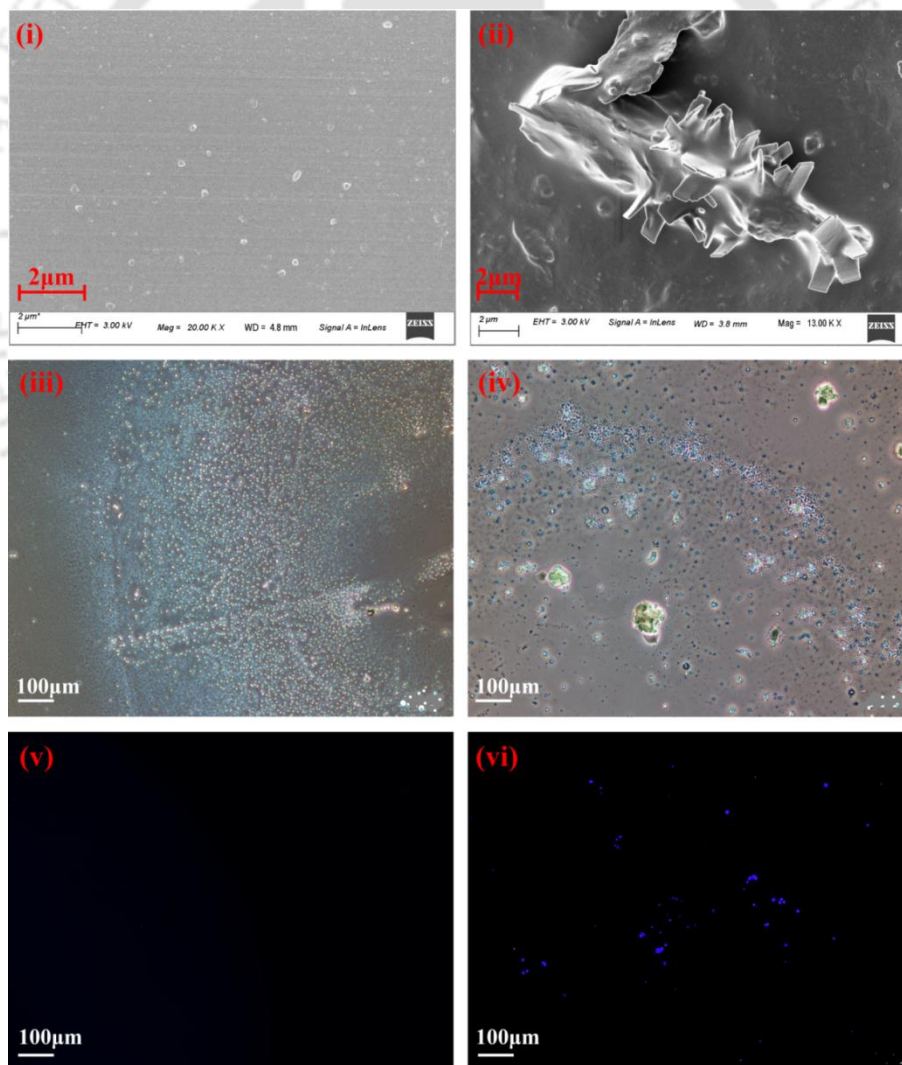


Figure 4.2: FESEM and Fluorescence Microscopic images of L₄ (0.2 μM) (i, iii, v) and L₄ (2 μM) (ii, iv, vi).

4.3 Photo physical Characterization of L₄

The photophysical properties of the L₄ was explicated by UV-visible absorption and fluorescence emission spectra in different solvents. L₄'s stock solution was prepared in dimethylsulfoxide (1.0 mM) and diluted accordingly with the experimental solutions (Figure A4.2). L₄ was strongly emissive in 100% acetonitrile, moderately emissive in methanol, and weakly emissive in 100% aqueous medium (Figure A4.3). Nevertheless, transpicuous aqueous solution of L₄ was evident to the naked eye, and it was entirely homogeneous without any visible precipitation, which may indicate the genesis of micro aggregates in the solution. The evolution of micro aggregates was also reinforced by the changes in L₄'s absorption spectra in water. The probe L₄ exhibited a sharp absorption maximum at 310 nm and a hump at 396 nm in acetonitrile. In water, the absorption peak at 310 nm broadened with reduced absorbance value, accompanied by the apparent upliftment in the baseline beyond 425 nm, which suggested the genesis of micro aggregates in the solution. The well-defined absorption peaks at 315 nm may be ascribed to the π - π^* transition of fluorene moiety.^{4.31}

4.4 Sensing Behavior

The fluorescence behavior of a fluorophore can be modulated by guest molecules, which are already well-established in the literature.^{4.32-4.35} In the current study, during the L₄ design, we anticipated that incorporating π electron-rich fluorene-naphthalene moiety with extended conjugation would enhance the possibility of intermolecular π - π stacking. It should possess adequate convergent -NH moieties as H-bond donor sites. So the sensing abilities of L₄ for a series of biomolecules and metallic ions were measured by UV-visible and fluorescence spectroscopy study.

4.5 UV-Visible Spectral Study

UV-visible spectral changes of a 2 μ M aqueous solution of L₄ ($\epsilon = 26115.5 \text{ M}^{-1} \text{ cm}^{-1}$) was investigated (Figure 4.3A) upon addition of various mono and dicarboxylic acids such as fumaric acid, malonic acid, citric acid, oxalic acid, tartaric acid, folic acid, benzoic acid, stearic acid, trifluoroacetic acid, glutamic acid. Surprisingly, it was observed that the presence of an excess of these carboxylic acids (50 equiv), L₄ displayed no such significant changes except for FA. Surplus addition of folic acid to L₄ in 100% aqueous medium rendered a remarkable increase in the absorption maximum ($\epsilon = 112761.5 \text{ M}^{-1} \text{ cm}^{-1}$) at 310 nm. This spectral result was supported by a significant visual change of the experimental solution from colorless to faint yellow, probably due to the interaction of L₄ with FA (Figure 4.3a, Inset). This visual color

change is gratifying enough for folic acid's naked eye detection using L_4 in the aqueous medium. A bar graph has been framed to differentiate the distinct changes in absorbance of L_4 at 310 nm upon subsequent addition of different carboxylic acids (Figure A4.4), and this bar graph also clearly attributes the significant colorimetric feature in the case of FA. To unravel the same selectivity and sensitivity of L_4 towards FA, we have carried on a detailed fluorescence study, followed by FESEM, DLS study, fluorescence microscopy, mass spectral analysis, NOESY experiment, and theoretical study.

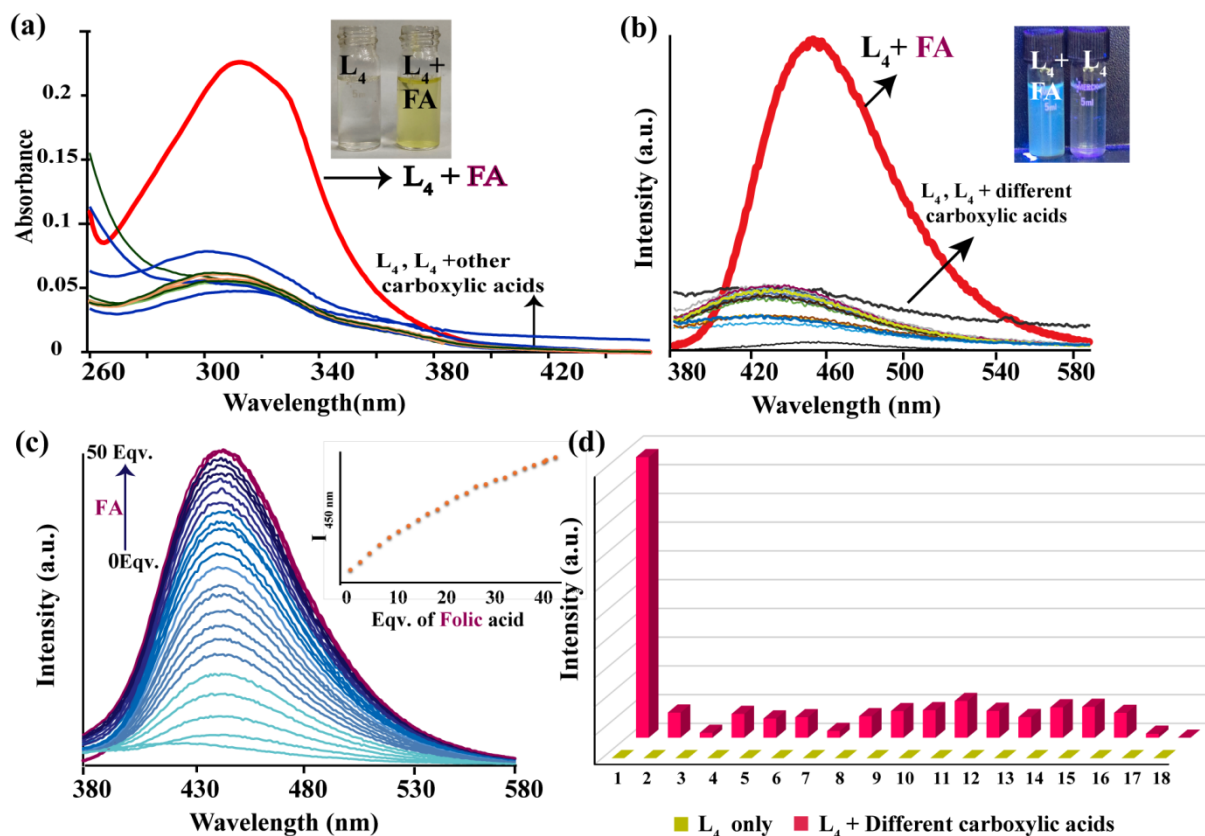


Figure 4.3: (A) UV–visible spectra of L_4 (2 μ M) in the presence of various carboxylic acids (50 Equiv). Inset: Visual color change of L_4 in the presence of FA. (B) Fluorescence spectra of L_4 (2 μ M) in various carboxylic acids (50 Equiv); Inset: Visual color change of L_4 in the presence of FA under UV light. (C) Fluorescence spectra of L_4 (2 μ M) in the presence of a differing concentration of FA; Inset: Changes in the emission intensity at 450 nm with folic acid equivalents. (D) Comparison of the normalized emission intensity of L_4 at 450 nm on interaction with various carboxylic acids (1= folic acid, 2= fumaric acid, 3= maleic acid, 4= cinnamic acid, 5= malonic acid, 6= citric acid, 7= oxalic acid, 8= tartaric acid, 9= aspartic acid, 10= benzoic acid, 11= stearic acid, 12= lactic acid, 13= capric acid, 14= ascorbic acid, 15= glutamic acid, 16= gallic acid, 17= phthalic acid, 18= picric acid).

4.6 Fluorescence Spectral Study

The luminescence behavior of L_4 was studied in the presence of various carboxylic acid molecules in a 100% aqueous medium (Figure 4.3b). The result demonstrated an enhancement in the fluorescence intensity of L_4 [Quantum yield (%) = 0.05 \longrightarrow 7.51] in the presence of FA

with a remarkable redshift from 430 nm to 450 nm, accompanying the apparent color change visible even to the naked eye (as illustrated in Figure 4.3b, Inset). However, this significant 16-fold enhancement in fluorescence intensity was attributed to interaction of **L**₄ with FA and the selective turn-on fluorescence response in aqueous medium. Presence of a redshift in the emission spectrum upon the gradual increase of folic acid, which is an indicator of the presence of a charge transfer due to the push-pull nature of the donating and withdrawing groups. The fluorescence titration of **L**₄ for FA was investigated to study the sensing behaviors in detail. The fluorescence spectra of **L**₄ with different equivalent concentrations of FA in 100% aqueous medium are exhibited in Figure 4.3c. It can be seen that with the increase of equivalent concentrations of FA, the fluorescence intensities enhanced rapidly initially but increased slowly when saturation was achieved. Moreover, the maximum emission wavelengths manifested remarkable redshifts from 430 nm to 450 nm. Job's plot analysis proposed that **L**₄ and FA form a 1:1 host-guest complex. As determined by the B-H plot, the apparent binding constant was $8.46 \times 10^4 \text{ M}^{-1}$ (Figure A4.5). The limit of detection (LOD) of **L**₄ for FA was 0.38 μM following the previously reported procedure in the literature (Figure A4.6).^{4.35-4.37} The linear correlation between the emission responses and the concentrations of added FA ($r^2 = 0.9909$) ensured a quantitative estimation of FA. To illustrate the mechanism of fluorescence enhancement, the time-resolved fluorescence decay of **L**₄ in the absence and presence of FA in the aqueous medium were also executed. The time-resolved emission spectra of **L**₄ ($\lambda_{\text{ex}} = 330 \text{ nm}$) revealed the existence of a short-lived excited state with single exponential decay ($\tau_{\text{av}} = 0.131 \text{ ns}$) and in the presence of folic acid a long-lived excited state with biexponential decay ($\tau_{\text{av}} = 6.769 \text{ ns}$) at 450nm (Figure A4.7) suggesting the proclivity of **L**₄ towards FA.

4.7 Detection of FA in real samples and bio-fluids

Common FA-containing foods (mung bean, oranges, and spinach) were taken as real samples to interpret the folic acid content (Figure 4.4a). Spinach, mung beans, and oranges were purchased from the local market (Guwahati, Assam). Chopped spinach and mung beans were first air-dried, homogenized for 10 min, and centrifuged at 12000 rpm for 10 min. The supernatant was collected after filtration. Oranges were peeled off, crushed, and centrifuged at 7500 rpm for 15 min, and the pH of the supernatant was adjusted to 6.5 with 1.0 mM NaOH.^{4.38-4.40} Now the three solutions containing FA were further studied by fluorescence-sensing analysis. The extract of the foods was taken in an appropriate amount and subjected to fluorescence spectral analysis. To evaluate the usefulness of **L**₄ to detect FA in real samples both fluorescence spectroscopic and colorimetric methods were applied.^{4.41} Titration experiment was carried out by spiking **L**₄

molecule with different concentration of FA, from where calibration curve was generated which was clear indication of possibility of using this probe to detect unknown concentration of FA. Although both values obtained from fluorescence spectroscopic method and UV-Visible spectroscopic methods (Table A4.1) are almost identical, the results were lower than the theoretical content due to the incomplete extraction of FA in samples. These results reveal that L_4 possesses good potential for determining the FA concentration in real samples.

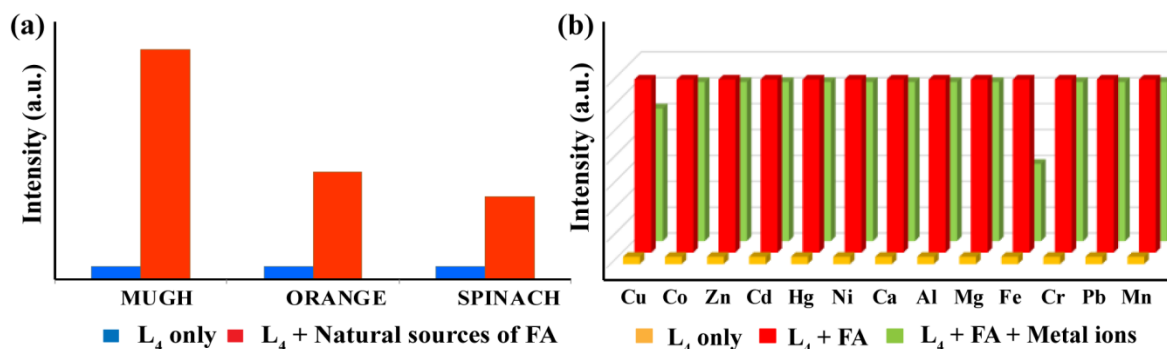


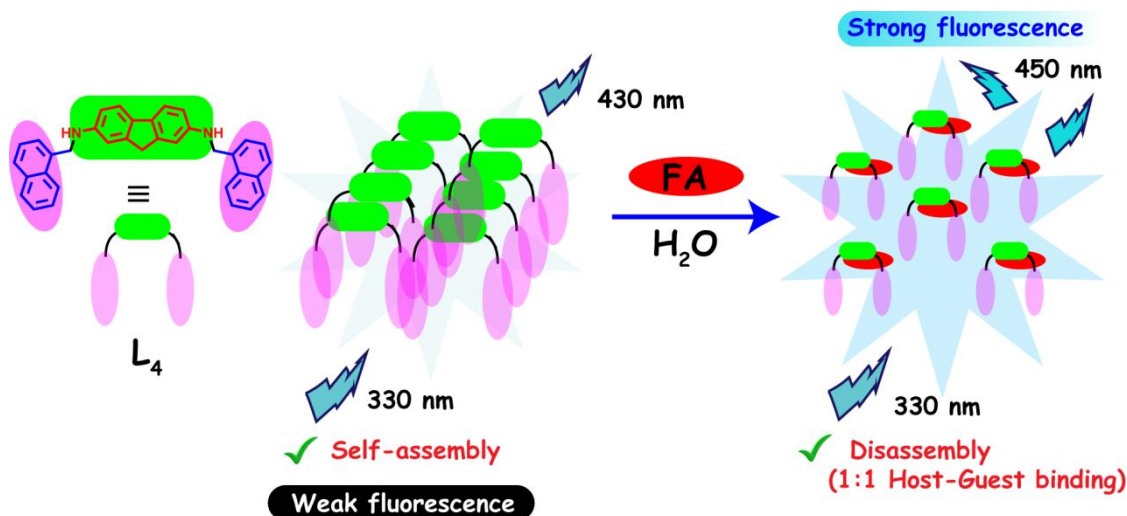
Figure 4.4: (A) Emission spectra of L_4 for sensing FA in real samples (mung bean, oranges, and spinach). (B) The selectivity of L_4 for FA in the presence of various cations (50 equiv).

Another real-life application of L_4 for sensing FA was investigated by employing three bio-fluidic samples instead of water. Furthermore, the result interpreted that L_4 was able to recognize FA in the gastric fluid (pH ~ 2), body fluid (pH ~ 7.4), and intestinal fluid (pH ~ 8) by displaying noticeable TURN-ON fluorescence changes. (Figure A4.8a).

4.8 Interference Experiment

The interference experiments were also assessed by examining L_4 's fluorescence spectra with FA in tap water, lake water, and river water. The fluorescence spectrum of pure L_4 exhibited the maximum emission wavelength at 430 nm, which shifted to 450 nm with enhancement in fluorescence intensity when folic acid was added to the solution. The fluorescence spectra still displayed similar redshifts, although the fluorescence intensity fluctuated slightly (Figure A4.8b). These results implied that L_4 possessed excellent sensing capability for folic acid, which was hardly interfered with by other species. Competitive binding studies were performed by mixing 50 equiv. of FA to an aqueous solution of L_4 , followed by the addition of 50 equiv. chloride salts of various cations such as Cu(II), Co(II), Zn(II), Cd(II), Hg(II), Ni(II), Ca(II), Al(III), Mg(II), Fe(III), Cr(III), Pb(II), Mn(II) (Figure 4.4b). It is notable to mention that the FA-induced manifold rise of the emission intensity of L_4 remained almost uninfluenced by these cations, except for Fe(III) (Figure A4.9). L_4 , which displayed a strong binding affinity for FA, in the presence of Fe(III) showed a significant fluorescence quenching likely due to the metal-FA

chelation effect.^{4.42-4.43} Gratifyingly, this would demonstrate strong binding for the L_4 -FA and thereby committed to the high selectivity of L_4 towards FA.



Scheme 4.2: Proposed binding model of L_4 with FA.

4.9 Plausible Mechanism for Sensing FA

The fluorescence TURN-ON mechanism can be explained by the donor–acceptor electron-transfer mechanism between the sensor and the FA. In the present context, upon excitation at a wavelength of 330 nm, electronic excitation from HOMO to LUMO of the donor L_4 happens and PET process is expected to take place.^{4.44} After addition of FA, there exist efficient spectral overlap between the donor L_4 and the acceptor FA (Figure A4.10) along with variance in luminescence lifetime before the addition of analyte FA ($\tau_{av} = 0.131$ ns) and after the addition of analyte FA ($\tau_{av} = 6.769$ ns), so FRET is found to be operative.^{4.45-4.49} Thus, PET together with FRET between L_4 and FA is found to be a reason for this TURN-ON sensing phenomenon. The HRMS spectrum of L_4 with excess FA showed a binding peak at 918.3726, following the stoichiometry of 1: 1 (Figure A4.11). The fluorescence Jobs' plot of L_4 and FA is displayed, indicating the inflection point at 0.5, suggesting the stoichiometry of 1:1. Furthermore, this 1:1 binding stoichiometry along with the high binding constant, obtained from the B–H plot, also suggested strong binding between L_4 and FA. Again, the 2D NOESY spectra (in a DMSO- d_6 medium) also exhibited additional cross-peaks due to the interaction of the L_4 with that of FA (Figure A4.12). Interestingly, due to this host-guest complexation between L_4 and FA led to the disassembly of the aggregated- L_4 (Scheme 4.2). Meanwhile, DLS analysis (Figure A4.13) was carried out to confirm the disaggregation of the self-assembled L_4 upon addition of FA. From the DLS data, it is evident that the average particle sizes of the aggregates of L_4 (400.5 nm) decreased significantly (253.9 nm) upon interaction with FA. We employed FESEM to probe the

aggregate formation in a 100% aqueous medium to gain further insight into the aggregation effects and their correlated morphological features. As shown in Figure 4.5, the FESEM analysis

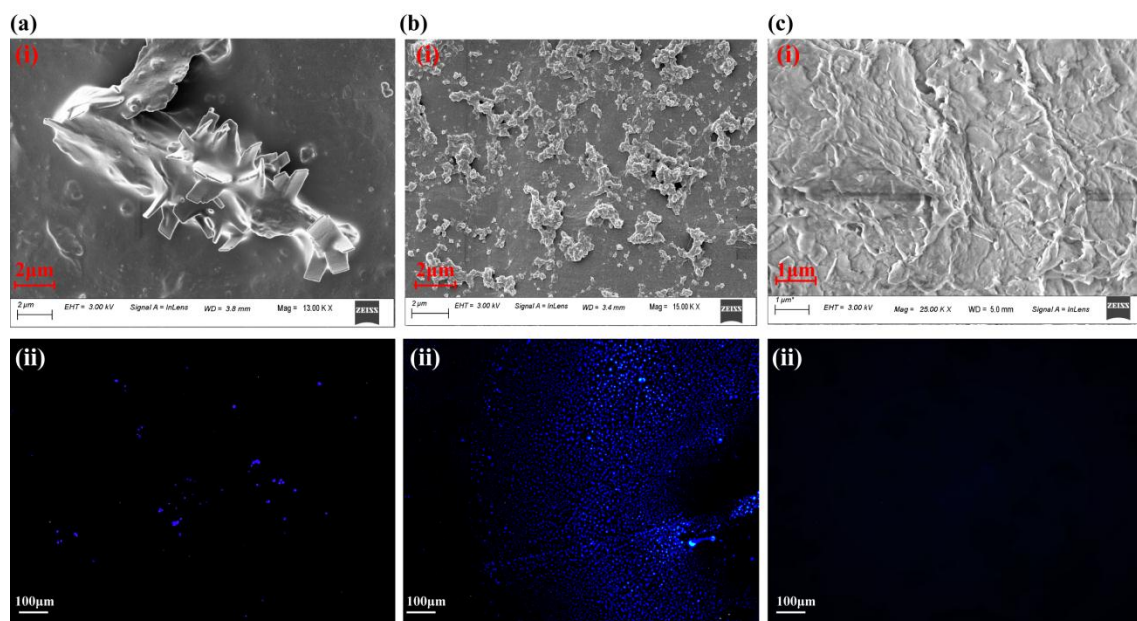


Figure 4.5: FESEM and Fluorescence microscope images of (a) L_4 (i and ii), (b) L_4 + FA (I and ii), and (c) only FA (i and ii) in 100% aqueous medium.

rod-shaped aggregate formation by the L_4 in the aqueous medium. Upon adding FA to L_4 's aqueous solution, rod-shaped aggregates are transformed into amorphous aggregates that demonstrate the influence of the FA on the self-assembly of L_4 .^{4,50} For further evidence for binding of L_4 with FA, fluorescence microscopy experiments (Figure 4.5) were also pursued where prominent blue fluorescence was detected upon addition of FA to the weakly emissive L_4 .

4.10 Theoretical Study

A rigorous density functional theory (DFT) calculations were carried out to interpret the theoretical aspect of this sensing mechanism. DFT optimizations of L_4 and L_4 -FA were carried out with the B3LYP/6-31 G (d, p) method basis set using the Gaussian 09 program.

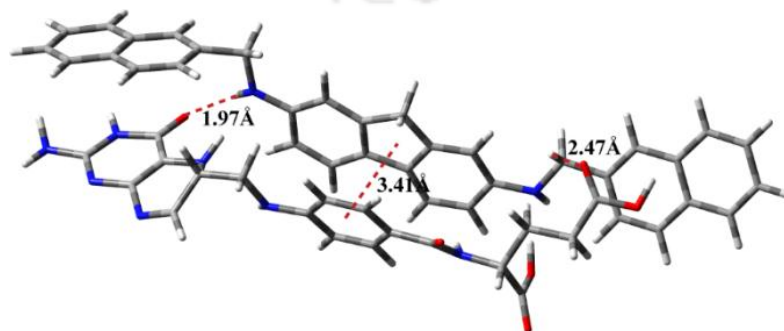


Figure 4.6: Optimized geometry of L_4 -FA complex.

The optimized geometry (Figure 4.6) and the highest occupied molecular orbital (HOMO), and the lowest unoccupied molecular orbital (LUMO) of the L_4 and L_4 -FA complex are demonstrated in Figure 4.7. The HOMO–LUMO energy calculation of the sensor treated with folic acid by DFT analysis revealed the spontaneity and energetically favourable process due to the decrease in the HOMO-LUMO energy gap of the L_4 -FA. This study unequivocally confirmed the theoretical aspect of the observed redshift in emission maxima also. It is interpreted that the hydrogen bonding (C=O---H-N; 1.97Å) and of π – π stacking (\sim 3.41-3.47Å) played vital roles for L_4 -FA 1:1 binding. These interactions resulted in fluorescence enhancement and redshift of maximum emission wavelength due to restricted rotation of fluorene-naphthalene moieties followed by π – π stacking of L_4 -FA.

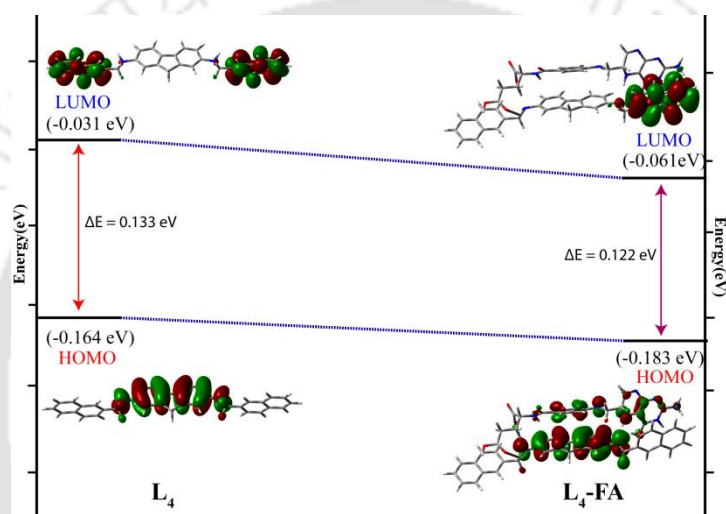


Figure 4.7: Frontier molecular orbital plots, optimized structures, and energy level diagrams of L_4 and L_4 -FA. The calculations were performed using B3LYP/6-31 G (d, p) implemented in Gaussian 09.

4.11 MTT Assay

An essential requisite for this venture was to ascertain the cytotoxicity of the L_4 . The well-established MTT-based cytotoxicity assay on the HeLa cell line (human cervical carcinoma cells) was accomplished (Figure A4.14). Interestingly, the cell-viability assay demonstrated that both L_4 and L_4 -FA complex had negligible cytotoxicity effect even at higher concentration.

4.12 Conclusions

In summary, we have described the synthesis of chemosensor L_4 , a fluorene bridged bis-naphthalene compound, using a straightforward method. The chemosensor formed stable electron donor–acceptor complexes with folic acid. From DLS and FESEM studies, it was evident that L_4 underwent self-aggregation to form aggregates by non-covalent interaction. Taking advantage of this property of L_4 , we further demonstrated the fluorescence sensing of

various mono and dicarboxylic acids, where the selective 1:1 sensing ability of folic acid was demonstrated. The sensing ability of FA by L₄ led to the disassembly of self-aggregated probe, which was well established by FESEM study, DLS study, fluorescence microscope study, HRMS study, fluorescence Job's plot, and theoretical DFT calculation. The detection limit of L₄ for folic acid was as low as 0.38 μ M. The sensor for folic acid was applied successfully for practical detection in bio-fluidic samples and the quantitative analysis of the real samples, e.g., mung bean, orange, and spinach. Thus the observations indicated that the present inexpensive protocol could be used for rapid on-site estimation of folic acid without involving sophisticated instrumental facilities, lavish reagents, or trained technicians.

References

- 4.1 Behpour, M.; Attaran, M. A.; Sadiany, M and M.; Khoobi, *Measurement*. 2016, **77**, 257–264.
- 4.2 Lyall, K.; Schmidt, J. R. and Hertz-Picciotto, I. *Int. J. Epidemiol.* 2014, **43**, 443–464.
- 4.3 Beitollahi, H.; Hamzavi, M. and Torkzadeh-Mahani, M. *Mater. Sci. Eng. C Mater. Biol. Appl.* 2015, **52**, 297–305.
- 4.4 Ren, W.; Fang, Y. and Wang, E. *ACS Nano*. 2011, **5**, 6425.
- 4.5 Prasad, B. B.; Tiwari, P. M.; Madhuri, R. and Sharma, S. P. *Anal. Chim. Acta*. 2010, **662**, 14–22.
- 4.6 Gao, X.; Yue, Y. H.; Huang, S.; Lin, Y. X.; Gao, A. P. X.; Wang, B.; Yao, H. L.; Wang, Y. W. and Guo, J. E. *Electroanal. Chem.* 2018, **808**, 189–194.
- 4.7 Obeid, R.; Oexle, K.; Reißmann, A.; Pietrzik, K. and Koletzko, B. *J. Perinat. Med.* 2016, **44**, 261–268.
- 4.8 Dietrich, M.; Brown, P. J. C. and Block, G. *J. Am. Coll. Nutr.* 2005, **24**, 266–274.
- 4.9 Ulrich, M. C. and Potter, D. J. *Cancer Epidemiology, Biomarkers & Prevention*. 2006, **15**, 2.
- 4.10 Xiao, F.; Ruan, P. C.; Liu, H. L.; Yan, R.; Zhao, Q. F. and Zeng, Z. B. *Sens. Actuat. B-Chem.* 2008, **134**, 895–901.
- 4.11 Zhang, R.; Ying, Y.; Rao, X. and Li, J. *J. Sci. Food Agric.* 2012, **92**, 2397–2408.
- 4.12 Araya-Farias, M.; Gaudreau, A.; Rozoy, E. and Bazinet, L. *J. Agric. Food Chem.* 2014, **62**, 4241–4250.
- 4.13 Zhang, T. B.; Zhao, L. and Lin, M. J. *Talanta*. 2008, **74**, 1154–1159.
- 4.14 Hau Fung Cheung, R.; Morrison, D. P.; Small, M. D. and Marriott, J. P. *J. Chromatogr. A*. 2008, **1213**, 93–99.
- 4.15 Wu, X.; Chen, X.; Gao, F.; Ma, W.; Xu, L.; Kuang, H.; Li, A. and Xu, C. *Biosens. Bioelectron.* 2016, **75**, 55.
- 4.16 Fajardo, V.; Alonso-Aperte, E. and Varela-Moreiras, G. *Food Chem.* 2015, **169**, 283–288.
- 4.17 Ray, A.; Bauri, A. and Bhattacharya, S. *J. Mol. Liq.* 2018, **263**, 64–71.
- 4.18 Tong, X.; Zhou, F. Y.; Jin, L.; Basu, K.; Adhikari, R.; Selopal, S. J.; Tong, X.; Zhao, G. H.; Sun, H. S.; Vomiero, A.; Wang, M. Z. and Rosei, F. *Nano Energy*. 2017, **31**, 441–449.
- 4.19 Jiang, S.; Hu, X.; Qiu, J.; Guo, H. and Yang, F. *Analyst*. 2019, **144**, 2662.

- 4.20 Samanta, S.; Goswami, S.; Ramesh, A. and Das, G. *J. Photochem. Photobiol. A*. 2015, **310**, 45-51.
- 4.21 Samanta, S.; Goswami, S.; Ramesh, A. and Das, G. *Sensor. Actuators, B. Chem.* 2013, **194**, 120-126.
- 4.22 Azagarsamy, M. A.; Yesilyurt, V. and Thayumanavan, S. *J. Am. Chem. Soc.* 2010, **132**, 4550-4551.
- 4.23 Ren, C.; Zhang, J.; Chen, M. and Yang, Z. *Chem. Soc. Rev.* 2014, **43**, 7257-7266.
- 4.24 Zhigang, X.; Xiaoxiao, S.; Meili, H.; Peng, X.; Yong-E, G.; Shiyong, L. and Yuejun, K. *Colloids and Surfaces B: Biointerfaces*. 2017, **150**, 50-58.
- 4.25 Zhang, W.; Wu, B.; Li, Z.; Wang, Y.; Zhou, J. and Yaping, L. *Spectrochimica Acta Part A: Molecular and Biomolecular Spectroscopy*. 2020, **229**, 117931.
- 4.26 Mote, S. U.; Patil, R. S.; Bhosale, H. S.; Han, H. S. and Kolekar, B. G. *Journal of Photochemistry and Photobiology B: Biology*. 2011, **103**, 16-21.
- 4.27 Shetty, A. S.; Zhang, J. and Moore, J. S. *J. Am. Chem. Soc.* 1996, **118**, 1019-1027.
- 4.28 Wurthner, F.; Chen, Z.; Dehm, V. and Stepanenko, V. *Chem. Commun.* 2006, 1188-1190.
- 4.29 Chowdhury, S. R.; Mukherjee, S.; Das, S.; Patra, C. and Iyer, P. K. *Chem. Sci.* 2017, **8**, 7566-7575.
- 4.30 Muthuraj, B.; Mukherjee, S.; Patra, C. R. and Iyer, P. K. *ACS Appl. Mater. Interfaces*, 2016, **8**, 32220-32229.
- 4.31 Deng, Y.; Yuan, W. and Liu, G. *J. Phys. Chem. B*. 2014, **118**, 14536-545.
- 4.32 Chang, J.; Lu, Y.; He, S.; Liu, C.; Zhaoab, L. and Zeng, X. *Chem. Commun.* 2013, **49**, 6259-6261.
- 4.33 Gao, C.; Gao, G.; Lan, J. and You, J. *Chem. Commun.* 2014, **50**, 5623-5625.
- 4.34 Gui, S.; Huang, Y.; Hu, F.; Jin, Y.; Zhang, G.; Yan, L.; Zhang, D. and Zhao, R. *Anal. Chem.* 2015, **87**, 1470-1477.
- 4.35 Maity, A.; Ali, F.; Agarwalla, H.; Anothumakkool, B. and Das, A. *Chem. Commun.* 2015, **51**, 2130-2133.
- 4.36 Bhalla, V.; Arora, H.; Singh, H. and Kumar, M. *Dalton. Trans.* 2013, **42**, 969-974.
- 4.37 Gogoi, A.; Mukherjee, S.; Ramesh, A. and Das, G. *Anal. Chem.* 2015, **87**, 6974-6979.
- 4.38 Samanta, S.; Kar, C. and Das, G. *Anal. Chem.* 2015, **87**, 9002-9008.
- 4.39 Li, W.; Zhang, X.; Miao, C.; Li, R. and Ji, Y. *Analytical and Bioanalytical Chemistry*. 2020, **412**, 2805-2813.
- 4.40 Qian, J.; Quan, F.; Zhao, F.; Wu, C.; Wang, Z. and Zhou, L. *Sensors and Actuators B*. 2018, **262**, 444-451.
- 4.41 Li, C.; Yang, Q.; Wang, X.; Arabi, M.; Peng, H.; Li, J.; Xiong, H. and Chen, L. *Food Chemistry*. 2020, **319**, 126575.
- 4.42 Nghia, N. N.; Huy, T. B. and Lee, Y. *Journal of Industrial and Engineering Chemistry*. 2020, **81**, 352-359.
- 4.43 Hamed, E.; Attia, S. M. and Bassiouny, K. *Bioinorg Chem Appl.* 2009, **2009**, 979680.
- 4.44 Jiao, Y.; Zhu, B.; Chen, J. and Duan, X. *Theranostics*. 2015, **5**, 173-187.
- 4.45 El-Wahed, M.G.; Refat, M.S. and El-Megharbel, S. M. *Spectrochimica Acta A*. 2008, **70(4)**, 916-922.
- 4.46 Chakravartya, S.; Dutta, P.; Kalita, S. and Sarmaa, S. N. *Sensors and Actuators B*. 2016, **232**, 243-250.

- 4.47 Rong, M.; Lin, L.; Song, X.; Zhao, T.; Zhong, Y.; Yan, J.; Wang, Y. and Chen, X. *Anal. Chem.* 2015, **87**, 1288–1296.
- 4.48 Dutta, P.; Saikia, D.; Adhikary, C. N. and Sarma, S. N. *ACS Appl. Mater. Interfaces.* 2015, **7**, 24778–24790.
- 4.49 Wen, L. Q.; Pu, F. Z.; Yang, J. Y.; Wang, J.; Wu, C. B.; Hu, L. Y.; Liu, P.; Ling, J. and Cao, Q. *Microchemical Journal.* 2020, **159**, 105364.
- 4.50 Roy, S.; Gunukula, A.; Ghosh, B. and Chakraborty. C. *Sensors & Actuators: B. Chemical.* 2019, **219**, 337–344.



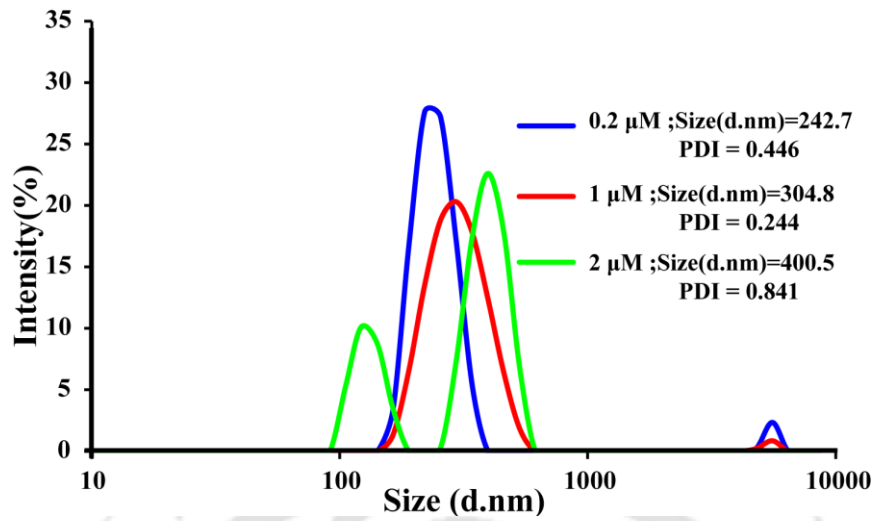
Appendix - Chapter 4

Figure A4.1: DLS-based particle size analysis; change in particle size of L_4 in the aqueous medium in different concentrations (0.2-2 μM).

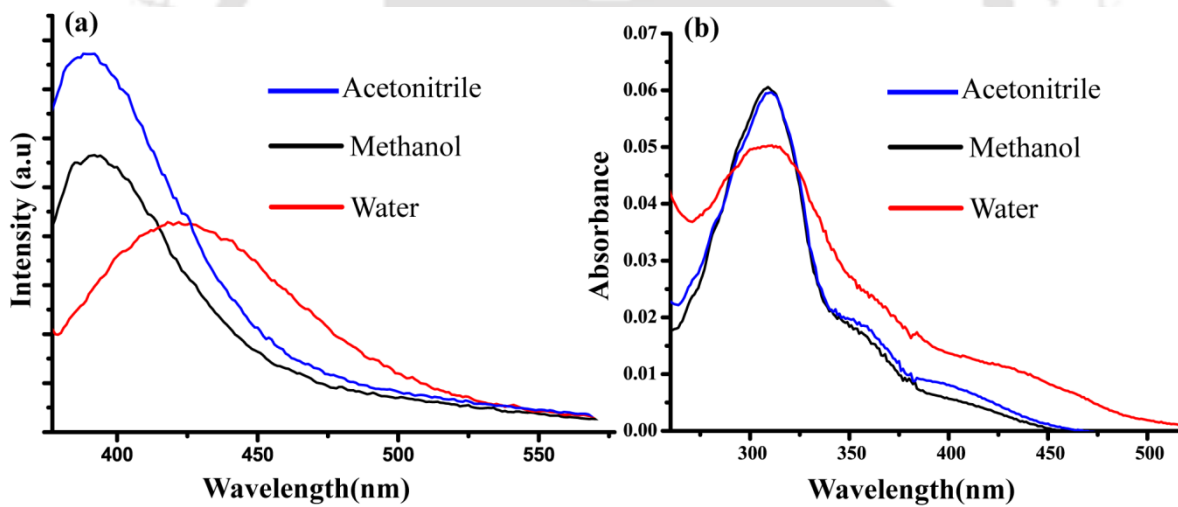


Figure A4.2: (a) Fluorescence and (b) UV-Vis changes of L_4 (2 μM) in several solvents at room temperature.

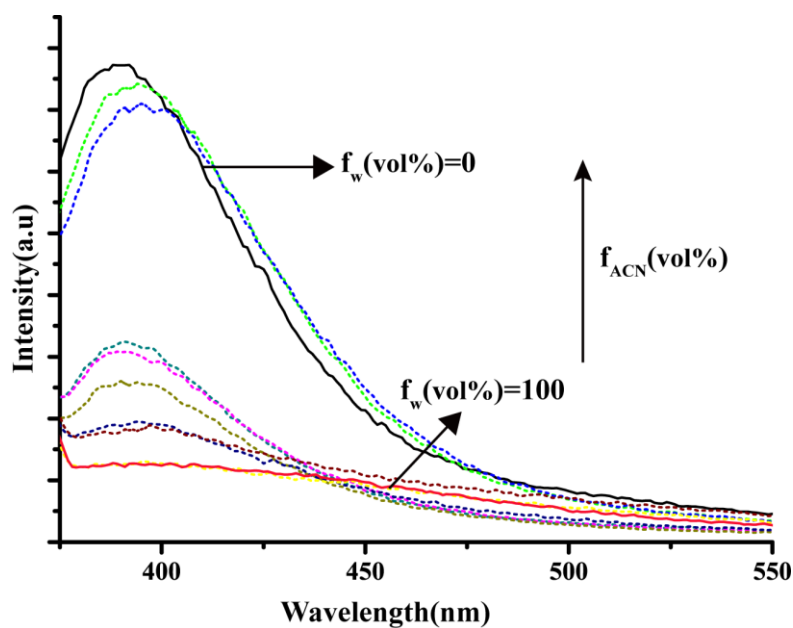


Figure A4.3: Fluorescence spectral changes of L_4 with increasing water content in acetonitrile solution ($\lambda_{\text{ex}} = 330 \text{ nm}$, slit = 3nm / 3nm).

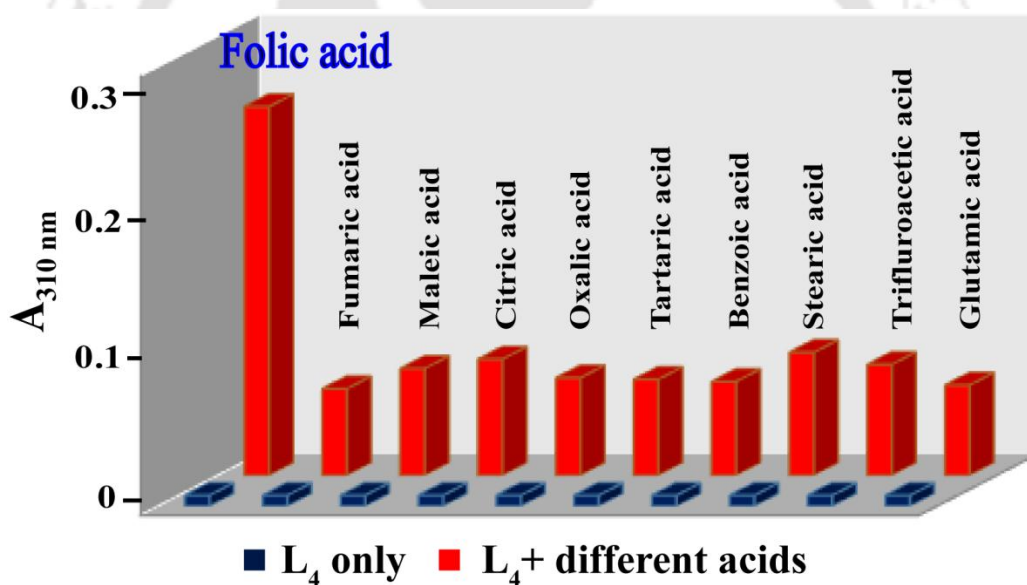


Figure A4.4: Comparison of the absorbance at 310 nm of L_4 on interaction with various carboxylic acids.

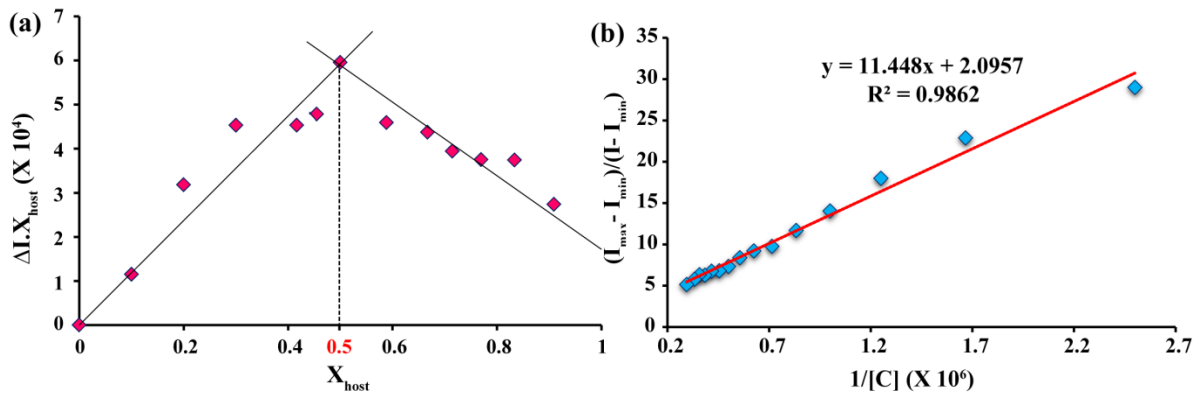


Figure A4.5: (a) Job's plot for determining L_4 's stoichiometry with FA (1:1 host-guest complex). (b) Determination of affinity constant of L_4 for FA in aqueous medium using the Benesi-Hildebrand method considering 1:1 interaction.

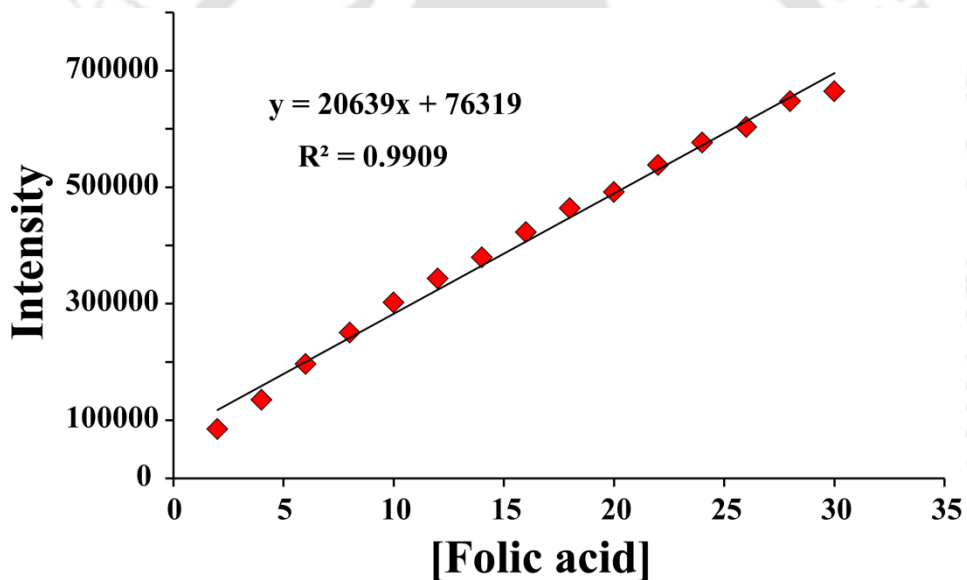


Figure A4.6: Fluorescence emission intensity of L_4 at 450 nm vs. FA concentration to calculate the detection limit.

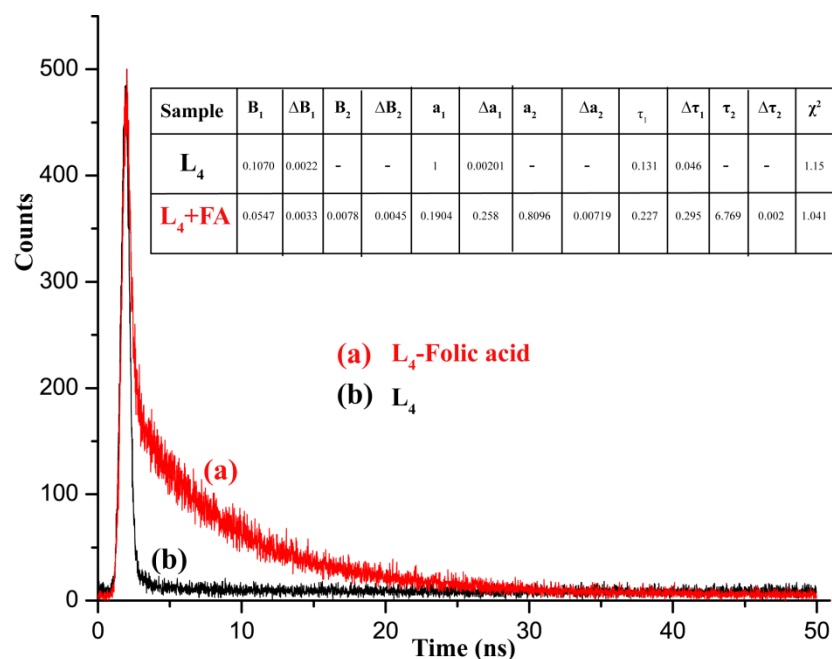


Figure A4.7: Fluorescence lifetime decay profiles of L_4 (2 μM) and L_4 in excess FA in the aqueous medium. Inset: Lifetime of L_4 and L_4 in presence of FA.

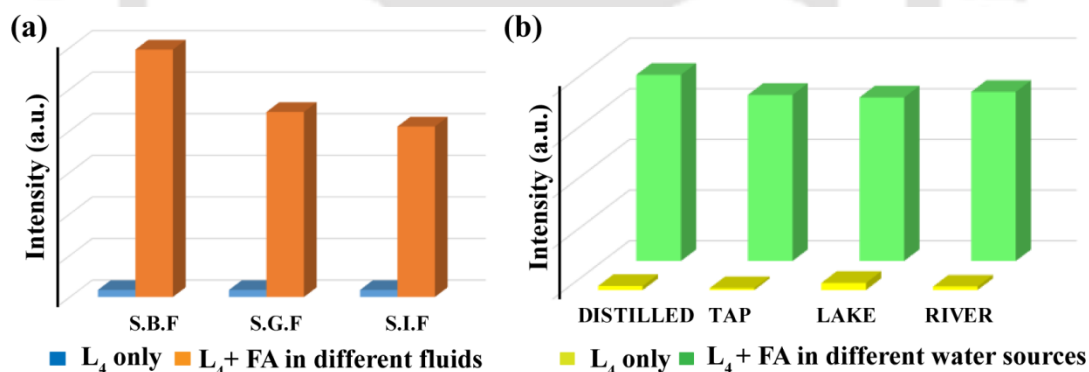


Figure A4.8: (A) Changes in the emission intensity of L_4 (2 μM) at 450 nm in the presence of excess FA in bio-fluidic samples [SBF- Simulated Body Fluid (pH~7.4), SGF- Simulated Gastric Fluid (pH~2.0) and SIF- Simulated Intestinal Fluid (pH~8.0)]. (B) Changes in the emission intensity of L_4 (2 μM) at 450 nm in the presence of excess FA in different sources of water.

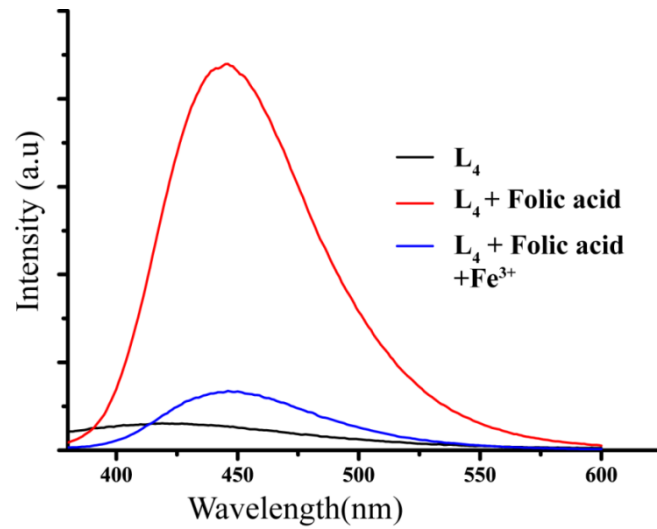


Figure A4.9: Fluorescence spectral changes of L_4 -FA complex after Fe^{3+} addition in aqueous medium ($\lambda_{\text{ex}} = 330 \text{ nm}$, slit = 3nm / 3nm).

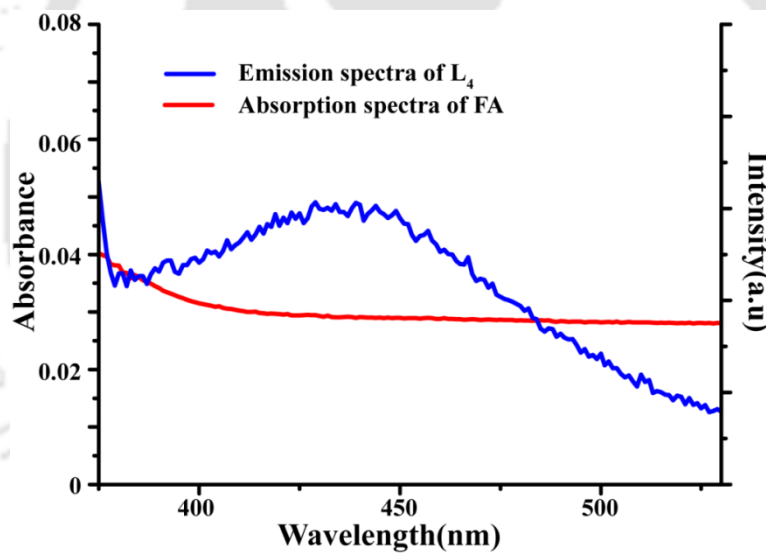


Figure A4.10: Spectral overlap of emission spectra of L_4 and absorption spectra of FA.

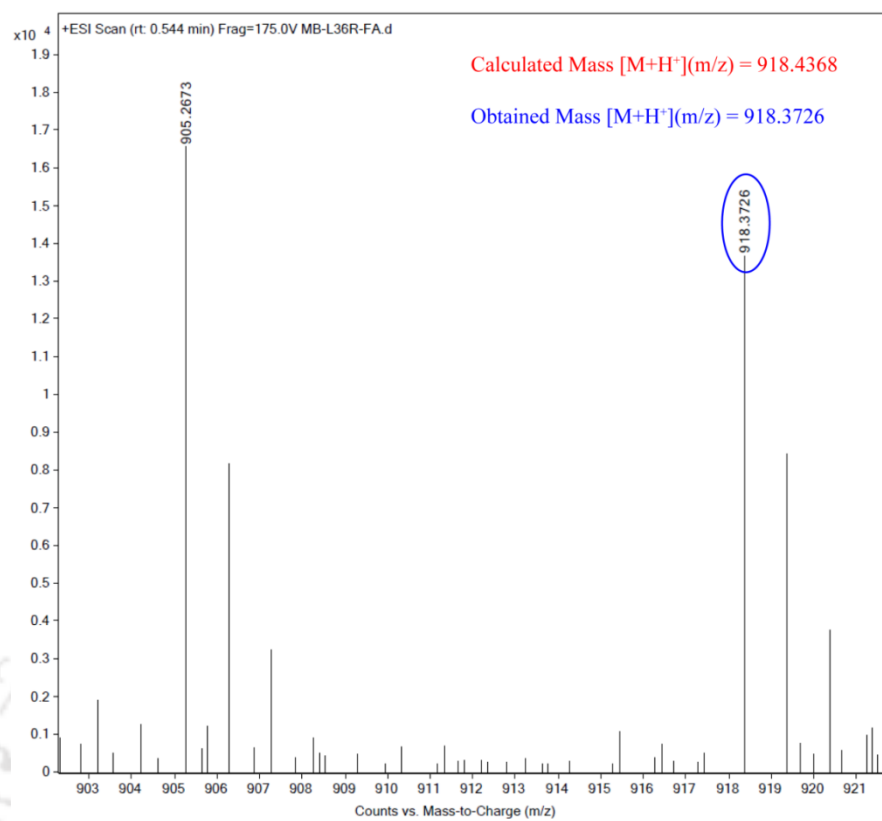


Figure A4.11: ESI-mass spectra of L_4 in the presence of FA in positive ionization mode.

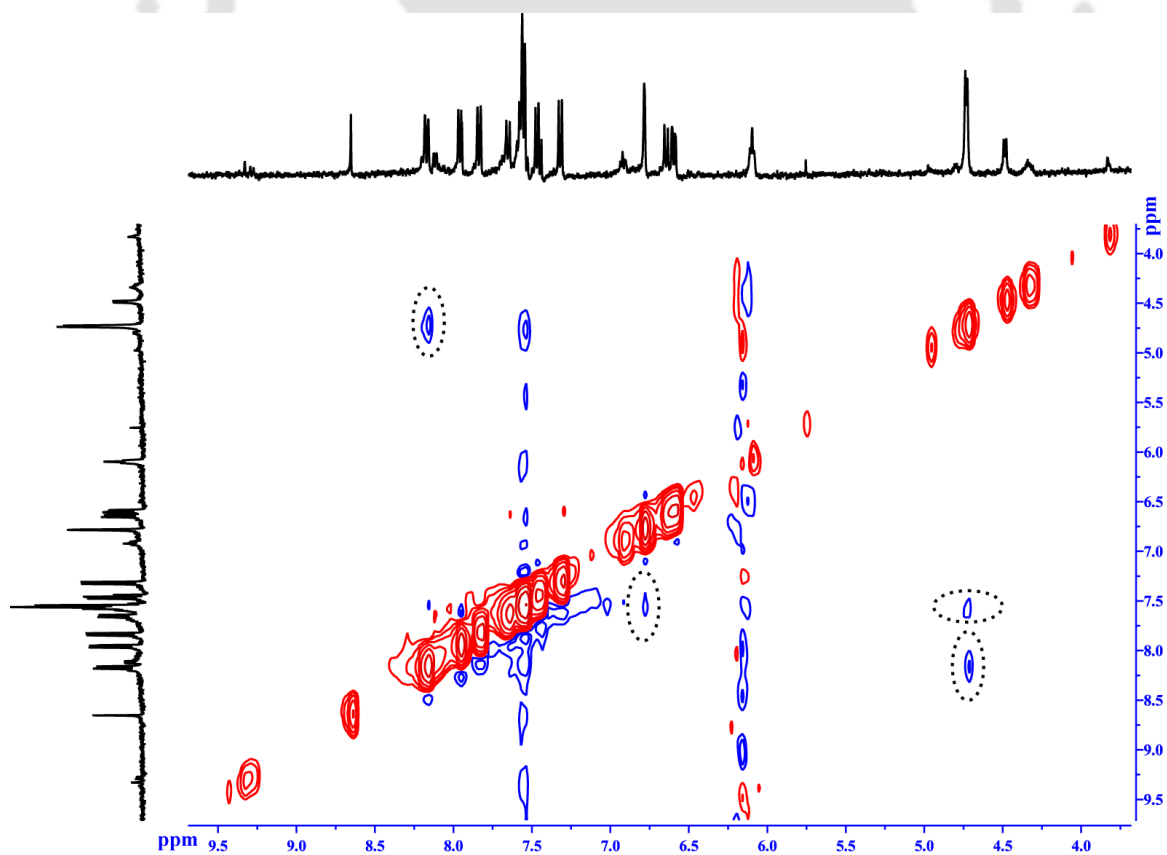


Figure A4.12: NOESY NMR of L_4 -FA.

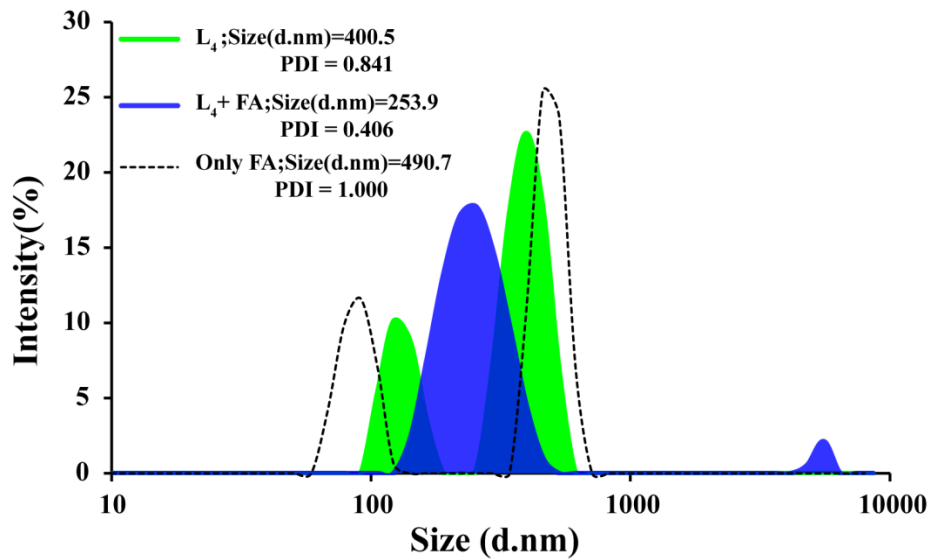


Figure A4.13: DLS-based particle size analysis; particle size of L_4 , in presence of FA and only FA in the aqueous medium.

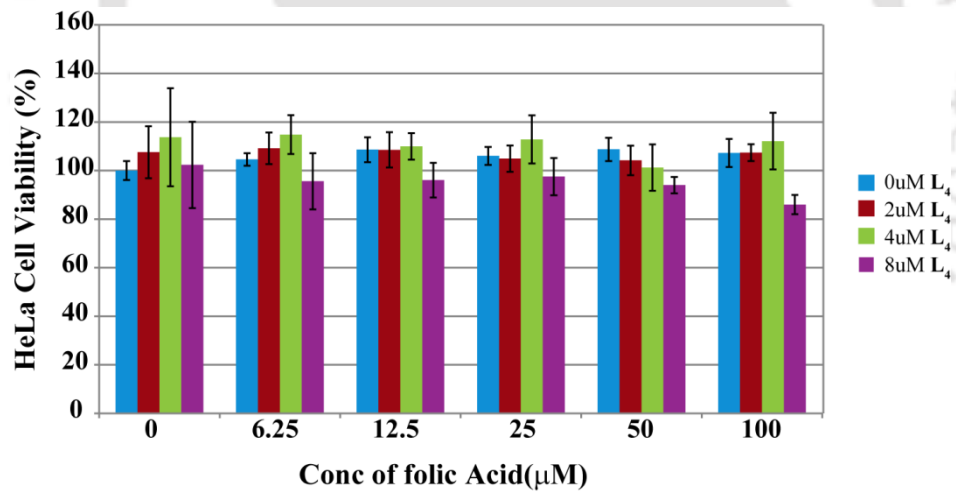


Figure A4.14: MTT based cytotoxicity assay for L_4 , L_4 -FA ensemble, and only FA at various concentrations.

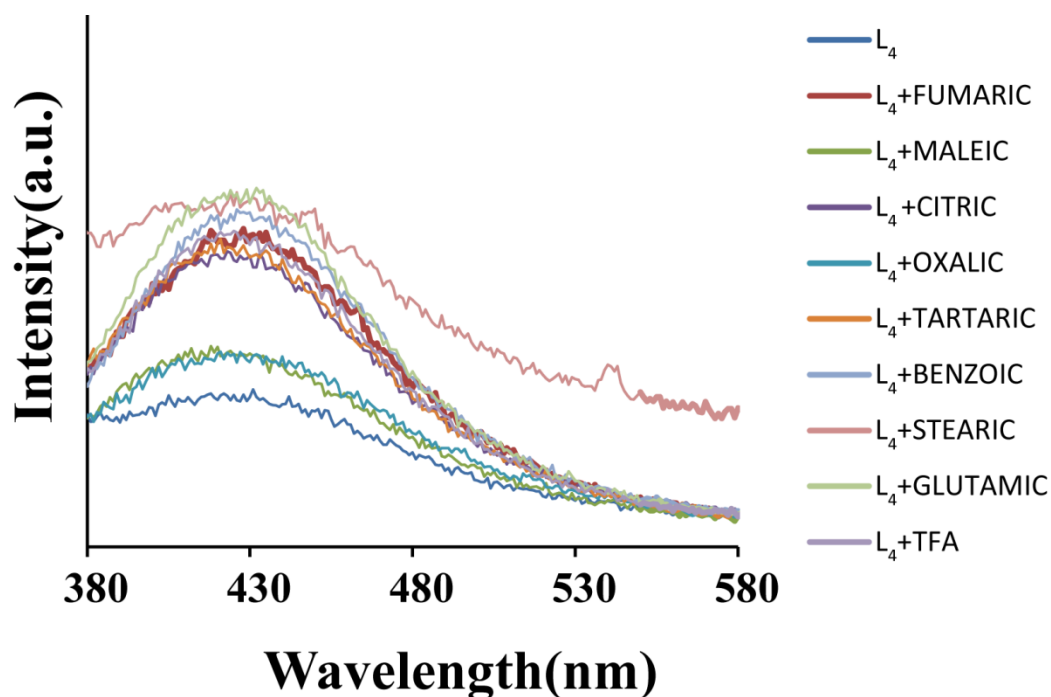


Figure A4.15: Fluorescence emission spectra of L_4 in presence on different carboxylic acids.

Table A4.1: Determination of FA by L_4 in real samples.

Sample	Using Fluorescence Spectroscopy	Using UV Visible-Spectroscopy
Mugh	1.8 μ M	1.8 μ M
Spinach	2.2 μ M	2.0 μ M
Orange	0.9 μ M	0.8 μ M

Table A4.2: Photophysical Characterization data of L_4 and L_4 -FA.

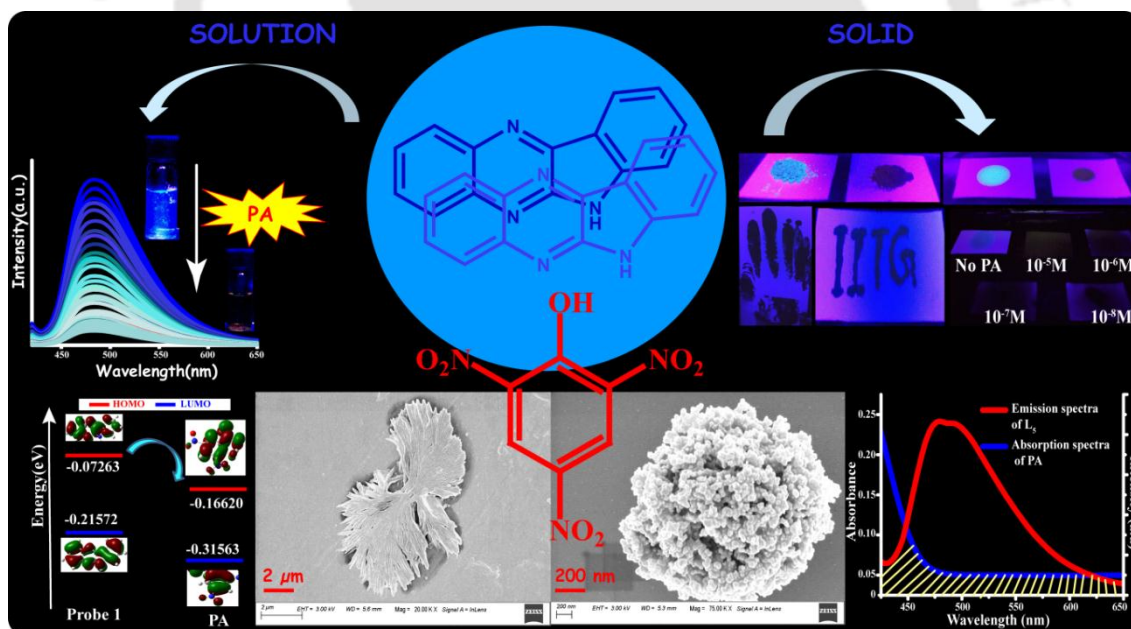
Sample	Quantum Yield(QY)	Δ QY	Lifetime(τ) (ns)	Δ τ	Extinction Coefficient(ϵ) ($M^{-1} cm^{-1}$)	$\Delta \epsilon$
L_4	0.05	0.000	0.131	0.046	26115.5	0.0053
L_4 -FA	7.51	0.014	6.769	0.002	112761.5	0.01604

Table A4.3: Latest progress in the field of FA sensing, a comparative study.

SI No.	References	Receptor type	LOD of Folic acid	Solvent System/Mode of Approach
1.	Present work	Probe L₄ alone	0.38 μM	100% Aqueous medium
2.	Spectrochimica Acta Part A: Molecular and Biomolecular Spectroscopy, 2020, 229, 117931	Carbon quantum dots (CQDs)	0.38 μ M	Methanol
3.	Journal of Industrial and Engineering Chemistry, 2020, 81, 352–359	RhB-HS-Cu ²⁺ (rhodamine-B derivative)	0.022 μ M	Paper-based
4.	Analyst, 2019, 144, 2662–2669	Probe alone	0.636 μ M	THF/water(5:95)
5.	Applied Surface Science, 2019, 471, 168–175	molecularly imprinted PDMS elastomer	0.0031 μ g/ml	Surface initiated reversible addition-fragmentation chain transfer (SI-RAFT) polymerization
6	RSC Adv., 2017, 7, 50072–50078	TiO ₂ Pt–graphene nanocomposite (TiO ₂ Pt/rGO) with α , β , and γ -cyclodextrins (CD)	0.0453 μ M	Plastic tip, electrical contact using an Ag wire
7.	Spectrochimica Acta Part A: Molecular and Biomolecular Spectroscopy, 2015, 137, 58–65	hydroxyapatite (HA) nanoparticles (NPs)	0.075 μ M	Electrocatalytic activity

CHAPTER 5

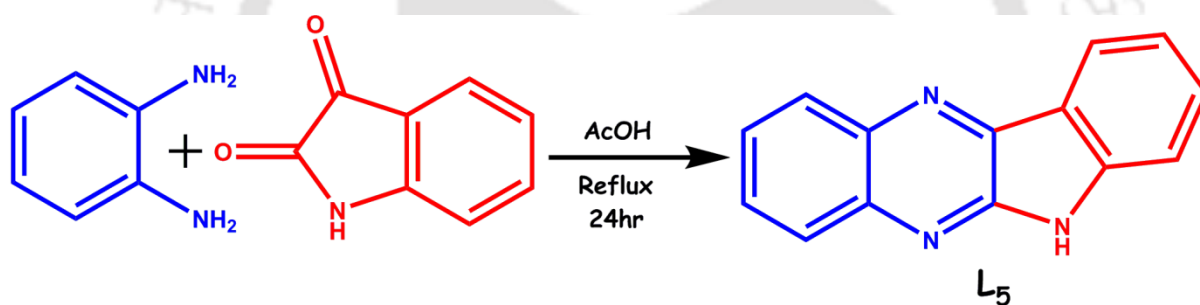
Quinoxaline Based probe: Nitro-aromatics induced disassembly and selective Turn-off detection in water



5.1 Background and focus of the chapter

Detection of trace explosives have gained imperative attention in the past few decades to mitigate counter-terrorism, homeland defense, environmental pollution, and forensic interrogation.^{5.1-5.3} Chemical explosives encompass an array of nitroaromatic compounds (NACs), nitramines, nitrate esters, and peroxides.^{5.4} Amidst these, the NACs are highly energetic explosives, which warrant sensitive and specific detection and therefore the prime concern of our work. Picric acid (PA) and trinitrotoluene (TNT) are utilized as primary and secondary explosives,^{5.5} with the explosive power of PA being superior than TNT.^{5.6} PA is also used in battery, matches, and leather manufacturing units, rocket fuels processing, textile, fireworks, and dye industries.^{5.7-5.11} Picric acid is a versatile compound and an embodiment of dual chemistry - one facet as an explosive and another as an antiseptic for treatment of burns, malaria, and smallpox^{5.12-5.14} and an analytical reagent. Nevertheless, due to PA's high water-soluble character, soil and the aquatic system get contaminated instantaneously.^{5.15-5.16} As per WHO,^{5.17} 0.001 mg L⁻¹ is the permissible PA concentration in groundwater. Consistent long-term exposure to picric acid may affect the respiratory organ, red blood cell, kidney, liver, spleen, and nervous system.^{5.18-5.19} Hence, chemists have a crucial task to fabricate new sensors for selective and sensitive detection of PA in the aqueous matrix, which will minimize cost, render a low limit of detection but maximize portability. Widely used methodologies such as gas chromatography,^{5.20-5.21} surface plasmon resonance,^{5.22} thermal neutron analysis,^{5.23} SERS,^{5.24-5.25} X-ray imaging^{5.26} etc., have been reported for efficient detection of PA. However, these techniques have limited practical applicability due to expensive instrumentation, lack of trained technicians, time-consuming calibration, intervention from other components, and poor sensitivity. In this regard, the self-assembly of simple fluorophore molecules for nitro explosive detection can be a viable approach. Such probes manifest high fluorescence quantum yields and enhanced sensitivity with remarkable electron-donating capacity, while the cognate analytes are electron-deficient explosives, which exhibit non-fluorescence properties.^{5.27-5.28} Efficient π - π stacking between these molecules followed by intramolecular charge-transfer transition effectively suppresses self-quenching and could provide a unique molecular design for emissive

organic self-aggregates. The donor-acceptor interaction phenomena via π - π interconnection and the strongest N-H interaction with nitro explosives trigger luminescence quenching.^{5.29-5.31} Hence, the development of self-assembled molecular probes that can engage in assembly-disassembly processes in the presence of PA and subsequently render ultra-trace detection of picric acid in a 100% aqueous matrix is our utmost concern. In light of this premise, we designed and synthesized a simple quinoxaline-based fluorescence self-aggregated probe for discriminative detection of PA in water via "turn-off" mode. The aforementioned self-assembled fluorescence sensor, which belongs to the family of small π -conjugated linear fluorophore, is scarce compare to widely explored naphthalimide, pyrene, thienylazulene, pyrazoline-based fluorescent aggregates^{5.32-5.34} for recognition of PA. Owing to its high fluorescence quantum yield, simple single-step synthesis, better sensitivity with high K_{sv} value, the self-aggregated probe(Scheme 5.1) is suitable to recognize PA in complex samples i.e., soil and groundwater samples. Convenient low-priced, portable paper strips were also prepared for an instant, on-site detection of PA, devoid of sophisticated analytical equipments. The application potential of the developed probe is substantiated by detecting intracellular PA in live cell imaging studies.



Scheme 5.1: Synthetic Scheme of the probe L₅.

5.2 Photophysical Investigation

The photophysical properties of L₅ were explored in various solvents by UV-visible absorption and fluorescence spectroscopy at room temperature. For these studies, a 1.0 mM stock solution of L₅ was prepared in dimethylsulfoxide (DMSO) and diluted consequently with the experimental solutions. The UV-visible spectra of L₅ (5.0 μ M) in pure acetonitrile and pure water is depicted in Figure 5.1a. L₅ manifested absorption bands at 321, 335, 351 nm and a hump at 383 nm in acetonitrile. In water, the absorption maxima were slightly right-shifted to 322, 337, 360 nm along with a broad hump around 410 nm, which can be assigned to π - π^* electronic transitions^{5.35} of quinoxaline moiety. Water content also reduced the intensity of absorption followed by a tailing beyond 440 nm, which can perhaps be ascribed to Mie scattering^{5.36} owing to the presence of micro-aggregates in an aqueous solution. Nevertheless,

naked-eye inspection suggested that the aqueous solution of L_5 was transparent with no apparent precipitation. The fluorescence spectra was recorded by varying the content of water in a solution of L_5 in acetonitrile (Figure A5.1a). The fluorescence spectra of L_5 in acetonitrile/water mixtures gave emission maxima between 460-462 nm. But upon enhancing the amount of water to 100%, the emission maxima with considerably reduced intensity was red-shifted to 484 nm. The redshift observed in the emission maxima suggested the transformation of a single probe molecule into a self-aggregated entity via intermolecular non-covalent interactions. This further confirmed the self-assembly of L_5 molecule in presence of 100% water.

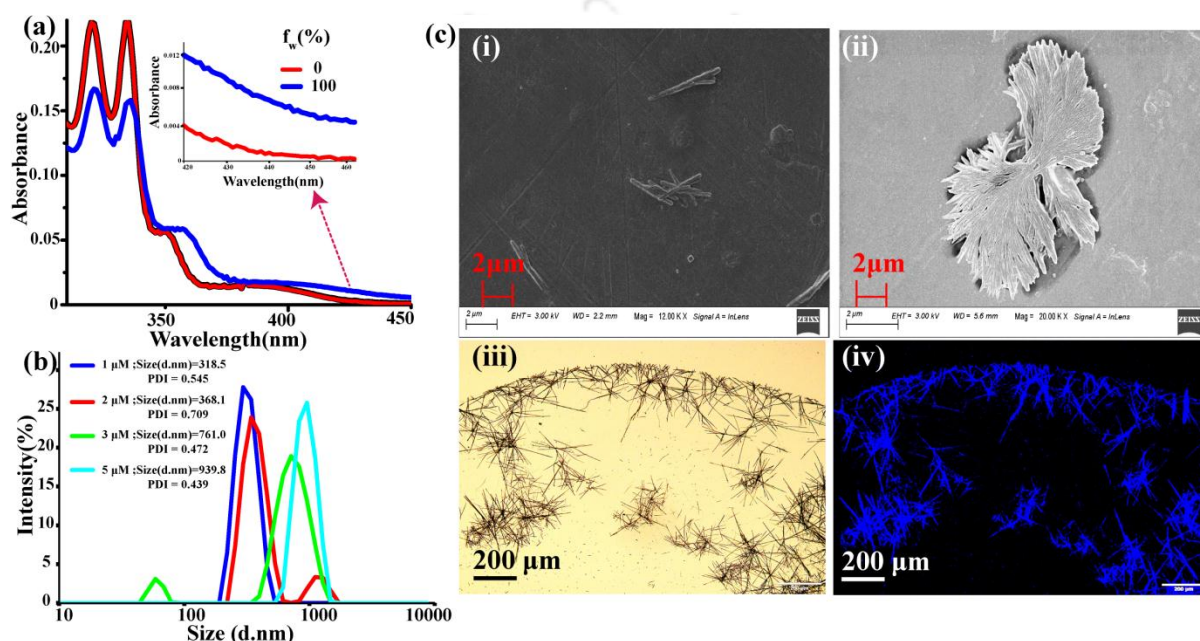


Figure 5.1: (a) UV-visible spectra of L_5 (5 μ M) in different water fractions at room temperature. (b) DLS spectra of L_5 for various concentrations in aqueous medium. (c) FESEM image for (i) 1.0 μ M, (ii) 5.0 μ M concentration of L_5 and Fluorescence microscopy images for 5.0 μ M L_5 . (iii) Bright field (iv) Darkfield.

The concentration-dependent fluorescence spectra of L_5 in water also validated the rise in emission intensity upon self-assembly (Figure A5.1b). Furthermore, to validate the formation of aggregates, DLS and FESEM studies were also pursued in acetonitrile and aqueous medium. DLS study was accomplished in various concentrations ranging from 1.0 μ M to 5.0 μ M. The result indicated formation of self-aggregated L_5 as the average hydrodynamic radius ranged from 318.5 nm to 939.8 nm with PDI 0.545 to 0.439 in the aqueous medium (Figure 5.1b) whereas, in acetonitrile, no variation in hydrodynamic radius was observed. In an aqueous medium, variation in the hydrodynamic radius was observed due to efficient π - π interaction leading to self-assembled aggregate formation. In solution, π - π interaction influencing intermolecular aggregation phenomenon is well documented in the literature for polyaromatic planar molecules.^{5.37-5.39} FESEM study indicated that L_5 (5.0 μ M) exhibited a propensity to self-

assemble to generate leaf-like aggregates in pure water (Figure 5.1c; i, ii). Fluorescence microscope images also confirmed the presence of self-aggregated L_5 emitting bright blue fluorescence (Figure 5.1c; iii, iv).

5.3 Sensing Performance toward PA

The π electron-rich and strongly emissive nature of self-assembled L_5 encouraged us to investigate its prospective application as a fluorescent chemosensor for nitroaromatics (NACs), which are likely to interact strongly with electron-rich self-aggregated fluorescent L_5 . Further, it was conceived that owing to insufficient electron density in NACs, electron transfer would ensue smoothly between the fluorescent probe and electron-poor NACs resulting in the probe's rapid fluorescence quenching.

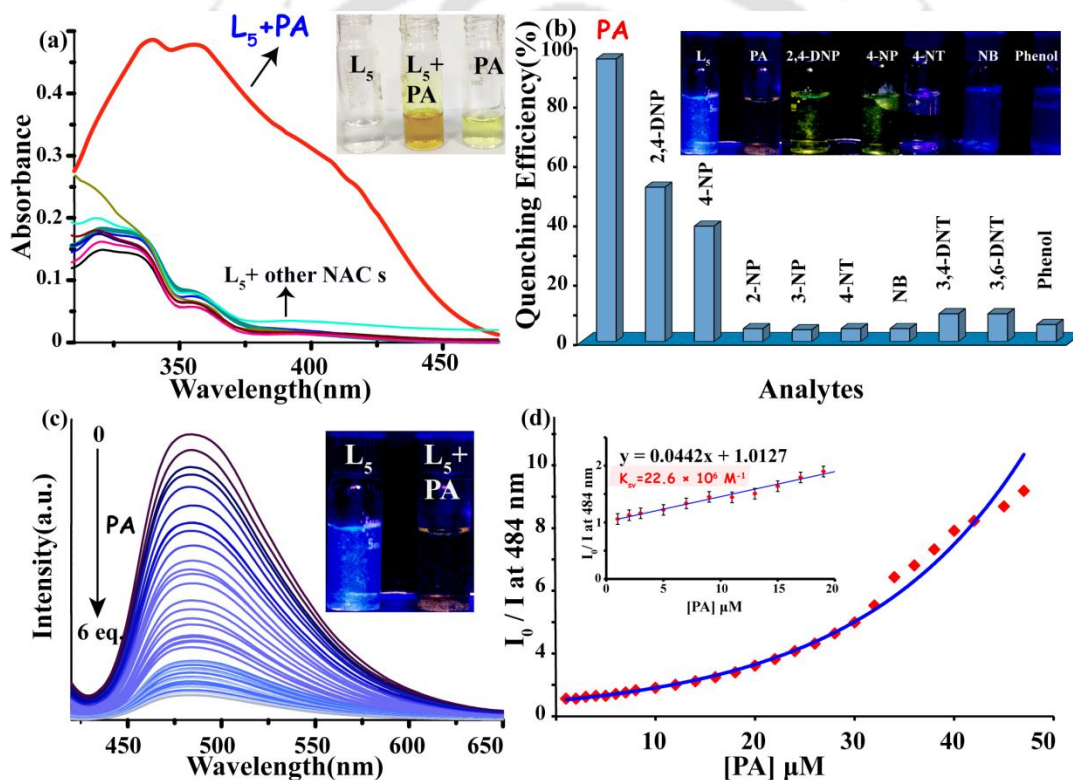


Figure 5.2: (a) Absorption spectra of L_5 ($5.0 \mu\text{M}$) in the presence of various NACs (50 Equiv) in aqueous medium; Inset: Visual color change of L_5 solution in the presence of PA. (b) Fluorescence quenching efficiency ($\lambda_{\text{ex}} = 400 \text{ nm}$) of L_5 ($5.0 \mu\text{M}$) in water in the presence of various analytes (50 Equiv.). Inset: Visual change in fluorescence intensity of L_5 observed under UV light upon addition of different analytes. (c) Change in fluorescence spectra of L_5 ($5.0 \mu\text{M}$, $\lambda_{\text{ex}} = 400 \text{ nm}$) upon addition of PA. Inset: Visual color change of L_5 in presence of PA. (d) Stern-Volmer plot: I_0/I vs. $[\text{PA}]$. Inset: Stern-Volmer plot achieved at a lower concentration of PA ($0 \mu\text{M} - 20 \mu\text{M}$).

To explore the self-aggregated probe's sensing ability towards nitroaromatics, we assessed the effect of various nitroaromatic compounds in aqueous medium. When an aqueous solution of L_5 ($5.0 \mu\text{M}$) was treated with various NACs such as picric acid (PA), 2,4-dinitrophenol (2,4-DNP),

4-nitrophenol (4-NP), 3-nitrophenol (3-NP), 2-nitrophenol (2-NP), 4-nitrotoluene (4-NT), 3,4-dinitrotoluene (3,4-DNT), 3,6-dinitrotoluene (3,6-DNT), nitrobenzene (NB) and non-nitro compound like sodium nitrite, phenol (Figure A5.2), the absorption spectra of L_5 ($\epsilon = 30914.6 \text{ M}^{-1} \text{ cm}^{-1}$) changed remarkably in the presence of only PA, indicating a strong interaction between PA and L_5 ($\epsilon = 98697.4 \text{ M}^{-1} \text{ cm}^{-1}$) (Figure 5.2a). Further, the visual appearance of L_5 in solution changed immediately from colorless to mustard yellow, possibly due to the formation of the charge-transfer complex. The fluorescence spectra of self-assembled L_5 (5.0 μM , Quantum yield = 0.91) manifested an intense emission maxima at 484 nm when excited at 400 nm in an aqueous solution. Surprisingly, after the addition of various NACs and non-nitro compounds, prominent quenching was observed in the case of nitrophenol solutions, while the others revealed minimal changes. A significant quenching of emission (~95%) was observed upon addition of 6 Equiv. of PA, while for 2,4-DNP and 4-NP, quenching efficiency was only 51% and 38%, respectively (Figure 5.2b). As the number of nitro groups increased, electron deficiency enhanced in NACs, and electron drifts were elevated from the electron-rich sensor to NACs followed by strong intermolecular interactions, leading to a higher extent of fluorescence quenching. Consequently, with the addition of PA, the quenching efficiency was maximum (Quantum yield = 0.087) as compared to other nitroaromatics, suggesting the selectivity of self-aggregated L_5 toward PA. Since nitrophenols displayed substantial quenching among all other NACs, fluorescence titration experiments with only PA (Figure 5.2c), 2,4-DNP and 4-NP were pursued. For these three nitrophenols, the emission intensity of L_5 decreased with the incremental addition of the analyte. The quenching mechanism was also evaluated by Stern-Volmer (SV) equation. The SV plot was found to be linear at a lower concentration of PA with a Stern-Volmer constant (K_{sv}) of $22.6 \times 10^6 \text{ M}^{-1}$ (Figure 5.2d, inset), which is more significant than earlier reported values in the literature,^{5,40} while at a higher concentration of PA, the plot was apparently exponential (Figure 5.2d). The linear response at lower concentration of PA and a high K_{sv} value may be ascribed to static quenching, while the non-linear nature at higher concentration of PA signified the involvement of dynamic quenching in presence of an additional energy transfer process.^{5,41} Interestingly, K_{sv} values for 2,4-DNP and 4-NP were lower than the K_{sv} value for PA ($22.6 \times 10^6 \text{ M}^{-1}$) and was estimated to be 4.26×10^6 and $1.68 \times 10^6 \text{ M}^{-1}$, respectively with a linear response plot (Figure A5.3 and A5.4). Hence, the K_{sv} values could render discrimination amongst PA, DNP, and NP. To illustrate the mechanistic aspect of fluorescence quenching, time-resolved fluorescence spectra of L_5 (5.0 μM , $\lambda_{ex} = 400 \text{ nm}$) in an aqueous medium was recorded before and after the addition of PA. Both the time-resolved decays were fitted to bi-exponential decay along with a significantly decreased lifetime from

3.85 ns to 1.52 ns upon addition of PA (Table A5.1). The decrease in lifetime with the gradual addition of PA signified a dynamic quenching mechanism, i.e., diffusion-controlled collision^{5.42} between the excited sensor and the quencher. The limit of detection^{5.43} for PA was calculated to be ~56 ppb (Figure A5.5) using an earlier reported procedure in the literature.^{5.44} The K_{sv} and LOD obtained for the probe for PA detection in the current study compares well with previous reports. The limit of quantification (LOQ) for PA was estimated to be 186 ppb (Figure A5.5). The interference and selectivity studies with other NACs, common cations and anions (2,4-DNP; 4-NP, 2-NP, 3-NP, 4-NT, NB, 3,4-DNT, 3,6-DNT, phenol, Fe^{3+} , Al^{3+} , Cr^{3+} , Hg^{2+} , Cd^{2+} , Pb^{2+} , Cu^{2+} , Co^{2+} , Ni^{2+} , Zn^{2+} , Ca^{2+} , Mg^{2+} , PO_4^{3-} , Cl^- , I^- , $H_2PO_4^-$, HSO_4^- , NO_3^- , OH^- , HSO_3^- , HCO_3^- , SH^- , oxalate²⁻) were also examined. Their effect on sensitivity and selectivity of L_5 for PA was very negligible (Figure A5.6).

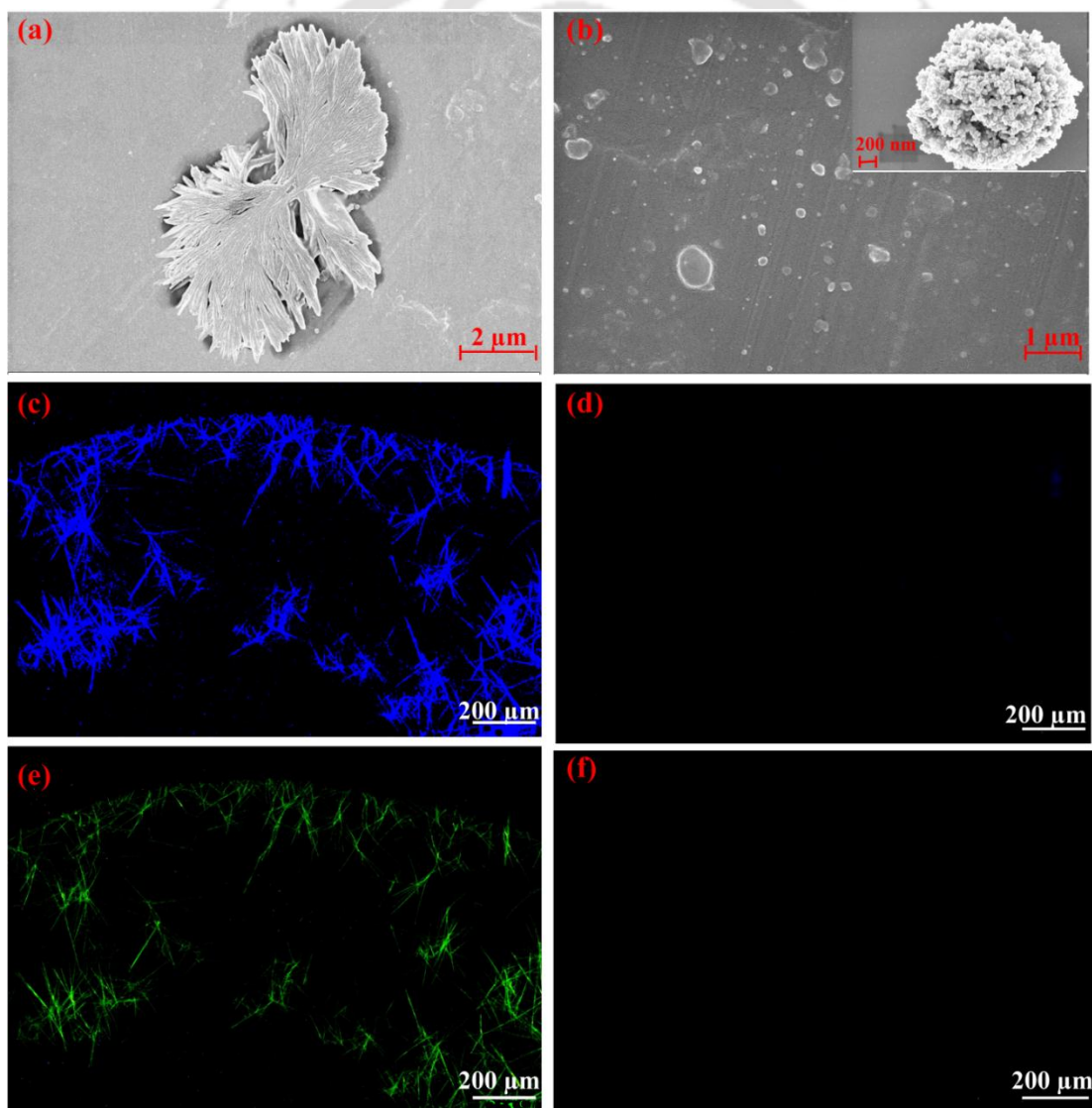
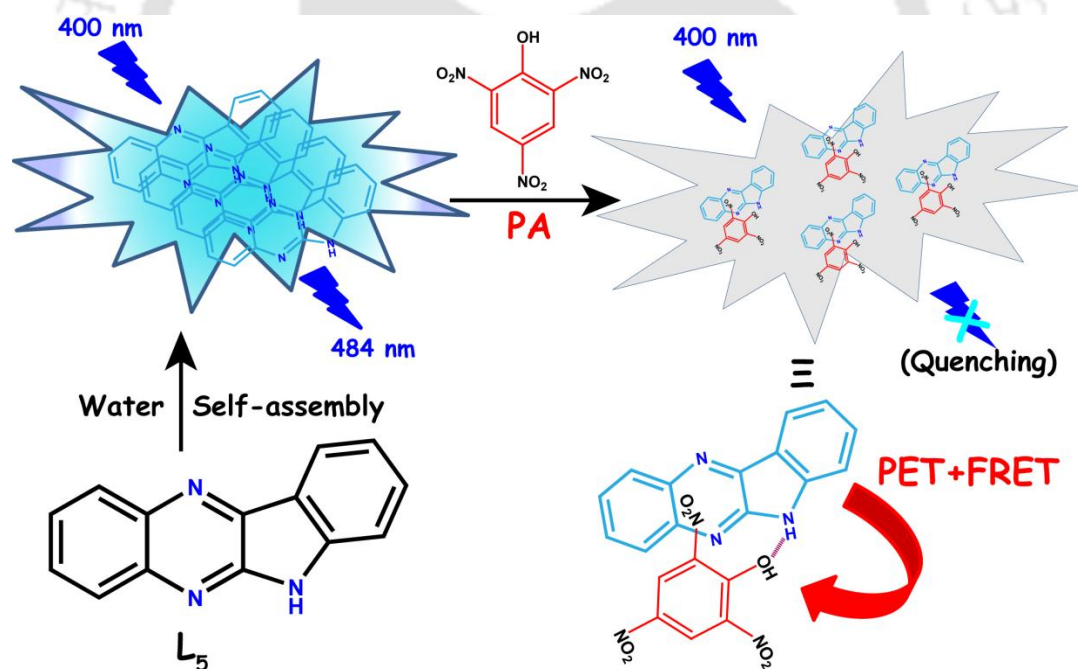


Figure 5.3: FESEM and Fluorescence microscope images of L_5 (5.0 μ M) (a, c and e), L_5 + PA (b; Inset: Magnified view, d, and f) in 100% aqueous medium.

FESEM analysis and fluorescence microscopic studies were conducted to ascertain the variation in surface morphology of self-assembled L_5 in the absence and presence of PA. Self-assembled L_5 exhibited leaf-like morphology, which became smaller and displayed round-shaped morphology upon interaction with PA (Figure 5.3a, 5.3b). In fluorescence microscope analysis, the intense fluorescence emitted by the self-assembled probe was completely dissipated upon interaction with PA (Figure 5.3c-5.3f). Conceivably, interaction with PA resulted in disaggregation of the self-assembled L_5 . This tenet was corroborated by DLS studies, wherein the self-assembled L_5 displayed a higher hydrodynamic radius (939.8 nm) as compared to L_5 -PA complex (353.7 nm) (Figure A5.7), strongly suggesting dissociation of the self-assembled L_5 . In order to gain further insight into the sensing phenomenon (Scheme 5.2), Job's plot was generated, which indicated that L_5 -PA formed a 1:1 stoichiometric complex (Figure A5.8). HRMS studies further verified the complexation between L_5 and PA. (Figure A5.9). Additionally, ^1H NMR study (Figure A5.10) was also carried out, which revealed that the N-H proton's signal was downfield shifted ($\Delta\delta = 0.233$ ppm) along with a slight downfield shift of aromatic protons of L_5 upon addition of 1 Equiv. PA.^{5.45}



Scheme 5.2: Schematic representation of the proposed binding model for self-assembled L_5 and PA.

This kind of ^1H NMR signal pattern might be ascribed to the complexation possibility between L_5 and PA due to probable hydrogen bonding between N-H with phenolic -OH in PA, which was further verified by the DFT-optimised structure of L_5 -PA (Figure 5.4) where the shortest hydrogen bonding distance between these two moieties was found to be 3.23 Å and the average plane distance between L_5 and the benzene ring of PA was around 3.45 Å.^{5.46-5.47}

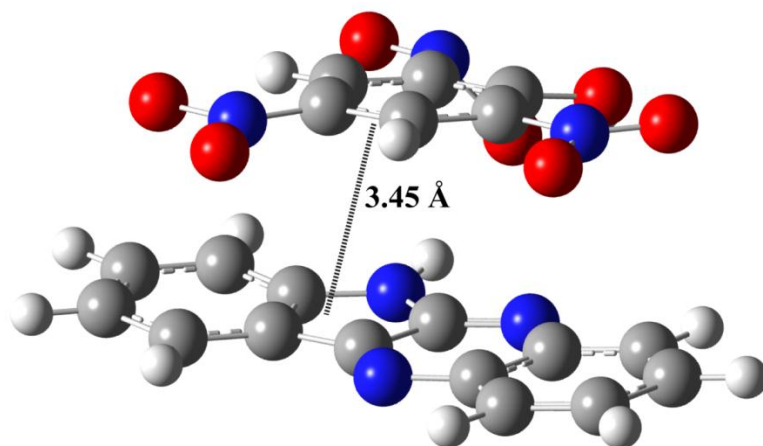


Figure 5.4: Optimized geometry of L_5 -PA ensemble.

5.4 Quenching Mechanism of PA Sensing

To investigate the fluorescence "turn-off" mechanism of L_5 with PA, density functional theory (DFT) calculations were accomplished with the B3LYP/6-31 G (d, p) method basis set using the Gaussian 09 program.^{5,48} The optimized geometry (Figure 5.4) and the highest occupied molecular orbital (HOMO), and the lowest unoccupied molecular orbital (LUMO) of L_5 and L_5 -PA complex are depicted in Figure 5.5. In general, when an electron-rich fluorophore interacts with an electron-deficient species, there will be facile photoinduced electron transfer (PET) from LUMO of the excited fluorophore to the LUMO of the NACs followed by reverse electron transfer to the HOMO of the probes in a non-radiative process leading to the extinction of the emission intensity of the fluorophore. Hence the DFT results confirmed that there is a probability of PET from L_5 LUMO (-0.07263 eV) to the PA LUMO (-0.16620 eV) (Figure 5.5a), which was also assisted by static quenching, i.e., the generation of non-fluorescent ground state complex as evident from the S-V plot.^{5,49} LUMO levels of 2,4-DNP (-0.13879 eV) and 4-NP (-0.02944 eV) are usually higher than LUMO of PA, resulting in lower efficiency of fluorescence quenching. In comparison to other nitro explosives such as 2-NP (-0.00913 eV), 3-NP (-0.00864 eV), and NB (-0.02452 eV), the PA LUMO energy level is the lowest; consequently, the effect of quenching was insignificant for them (Figure A5.11).^{5,50} The energy difference between the HOMO and LUMO of the L_5 -PA ensemble (0.13578 eV) dropped compared to that of L_5 (0.14309 eV), indicating that the complexation of L_5 -PA is energetically more favorable (Figure 5.5b). In addition to PET, small spectral overlap (Figure 5.5c) ensued between the emission spectra of self-assembled L_5 and UV-visible spectra of PA along with the variation in the fluorescence decay time of L_5 after the addition of PA (Figure 5.5d). So, it is plausible that FRET may account for fluorescence quenching to some extent and established the dynamic quenching mechanism too. As reported in previous publications,^{5,51} it is conspicuous

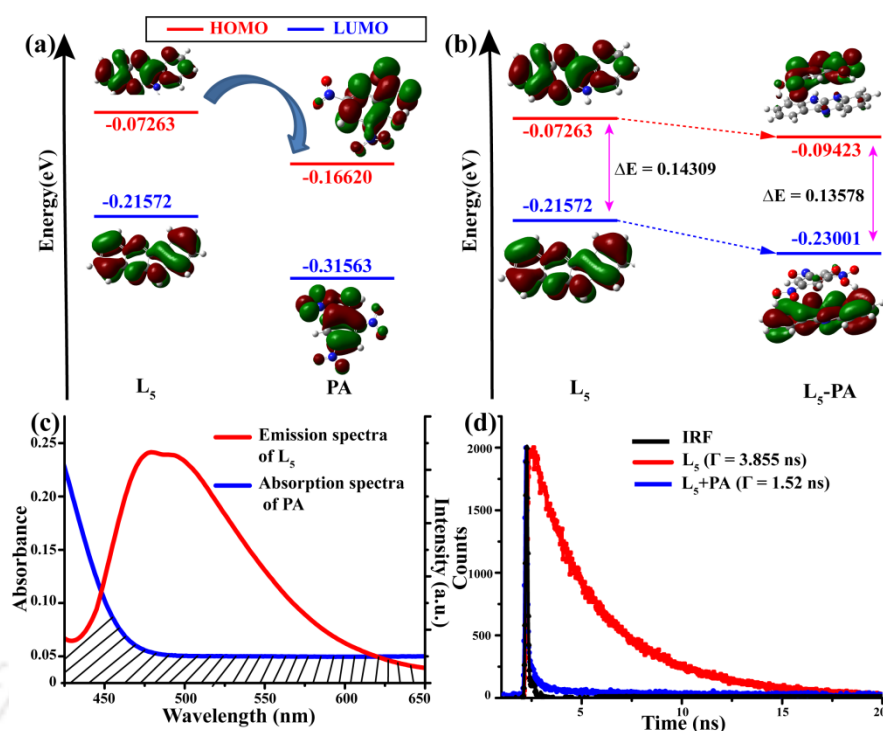


Figure 5.5: (a) Graphical representation of the suggested photoinduced electron transfer (PET) from LUMO of L_5 to LUMO of PA. (b) Relative energy levels (HOMO and LUMO) of L_5 and L_5 -PA. (c) Spectral overlap of the emission spectra of L_5 (red line) and the absorption spectra of PA (blue line) in the aqueous medium. (d) Time-resolved fluorescence spectra of L_5 (5.0 μ M) and in the presence of PA.

that self-aggregated L_5 displayed excellent selectivity and sensitivity towards PA due to concomitant occurrence of PET and FRET^{5,52} from the electron enriched L_5 to the electron-scarce PA, which resulted in the noteworthy "turn-off" luminescence emission among all NACs.

5.5 Detection of PA in natural water samples, soil samples, and bio-fluid samples

Following a military operation, water and soil pollution by PA is very common, and overexposure to PA (above 20 ppm) could be hazardous. To authenticate the suitability of L_5 it was pertinent to ascertain whether the probe could detect PA in groundwater samples in presence of common anions and metal ions. Lake water and river water specimens were brought from the Serpentine lake (IIT Guwahati Campus) and Brahmaputra river (near IIT Guwahati Campus). Tap water was available in the laboratory. These water samples were initially centrifuged at 10000 rpm for 5 min and then filtered using a 0.22 μ m membrane filter to separate any particulate matter. Subsequently, fluorescence spectroscopic studies with L_5 was carried out with these real water samples for detection of PA according to the previously reported literature.^{5,53} The fluorescence spectra of L_5 (5.0 μ M) displayed emission maxima at 484 nm in real water samples, and showed approximately similar quenching efficiency (Figure 5.6a) as that of distilled water when PA was added to the solution without any significant interference from

common ions. The results of the quantitative recovery of spiked specimens of analyte is shown in Table A5.2.

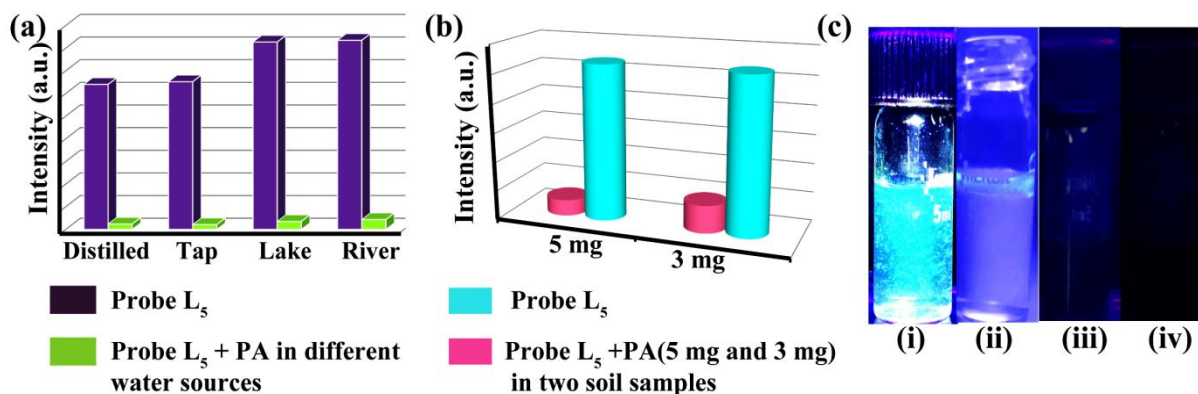


Figure 5.6: (a) Changes in emission intensity of L_5 (5.0 μ M) at 484 nm in the presence of excess PA in natural sources of water. (b) Emission spectra of L_5 for detecting PA in real soil specimens (5.0 mg and 3.0 mg). (c) The visual appearance of PA in soil samples under 365 nm UV illumination (i) Only L_5 (5.0 μ M) (ii) L_5 (5.0 μ M) with 50 mg of soil but devoid of PA (iii) L_5 (5.0 μ M) with 50 mg of soil with 3 mg and 5 mg of PA respectively.

For on-site practical implementation of L_5 for PA sensing, we also widened our investigation by using soil specimen.^{5,54} Soil samples were accumulated from IIT Guwahati campus garden. A 1.0 g sample of fine-grained crushed soil was taken in two separate petri dishes. Next, 5.0 mg and 3.0 mg of PA were combined with two different soil samples individually and blended thoroughly. The soil sample devoid of PA was considered as blank. Finally, 50 mg soil sample from each was added to the aqueous solution of L_5 (5.0 μ M), each solution was filtered, and fluorescence was recorded wherein similar quenching behavior was observed (Figure 5.6b). The sample containing L_5 and only soil without PA exhibited high fluorescence intensity (Figure 5.6c), suggesting the usefulness of the self-aggregated L_5 for excellent PA detection in the soil. Another practical utility of L_5 for detecting PA was explored by varying the pH, i.e., in three different simulated bio-fluid samples instead of water. Interestingly, the outcome revealed that L_5 was able to recognize PA in the simulated body fluid (pH~7.4), gastric fluid (pH ~2.0), and intestinal fluid (pH ~8.0) by rendering distinguishable "turn-off" fluorescence changes (Figure A5.12).

5.6 Contact mode estimation of PA

The contact mode analysis was executed by rubbing few crystals of PA on the right hand (nitrile gloved) and pressing onto a white paper. The paper was already coated with fine particles of L_5 .

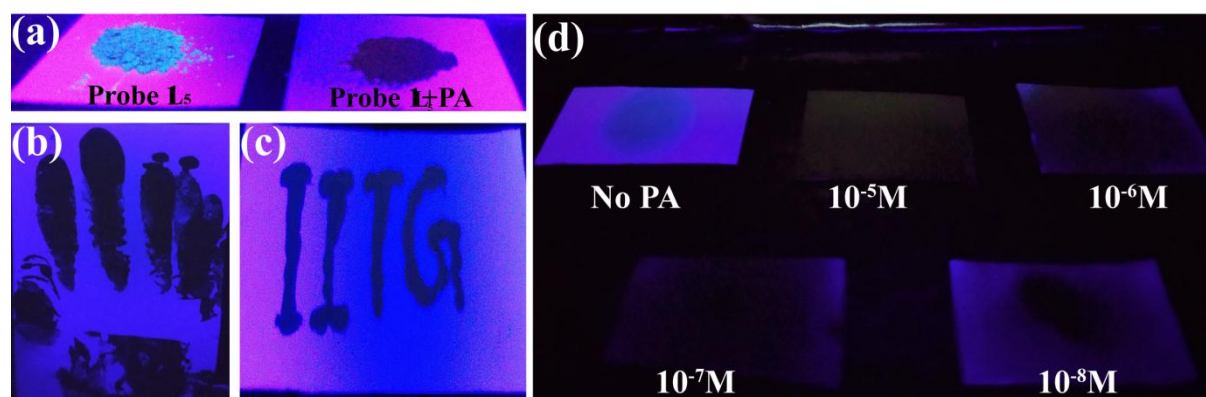


Figure 5.7: (a) Visual appearance of solid probe L_5 powder before and after addition of PA under 365 nm UV illumination. (b) Quenched luminescence of PA exposed handprint on probe L_5 coated white paper. (c) Photograph of quenched fluorescence on contact mode. (d) Visual detection of L_5 ($5 \mu\text{M}$) coated test strips before and after adding different PA concentrations under 365 nm light.

Finally, the paper was exposed to UV light to detect trace amount of PA. PA exposure was evident from the quenching of the emission when the samples were irradiated with the UV lamp (Figure 5.7a-c).

5.7 Paper-based detection of PA

Following solution-phase detection of PA successfully, our subsequent goal was to pursue contact mode detection of PA, which would render beneficial implications in forensic and analytical research. Whatman filter paper (Whatman 42) was immersed into the solution of probe L_5 ($5 \times 10^{-6} \text{ M}$) in DMSO and allowed to dry at room temperature. When the solvent evaporated completely, the L_5 coated filter paper was cut into small portable test strips ($2.0 \text{ cm} \times 1.0 \text{ cm}$) and then used for rapid on-site estimation of PA. A small amount of freshly prepared PA solution ($10^{-5} - 10^{-8} \text{ M}$) was applied to the test strips, and a dark spot appeared in every case after visualizing under a hand-held 365 nm UV light (Figure 5.7d). According to the previously reported methods,^{5,55} in order to determine the minimum detection limit of L_5 solution soaked test strips, $10 \mu\text{L}$ volume from 10^{-8} M stock PA solution (22.9 pg PA) was applied on the test strips, which covered a surface area of about 1 cm^2 . The detection limit for these paper strips was 22.9 pg cm^{-2} for naked eye PA recognition. The initial fluorescence intensity of L_5 as well as L_5 -PA ensemble was found to be retained as a function of increasing exposure time (Figure 5.8a). To investigate the reusability of the L_5 coated paper strips, the strips were washed with distilled water and dried in oven. Emission intensity of the washed and dried strips were recorded and the whole process was repeated three times (Figure 5.8b). Therefore, these experiments and images demonstrate the utility and sensitivity of L_5 coated paper strips for instant and repeated visual detection of trace amount of PA.

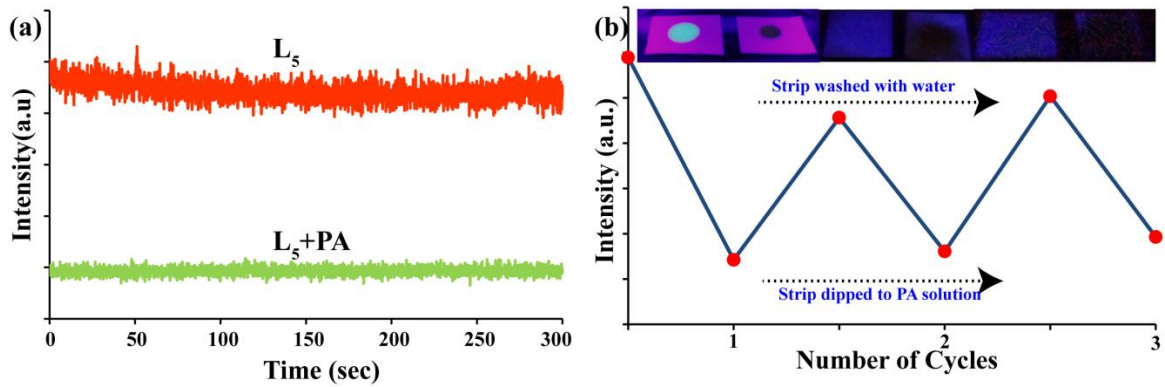


Figure 5.8: (a) Change in fluorescence intensity of L_5 and L_5 -PA by varying exposure time. (b) Reusability test of L_5 .

5.8 Live cell imaging for detection of PA

Based on the positive results obtained in solution and filter strip-based PA detection, it was envisaged that L_5 could be leveraged in fluorescence-based live cell imaging studies for the detection of intracellular PA. In order to pursue this objective, it was critical to initially ascertain the cytotoxic potential of L_5 . An *in vitro* MTT assay revealed that L_5 , L_5 -PA complex (1:1 complex) as well as PA alone used at a concentration ranging from 2.5 μM – 10 μM was not detrimental to the viability of HeLa cells (cell viability in excess of 80%) (Figure A5.13), which indicated that L_5 as well as L_5 -PA complex was essentially non-toxic at these tested concentrations. This finding was encouraging and it

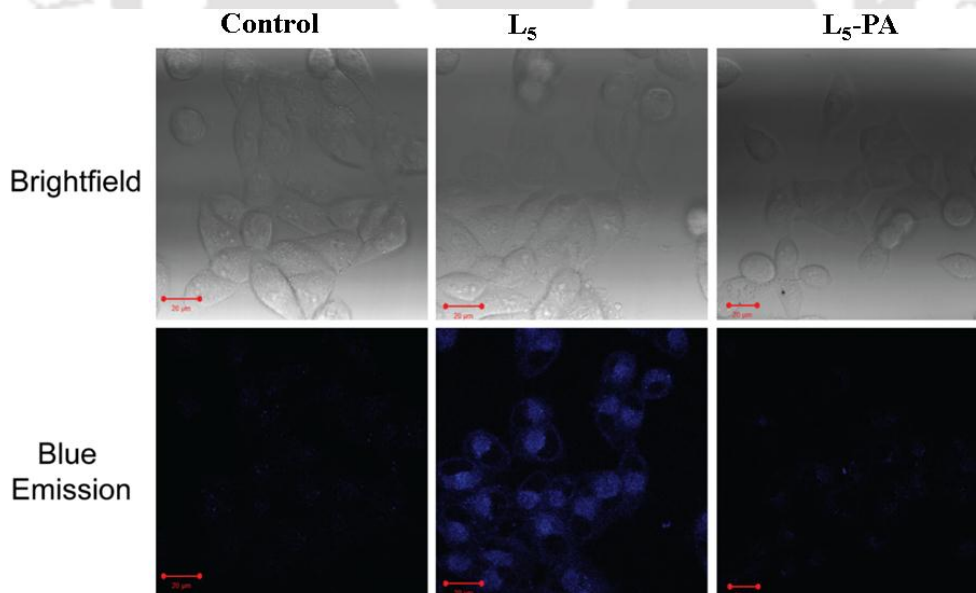


Figure 5.9: Confocal microscope-based fluorescence images of HeLa cells treated with 10 μM of L_5 alone and HeLa cells pre-treated with 10 μM of L_5 followed by addition of 10 μM PA solution. Scale bar for the images is 20 μm .

motivated us to ascertain the prospect of **L**₅ in detecting intracellular PA by fluorescence-based cell imaging. In this context, HeLa cells alone failed to exhibit any fluorescence (Figure 5.9, control panel), whereas a bright blue fluorescence emission was associated with HeLa cells incubated with **L**₅ when visualized under UV excitation (Figure 5.9, ligand panel). It may be mentioned here that the localization of the blue fluorescence emission in HeLa cells incubated with **L**₅ appeared to be cytoplasmic in nature. Interestingly, when HeLa cells were pre-treated with **L**₅ and then incubated with PA, a dramatic quenching of the intracellular fluorescence was observed (Figure 5.9, ligand-PA panel). It was also noted that the distinctive morphology of HeLa cells was retained during the imaging studies, which substantiated the non-toxic nature of **L**₅ and its suitability in detecting intracellular PA.

5.9 Conclusions

In summary, we report the synthesis of a small quinoxaline-based **L**₅ for effective and selective fluorescence-based detection of PA over other NACs in aqueous solution, natural water samples, solid and paper-based systems. Due to π - π stacking interaction, **L**₅ spontaneously self-assembled in an aqueous solution to leaf-like aggregates, which was disrupted to smaller round-shaped aggregates in presence of PA. FESEM study, fluorescence microscopic analysis along with DLS investigation corroborated the aggregation-disaggregation process. Based on the experimental evidence, disaggregation of the self-assembled sensor, and PET, FRET is concomitantly responsible for the discriminative detection of PA in water with high selectivity and sensitivity. Self-aggregated **L**₅ manifested high selectivity and good sensitivity towards PA as the K_{SV} was $22.6 \times 10^6 \text{ M}^{-1}$ and LOD was ~ 56 ppb. Paper-based detection for PA was achieved at the picogram level, enabling rapid and real on-site detection. The developed probe could also be employed in imaging studies for non-invasive fluorescence-based sensing of PA in live HeLa cells. Based on its non-toxic nature, it is envisaged that the probe can bear interesting prospect in future as a non-destructive imaging handle for PA detection in *in vivo* cellular system.

References

- 5.1 M. E. Germain and M. J. Knapp, *Chemical Society Reviews*, 2009, **38**, 2543–2555.
- 5.2 Y. J. Li, Y. F. Zhang, Y. M. Zhang, Z. H. Wang, H. L. Yang, H. Yao, T. B. Wei and Q. Lin, *Dyes and Pigments*, 2020, **181**, 108563.
- 5.3 J. Yinon, *Counterterrorist detection techniques of explosives*, Elsevier B.V., 2007.
- 5.4 L. Murray, *Federal Register*, 2010, **75** (229), 73935–74604.
- 5.5 S. Madhu, A. Bandela and M. Ravikanth, *RSC Advances*, 2014, **4**, 7120–7123.

- 5.6 J. Akhavan, *The Chemistry of Explosives*, Royal Society of Chemistry, 2011.
- 5.7 K. Acharyya and P. S. Mukherjee, *Chem. Commun.*, 2014, **50**, 15788-15791.
- 5.8 Y. Xu, B. Li, W. Li, J. Zhao, S. Sun and Y. Pang, *Chem. Commun.*, 2013, **49**, 4764-4766.
- 5.9 B. Roy, A. K. Bar, B. Gole and P. S. Mukherjee, *J. Org. Chem.*, 2013, **78**, 1306-1310.
- 5.10 R. Guo, T. Jiao, R. Li, Y. Chen, W. Guo, L. Zhang, J. Zhou, Q. Zhang and Q. Peng, *ACS Sustainable Chem. Eng.*, 2018, **6**, 1279-1288.
- 5.11 R. Geng, R. Chang, Q. Zou, G. Shen, T. Jiao and X. Yan, *Small*, 2021, **17**, 2008114.
- 5.12 V. Venkatramaiah, S. Kumar and S. Patil, *Chem. Commun.*, 2012, **48**, 5007-5009.
- 5.13 W. Xie, S. R. Zhang, D. Y. Du, J. S. Qin, S. J. Bao, J. Li, Z. M. Su, W. W. He, Q. Fu and Y. Q. Lan, *Inorg. Chem.*, 2015, **54**, 3290-3296.
- 5.14 Y. Peng, A. J. Zhang, M. Dong and Y. W. Wang, *Chem. Commun.*, 2011, **47**, 4505-4507.
- 5.15 Y. Yao, M. Xue, J. Chen, M. Zhang and F. Huang, *J. Am. Chem. Soc.*, 2012, **134**, 15712-15715.
- 5.16 L. R. Adil, P. Gopikrishna and P. Krishnan Iyer, *ACS Appl. Mater. Interfaces*, 2018, **10**, 27260-27268.
- 5.17 Environmental Protection Agency, innovative treatment technologies: Annual status report, 8th edn, 1996, EPA-542- R-96-010.
- 5.18 K. M. Wollin and H. H. Dieter, *Arch. Environ. Contam. Toxicol.*, 2005, **49**, 18-26.
- 5.19 S. Hussain, A. H. Malik, M. A. Afroz and P. K. Iyer, *Chem. Commun.*, 2015, **51**, 7207-7210.
- 5.20 M. E. Walsh, *Talanta*, 2001, **54**, 427-438.
- 5.21 C. Qian, R. Wang, M. Li, X. Li, B. Ge, Z. Bai and T. Jiao, *Colloids and Surfaces A*, 2021, **608**, 125616.
- 5.22 C. Byram, S. S. B. Moram, A. K. Shaik and V. R. Soma, *Chem. Phys. Lett.*, 2017, **685**, 103-107.
- 5.23 G. Vourvopoulos and P. C. Womble, *Talanta*, 2001, **54**, 459-468.
- 5.24 A. Hakonen, F. Wang, P. O. Andersson, H. Wingfors, T. Rindzevicius, M. S. Schmidt, V. R. Soma, S. Xu, Y. Li, A. Boisen and H. Wu, *ACS Sensors*, 2017, **2**, 198-202.
- 5.25 R. Wang, X. Yan, B. Ge, J. Zhou, M. Wang, L. Zhang and T. Jiao, *ACS Sustainable Chem. Eng.*, 2020, **8**, 4521-4536.
- 5.26 K. E. Brown, M. T. Greenfield, S. D. McGrane and D. S. Moore, *Anal. Bioanal. Chem.*, 2016, **408**, 49-65.
- 5.27 S. Sharma, G. Dubey, B. S. Sran, P. V. Bharatam and G. Hundal, *ACS Omega*, 2019, **4**, 18520-18529.
- 5.28 L. Wang, M. Cui, H. Tang, D. Cao, *Dyes and Pigments* 2018, **155**, 107-113.
- 5.29 K. Balakrishnan, A. Datar, W. Zhang, X. Yang, T. Naddo, J. Huang, Zuo, J.; M. Yen, J. S. Moore and L. Zang, *J. Am. Chem. Soc.*, 2006, **128**, 6576-6577.
- 5.30 T. Liu, L. Ding, K. Zhao, W. Wang and Y. Fang, *J. Mater. Chem.*, 2012, **22**, 1069-1077.
- 5.31 V. Bhalla, A. Gupta, M. Kumar, D. S. S. Rao and S. K. Prasad, *ACS Appl. Mater. Interfaces*, 2013, **5**, 672-679.
- 5.32 H. H. Lin,; Y. C. Chan, J. W. Chen and C. C. Chang, *J. Mater. Chem.*, 2011, **21**, 3170-3177.
- 5.33 K. Itami, Y. Ohashi and J. I. Yoshida, *J. Org. Chem.*, 2005, **70**, 2778-2792.

- 5.34 B. K. An, S. K. Kwon, S. D. Jung and S. Y. Park, *J. Am. Chem. Soc.*, 2002, **124**, 14410–14415.
- 5.35 R. Dowlatabadi, A. Khalaj, S. Rahimian, M. Montazeri, M. Amini, A. Shahverdi and E. Mahjub, *Synthetic Communications*, 2011, **41**, 1650–1658.
- 5.36 L. Marin, L. Lutsen, D. Vanderzande and W. Maes, *Org. Biomol. Chem.*, 2013, **11**, 5866–5876.
- 5.37 J. Zhao, S. Ji, Y. Chen, H. Guo and P. Yang, *Phys. Chem. Chem. Phys.*, 2012, **14**, 8803–8817.
- 5.38 S. Mukherjee, A. V. Desai, A. I. Inamdar, B. Manna and S. K. Ghosh, *Cryst. Growth Des.*, 2015, **15**, 3493–3497.
- 5.39 A. S. Shetty, J. Zhang and J. S. Moore, *J. Am. Chem. Soc.*, 1996, **118**, 1019–1027.
- 5.40 L. I. Markova, V. L. Malinovskii, L. D. Patsenker and R. Häner, *Chem. Commun.*, 2013, **49**, 5298–5300.
- 5.41 G. Das, B. P. Biswal, S. Kandambeth, V. Venkatesh, G. Kaur, M. Addicoat, T. Heine, S. Verma, R. Banerjee, *Chem. Sci.* 2015, **6**, 3931–3939.
- 5.42 B. Pramanik, N. Singha and D. Das, *ACS Appl. Polym. Mater.*, 2019, **1**, 833–843.
- 5.43 J. Liu, Y. Zhong, P. Lu, Y. Hong, J. W. Y. Lam, M. Faisal, Y. Yu, K. S. Wong and B. Z. Tang, *Polym. Chem.*, 2010, **1**, 426–429.
- 5.44 O. Pinrat, K. Boonkitpatarakul, W. Paisuwan, M. Sukwattanasinitt and A. Ajavakom, *Analyst*, 2015, **140**, 1886–1893.
- 5.45 C. Pherkkhantod, V. Ervithayasuporn, S. Chanmungkalakul, C. Wang, X. Liu, D. J. Harding and S. Kiatkamjornwong, *Sensors and Actuators B: Chemical*, 2021, **330**, 129287.
- 5.46 C. Vijayakumar, G. Tobin, W. Schmitt, M. J. Kim and M. Takeuchi, *Chem. Commun.*, 2010, **46**, 874–876.
- 5.47 K. Jiang, S. H. Luo, C. M. Pang, B. W. Wang, H. Q. Wu and Z. Y. Wang, *Dyes and Pigments*, 2019, **162**, 367–376.
- 5.48 A. Shylaja, S. R. Rubina, S. S. Roja and R. R. Kumar, *Dyes and Pigments*, 2020, **174**, 108062.
- 5.49 M. Fisch, G. Trucks, H. Schlegel, G. Scuseria, M. Robb, J. Cheeseman, G. Scalmani, V. Barone, B. Mennucci, G. Petersson, Gaussian 09 (Revision A. 02), Wallingford, CT, 2009.
- 5.50 N. Meher and P. K. Iyer, *Nanoscale*, 2017, **9**, 7674–7685.
- 5.51 R. Martínez-Máñez and F. Sancenón, *Chem. Rev.*, 2003, **103**, 4419–4476.
- 5.52 K. K. Kartha, S. S. Babu, S. Srinivasan and A. Ajayaghosh, *J. Am. Chem. Soc.*, 2012, **134**, 4834–4841.
- 5.53 A. H. Malik, S. Hussain, A. Kalita and P. K. Iyer, *ACS. Appl. Mater. Interfaces*, 2015, **7**, 26968–26976.
- 5.54 S. Kumari, S. Joshi, T. C. Cordova-Sintjago, D. D. Pant and R. Sakhuja, *Sensors and Actuators B: Chemical*, 2016, **229**, 599–608.
- 5.55 S. Kaja, D. P. Damera and A. Nag, *Analytica Chimica Acta*, 2020, **1129**, 12–23.
- 5.56 J. F. Xiong, J. X. Li, G. Z. Mo, J. P. Huo, J. Y. Liu, X. Y. Chen and Z. Y. Wang, *J. Org. Chem.*, 2014, **79**, 11619–11630.

Appendix - Chapter 5

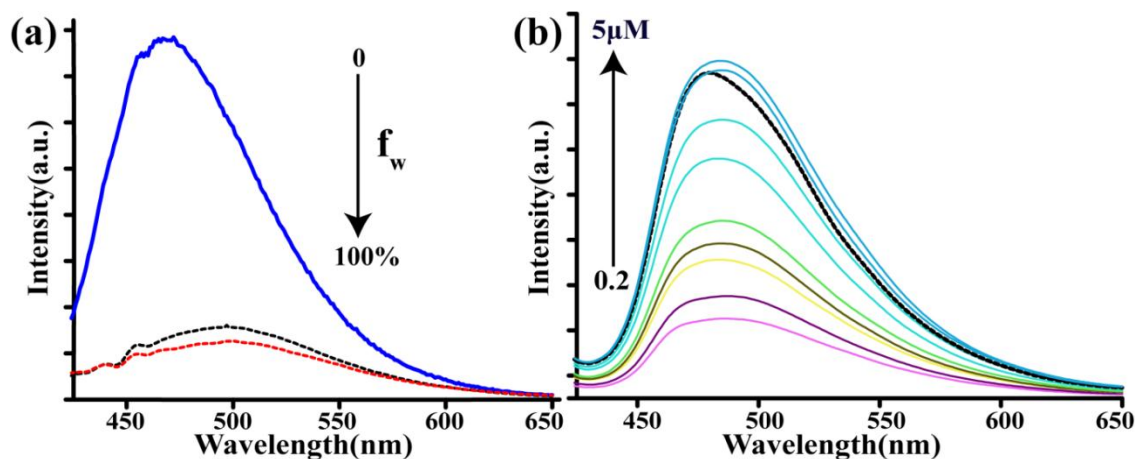


Figure A5.1: (a) Fluorescence emission spectra of L_5 with increasing water content in acetonitrile solution ($\lambda_{\text{ex}} = 400 \text{ nm}$, slit = 3nm / 3nm). (b) Concentration-dependent fluorescence emission spectra of L_5 in aqueous medium.

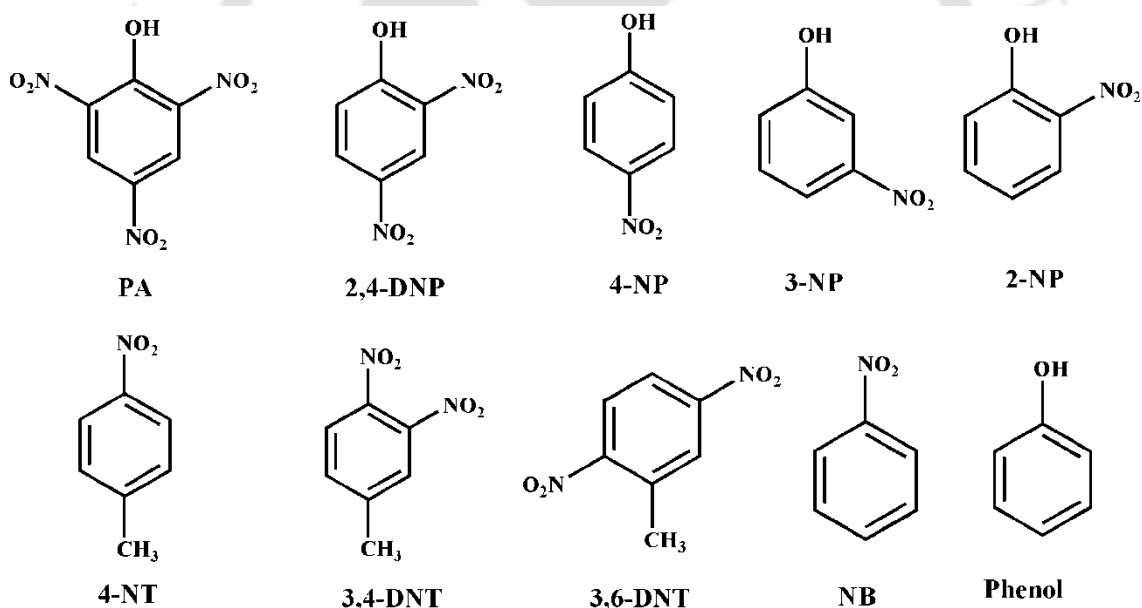


Figure A5.2: Chemical structures of different nitro aromatic compounds (NACs) and non-nitro compounds used in our study.

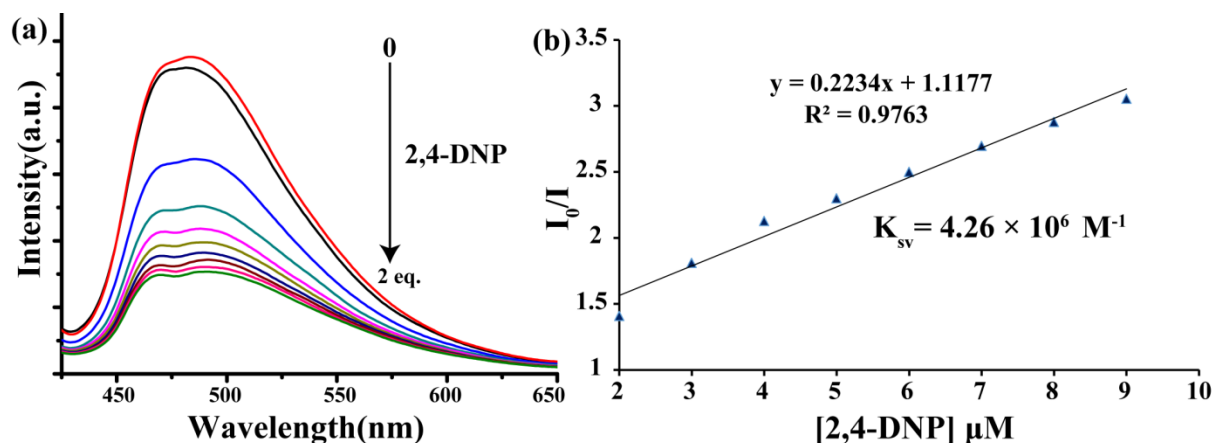


Figure A5.3: (a) Change in fluorescence spectra of L_5 (5.0 μM) upon addition of 2,4-DNP. (b) Stern-Volmer I_0/I vs [2,4-DNP].

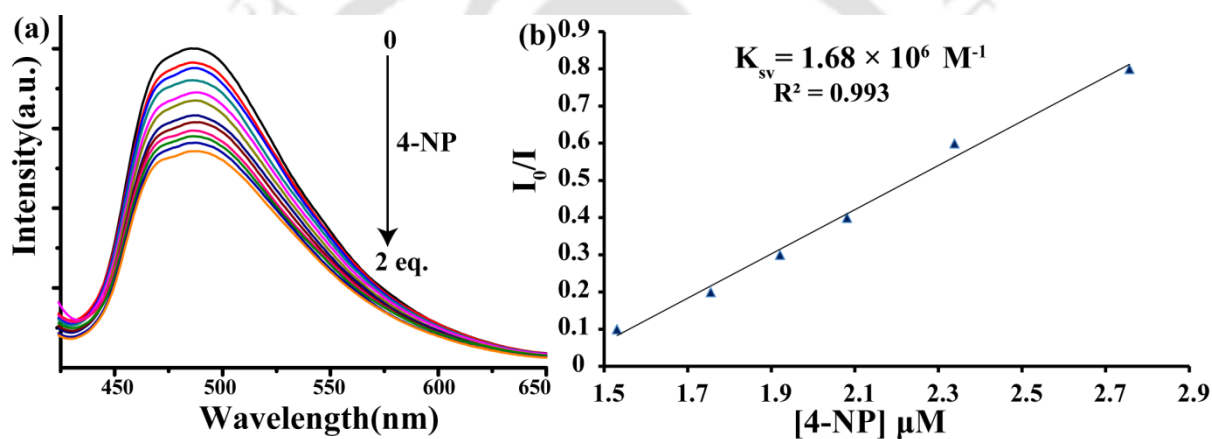


Figure A5.4: (a) Change in fluorescence spectra of L_5 (5.0 μM) upon addition of 4-NP. (b) Stern-Volmer I_0/I vs [4-NP].

Table A5.1: Fluorescence lifetime values of L_5 (5 μM) and L_5 -PA in aqueous medium.

Sample	B_1	ΔB_1	B_2	ΔB_2	a_1	Δa_1	a_2	Δa_2	τ_1	$\Delta \tau_1$	τ_2	$\Delta \tau_2$	$\langle \tau \rangle$ (ns)	χ^2
L_5	0.1042	0.0349	0.0985	0.0149	0.3218	0.10	0.6781	0.1026	2.104	0.010	4.687	0.002	3.8553	1.030
L_5 +PA	0.1033	0.0176	0.0053	0.0001	0.5016	0.085	0.4983	0.01017	0.150	0	2.90	0	1.5201	1.065

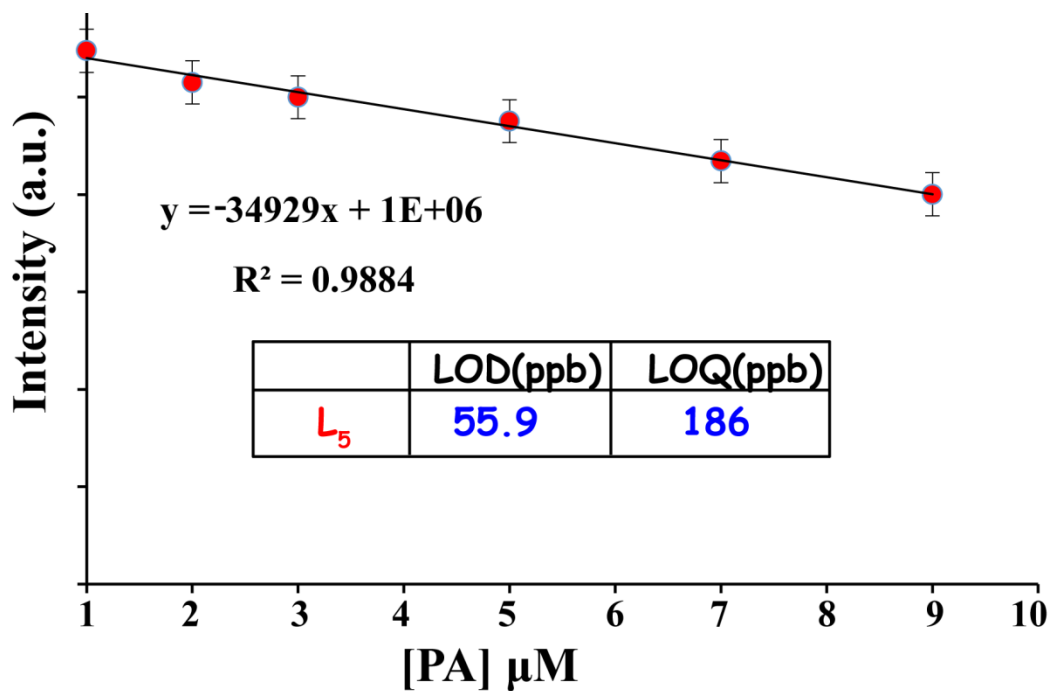


Figure A5.5: Fluorescence emission intensity of L_5 at 484 nm vs. PA concentration to calculate the limit of detection (LOD) and limit of quantification (LOQ).

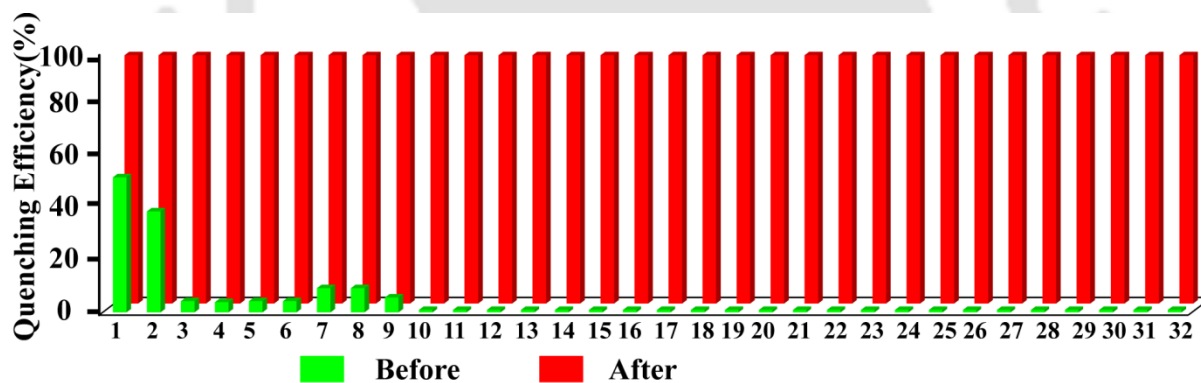


Figure A5.6: Fluorescence response of L_5 (5.0 μ M) to various analytes (1= 2,4-DNP, 2= 4-NP, 3= 2-NP, 4= 3-NP, 5= 4-NT, 6= NB, 7= 3,4-DNT, 8= 3,6-DNT, 9= phenol, 10= Fe^{3+} , 11= Al^{3+} , 12= Cr^{3+} , 13= Hg^{2+} , 14= Cd^{2+} , 15= Pb^{2+} , 16= Cu^{2+} , 17= Co^{2+} , 18= Ni^{2+} , 19= Zn^{2+} , 20= Ca^{2+} , 21= Mg^{2+} , 22= PO_4^{3-} , 23= Cl^- , 24= I^- , 25= $H_2PO_4^-$, 26= HSO_4^- , 27= NO_3^- , 28= OH^- , 29= HSO_3^- , 30= HCO_3^- , 31= SH^- , 32= oxalate²⁻) before (green bars) and after (red bars) addition of PA.

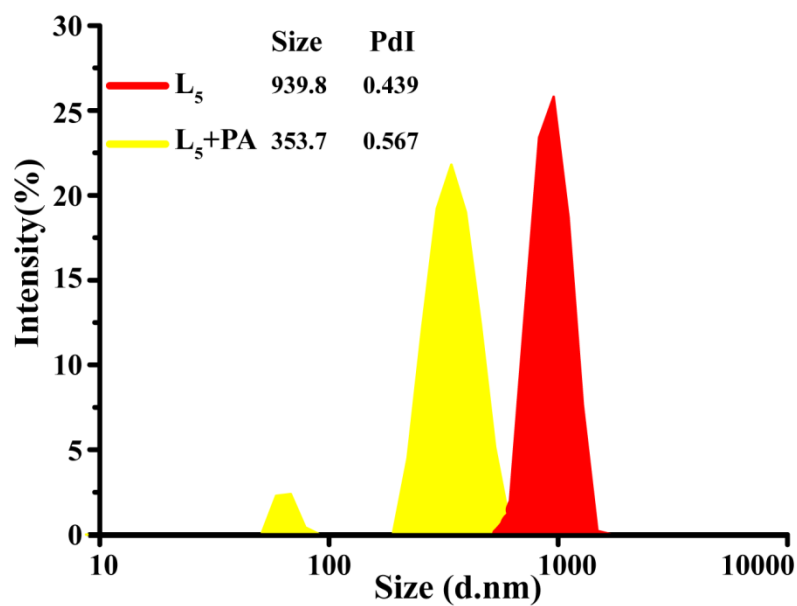


Figure A5.7: DLS analysis of L_5 (5.0 μM) and $L_5 + PA$ in aqueous medium.

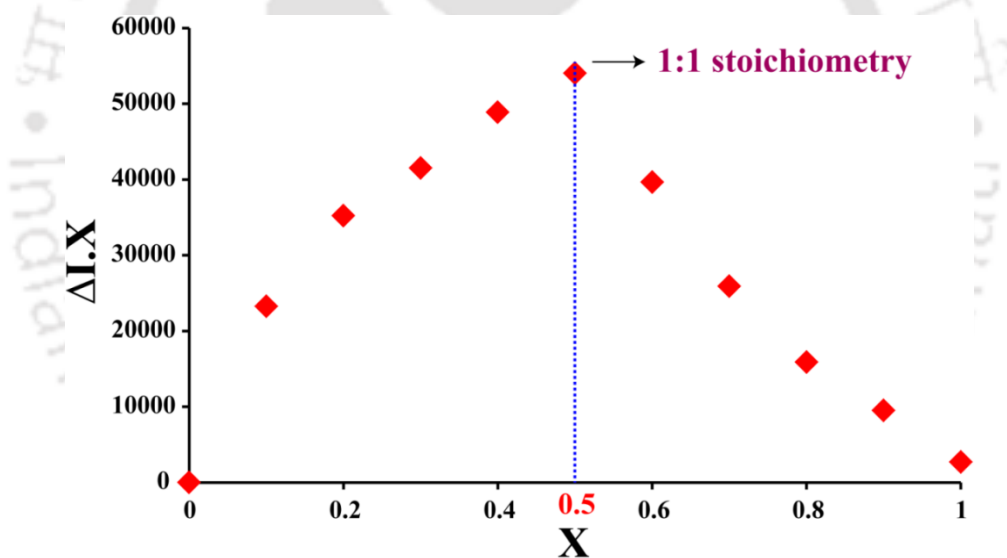


Figure A5.8: Job's plot for the determination of binding stoichiometry between L_5 and PA in 100% solution ($\lambda_{\text{ex}} = 400 \text{ nm}$).

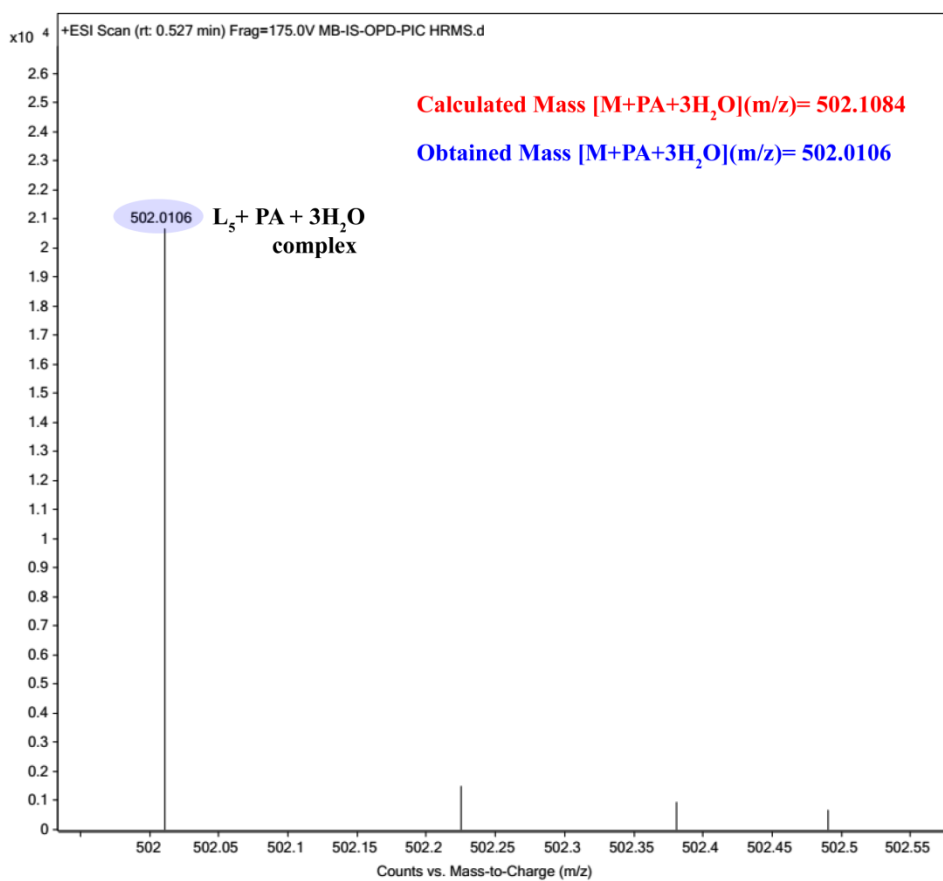


Figure A5.9: HRMS spectra of L_5 in 1:1 water-acetonitrile in the presence of PA in positive ionization mode.

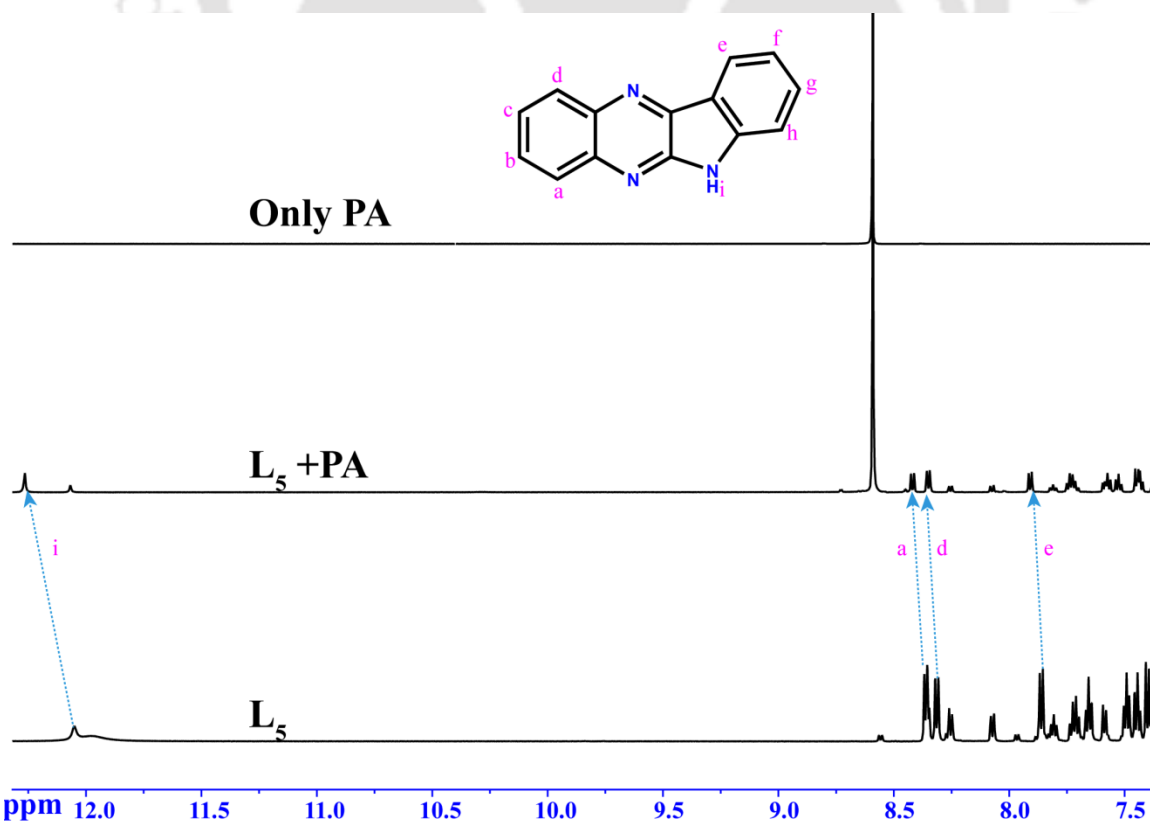


Figure A5.10: 1H NMR spectral changes of L_5 in DMSO- d_6 upon addition of 1 equiv. PA.

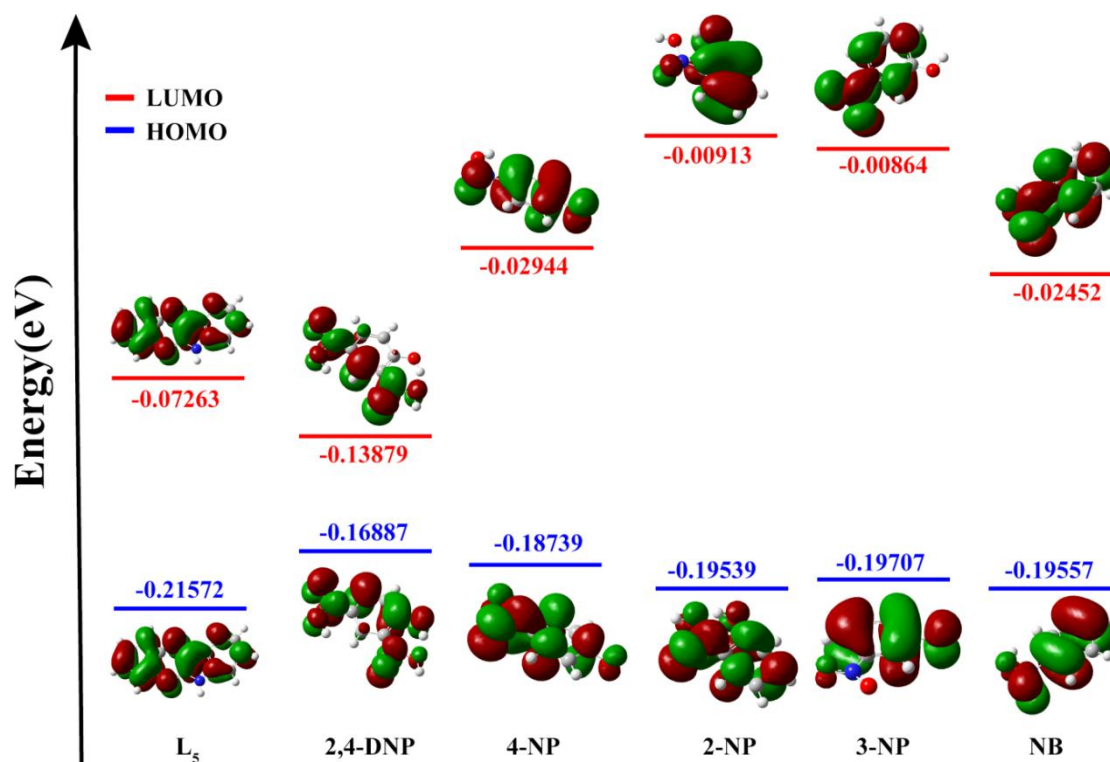


Figure A5.11: DFT calculated HOMO-LUMO energy profiles of L_5 , 2,4- DNP, 4- NP, 2- NP, 3- NP and NB.

Table A5.2: Detection of PA in natural water samples.

sample	Added (μM)	Detected (μM)	Recovery (%)
Tap water	5.0	4.44	93.9
Lake water	5.0	4.25	85
River water	5.0	5.26	105

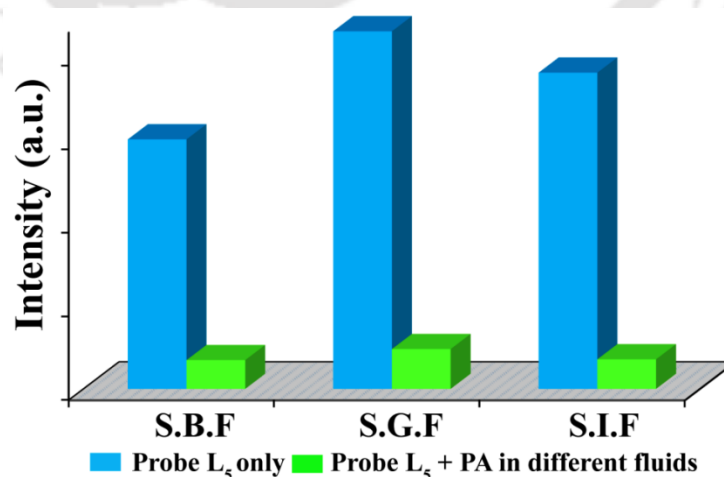


Figure A5.12: Changes in the emission intensity of L_5 ($5.0 \mu\text{M}$) at 484 nm in the presence of excess PA in simulated fluid samples. [S.B.F- Simulated Body Fluid (pH~7.4), S.G.F- Simulated Gastric Fluid (pH~2.0) and S.I.F- Simulated Intestinal Fluid (pH~8.0)].

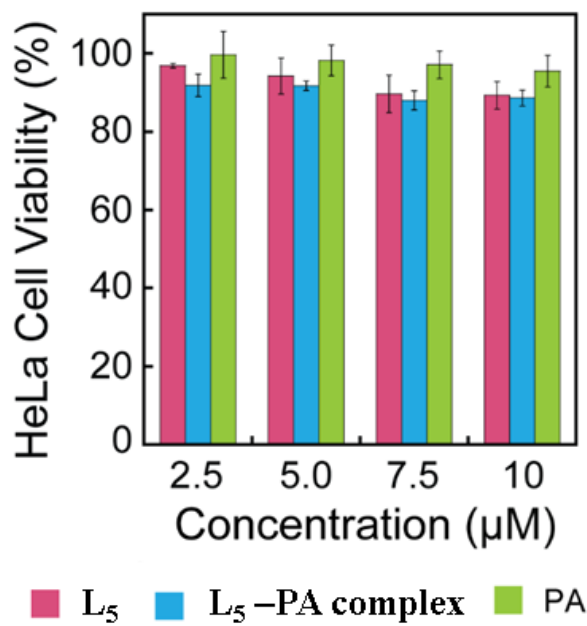


Figure A5.13: MTT assay-based evaluation of the cytotoxic potential of L₅, L₅-PA complex and PA alone against HeLa cells. Each data point represent mean \pm standard deviation from six samples.

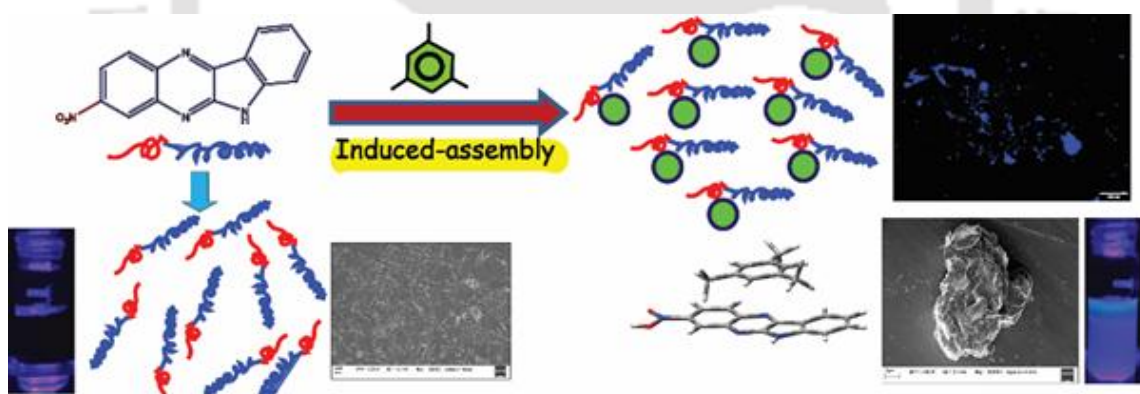
Table A5.3: A comparative study of K_{sv} values and the detection limits achieved till now along with the receptor and solvent system used for the detection of PA.

SI No.	References	Receptor	Solvent System	LOD(ppb)	$K_{sv}(M^{-1})$
1.	Present work	Self-assembled Quinoxaline derivative	100% Aqueous medium	55.9	22.6×10^6
2.	Sensors and Actuators: B. Chemical., 2021, 330 129287	Polyaromatic-based imidazolium	Aqueous medium	1145.5 (5 μ M)	9.57×10^6
3.	Anal. Chem., 2019, 91, 13675-13680	BODIPY probe	Acetonitrile/water (8:2) mixture	100 (0.44 μ M)	Not reported
4.	Spectrochimica Acta Part A: Molecular and Biomolecular Spectroscopy, 2019, 223, 117201	Coumarin based probe	Acetonitrile/water (1:9) mixture	2176.5 (9.5 μ M)	2.21×10^5
5.	Dyes and Pigments, 2020, 181, 108563	Tripodal naphthalimide derivative	DMF/H ₂ O (1 : 9, v/v) solution	10.83	73.6×10^3
6.	Sensors and Actuators B, 2017, 250, 215–223	Lanthanide complexes	Aqueous medium	114.5 (0.5 μ M)	8.553×10^4
7.	J. Am. Chem. Soc. 2017, 139, 2421-2427	Conjugated Covalent Organic Frameworks	Dichloromethane	Not reported	Not reported
8.	J. Am. Chem. Soc., 2016, 138, 3302–3305	Pyrene-based self-assembly	DMF	Not reported	3.1×10^4
9.	J. Fluoresc. 2016, 26, 395-401	Perylene diimide derivatives	DMF	229.1	Not reported
10.	RSC Adv. 2016, 6, 84319-84325	Arcriidine derivatives	MeOH	549.84	1.8×10^4



CHAPTER 6

Nitro substituted Quinoxaline framework: Benzene group of VOC triggered self-assembly and selective Turn-on detection in water

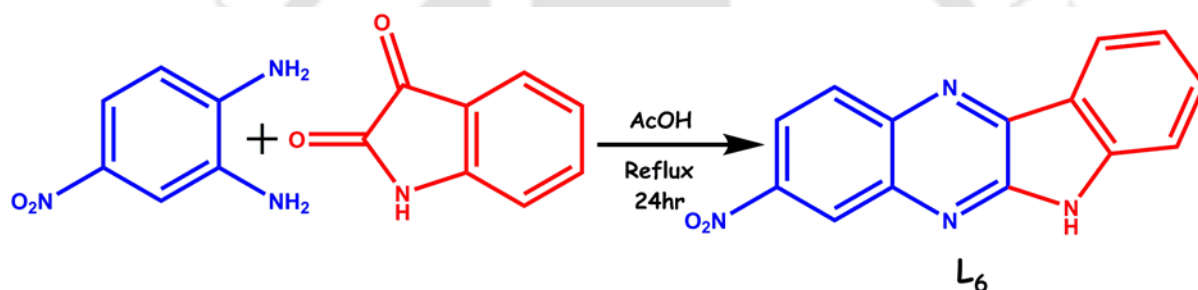


6.1 Background and focus of the chapter

Over the last few years, numerous research groups have been looking over the invention of chemosensors for the recognition of volatile organic compounds (VOCs). VOCs are harmful mutagenic carbon-based compounds categorized according to their boiling point (extending from 50°C to 260°C) and retention time.^{6.1} Volatile organic compounds are predominantly generated from anthropogenic activities such as industrial sources, fuel, biomass combustion, household activities, vehicular exhausts, followed by natural biogenic emissions. Subsequently dispersed into the environment polluting air, soil, and water bodies surface.^{6.2-6.3} Exposure to VOCs can give rise to various physiological disorders such as irritations of the eyes, nose, throat, asthma, nausea, neurological problems, and dementia, while persistent damage of various internal organs such as the liver, kidney, and central nervous system.^{6.4} Different VOCs have been associated with profuse disorders, including cancer,^{6.5} one of the prime causes of death in the world. Previously documented studies have also revealed that cancerous cells *in vitro* ingest specific VOCs that can perform as potential biomarkers differentiating malignant cells from benign cells.^{6.6} Hence, researchers must establish an accurate technique and proper protocol for selective detection of VOCs in ambient conditions.

Myriad conventional analytical techniques, e.g., gas chromatography-mass spectrometry,^{6.7} field-effect transistors,^{6.8} two-dimensional gas chromatography-quadrupole mass spectrometry,^{6.9} quartz crystal microbalances,^{6.10} electrochemical resistors,^{6.11-6.12} etc. are well exploited so far to distinguish various forms of VOCs. Nevertheless, all these traditional techniques need extravagant instrumentation, which is a cumbersome and tedious task and they require trained personnel to employ. Furthermore, these typical approaches are practically impossible to opt for large-scale and on-field monitoring of VOCs. To bridge the gap, the fabrication of cost-effective luminescence sensors for discriminative sensing of various harmful VOCs is a desirable area of research due to fast-response, efficient portability, high selectivity, and sensitivity.^{6.13} In recent years fluorescent chemosensors have been prospered extensively in supramolecular chemistry to analyze biologically and environmentally relevant and harmful species. However, most of them recognize the analyte in an organic solvent.

Furthermore, benzene and methyl-substituted benzene derivatives generated pollution gives rise to a severe warning as these hydrocarbon derivatives are highly impervious to degrade. In the absence of competent bacteria that can degrade them, these toxic xenobiotics can accumulate in massive amounts in environmental groundwaters.^{6,14} These toxic xenobiotics can contact the wetlands and groundwater due to straining from underground storage tanks and hazardous waste dumps. In April 2014, in Lanzhou, China, benzene spillage had provoked a catastrophe, where groundwater got contaminated; as a result, more than 2.4 million people were affected severely. Moreover, these hydrocarbons are devoid of active functional groups, making their direct recognition methods arduous to execute. Therefore, a significant effort is required to manufacture new novel sensors that pronounce a selective response towards the benzene group of VOCs such as xylenes, toluene, mesitylene, benzene, etc., in an aqueous medium.



Scheme 6.1: Synthesis of the probe L_6 .

In light of the potential as mentioned above, herein, we have chosen one widely studied π -conjugated quinoxaline scaffold but highly scarce in the progress of fabricating sensitive fluorescence detection of electronically enriched benzene derived VOCs. To the best of our knowledge, this is the first report where electron-deficient quinoxaline derivative has been exploited as a sensor to detect mesitylene amidst all benzene-based VOCs in an aqueous medium via “Turn-On” mode. Another beneficial design method is introducing electron-withdrawing $-\text{NO}_2$ group into quinoxaline framework to form D-A type ensemble (Scheme 6.1), which can elevate charge transfer and inflate the sensitivity. We also demonstrated that the possible complexation between the probe and mesitylene endorsed by the mesitylene triggered assembly of probe molecules from fibril-network-like morphology to higher-order stone-shaped morphology and consequent fluorescence response.

6.2 Photophysical studies

The photophysical investigation of **L**₆ was pursued in certain polar aprotic and polar protic solvents by UV-Visible and fluorescence spectroscopic study at room temperature. For these spectral analyses, a 1.0 mM stock solution of **L**₆ was prepared in dimethylsulfoxide (DMSO) and diluted accordingly with the experimental solutions. **L**₆ displayed an absorption band at 287 nm and a broad peak at 364 nm (Figure A6.1a) in acetonitrile which may be attributed to the π - π^* electronic transitions quinoxaline moiety.^{6.15} In an aqueous medium, the absorption maxima were slightly right-shifted to 288 and 370 nm, followed by levelling off the tails beyond 420 nm, probably due to nano-aggregates generation in the solution.^{6.16} The photoluminescence spectra were recorded by differing amounts of poor solvent (water) to a solution of **L**₆ in acetonitrile (Figure A6.1b). The fluorescence spectrum of **L**₆ in acetonitrile gave emission maxima at 453 nm while enhancing the amount of water to 100%; the emission maxima was red-shifted to 463 nm.

6.3 Sensing response towards VOCs in water

To investigate the sensory performance of the electron-deficient probe (2 μ M) in an aqueous medium at room temperature, several VOCs such as mesitylene, o-xylene, p-xylene, m-xylene, toluene, benzene, acetone, tetrahydrofuran (THF), dimethylsulfoxide (DMSO), dichloromethane (DCM), dimethylformamide (DMF), hexane (Figure A6.2) was tested. It is interesting to note that the photoluminescence response of **L**₆ varied notably only upon inclusion of 50 equivalent of mesitylene and to some extent for o-xylene amidst different VOCs. The spectral outcome revealed that the initial emission maxima of **L**₆ in an aqueous medium at 463 nm switched to three emission maxima at about 456 nm, 481 nm, and 508 nm, followed by an 18-fold enhancement in fluorescence emission intensity after the addition of mesitylene in aqueous solution. Whereas for o-xylene 4.5-fold growth was spotted (Figure 6.1a). These phenomena were also associated with the consequential change of the quantum yield (Φ) of **L**₆ in the presence of mesitylene in an aqueous medium. The probe was having a quantum yield of 0.08, whereas, in the presence of mesitylene in water, the relative quantum yield was significantly higher and equal to 0.11. The fluorescence titration experiments (Figure 6.1b) of **L**₆ for mesitylene were carried out in the water to investigate the detailed sensing performance. There was pronounced enhancement in the emission spectrum upon continuous addition of mesitylene. As the analyte concentration gradually escalated, the emission spectrum exhibited sustainable growth until saturation was attained.

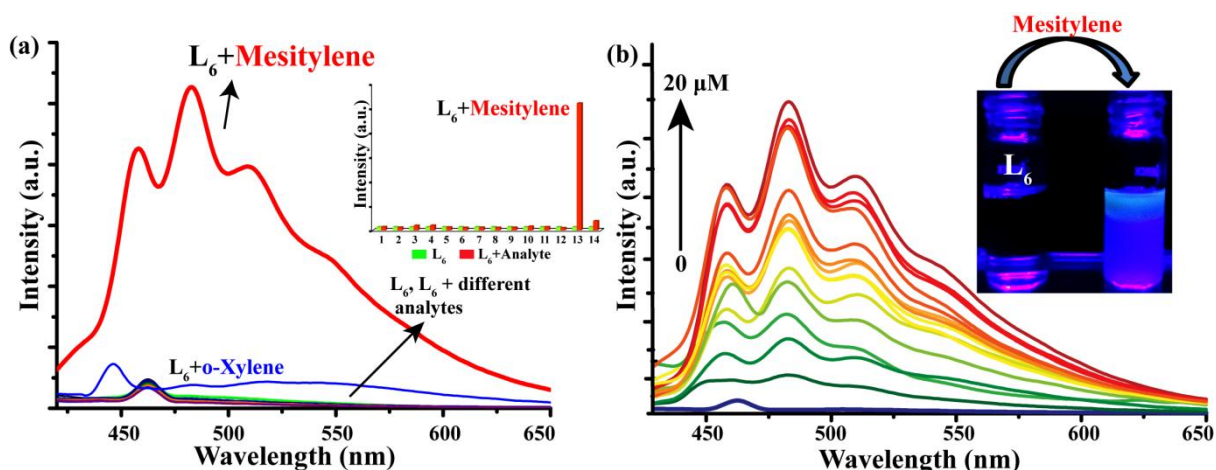


Figure 6.1: (a) Fluorescence spectra of L_6 (2 μ M, λ_{ex} = 400 nm) in presence of various VOCs (50 Equiv); Inset: normalized emission intensity of L_6 at 481 nm in presence of various VOCs (1= p-xylene, 2= m-xylene, 3= benzene, 4= toluene, 5= phenol, 6= THF, 7= DCM, 8= DMSO, 9= DMF, 10= methanol, 11= acetone, 12= hexane, 13= mesitylene, 14= o-xylene). (b) Fluorescence titration analysis of L_6 upon varying concentration of mesitylene; Inset: Photograph of L_6 and in presence of mesitylene under UV illumination.

The change in intensity was noteworthy, which was quickly identified by the naked eye after illuminating in a 365 nm UV lamp (Figure 6.1b, Inset). Job's plot analysis (Figure A6.3) was also executed to determine the stoichiometric ratio of the L_6 -mesitylene ensemble in the aqueous medium. The result conveyed that the utmost fluorescence intensity was procured at the 0.5 molar fraction, suggesting a 1:1 binding stoichiometry ratio. Furthermore, the formation of 1:1 stoichiometric complex was validated by HRMS spectrometric study (Figure A6.4), where the mass signal at m/z 384.1193 was designated (calculated m/z 384.1586) to L_6 -mesitylene complex. Eventually, the apparent binding constant calculated for the complex according to Benesi-Hildebrand (B-H) equation, was $16.67 \times 10^8 \text{ M}^{-1}$, and the limit of detection (LOD) computed as low as 2.66 ppm (Figure A6.5) in the aqueous matrix, which imparted highly improved values from earlier reported literature.^{6.17-6.18} The well-organized linear correlation plot among the fluorescence emission responses and the concentrations of added mesitylene ($r^2 = 0.9882$) corroborated a sensitive quantitative estimation of mesitylene. To understand the mechanistic behaviour of L_6 (2 μ M, λ_{ex} = 400 nm) in presence of mesitylene, the fluorescence lifetime decay profiles were accomplished before and after the addition of 50 equivalents of mesitylene in the aqueous medium. Albeit the lifetime decay spectra of L_6 were fitted into bi-exponential decay curve ($\tau_{av} = 0.591 \text{ ns}$) but upon addition of mesitylene tri-exponential decay spectra was noticed along with significantly enhanced lifetime from 0.591 ns to 1.924 ns (Table A6.1), urging the complexation of L_6 towards mesitylene. Moreover, the 2D NOESY spectra of

L₆ with mesitylene also displayed additional cross-peaks due to possible π - π interactions between them (Figure A6.6). To appraise the interference of other VOCs, common abundant cations and anions, competitive experiments were executed under identical conditions (2 μ M **L**₆ with 50 equivalent different analytes), which resulted in negligible impact on mesitylene induced fluorescence enhancement. This phenomenon verified the high selectivity and sensitivity of **L**₆ towards mesitylene over other VOCs in the aqueous medium (Figure A6.7).

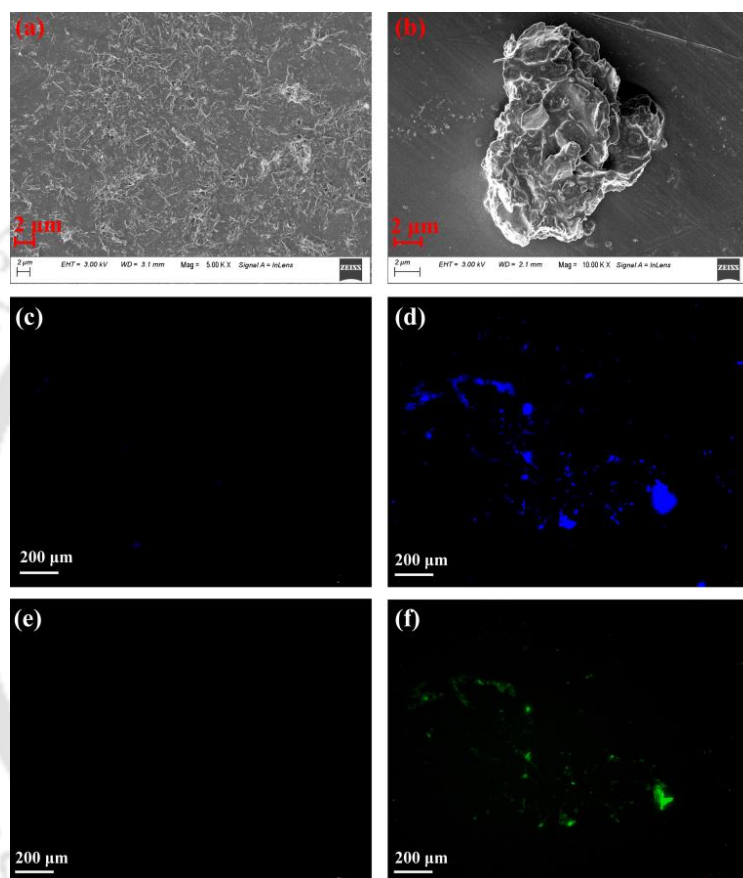
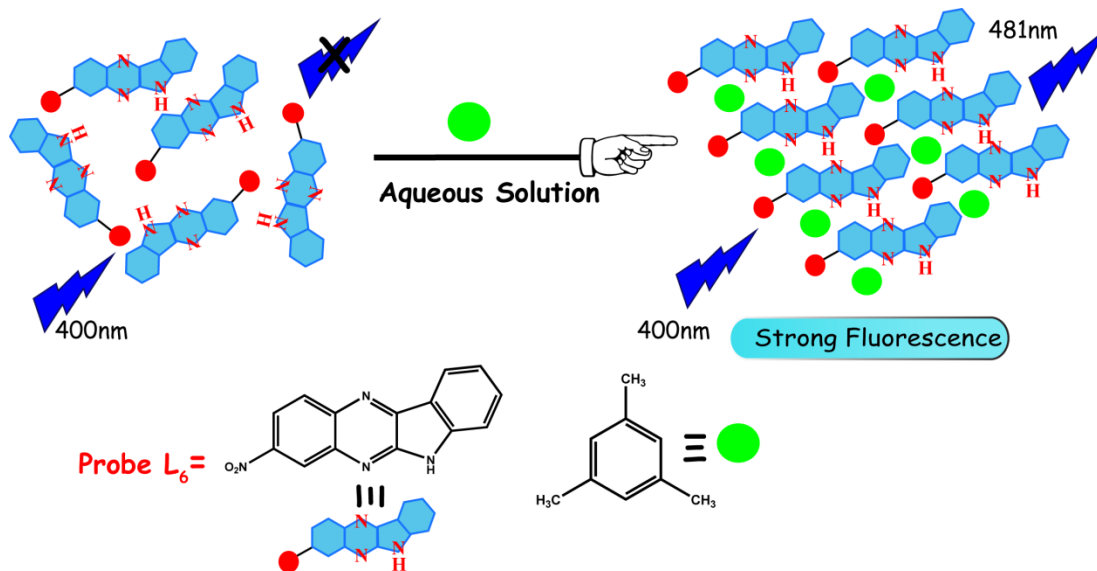


Figure 6.2.: FESEM and Fluorescence microscope images of **L**₆ (2 μ M) (a, c and e), **L**₆ + mesitylene (b, d, and f) in aqueous medium.

To investigate the morphology variation in underlying complexation mechanism, field-emission scanning electron microscopic (FESEM) analysis, dynamic light scattering (DLS), and fluorescence microscopic studies were also carried out. FESEM analysis revealed that the fibril network-like distribution of **L**₆ (2 μ M) transformed into a sizeable stone-shaped hetero-structure upon interaction with mesitylene (Figure 6.2a, 6.2b). The possible complexation between **L**₆ and mesitylene could be ascribed to the analyte induced assembly of feebly aggregated probe molecules into multi-molecular aggregates (Scheme 6.2). The morphological transition of **L**₆ (2 μ M) was authenticated by DLS experiment as the hydrodynamic diameter of **L**₆ got changed upon gradual addition of analyte in the aqueous medium. The average hydrodynamic size of **L**₆

enhanced abruptly after the addition of mesitylene suggesting due to analyte-assistant self-assembly (Figure A6.8). Moreover, this observed effect was verified by confocal fluorescence microscopy as well, where immense blue colour emission had been visualized significantly from hetero-structures of increased diameter (Figure 6.2d-6.2 f).



Scheme 6.2: Schematic representation of plausible mechanism.

6.4 Plausible sensing mechanism

The observed fluorescence “Turn-On” behavior could be elucidated by the π - π interactions between electron-deficient L_6 and electron-rich benzene derivatives, ensuing enhanced electron transfer between the sensor and mesitylene. To authenticate the speculation, density functional theory (DFT) calculations were carried out with the B3LYP/6-31 G (d, p) method basis set utilizing the Gaussian 09 program.^{6.19} Moreover, upon exciting at 400 nm, the electronic transition from HOMO to LUMO is expected to take place, and thereby PET process is triggered to quench the fluorescence of L_6 .^{6.20} Additionally, sufficient spectral overlap between the donor mesitylene and the acceptor L_6 (Figure 6.3a), along with increment in luminescence lifetime from 0.591 ns to 1.924 ns (Figure 6.3b) after the addition of excess analyte mesitylene, strongly indicated the probability of FRET phenomenon.^{6.21} Furthermore, PET and FRET between L_6 and mesitylene unitedly found to be responsible for this discriminant “Turn-On” detection of benzene derivatives. From DFT calculations, the gas phase geometry of L_6 with minimum energy was optimized. The highest occupied molecular orbital (HOMO) of L_6 is located on the entire quinoxaline framework except $-NO_2$ moiety whereas in the lowest

unoccupied molecular orbital (LUMO) electronic distribution has been changed including $-\text{NO}_2$ group (Figure 6.4a), giving rise to an energy gap up to 0.119 eV. Moreover, the electron-rich analytes comprised higher-lying LUMOs in contrast to

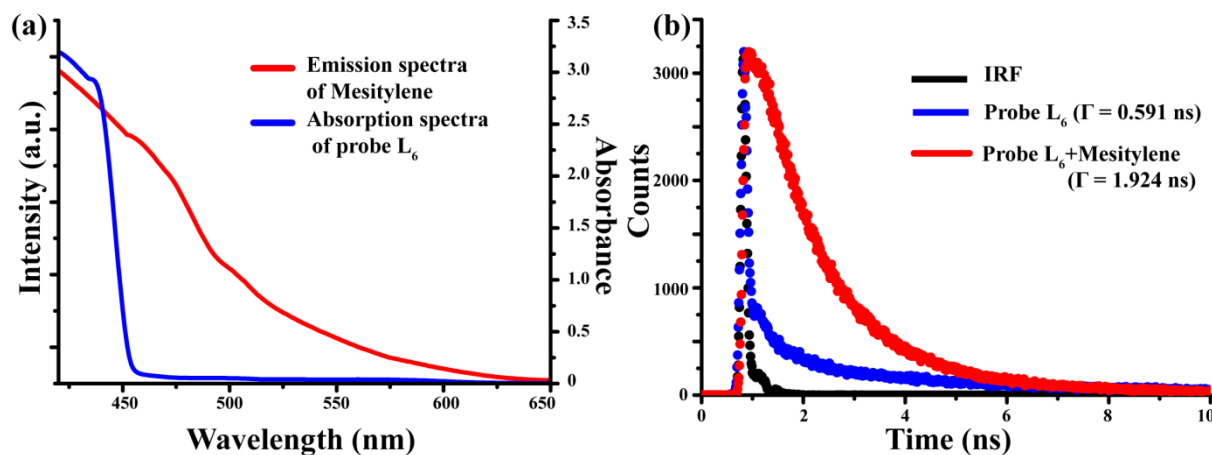


Figure 6.3: (a) Spectral overlap of the emission spectra of L₆ (blue line) and the absorption spectra of mesitylene (red line) in the aqueous medium. (b) Time-resolved fluorescence spectra of L₆ and in the presence of mesitylene.

of L₆, resulting in facile electron transfer from electron-rich VOCs to L₆^{6.22} (Figure A6.9). As the LUMO energy difference between VOCs and L₆ [$\Delta E_{\text{LUMO}} = E_{\text{LUMO}}(\text{VOCs}) - E_{\text{LUMO}}(\text{L}_6)$] raised, consequently the extent of fluorescence intensification. However, the HOMO–LUMO energy computation of the probe treated with mesitylene confessed the energetically favourable and spontaneous process due to lowering the HOMO, LUMO energies of the L₆-mesitylene ensemble. DFT-optimized structure predicted the average distance between L₆-mesitylene complex was around 3.335 Å which could suggest the involvement of π - π interaction (Figure 6.4b).

6.5 Detection of Mesitylene in natural samples

To substantiate the worthiness of L₆ in presence of common metal ions and anions, it is mandatory to recognize mesitylene in environmentally contaminated water body samples.^{6.23} River water and lake water specimens were collected from the Brahmaputra river (near IITG Campus) and Serpentine lake (IITG Campus). Industrial wastewater was supplied by the IITG Chemical Engineering department. Tap water was accessible in the laboratory. Initially, these water samples were centrifuged at 10000 rpm for 5 min followed by filtration using a 0.22 μm membrane filter and then spiked with mesitylene before the addition of L₆. Eventually, the emission maximum of L₆ (2 μM) in the presence of mesitylene at 481 nm with similar

fluorescence enhancement was recorded (Figure 6.4c). The results of the quantitative recovery amount of spiked specimens of analyte are shown in Table A6.2.

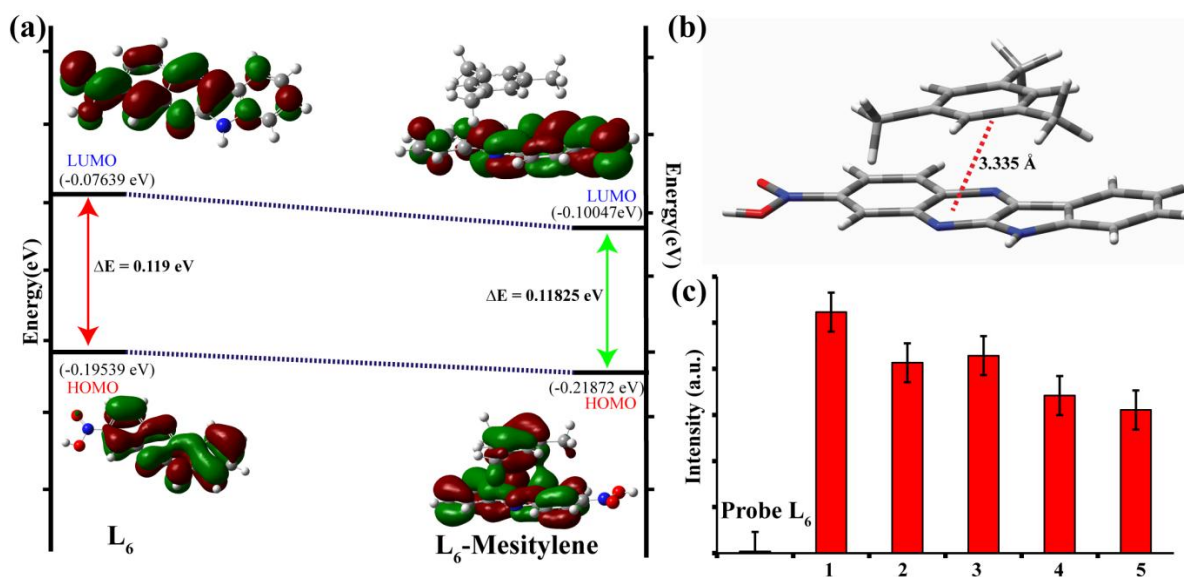


Figure 6.4: (a) HOMO-LUMO energy profiles of L_6 and L_6 -Mesitylene ensemble. (b) Optimized geometry of L_6 -Mesitylene ensemble. (c) Fluorescence emission intensity changes for L_6 ($2 \mu\text{M}$) at 481 nm in the presence of excess Mesitylene in natural sources of water (1= distilled water, 2= tap water, 3= lake water, 4= river water, 5= industrial wastewater).

Another salient perspective of detection of VOCs is that they can serve as potential biomarkers of cancer which can differentiate cancerous cells from the benign cell.^{6.24-6.25} To inspect VOCs as cancer biomarkers, analysis of body fluids and urine samples has become very popular for early detection of different types of cancer in recent years^{6.26} Consequently, to authenticate the real-life execution of L_6 for sensing mesitylene, bio-fluidic samples and artificial urine^{6.27} were chosen instead of water. Moreover, the result explicated that L_6 ($2 \mu\text{M}$) was able to recognize mesitylene in the intestinal fluid (pH \sim 8), body fluid (pH \sim 7.4), gastric fluid (pH \sim 2), and artificial urine specimens by exhibiting similar appreciable “Turn-On” fluorescence enhancement (Figure A6.10).

6.6 Paper-based analysis of mesitylene

Because of the significance as mentioned above, the final applicability of the sensor was demonstrated by fabricating low-cost, simple portable paper strips (Figure 6.5a) coated with L_6 for rapid on-site detection of mesitylene.^{6.28-6.30} For portable test strips preparation, the filter paper was cut into small strips of size (2 cm \times 1 cm) and allowed to get dry after immersing into the solution of L_6 (2×10^{-6} M) in DMSO at room temperature. When the solvent evaporated

utterly, the L_6 coated filter paper was ready and then used for rapid on-site estimation of mesitylene. A small amount of freshly prepared mesitylene solutions (10^{-4} - 10^{-7} M) were drop-casted on the test strips, and bright blue spots appeared in every case after visualizing under a convenient 365 nm UV light. A further study on the L_6 ($2\mu\text{M}$) coated paper-based sensor was also accomplished to detect mesitylene vapor.^{6.31-6.32} Glass vials containing mesitylene solution were made ready and their open mouths were covered by L_6 impregnated test strips for 30 minutes. Moreover, this whole experiment was accomplished in a closed desiccator. After 30 minutes, the vapour fumigated paper-based sensors, when exposed to UV light, manifested a similar result, which could easily be identified by naked-eye (Figure 6.5b). Owing to the above-demonstrated experiments, L_6 soaked paper-based sensor can likely be applied for on-site visual recognition of mesitylene in vapour and liquid states.

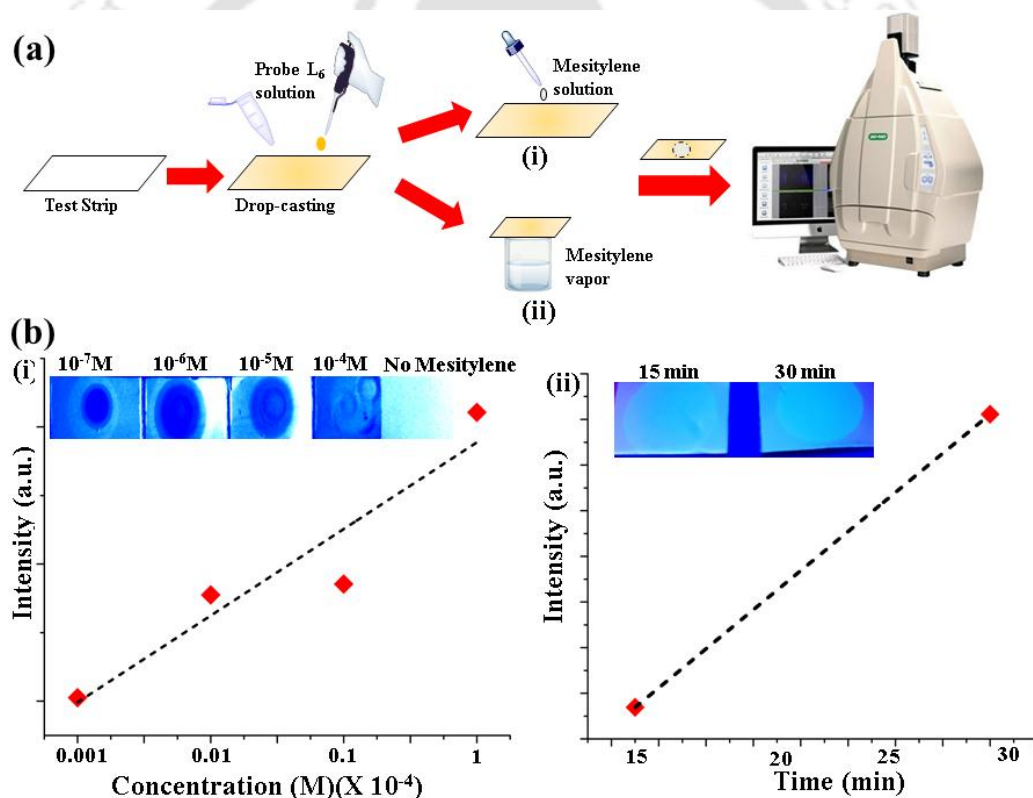


Figure 5. (a) Schematic illustration of preparation of L_6 ($2\mu\text{M}$) coated test strips. (b) (i) Linear plot for intensity vs different concentration of mesitylene, Inset: Visual detection of L_6 coated test strips before and after adding different concentrations of mesitylene under 365 nm illumination. (ii) Linear relationship with intensity vs mesitylene exposure time, Inset: The visual appearance of L_6 loaded paper strips after exposure to mesitylene vapour for 15 and 30 minutes.

6.7 Conclusions

In conclusion, we have designed and fabricated a quinoxaline-based fluorophore, L_6 , which was introduced as an effective chemosensor for the detection of benzene-derived VOCs in the

aqueous medium. The probe displayed a differential “Turn-On” fluorescence response towards mesitylene (LOD= 2.66 ppm) uninfluenced by other VOCs. The sensing mechanism involved mesitylene detection induced assembly formation as the fibril network transformed into stone-shaped morphology. The detection tuneable morphological controllability was also justified by DLS study and fluorescence microscopic experiments. The probe possessed a notably high binding constant of $16.67 \times 10^8 \text{ M}^{-1}$ with mesitylene followed by 1:1 stoichiometric binding ratio. The probe was employed ideally for practical detection in natural contaminated water sources i.e., lake water, river water, tap water, industrial wastewater along with bio-fluidic samples, artificial urine as VOCs had become potential biomarkers of cancer. The current inexpensive strategy could be helpful for rapid, efficient estimation of mesitylene in an aqueous medium without involving modern equipment facilities, costly chemicals, or professionally trained operators.

References

- 6.1 WHO, Indoor Air Quality: Organic Pollutants. Report on a WHO Meeting, Berlin (West), 1987, World Health Organization Regional Office for Europe, Copenhagen, Denmark, 1989.
- 6.2 P. Kustrowski, A. Rokicinska and T. Kondratowicz, *Adv. Inorg. Chem.*, 2018, **72**, 385-419
- 6.3 United States Environmental Protection Agency. Volatile Organic Compounds (VOCs), Technical Overview, 2011.
- 6.4 G. Orellana and D. Haigh, *Curr. Anal. Chem.*, 2008, **4**, 273-295.
- 6.5 International Agency for Research on Cancer, List of agents classified by the IARC monographs International Agency for Research on Cancer, IARC, Lyon, France, 2017, 1–105.
- 6.6 K. Schmidt and I. Podmore, *Journal of Biomarkers* (Article ID 981458), 2015.
- 6.7 J.H. Lee, S.M. Hwang, D.W. Lee and G.S. Heo, *Bull. Korean Chem. Soc.*, 2002, **23**, 488-496.
- 6.8 C. Bur, M. Bastuck, D. Puglisi, A. Schütze, A.L. Spetz and M. Andersson, *Sens. Actuators, B.*, 2015, **214**, 225-233.
- 6.9 X. Guan, Z. Zhao, S. Cai, S. Wang and H. Lu, *J. Chromatogr. A.*, 2019, **1587**, 227-238.
- 6.10 L.R. Khot, S. Panigrahi and D. Lin, *Sens. Actuators, B.*, 2011, **153**, 1-10.
- 6.11 A. Lipatov, A. Varezchnikov, P. Wilson, V. Sysoev, A. Kolmakov and A. Sinitskii, *Nanoscale*, 2013, **5**, 5426-5434.
- 6.12 L. Lu, X. Han, J. Lin, Y. Zhang, M. Qiu, Y. Chen, M. Li and D. Tang, *Analyst*, 2021, **146**, 2664-2669.
- 6.13 S.K. Jha, R.D.S. Yadava, K. Hayashi and N. Patel, *Chemometr. Intell. Lab. Syst.*, 2019, **185**, 18-31.
- 6.14 G. Fuchs, M. Boll and J. Heider, *Nat. Rev. Microbiol.*, 2011, **9** (11), 803–816.
- 6.15 L. Marin, L. Lutsen, D. Vanderzandea, and W. Maes, *Org. Biomol. Chem.*, 2013, **11**, 5866–5876.

- 6.16 J. Zhao, S. Ji, Y. Chen, H. Guo and P. Yang, *Physical Chemistry Chemical Physics.*, 2012, **14** (25), 8803–8817.
- 6.17 J. S. Ovens and D. B. Leznoff, *Chem. Mater.*, 2015, **27**, 1465.
- 6.18 X. L. Yang, X. Chen, G. H. Hou, R. F. Guan, R. Shao and M. H. Xie., *Adv. Funct. Mater.*, 2016, **26**, 393.
- 6.19 M. Frisch, F. Clemente, M.J. Frisch, G.W. Trucks, H.B. Schlegel, G.E. Scuseria, M.A. Robb, J.R. Cheeseman, G. Scalmani, V. Barone, B. Mennucci, G.A. Petersson, H. Nakatsuji, M. Caricato, X. Li, H.P. Hratchian, A.F. Izmaylov, J. Bloino and G. Zhe, Gaussian 09, Revision A. 01, 2009.
- 6.20 Y. Jiao, B. Zhu, J. Chen and X. Duan, *Theranostics.*, 2015, **5**, 173–187.
- 6.21 N. Meher and P. K. Iyer, *Angew. Chem. Int. Ed.*, 2018, **57**, 8488–8492.
- 6.22 J. Dong, A. K. Tummanapelli, X. Li, S. Ying, H. Hirao, and D. Zhao, *Chem. Mater.*, 2016, **28**, 7889-7897.
- 6.23 S. Ray, S. Panjekar, and R. Anand, *ACS Sens.*, 2018, **3**, 1632-1638.
- 6.24 C. L. Silva, M. Passos, and J. S. Camara, *Talanta*, 2012, **89**, 360–368.
- 6.25 J. Huang, S. Kumar, N. Abbassi-Ghadi, P. Spanel, D. Smith, and G. B. Hanna, *Anal. Chem.*, 2013, **85**, 3409–3416.
- 6.26 C. L. Silva, M. Passos, and J. S. Camara, *British Journal of Cancer*, 2011, **105**, 1894–1904.
- 6.27 T. Brooks and C.W. Keevil, *Letters in Applied Microbiology*, 1997, **24**, 203–206.
- 6.28 H. Jiangting, L. Yang, Z. Xunxue, H. Hongliang, L. Zhongfeng and H. Tianyu, *Dyes and Pigments*, 2021, **192**, 109393.
- 6.29 S. Lv, Y. Tang, K. Zhang and D. Tang, *Anal. Chem.*, 2018, **24**, 14121-14125.
- 6.30 Z. Qiu, J. Shu and D. Tang, *Anal. Chem.*, 2017, **89**, 5152-5160.
- 6.31 S. Pramanik, C. Zheng, X. Zhang, T. J. Emge and J. Li, *J. Am. Chem. Soc.*, 2011, **133**, 4153-4155.
- 6.32 J. Dong, Y. Zhou, F. Zhang and Y. Cui, *Chem.- Eur. J.*, 2014, **20**, 6455-6461.

Appendix - Chapter 6

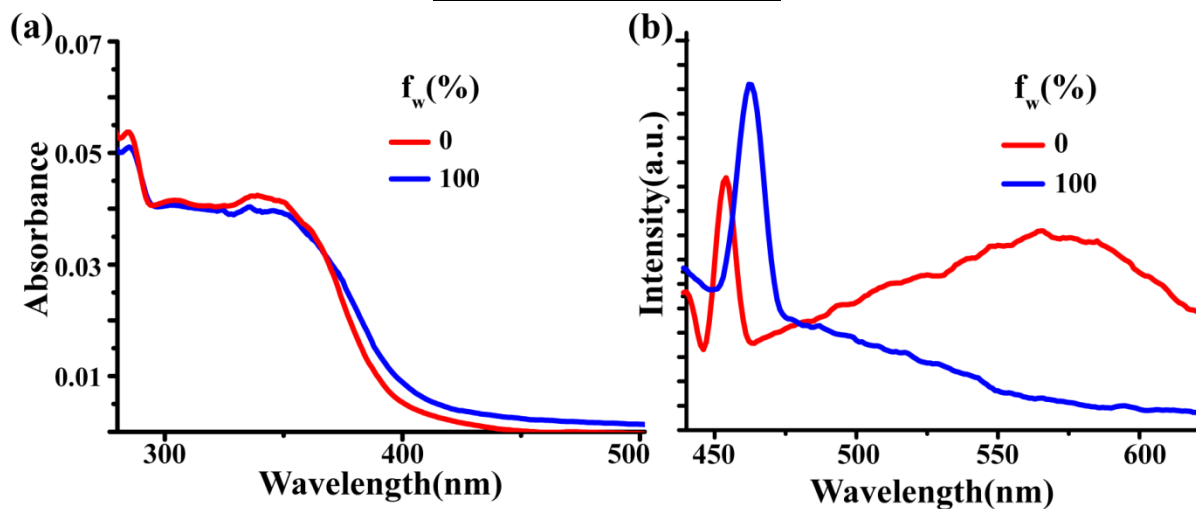


Figure A6.1: (a) UV-Vis and (b) Fluorescence changes of L_6 ($2 \mu\text{M}$) in different water fractions at room temperature.

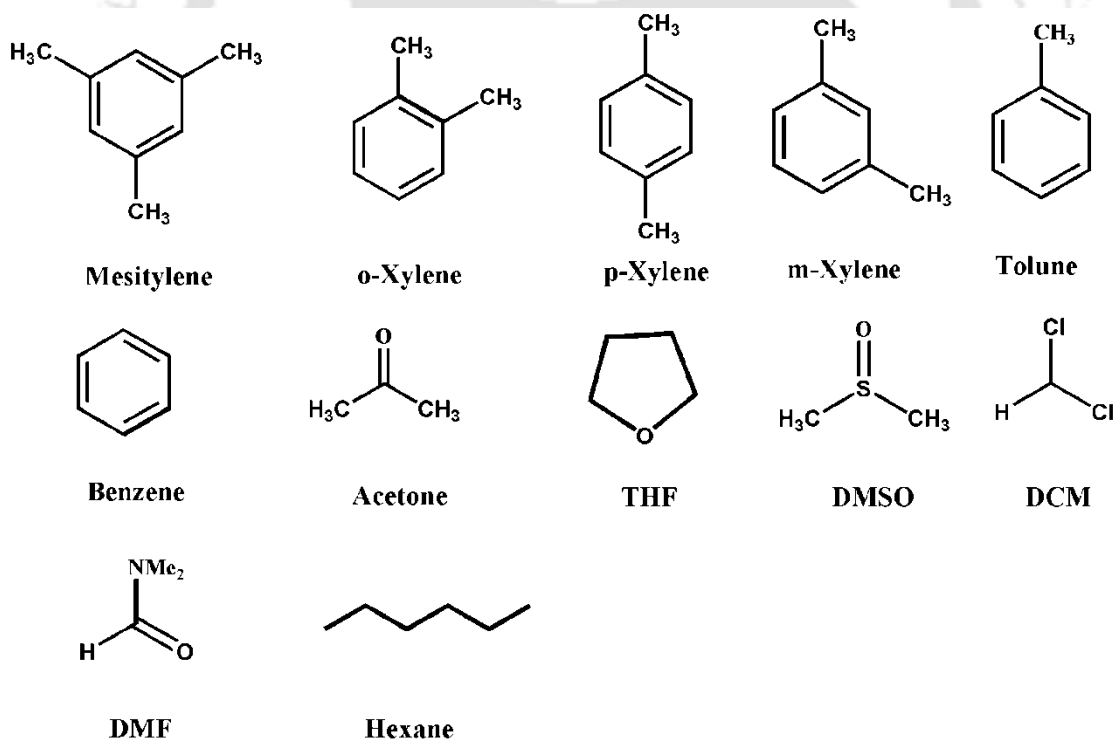


Figure A6.2: Chemical structures of different aromatic and non-aromatic VOC compounds used in our study.

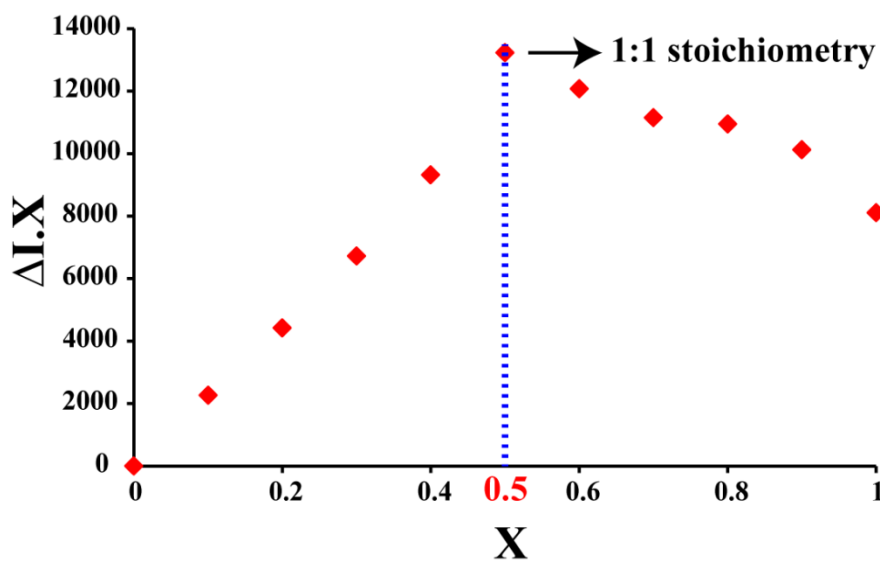


Figure A6.3: Job's plot calculation to determine the binding stoichiometry between L_6 and Mesitylene in 100% solution ($\lambda_{\text{ex}} = 400 \text{ nm}$).

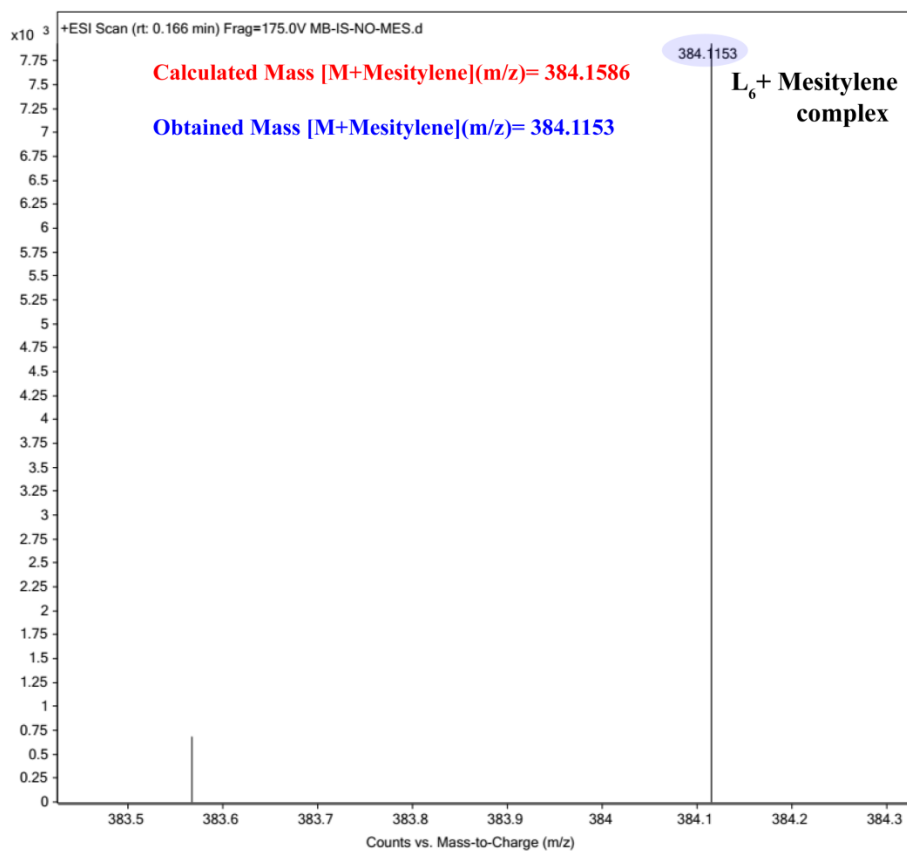


Figure A6.4: HRMS spectra of L_6 in 1:1 water-acetonitrile in the presence of Mesitylene in positive ionization mode.

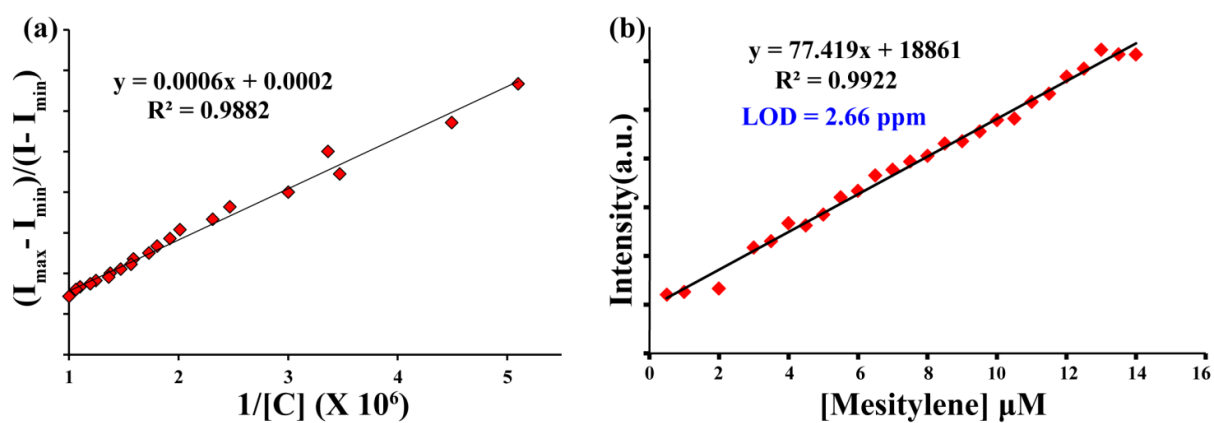


Figure A6.5: (a) Determination of binding constant of L_6 for Mesitylene in aqueous medium using the Benesi-Hildebrand method considering 1:1 interaction. (b) Fluorescence emission intensity of L_6 at 481 nm vs. Mesitylene concentration to calculate the detection limit.

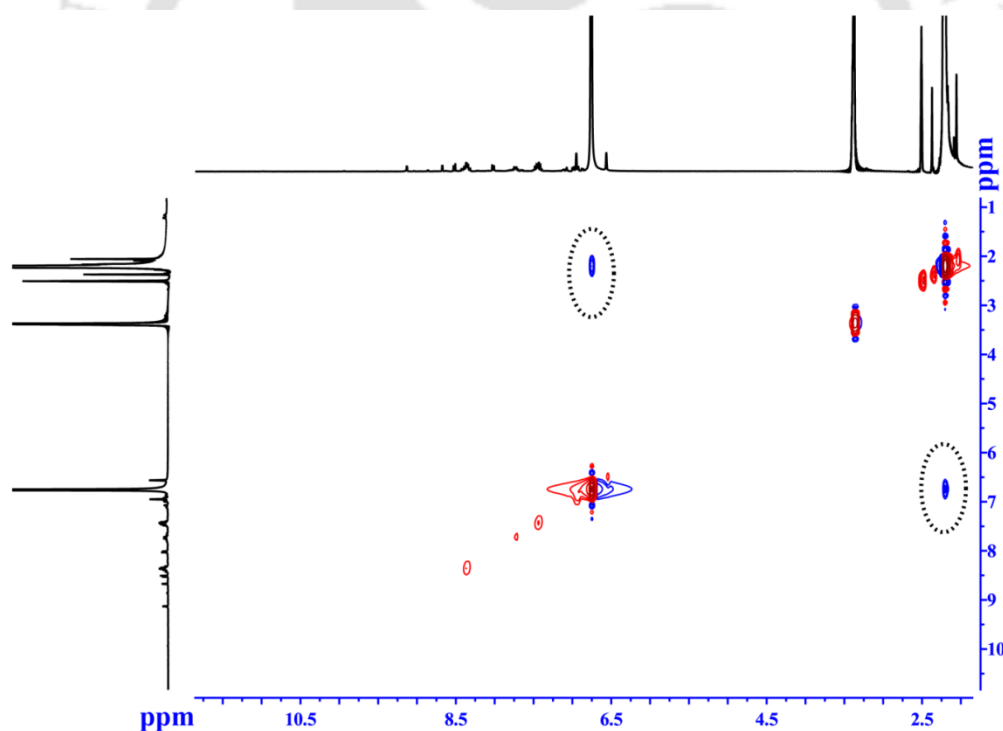


Figure A6.6: NOESY NMR spectra of L_6 -Mesitylene.

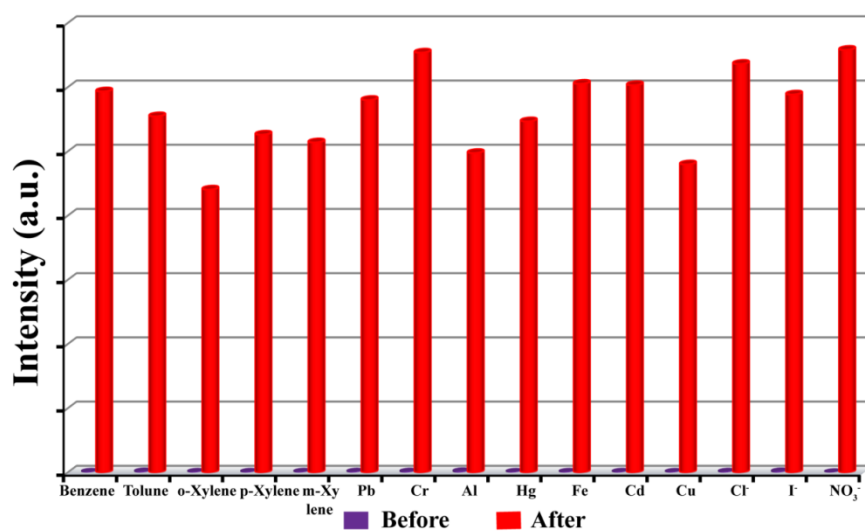


Figure A6.7: Fluorescence response of L_6 (2 μ M) to various analytes, before (violet bars) and after (red bars) addition of Mesitylene.

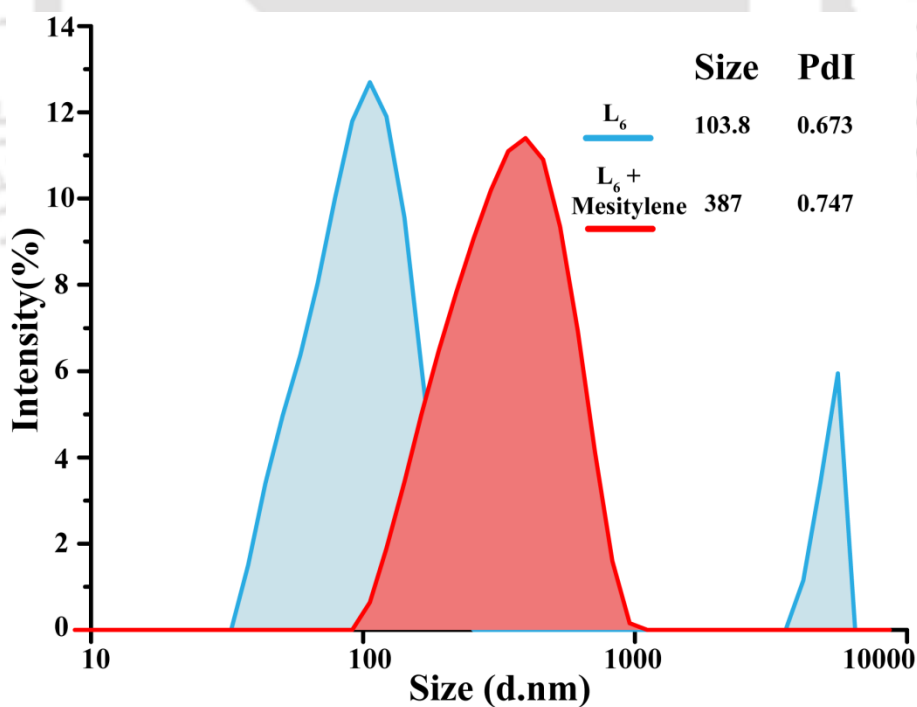


Figure A6.8: DLS spectra of L_6 (2 μ M) and L_6 + Mesitylene in the aqueous medium.

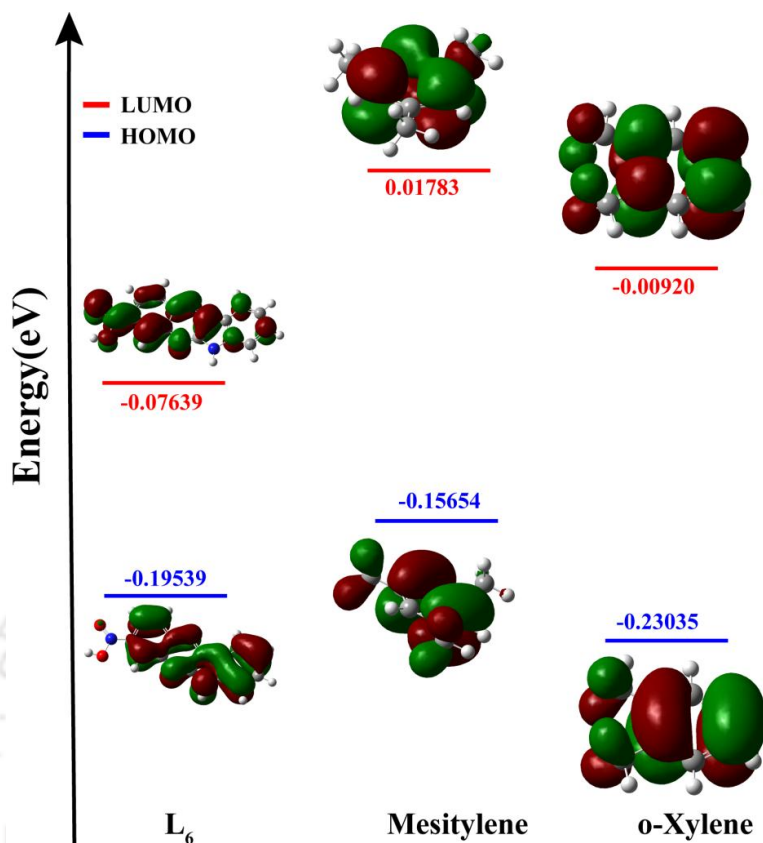


Figure A6.9: DFT calculated HOMO-LUMO energy profiles of L_6 , Mesitylene and o-Xylene.

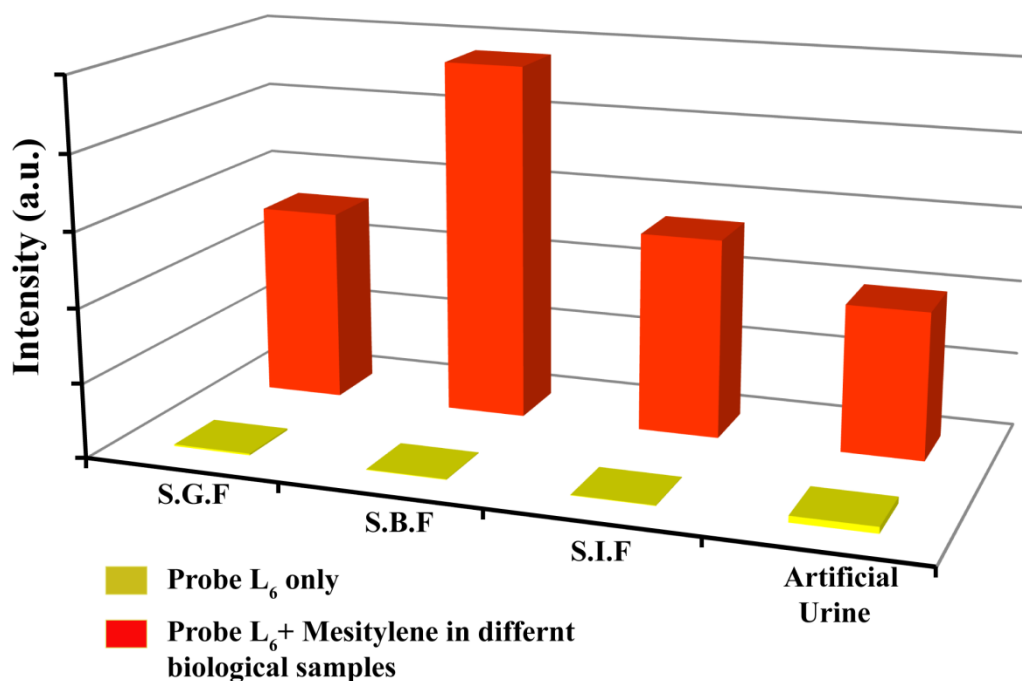


Figure A6.10: Changes in the emission intensity of L_6 ($2 \mu\text{M}$) at 481 nm in the presence of excess Mesitylene in bio-fluidic samples [S.G.F- Simulated Gastric Fluid (pH~2.0), S.B.F- Simulated Body Fluid (pH~7.4), S.I.F- Simulated Intestinal Fluid (pH~8.0) and Artificial Urine].

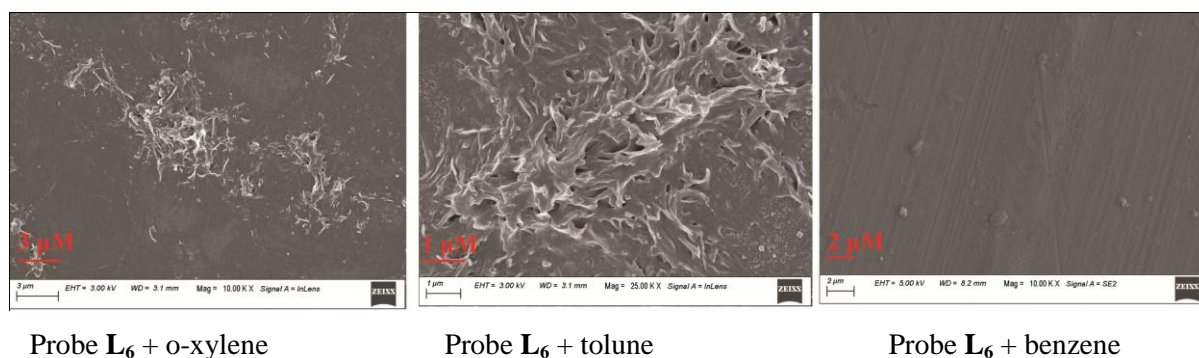


Figure A6.11: FESEM images of L_6 with different VOCs.

Table A6.1: Fluorescence lifetime values of L_6 ($2\mu\text{M}$) and L_6 -Mesitylene in aqueous medium.

Sample	B_1	B_2	B_3	a_1	a_2	a_3	τ_1	τ_2	τ_3	$\langle\tau\rangle$ (ns)	χ^2
L_6	0.0198	2.0809	-	0.7220	0.2779	-	0.818	0.003	-	0.591	1.089
L_6 + Mesitylene	0.0836	0.0153	0.0018	0.6667	0.2465	0.0866	1.136	2.290	6.955	1.924	1.024

Table A6.2: Comparative analysis for detection of Mesitylene in natural water samples.

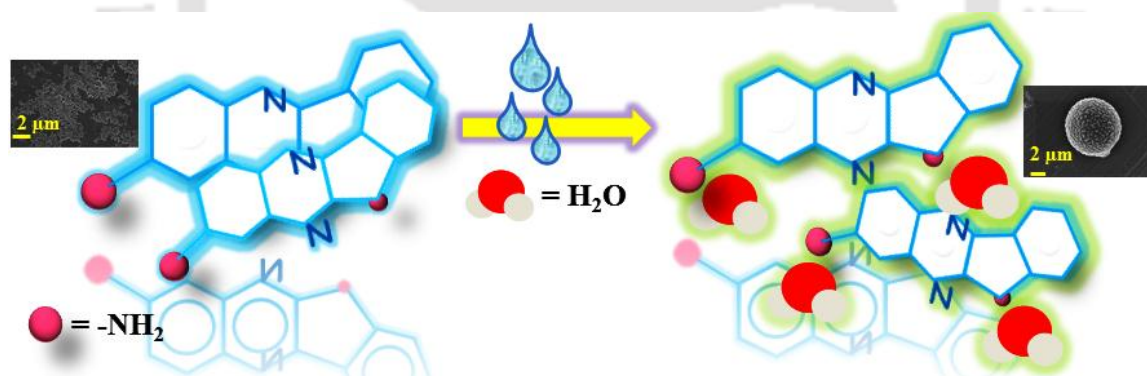
Sample	Fluorescence Spectroscopy			UV-Visible Spectroscopy		
	Added (μM)	Detected (μM)	Recovery (%)	Added (μM)	Detected (μM)	Recovery (%)
Industrial wastewater	5.0	5.30	103	5.0	6	105
Lake water	5.0	4.00	85	5.0	4.8	88
River water	5.0	4.8	93	5.0	5.1	101

Table A6.3: Comparison of the detection limits achieved till now along with the receptor and solvent system used for the detection of VOCs

SI No.	References	Receptor	Analytical Methods	Medium Used	L.O.D. (ppm)
1.	Present work	Quinoxaline derivative	Fluorescence Spectroscopy	100% Aqueous medium, Vapor, Paper Strip	2.66
2.	Sensors & Actuators: B. Chemical, 2020, 311, 127904	Poly(maleic anhydride-alt-1-octadecene) (PMAO) nanoparticles	Fluorescence Spectroscopy	Aqueous medium	7
3.	Chem. Sci., 2018, 9, 1892–1901	Organoboron polymer	Fluorescence Spectroscopy	Vapor	3.7
4.	Molecules 2017, 22, 1306	Polystyrene films	Fluorescence Spectroscopy	Vapor	150
5.	Anal. Chem., 2017, 89, 3814	Perylene monoimide	Fluorescence Spectroscopy	Vapor	8
6.	Chem. Mater. 2016, 28, 7889	TPE based M.O.F.	Fluorescence Spectroscopy	Solution	-
7.	Scientific Reports, 2015, 5, 12462	Molecularly imprinted polymer	Potentiometry	Vapor	3.5
8.	J. Am. Chem. Soc. 2014, 136, 7241	2D M.O.F.	Fluorescence Spectroscopy	Solution	-
9.	Chem. Mater. 2015, 27, 1465	Coordination Polymer	Raman Spectroscopy	Solution/ Vapor	500
10.	Chem. Commun., 2011, 47, 1160–1162	Silver(I) pyrazolate	Fluorescence Spectroscopy	Vapor	-

CHAPTER 7

Amine substituted Quinoxaline framework: Water induced self-assembly and simultaneous detection moisture

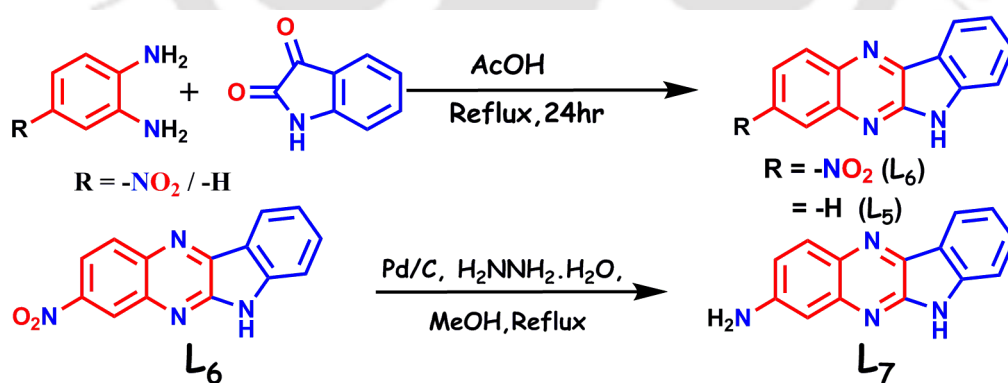


Chapter 7

7.1 Background and focus of the chapter

Organic solvents have ubiquitous consumption in both industrial processes and academic research purposes. Trace water is regarded as an impurity and contaminant for routinely used solvents and several chemical reagents. As a result yield of such sensitive chemical reactions gets affected, the reactivity of organometallic compounds gets quenched sometimes the presence of water leads to a massive tragedy like fires and explosions, hence qualitative and quantitative identification of water content in organic solvents and chemical reagents in textile, petroleum, food industries remain an area of intense interest. Conventional analytical techniques such as Karl Fischer titration,^{7.1} chromatographic, and electrochemical processes^{7.2} are available for the detection of trace amounts of moisture in organic solvents. Although Karl Fischer's method imparts ppm-level detection of water it involves drawbacks of using toxic chemicals (SO₂, I₂, alcohol), insufficiency of real-time recording, time-consuming tedious methods. Moreover, electronic moisture sensors are smoothly commercially accessible, but they are expensive, might have health and environmental impact, and possess their lifetime.^{7.3} The main drawback associated with the progress of new moisture sensors is to evolve reasonable methods for mass-scale production and widespread usage. Therefore, chemical sensors that change the optical/fluorescence signal on exposure to a trace amount of moisture or humidity have fascinated appreciable attention in environmental purposes, industrial processing, food production, and biomedical applications. Out of the fluorescent probes, solvatochromic probes, which manifests distinct absorption and emission spectra regulated by solvent polarity, represents a fascinating class of organic dyes that are useful for chemical and biochemical research including protein folding, protein-protein interactions in the field of proteomics^{7.4} along with in vitro and in vivo analysis of lipid organization and dynamics in cellular membranes.^{7.5} Owing to the high dielectric constant and proton accepting-donating properties, universal solvent water may provoke several distinctive interactions with exciting sensory probes. Until today, researchers have documented a large number of solvatochromic molecular probes i.e. naphthalimide, thioxanthone,^{7.6-7.8} 3-hydroxy flavone, etc. based fluorophores^{7.9-7.12} but quinoxaline, polycyclic pharmacophore-based

fluorophores are scarcely available. To instigate utmost sensitivity and response to foreign stimuli of small molecule solvatochromic probes, various fundamental characteristics should be considered, along with the coplanar π -conjugated framework, degree of polarization, and push-pull charge-transfer (CT) property.^{7.13-7.15} Incorporation of polar functional moieties in the molecule, for example, nitro, amino, carbonyl, cyano, or heteroaryl groups avail high polarization. Furthermore, high-level extended π -conjugation with backbone coplanarity was the principle design strategy for evolving top-performing solvatochromic chemosensors.^{7.16-7.17} In the present work, aiming at procuring novel fluorescent chemosensor it was attempted to design and synthesize pharmacologically active quinoxaline-based probe (**L**₇)(Scheme 7.1), one kind of rarely used chromophores with strong solvatochromism and high fluorescence efficiency. Expansion of π -conjugation by the introduction of electron-donating $-\text{NH}_2$ moiety helps the intramolecular charge-transfer (ICT) extremely sensitive towards the variation of solvent polarity. However, to the best of our knowledge, quinoxaline scaffold with excellent solvatochromism and acting as moisture indicator in four commonly used organic solvents, raw food materials, building materials are relatively rare. Moreover, some **L**₇ soaked test strips were also arranged to authenticate the practical utility of qualitative identification of different fractions of water content in dry acetonitrile solvent using smartphone-assisted RGB analysis.



Scheme 7.1: Synthesis of the probe **L**₇.

7.2 Photophysical and Solvatochromic behavior of probe **L**₇

The photophysics of amine incorporated indolo-quinoxaline scaffold (**L**₇) in solution is highly dependent on the solvent polarity, hence the UV-visible and fluorescence spectra of the chemosensor were carried out in nine different solvents of distinct polarities and hydrogen

bonding potentialities. The photophysical studies of **L**₇ were recorded in different organic solvents [millipore water, methanol (MeOH), acetonitrile (MeCN), dimethylformamide (DMF), dimethylsulfoxide (DMSO), tetrahydrofuran (THF), ethylacetate (EtOAc), acetic acid (AcOH) and hexane] further diluting to 2×10^{-6} mol L⁻¹ at $\lambda_{\text{ex}} = 410$ nm. Our strategy was established on the following design postulates: modification of quinoxaline backbone with electron-rich amine substitution (**L**₇) would help to procure superb optical performance based on the coplanar, long electron-rich π -conjugated framework and bestow the chemosensor with maximum solvatochromism by a ready intramolecular charge transfer (ICT) process.

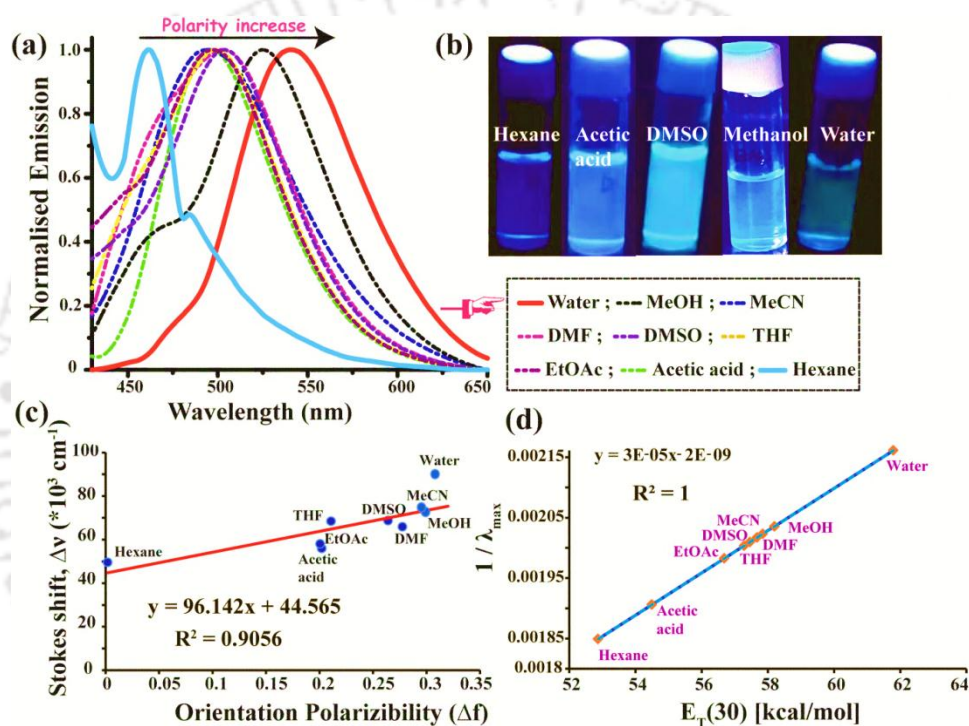


Figure 7.1: (a) Normalized fluorescence spectra of probe **L**₇ (2.0 μ M) in organic solvents of different polarity. (b) Photographs of **L**₇ (2.0 μ M) in several organic solvents under 365 nm UV lamp. (c) Lippert-Mataga plot; Stokes shifts of **L**₇ vs Δf . (d) A plot of $1/\lambda_{\text{max}}$ vs. $E_T(30)$ for nine surveyed solvents.

Absorption spectra were normalized to unity and the absorption spectrum of **L**₇ displayed negligible changes in different solvents (spectra computed in selected nine solvents are demonstrated in Figure A7.1a). Moreover, the electronic absorption spectra of **L**₇ (2.0 μ M) rendered maximum emission band at 340 nm, which can be attributed to π - π^* transitions and a shoulder band centered around 405 nm which might be attributed to n - π^* within the aromatic quinoxaline moiety. While probe **L**₇ manifested a minimal solvent dependency, an insignificant bathochromic shift of ~ 10 nm was observed with enhancing the solvent polarity; no crucial change in the absorbance value or spectrum shape was perceived. In contrast, as the solvent

polarity enhanced from hexane to water, the luminescence emission peaks of probe **L**₇ progressively redshifted from 462 nm to 540 nm, depicting an impressive bathochromic effect (Figure 7.1a) whereas **L**₅, and **L**₆ unveiled negligible results (Figure A7.1b-A7.1c). Furthermore, the probe displayed dramatic fluorescent color variations under hand-held 365 nm UV illumination from blue to greenish-yellow by changing the solvent from hexane to water (Figure 7.1b), as accordant with the fluorescence emission spectra. Concurrently, broadening of the emission bands and an apparent decrement in fluorescence quantum yield (Φ) of chemosensor **L**₇ from nonpolar hexane ($\Phi = 0.50$ %) to strongly polar water ($\Phi = 0.08$ %) medium were noted. The fluorescence quantum yields (Φ) were evaluated to be 0.38, 0.41, and 0.44 in MeOH, MeCN, and THF, respectively. The fluorescence spectral results could be elucidated with stabilization of the charge-separated excited states of quinoxaline after illumination under UV-lamp. Incorporation of electron-rich amine moiety in **L**₇ provoked intramolecular charge transfer and the charge-separated excited state might be stabilized more effectively in the polar solvent than the ground state, which induces a noteworthy bathochromic shift of emission maxima.^{7.18-7.19} Meantime, the fluorescence lifetime was measured to be 5.92 ns and 4.97 ns fitted with double exponential decaying in acetonitrile and methanol respectively, the value was reduced substantially to 2.85 ns with χ^2 of 1.001 in the pure aqueous medium (Figure A7.2). Based on previous literature, the distinct solvatochromic shifts, as well as the enhancement of the fluorescence lifetime of **L**₇ in different solvents, could be ascribed to the ICT effect since the ICT excited state got stabilized by the presence of polar solvents, lowering the excitation energy and hence prominent red-shift of the λ_{max} .^{7.20-7.21} The solvatochromism of chemosensor **L**₇ was assessed employing Lippert-Mataga equation,^{7.22} which related the Stokes shift ($\Delta\nu$) to solvent orientation polarizability (Δf), in nine different solvents with a wide range of polarity. A good linear relationship manifested strong solvent-polarity dependence with a slope of 96142 cm⁻¹ in the $\Delta\nu$ - Δf plot (Figure 7.1c). The large slope implied that the probe possesses strong solvatochromism, where the spectral behavior of **L**₇ emission is certainly relevant to ICT characteristics. Interestingly, we were fortunate to find another perfect linear plot of $1/\lambda_{\text{max}}$ as a function of $E_{\text{T}}(30)$ with a strong correlation coefficient, which is at per with the experimentally observed positive solvatochromic behavior (Figure 7.1d).

7.3 Detection of trace Water content in common organic solvents

According to the above discussions, it is interesting to be noted that the luminescence spectra of L_7 are strongly dependent on solvent polarity. To gain insight into the capability of chemosensor L_7 ($2.0 \mu\text{M}$) as a fluorescent probe for the detection of water content in commonly used laboratory solvents i.e. acetonitrile, THF, DMF, and methanol. Other solvents were avoided because of the solubility problem and poor spectral output. The fluorescence emission was gradually suppressed along with a considerable bathochromic shift (54 nm) upon increasing the water content (0 %–100 %) in acetonitrile (Figure 7.2a).

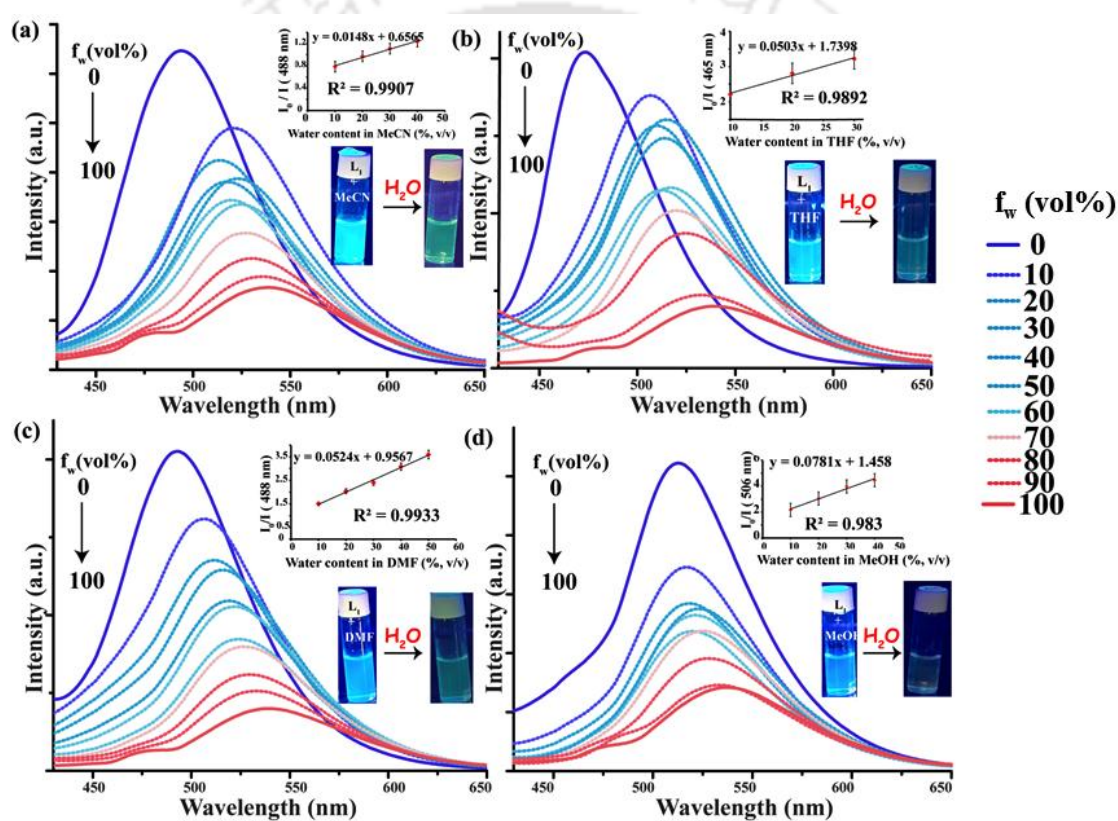


Figure 7.2: (a) Fluorescence emission spectrum of Sensor L_7 ($2 \mu\text{M}$; $\lambda_{\text{ex}} = 410 \text{ nm}$): (a) MeCN solution, (b) THF solution, (c) DMF solution, (d) MeOH solution in the presence of enhancing amounts of water (0-100%, v/v). Inset: Stern Volmer plot I_0/I vs. percentage of water content.

The positive solvatochromic shift along with pronounced quenched fluorescence intensity can be assigned to the general solvent effects and the intermolecular hydrogen-bonding interaction between amino groups and water molecules.^{7.23-7.24} For THF, DMF, and methanol the variations in spectral behaviors in response to water content were very much alike to acetonitrile excepting the bathochromic shifts $\sim 60 \text{ nm}$, $\sim 40 \text{ nm}$, and $\sim 20 \text{ nm}$ in the respective three solvents (Figure 7.2b, 7.2c, 7.2d). The quenched fluorescence intensity of the investigated chemosensor L_7 due to

the introduction of water in the above-mentioned solvents could be delineated by the Stern-Volmer equation.^{7.25} A non-linear Stern-Volmer plot was obtained using I_0/I vs water percentage (%) for the aforesaid organic solvents (Figure A7.3), but the water sensor manifested a good linear relationship between I_0/I vs $f_w(\%)$ at low concentrations. Moreover, the ratio of blank luminescence intensity to quenched intensity (I_0/I) in acetonitrile, THF, DMF and methanol are linearly proportional (Inset; Figure 7.2a, 7.2b, 7.2c, 7.2d) to water concentrations ranging from 0%-40% (v/v), 0%-30% (v/v), 0%-50% (v/v), 0%-40% (v/v) respectively with the detection limits (LOD) of 0.018% in acetonitrile, 0.027% in THF, 0.012% in DMF and 0.420% in methanol, respectively (Figure A7.3). Compared with the previously documented reports,^{7.26-7.28} the detection limit of sensor **L**₇ was quite low, signifying that the probe was sensitive to trace level water content in four frequently used water-miscible organic solvents. The contrasting fluorescence responses of probe **L**₇ generated by water could be assigned to stronger water-fluorophore hydrogen bonding interaction as well as an increment in the polarity of the solvent medium.

7.4 Water-directed self-assembly of probe **L**₇ and Plausible sensing mechanism

We investigated the morphology of self-aggregates formed by **L**₇ in varying ratios of acetonitrile-water and MeOH-water binary systems using a drop-casting method on an Al-foil wrapped glass slide. The field-emission scanning electron microscopy (FESEM) images revealed fibrous network-like morphology for **L**₇ in acetonitrile (0% water) having a length of several micrometers (Figure 7.3a) while enhancement in the water content (90%) transformed into spherical self-aggregates (Figure 7.3b). Similarly for the MeOH-water system, the irregular bushy aggregates converted into well-defined spherical architecture upon increasing the water percentage (90%) in methanol too (Figure 7.3c, 7.3d). Analogous morphology variation was also noted in the corresponding self-aggregates of THF-water, DMF-water, and EtOAc-water solvent mixtures (Figure A7.4). Fluorescence microscopy images ensured the formation of spherical-shaped self-assembly owing to the light-emitting behavior of the aggregates (Figure 7.3e, 7.3f, 7.3g, 7.3h). Variation in the binary solvent systems after the addition of water in acetonitrile or methanol exhibited a significant impact in the morphology transformation of **L**₇ self-assemblies. The evolution from fibre to spherical aggregates upon increasing water content probably proceeded through the separation of a fibrous network to spherical assemblies due to the rise in the polarity/dielectric constant of the solvent, which had always been a pivotal criterion for self-assembly formation.^{7.29-7.30}

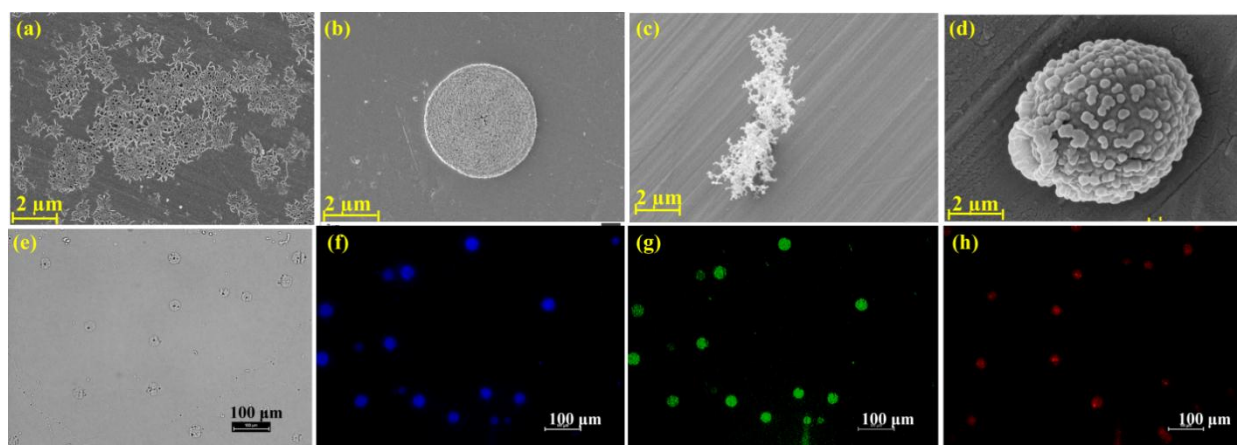


Figure 7.3: FESEM images of L_7 (2.0 μM ; in acetonitrile and methanol medium) (a and c), L_7 (2.0 μM ; in acetonitrile and methanol medium) in presence of water (b,d). Fluorescence microscopy images of L_7 in acetonitrile after addition of water (e, f, g, h).

The trend in the observed hydrodynamic diameter of L_7 self-aggregates computed by DLS in different solvent percentages was in accordance with that of the microscopic experiments (Figure A7.5). Solvent-dependent $^1\text{H-NMR}$ (in DMSO-d_6) experiment was pursued to investigate the involvement of different interactions during self-aggregation of probe L_7 where the protons of indole $-\text{NH}$ and primary $-\text{NH}_2$ exhibited NMR peaks at $\delta = 11.68$ ppm and $\delta = 6.936$ ppm respectively. With an increase in the percentage of D_2O content, NMR signals of $-\text{NH}$ got almost vanished whereas $-\text{NH}_2$ signal slightly downfield shifted to $\delta = 6.955$ ppm i.e. probable intermolecular hydrogen bonding rendering water-assisted self-assembly formation (Figure A7.6), hence red-shifted quenched emission.^{7.31} To correlate the influence of the solvatochromic behavior of probe L_7 , density functional theory (DFT) calculations and time-dependent density functional theory (TDDFT) were conducted utilizing the Gaussian 09 program package.^{7.32} As displayed in Figure 7.4, the HOMO of probe L_7 was located on the amine attached quinoxaline framework whereas the LUMO was localized predominantly on aromatic ring excluding indole $-\text{NH}$ moiety. The addition of less polar (e.g. THF) to more polar solvents (e.g. water) resulted in favorable bonding interactions at either the electron acceptor or donor regions, thus causing an alteration in the dipole strength of the donor-acceptor system, which is generally accompanied by variation in intensity and spectral shifts.^{7.33} The bathochromic shift in emission maxima also correlated with Commission Internationale de l'Éclairage (CIE) coordinates upon changing solvent polarity from hexane to water (Figure 7.4b).^{7.34} The comparative energy analysis in three different polarity solvents disclosed that upon solvation of probe L_7 with THF, acetonitrile, and water independently resulted in a smaller energy gap compared to the probe in vacuo.

Furthermore, the estimated frontier orbital energy gap of L_7 with THF (3.5204 eV), with acetonitrile (3.5000 eV), and with water (3.4973 eV) were decreased in comparison to chemosensor L_7 (3.6197 eV) in vacuo, hence unequivocally manifesting the theoretical outlook of observed solvatochromism (Figure 7.4c). Meanwhile, according to methods reported by Pisman et al., the excited state dipole moment computed by TDDFT in water (2.774 Debye; oscillator strength 0.2707), methanol (2.7484 Debye), and THF (2.6037 Debye) are greater than ground state dipole moment (1.9827 Debye; oscillator strength 0.0230),^{7.35} hence the energy of the excited state might be lessened by the interaction between polar solvent molecules and dipole moment thus resulting in the emission maxima at lower energy or longer wavelength.

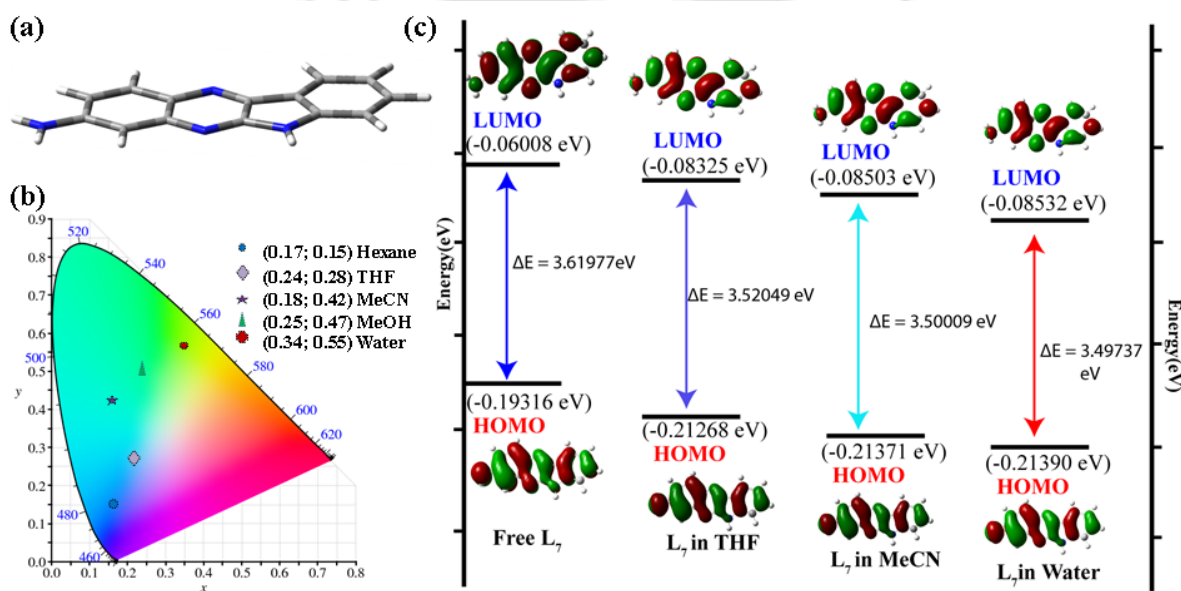


Figure 7.4: (a) Optimized geometry of L_7 in vacuo. (b) CIE diagram of the corresponding light emissions of probe L_7 in different solvents. (c) Energy level diagrams along with HOMO and LUMO distributions of L_7 , in vacuo, in THF, in acetonitrile, and water.

7.5 Qualitative detection of moisture or water content in commercial materials and raw food products

Moisture is a crucial constituent in commercial building materials and raw food products. High moisture content forced food products humidification affecting their stability and quality amid their storage. Hence, estimation of moisture content has become one of the most challenging areas in the food industry.^{7.36} Additionally, the presence of moisture in raw building materials decreases the strength and binding ability,^{7.37} which may cause the failure of construction. Therefore, we have studied the simple and possible use of probe L_7 for the determination of moisture content in several raw building materials i.e. cement, sand, limestone as well as food products salt, wheat, and commercial washing powder(surf excel). Raw building materials

(cement, sand, and limestone; 30 mg) were collected from the IIT Guwahati Civil engineering department whereas raw food products were bought from the IIT Guwahati market complex. These materials were added to the solution of L_7 ($2.0 \mu\text{M}$) in dry acetonitrile. After centrifuging at 12000 rpm for 10 minutes, the mixture was filtered to obtain a clear solution and allowed to collect the fluorescence emission intensity (I). Thus the obtained intensity from the above experiment was compared with the intensity (I_0) recorded from 30 mg of wholly dried raw materials. For complete dryness, materials were oven-dried at 100°C for 24 h and then kept in a desiccator to eliminate the moisture. The fluorescence intensity (I/I_0) for dried and moisture-containing samples was compared (Figure 7.5a).

The existence of high-level environmental moisture causes severe complications in the electronics, pharmaceutical, and fertilizer industries. Hence we tried to investigate the detection of moisture content in the refrigerator by employing probe L_7 ($2.0 \mu\text{M}$) dry acetonitrile system and satisfactory variation in fluorescence emission with bathochromic shift were monitored after six hours (Figure A7.7).

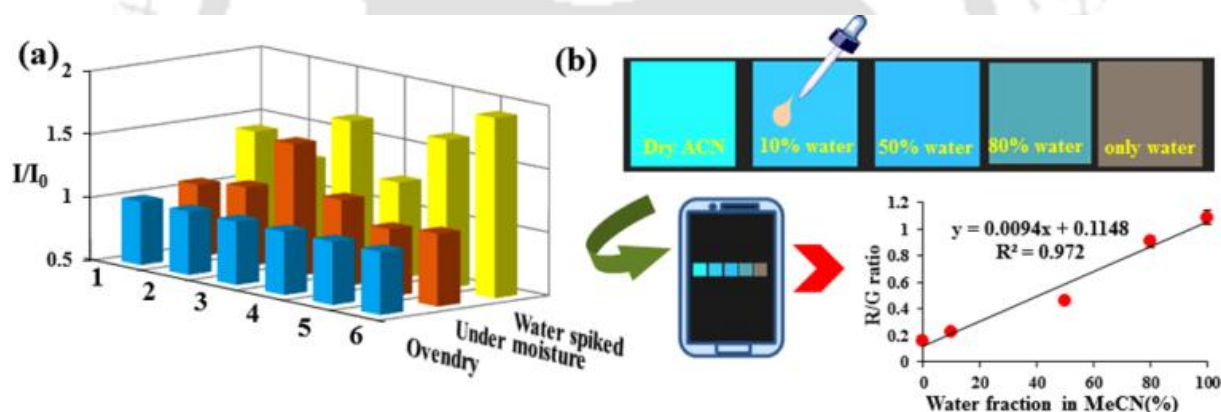


Figure 7.5: (a) Changes in emission intensities of L_7 ($2.0 \mu\text{M}$) ($\lambda_{\text{ex}} = 410 \text{ nm}$) in the presence of various commercial products in dry acetonitrile; 1= cement, 2= sand, 3= limestone, 4= salt, 5=wheat, 6= detergent powder. (b) Fluorescence color variations of paper strips incorporated with L_7 ($2.0 \mu\text{M}$) after being exposed to a different percentage of water spiked acetonitrile. Inset: Linear relationship between the R/G values versus varying water concentration.

7.6 Paper-based sensor for moisture detection

In cooperation with the fluorescence color variation in organic solvents upon addition of different water fractions, the fluorescent paper strip could simplify the detection process and recognize the quantitative analysis of convenient moisture detection (Figure 7.5). For portable test strips preparation, the Whatman filter papers were cut into small rectangular fixed shapes ($2 \text{ cm} \times 1 \text{ cm}$) and immersed into the stock solution of L_7 ($2 \times 10^{-6} \text{ M}$) for 20 min at room

temperature. Thereafter, **L**₇ soaked test papers were kept in a drying oven until the solvent evaporated entirely and stored for future use. After introducing different water% in pre-treated **L**₇ in dry acetonitrile coated paper strips under 365 nm UV illumination, the color of the strips transforms gradually (Figure 7.5b) photographs were taken by a smartphone, which resulted in specific RGB values through a smartphone application (Color recognizer) (Figure A7.8).^{7,38} Therefore, portable paper strips along with RGB analysis via smartphone sensing platform could be reliable for visual, on-site, and quantitative recognition of moisture since the human eye might not detect the minute color variation.

7.7 Conclusions

To sum up, we have developed three varieties of quinoxaline derivatives containing electron-withdrawing, electron-donating groups, and only quinoxaline framework in excellent yields, and it was found that the fluorescence intensity of {6H-indolo[2,3-b]quinoxalin-3-amine} (**L**₇) is strongly affected by solvent polarity, owing to excellent solvatochromism and large Stokes shift. Both experimental and theoretical analysis evinced that the incorporation of a strong electron-rich –NH₂ moiety to quinoxaline backbone notably enhanced the sensitivity of **L**₇ towards solvent polarity. The highest polar sensitivity of probe **L**₇ made it an effective water sensor towards frequently used organic solvents i.e. acetonitrile, THF, DMF, and methanol. The lowest limit of detection (LOD) for acetonitrile, THF, DMF, and methanol is 0.018%, 0.027%, 0.012%, and 0.420%, respectively, which provided an effective and suitable procedure for water/moisture detection in organic solvents. With an enhancement in water percentage, the fiber network-like morphology of probe **L**₇ transformed into light emitting spherical aggregates presumably due to the increasing polarity index of the binary systems. Moisture content in commercial building materials and food products was also quantitatively estimated by the sensor **L**₇ by switching ON-OFF emission intensities. However, after the probe stuff test strips were soaked, under 365 nm UV light the fluorescence color variations of dry common organic solvents in presence of different amounts of water could be noticed by the naked eye.

References

- 7.1 Y. Y. Liang, *Anal. Chem.*, 1990, **62**, 2504–2506.
- 7.2 R. Oguchi, K. Yamaguchi and T. Shibamoto, *J. Chromatogr. Sci.*, 1988, **26**, 588–590.
- 7.3 S.-I. Ohira, K. Goto, K. Toda and P. K. Dasgupta, *Anal. Chem.*, 2012, **84**, 8891–8897.
- 7.4 G. Loving and B. Imperiali, *J. Am. Chem. Soc.*, 2008, **130**, 13630-13638.

- 7.5 W. Nomura, N. Ohashi, A. Mori and H. Tamamura, *Bioconjugate Chem*, 2015, **26**, 1080-1085.
- 7.6 Z. Li, Q. Yang, R. Chang and G. Ma, *Dyes Pigment*, 2011, **88**, 307-314.
- 7.7 L. Ding, Z. Zhang, X. Lib and J. Su, *Chem Commun*, 2013, **49**, 6319-6321.
- 7.8 G. Weber and FJ. Farris, *Biochemistry*, 1979, **18**, 3075-3078.
- 7.9 G. Men, C. Chen, C. Liang, W. Han and S. Jiang, *Analyst*, 2015, **140**, 5454–5458.
- 7.10 Y. Ooyama, K. Furue, K. Uenaka and J. Ohshita, *RSC Adv.* 2014, **4**, 25330–25333.
- 7.11 S. A. Poteet and F. M. MacDonnell, *Dalton Trans.*, 2013, **42**, 13305–13307.
- 7.12 H. S. Jung, P. Verwilst, W. Y. Kim and J. S. Kim, *Chem. Soc. Rev.*, 2016, **45**, 1242–1256.
- 7.13 Y. Niko, S. Sasaki, S. Kawauchi, K. Tokumaru and G. Konishi, *Chem Asian J*, 2014, **9**, 1797-1807.
- 7.14 K. Takagi, K. Kusafuka, Y. Ito and K. Yamauchi, *J Org Chem*, 2015, **80**, 7172-7183.
- 7.15 S. R. Marder, W. E. Torruellas, M. Blanchard-Desce and V. Ricci, *Science*, 1997, **276**, 1233-1236.
- 7.16 J. K. Fang, D. L. An, K. Wakamatsu and T. Ishikawa, *Tetrahedron*, 2010, **66**, 5479-5485.
- 7.17 J. K. Fang, D. L. An, K. Wakamatsu and T. Ishikawa, *Tetrahedron Lett*, 2010, **51**, 917-920.
- 7.18 M. Collot, S. Bou, TK. Fam, L. Richert, Y. M'ely and L. Danglot, *Anal Chem*, 2019, **91**, 1928–1935.
- 7.19 O.A. Kucherak, P. Didier, Y. Mely and A. S. Klymchenko, *J Phys Chem Lett*, 2010, **1**, 616–620.
- 7.20 Z. R. Grabowski, K. Rotkiewicz and W. Rettig, *Chem. Rev.*, 2003, **103**, 3899–4032.
- 7.21 B. Valeur, *Molecular Fluorescence: principles and applications*, Wiley-VCH Verlag GmbH, New York, 2001.
- 7.22 N. Mataga, Y. Kaifu and M. Koizumi, *Bull Chem Soc Jpn* 1956, **29**, 465-469.
- 7.23 L. Ding, ZY. Zhang, X. Li and JH. Su, *Chem Commun*, 2013, **49**, 7319-7321.
- 7.24 D. Seth, S. Sarkar, R. Pramanik, C. Ghatak, P. Setua and N. J Sarkar, *Phys Chem B*, 2009, **113**, 6826–6833.
- 7.25 Li. Zhiwei, Yang. Qiwu, Chang. Ruixiang, Ma. Guochun, C. Mingxi, Z. Wenqin, *Dyes and Pigments*, 2011,**88**.
- 7.26 G.W. Men, G.R. Zhang, C.S. Liang and H.L. Liu, *Analyst*, 2013, **138**, 2847-2857.
- 7.27 G.W. Men, C. R. Chen, C. S. Liang, W. K. Han and S. M. Jiang, *Analyst*, 2015, **140**, 5454–5458.
- 7.28 D. Mandal, S. Dinda, P. Choudhury and P. K. Das, *Langmuir*, 2016, **32**, 9780–9789
- 7.29 X. Shang, I. Song, H. Ohtsu, J. Tong, H. Zhang and J. H. Oh, *Sci. Rep.*, 2017, **7**, 5508–5518.
- 7.30 D. Chakraborty, D. Sarkar, A. K. Ghosh and P. K. Das, *Soft Matter*, 2021, **17**, 2170.
- 7.31 H. S. Jung, P.Verwilst, W. Y. Kim and J. S. Kim, *Chem. Soc. Rev.*, 2016, **45**, 1242
- 7.32 M. Fisch, G. Trucks, H. Schlegel, G. Scuseria, M. Robb, J. Cheeseman, G. Scalmani, V. Barone, B. Mennucci and G. Petersson, *Gaussian 09 (Revision A. 02)*, Wallingford, CT, 2009.
7. 33 M. H. Lee, J. S. Kim and J. L. Sessler, *Chem. Soc. Rev.*, 2015, **44**, 4185.
- 7.34 V. Anand and Ra. Dhamodharan, *New J. Chem.*, 2017, **41**, 9741
- 7.35 P. Pasma, F. Rob and J. W. Verhoeven, *J. Am. Chem. Soc.*, 1982, **104**, 5127–5133.

7.36 P. Kumar, R. Kaushik, A. Ghosh, and D. Amilan Jose, *Anal. Chem.*, 2016, **88**, 11314–11318.

7.37 P. Kumar, A. Ghosh and D. Amilan Jose, *Analyst*, 2019, **144**, 594.

7.38 M. Ö. Alaş and R. Genç, *ACS Appl. Nano Mater.*, 2021, **4**, 7974–7987



Appendix - Chapter 7

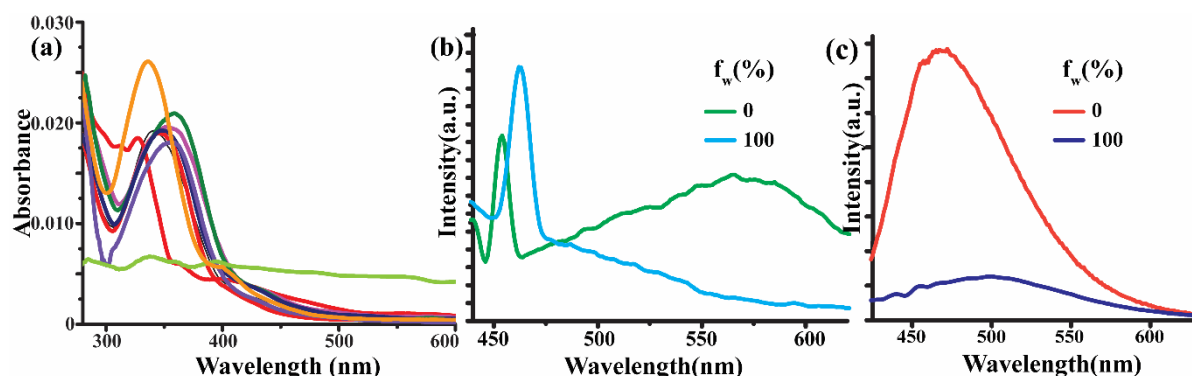


Figure A7.1: (a) UV-visible spectra of L_7 in nine different solvents at room temperature. (b) Fluorescence emission spectra of L_6 in acetonitrile and aqueous medium at room temperature ($\lambda_{ex} = 400$ nm, slit = 3nm / 3nm). (c) Fluorescence emission spectra of L_5 in acetonitrile and aqueous medium at room temperature ($\lambda_{ex} = 400$ nm, slit = 3nm / 3nm).

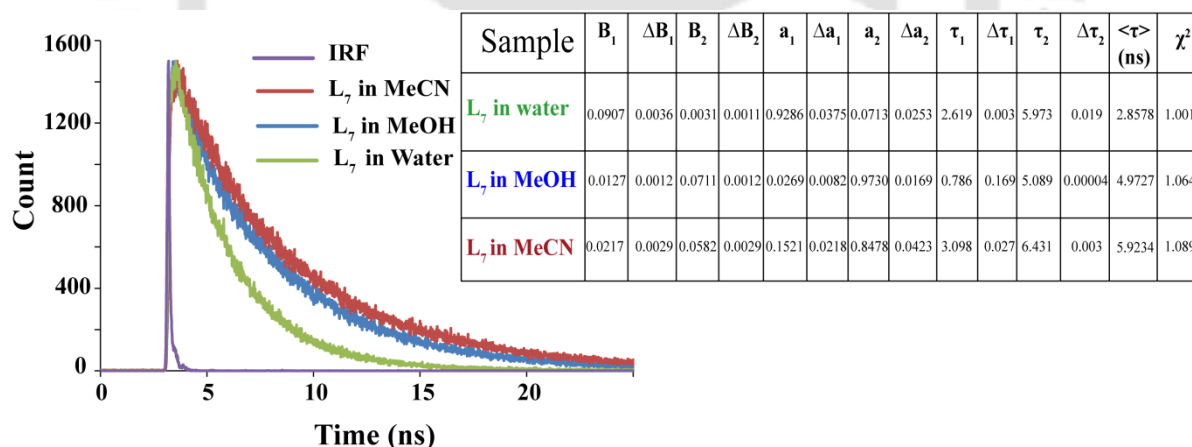


Figure A7.2: Time-resolved fluorescence emission spectra of L_7 (2 μ M) in acetonitrile, methanol and aqueous medium. Inset: Fluorescence lifetime values of L_7 (2.0 μ M) three different mediums.

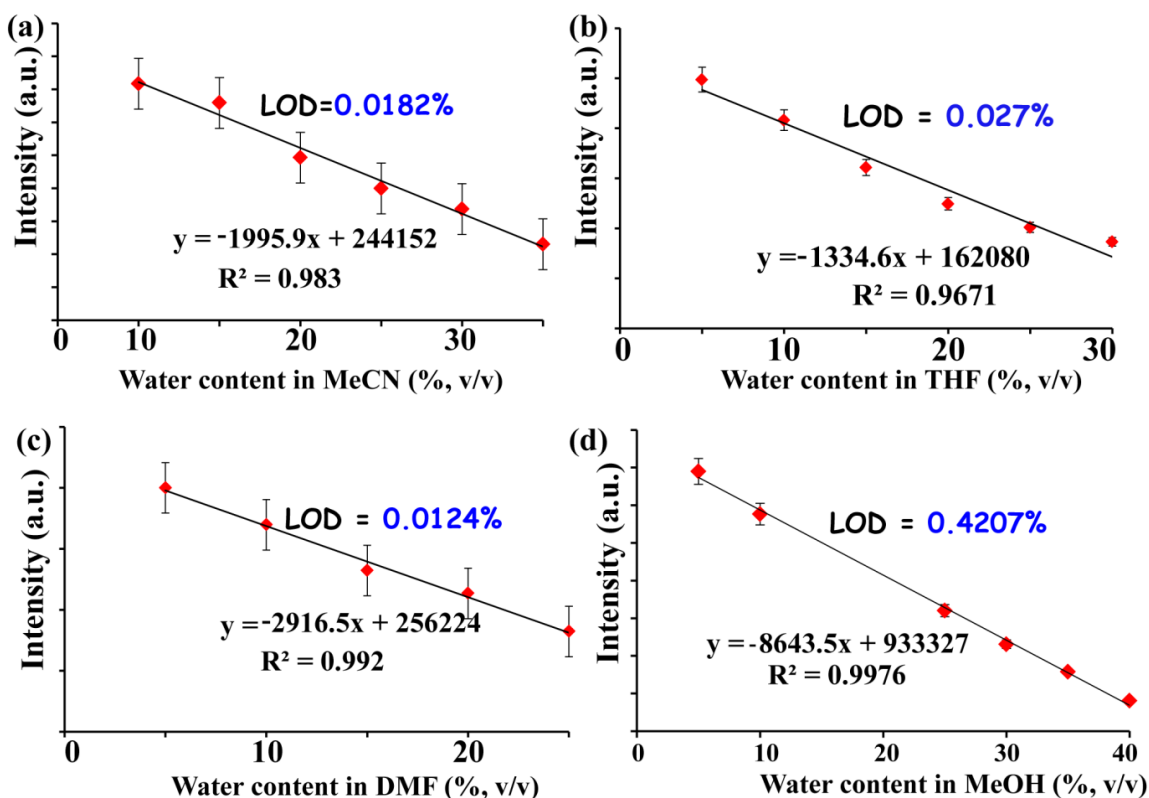


Figure A7.3: Fluorescence emission intensity of L_7 (2 μM) vs. water content in organic solvents(%) i.e. (a) acetonitrile (b) tetrahydrofuran (c) dimethylformamide (d) methanol respectively to calculate the limit of detections (LOD).

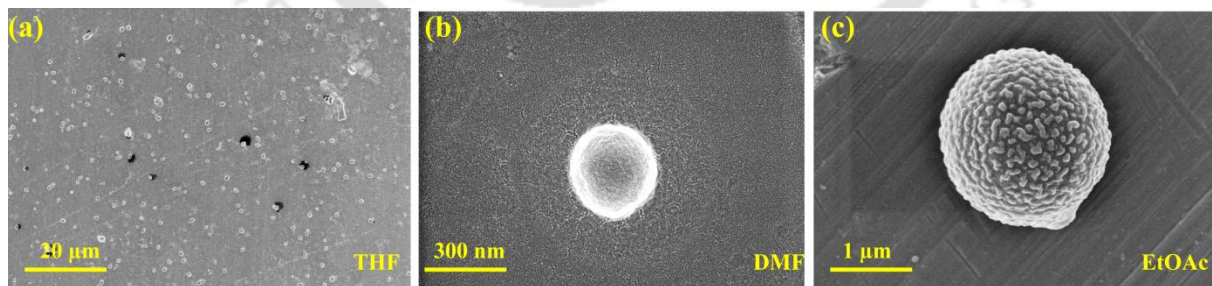


Figure A7.4: FESEM images of L_7 (2.0 μM) in (a) tetrahydrofuran (b) dimethylformamide and (c) ethyl acetate mediums upon addition of water.

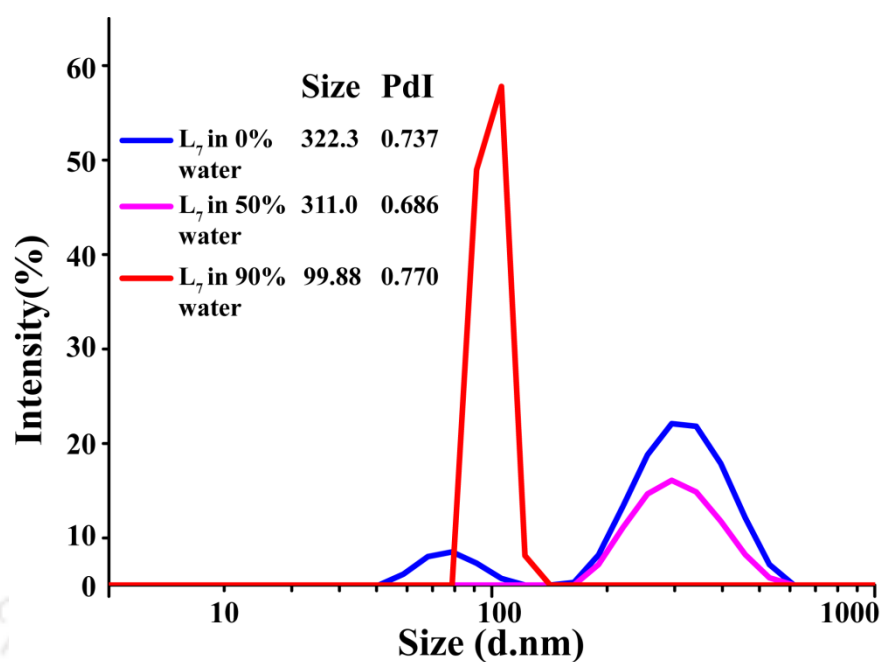


Figure A7.5: DLS analysis of L₇ (2.0 μM) acetonitrile medium upon addition of different fractions of water(%).

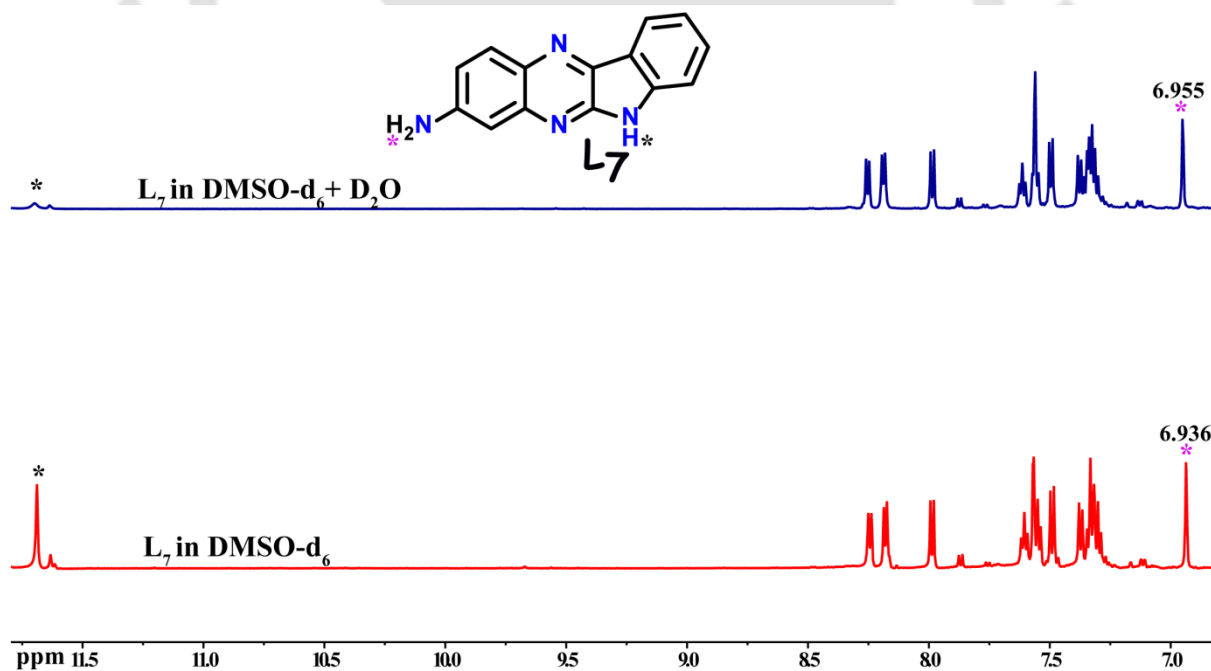


Figure A7.6: ¹H NMR spectral changes of L₇ in DMSO-d₆ upon addition of 1 equiv.D₂O.

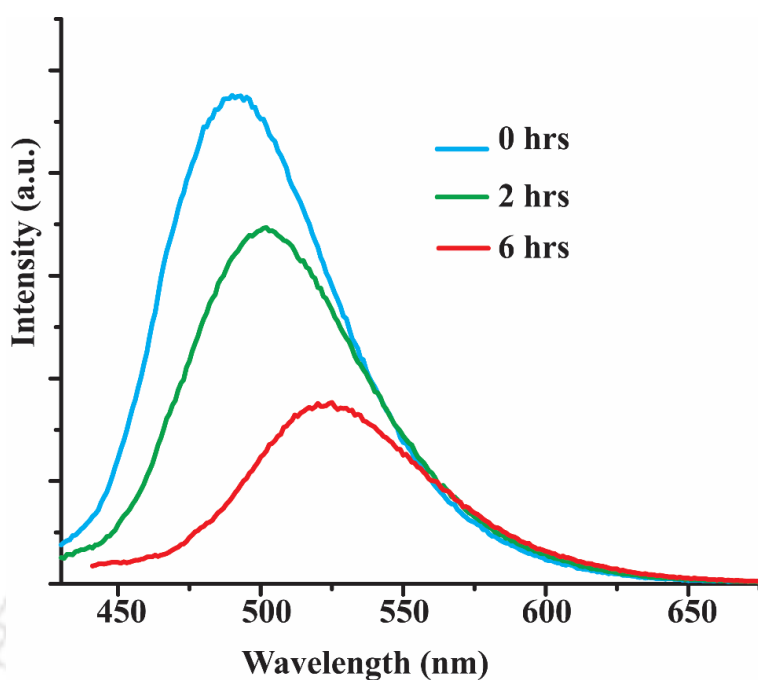


Figure A7.7: Time dependent emission spectra of L_7 (2.0 μM) dry acetonitrile medium placed in refrigerator.





	Heathered Grey //Grey → Orange RGB: (153, 141, 128) #998D80 HSV: (31°, 16%, 60%) ● ~RAL 7048 \ Pearl mouse grey
	Royal Blue //Cyan RGB: (56, 254, 254) #38FEFE HSV: (180°, 78%, 100%) <input type="radio"/> no matched code
	Turquoise Blue //Cyan:Blue RGB: (75, 211, 254) #4BD3FE HSV: (194°, 70%, 100%) <input type="radio"/> no matched code
	Summer Sky //Cyan:Blue RGB: (72, 199, 254) #48C7FE HSV: (198°, 72%, 100%) <input type="radio"/> no matched code

Figure A7.8: RGB analysis by the color recogniser app.

Conclusion and Future Perspective

In conclusion, the overall thesis not only explained some important results in the field of developing advanced chemosensors for some biologically, environmentally relevant/harmful neutral analytes, but also enlightens the significant consequences in realization of assembly/disassembly prospective of certain fluorene and quinoxaline based derivatives and their stimuli-responsive fluorescence response. The cumulative studies during the research endeavour furnishes some interesting findings in aggregation/disaggregation aspect of probe molecules and insightful route in morphological transformation regarding design, synthesis and characterization of small neutral guest analytes with contrasting aggregation prospect. As mentioned in the introduction, our primary aim was to introduce sensing systems that can rapidly sense target analytes by avoiding aggregation caused quenching (ACQ) effect and introducing some assembly/disassembly triggered fluorescence responses which is conspicuous by naked eye under UV illumination; so that even an uneducated person could identify the sensing outcomes. Hence, all of the reported probes in this thesis were purposely designed to have the inherent feature of naked eye sensing ability under UV chamber. In general, the research works described in the thesis provide a clear insight of the design principle involved in developing simple organic optical chemosensor molecules (**L**₁- **L**₇) which can detect various neutral species in aqueous solution, simulated biological media and/or inside living cells.

In summary, during the research period, we started with the purposely developed probe compounds **L**₁, **L**₂ and **L**₃, and the change in their terminal substitution in molecular backbone simply driven us to create the variation in subsequent spectroscopic investigation towards Hg²⁺ (LOD~17.35 ppb) and GSH (LOD~25.83 ppb) respectively over other coexisting analytes in the aqueous medium. The sensing mechanism of **L**₁ towards Hg²⁺ additionally involved analyte recognition triggered self-assembly formation since rod-shaped morphology of **L**₁ transformed into a massive butterfly-shaped network upon treatment with Hg²⁺. Moreover, we synthesized another simple and easy-to-operate organic luminophore based on fluorene bridged dipodal naphthalene moiety **L**₄, that can preferentially self-assemble to form aggregates in aqueous medium. The probe shows selective and sensitive 1:1 binding ability towards FA (LOD~0.38 μM) among various carboxylic acids through an enhanced "turn-on" fluorescence emission in totally aqueous solution leading to the disaggregation of the self-assembled probe. Another quinoxaline-based probe **L**₅ exhibited effective and selective fluorescence-based detection of PA (LOD~ 56 ppb) over other NACs in aqueous solution, natural water samples, solid and paper-based systems. Due to π-π stacking interaction, **L**₅ spontaneously self-assembled in an aqueous solution to leaf-like aggregates, which was disrupted to smaller round-shaped

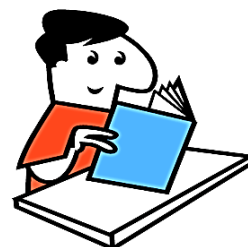
aggregates in presence of PA. Alongside, nitro-incorporated quinoxaline-based fluorophore, **L₆** was introduced as an effective chemosensor for the detection of benzene-derived VOCs in the aqueous medium. The probe displayed a differential “Turn-On” fluorescence response towards mesitylene (LOD= 2.66 ppm) uninfluenced by other VOCs. The sensing mechanism involved mesitylene detection induced assembly formation as the fibril network transformed into stone-shaped morphology. Lastly, sensing probe **L₇**, owing to excellent solvatochromism and large Stokes shift made it an effective water sensor towards frequently used organic solvents i.e. acetonitrile, THF, DMF, and methanol. The lowest limit of detection (LOD) for acetonitrile, THF, DMF, and methanol is 0.018%, 0.027%, 0.012%, and 0.420%, respectively, which provided an effective and suitable procedure for water/moisture detection in organic solvents. With an enhancement in water percentage, the fiber network-like morphology of probe **L₇** transformed into light emitting spherical aggregates presumably due to the increasing polarity index of the binary systems.

Hence, we have designed, synthesized and investigated some unique sensing platforms (**L₁- L₇**) which encompassed both simple and complex structures of the sensing probes. It should be noted that besides the conventional PET/FRET strategies we have included some aggregation/disaggregation features in designing the sensing probes to upgrade and discriminate their selectivity and efficiency.

Applications of chemosensors in analytical chemistry, supramolecular science, biochemistry, physical chemistry, medicinal chemistry, toxicology, forensic sciences and even modern nanosciences have reached an advance stage. However, to develop a smart, ready to use chemosensor, it is necessary to embed some important features like water solubility, discriminative fluorescence response, non-cytotoxic nature, localization in particular compartment of cells, application in real samples, naked eye detection, rapid response, lowering cost and labour etc. in molecular design. Although we tried to incorporate all these features conveniently in the respective results in this thesis which are extremely useful from the perspective of progressive chemo-sensing, there are still other challenges in supramolecular chemistry to deal with.

Hence, the overall outcomes in the thesis revise the design strategy for developing functional assembly of small molecular system and successfully established the some of the various fundamental concepts of stimuli responsive aggregation/disaggregation prospect through sequential approach of spectroscopic and microscopic studies. In essence, we believe that this thesis would find meaningful contribution to both analytical chemistry and supramolecular

chemistry community for enhancing realization and development in the particular field of research. Hopefully, this thesis may inspire further exploration of interesting photophysical characteristics along with morphology study and sensing endeavor with this type of neutral guest molecule instructed aggregative/disaggregative nature.





MEGHA BASAK

Address: Department of Chemistry;
IIT Guwahati

Email: megha176122022@iitg.ac.in
meghabasak3@gmail.com

Contact: +91-9073312852
+91-7439560474

ORCID: <https://orcid.org/0000-0002-2422-184X>

**Academic Record**

- 2017- present **Ph.D.** student at Indian Institute of Technology Guwahati
Thesis title: “**Neutral Guest-Induced Assembly/Disassembly Approach for Concurrent Detection of Biologically Important Analytes under Physiological Condition**”.
Supervisor- Prof. Gopal Das
- 2016 **Master of Science**; University of Calcutta; Percentage of marks-80.7 (*1st Class*).
Project Title: “Synthesis and Crystal structure of tetranuclear Cobalt complex derived from Hexadentate ligand”.
Supervisor- Dr. Sanchita Goswami
- 2014 **Bachelor of Science (Chemistry)**; University of Calcutta; Percentage of marks-76.7 (*1st Class*).
- 2011 **Higher secondary (10+2)**; Begum Rokeya Smriti Balika Vidyalaya (WBCHSE); Percentage of marks-89 (*1st Division*).
- 2009 **Secondary(10)**; Ramakrishna Sarada Mission Sister Nivedita Girls’ School (WBBSE); Percentage of marks-82.4 (*1st Division*).

Awards and Achievements

- ❖ Qualified **Graduate Aptitude test in Engineering (GATE)** (2017 and 2018).
- ❖ Qualified **Joint CSIR-UGC Test For J.R.F and Eligibility for Lectureship (NET)** (18th June, 2017) (CSIR-JRF).
- ❖ Ranked 2nd (General category) in Ph.D entrance examination in IIT Guwahati (June 2017).
- ❖ Qualified **JAM** (Joint Admission test for M.Sc, 2014).
- ❖ Occupied **3rd** position in M.Sc (2016; Inorganic chemistry specialization).

- ❖ IEST Shibpur M.Sc Entrance test, 2014(AIR- 4).
- ❖ Selected for **PG Indira Gandhi Scholarship For Single Girl Child (University Grants Commission)** during M.Sc course (2014-2016).
- ❖ Ranked 138 in 2011 **West Bengal Higher Secondary Examination** and secured **1st** position in school, selected for an **fellowship** under the **Scheme of Scholarship for College and University students(WBCHSE)**.
- ❖ Performed A+ (Excellent) in **Science Aptitude & Talent search test** held on 2007.

Research Interests

- ❖ Preparation of pharmaceutically important novel heterocyclic architectures via short synthetic routes from readily available substrates. Selective recognition of toxic heavy metal ions, biologically crucial anions and environmentally harmful molecules with fluorescent and colorimetric sensors.
- ❖ Supramolecular chemistry of biologically and environmentally important anions: Solid and solution-state studies of biologically and environmentally significant anions in π -acidic receptors, and anion driven synthesis of supramolecular structural design.

Research Publications

1. Amine-incorporated quinoxaline based fluorescent sensor for detection of trace water: a solvent influenced self-assembly, **Megha Basak** and Gopal Das, *Spectrochim. Acta - A: Mol. Biomol. Spectrosc.* 2022, 280, 121521.
2. Fabrication and Photophysical Assessment of Quinoxaline based Chemosensor: Selective determination of Picric Acid in Hydrogel and Aqueous medium, Debolina Ghosh[‡], **Megha Basak[‡]**, Deepmoni Deka and Gopal Das ([‡] = equal contribution), *J. Mol. Liq.* 2022,363,119816.
3. Exploring cyclohexane/piperazine-urea motifs for spherical halide (X = Cl⁻/Br⁻) recognition effects on anion coordination, photoluminescence, and morphological tenability. **Megha Basak**, Aresh Das and Gopal Das, *Cryst. Eng. Comm.*, 2021, 23, 7771-7780.
4. Supramolecular Self-Assembly of Nitro-incorporated Quinoxaline Framework: Insights into the Origin of Fluorescence Turn-on Response towards Benzene group of VOCs; **Megha Basak** and Gopal Das, *Analyst*, 2021, 146, 6239-6244.

5. Self-assembled Quinoxaline Derivative: Insight into Disaggregation Induced Selective Detection of Nitro-Aromatics in Aqueous Medium and Live Cell Imaging; **Megha Basak**, Basu Bhattacharjee, Aiyagari Ramesh and Gopal Das, *Dyes. Pigm.*, 2021,196, 109779.
6. Folic acid Induced Disassembly of Self-assembled Fluorene-Naphthalene Based Receptor and Contemporaneous Detection of Folic acid in Aqueous Medium; **Megha Basak**, S. Halder and Gopal Das, *J. Photochem. Photobiol. A*, 2021, 414,113292.
7. Diazine based ligand supported Co^{II}_3 and Co^{II}_4 coordination complexes: role of the anions; Yeasin Sikdar, Ranadip Goswami, Ritwik Modak, **Megha Basak**, Maria Jose Heras Ojea, Mark Murrie and Sanchita Goswami, *New J. Chem.*, 2018,42, 17587-17596.
8. Mercury recognition triggered self-assembly and switch-on chemosensor for Glutathione in water: Application of dual-action fluorene-salicylaldehyde probe. **Megha Basak** and Gopal Das (**Submitted**).
9. Quinoxaline-Based Membrane-Targeting Therapeutic Material Implications in Rejuvenating Antibiotic and Curb MRSA Invasion in an In Vitro Bone Cell Infection Model. Basu Bhattacharjee, **Megha Basak**, Gopal Das and Aiyagari Ramesh (**Submitted**).

Analytical Skills

Software operation: Microsoft Office (Power Point, Excel and Word), Paint, Chem-Draw, Origin, Adobe Illustrator, ORTEP, Mercury, SHELXL, WINGX, Crystal Explorer, MestreNova, Win-EQNMR2, Bind-fit model, Image J, Gaussview etc.

Instruments operation: Spectrofluorometer, UV-Vis Spectrophotometer, FT-IR, NMR and Mass Spectra Analysis, Single crystal X-ray Diffractometer SCXRD, Fluorescence microscope, Dynamic Light Scattering (size and zeta-potential analysis), Thermogravimetric analysis, pH meter.

Teaching experience: Teaching assistantship at IIT Guwahati: Inorganic Tutorial Courses for undergraduate students (July- November, 2018 and July-November, 2019); multiple exam supervisions and answer script corrections.

Project and other activities

1. Summer Project (2014) in Galaxy Educare concepts Private Limited, Kolkata (Project Title: *Biochemistry*).

2. M.Sc project: (January 2016 - April 2016) under the supervision of Dr. Sanchita Goswami at Calcutta University (Project Title: *Synthesis and Crystal structure of tetranuclear Cobalt complex derived from Hexadentate ligand*). Presented a **Review Article** on “*Structural proposals of manganese clusters involved in water oxidizing catalysis (WOC)*”.

3. **Project assistant** (December 2016 - June 2017) under the guidance of Dr. Sourja Ghosh at Central Glass and Ceramic Research Institute, Kolkata.

Seminars, Conferences and Workshop

Oral presentations

- “*Fluorene-Naphthalene Based Receptor:Folic acid Induced Disassembly of Self-assembled probe and Contemporaneous Detection of Folic acid in Aqueous Medium*” in **AIMS 2020** organized by BMS Institute of Technology& Management, Bengaluru, India on 4-7 th August 2020.
- “*Temperature dependent Chemoselective Hydrosilylation of carbon di oxide to methanol or formaldehyde oxidation state*” organized by Calcutta University on May 2016.
- “*Role of Chelation Therapy on human being*” organized by Calcutta University on 18th November 2015.
- “*Phase Equilibria*” in a one day seminar organized by the Department of Chemistry, Vidyasagar College on 21st January 2014.
- “*Common Ion Effect*” in a science exhibition organized by Vidyasagar College, 2012.

Poster presentations

- “*Highly Sensitive Detection of Trace Tetracycline in water by AIE luminogen probe*” in **North-East Research Conclave(NERC)** organized by IIT Guwahati in association with Government of India, Ministry of Education on 20th-22nd May, 2022.
- “*Self-assembled Quinoxaline Derivative: Disaggregation Induced selective chemosensing of Nitro-Aromatics in Aqueous Medium*” in **ACMS** organized by Heritage Institute of Technology, Kolkata, India on 14th -16th April, 2022.
- “*Supramolecular Self-Assembly of Nitro-incorporated Quinoxaline Framework: Insight into the Origin of Fluorescence Turn-on Response towards Benzene group of VOCs*” in **NSC-CRSI Joint Symposium** organized by IIT Guwahati, India on 25th-27th March, 2022.
- “*Self-assembled Quinoxaline Derivative: Disaggregation Induced selective chemosensing of Nitro-Aromatics in Aqueous Medium and Live cell imaging*” in **2022 #RSCPoster Twitter Conference** organized by Royal Society of Chemistry (RSC) on 1st-2nd March, 2022.
- “*Self-assembled Quinoxaline Derivative: Disaggregation Induced selective chemosensing of Nitro-Aromatics in Aqueous Medium*” in **Research and Industrial Conclave 2022** organized by IIT Guwahati, India on 20th-23rd January, 2022.
- “*Supramolecular Self-Assembly of Nitro-incorporated Quinoxaline Framework: Insight into the Origin of Fluorescence Turn-on Response towards Benzene group of VOCs*” in **ChemSci2021** jointly organized by Royal Society of Chemistry (RSC) and The Jawaharlal Nehru Centre for Advanced Scientific Research (JNCASR) Bangalore, India in association with the *Chemical Science* journal on 13th-15th December, 2021.
- “*Self-assembled Quinoxaline Derivative: Disaggregation Induced selective chemosensing of Nitro-Aromatics in Aqueous Medium*” in **ACS-RTCS 2021** organized by Indian Chemical Society, Kolkata on 21-24 December; 2021.
- “*Supramolecular Self-Assembly of Nitro-incorporated Quinoxaline Framework: Origin of Fluorescence Turn-on Response towards Benzene group of VOCs*” in **RSC-TIC**

2021: Spectroscopic imaging and sensing jointly organized by The Royal Society of Chemistry (RSC) and JAPAN Analytical Instruments Manufacturers' Association (JAIMA) on 6-7th December; 2021.

- “Exploring urea motifs for spherical halide (X = Cl⁻/Br⁻) recognition effects on anion coordination” in **MTIC XVIII** organized by IIT Guwahati, India on 11th-14th December, 2019.

Workshops Attended

- “*Hands on Training on Scholarly Publications*” organized by CSIR-National Institute of Science Communications and Policy Research (SERB sponsored) on 12th-18th May 2022.
- “*Understand and Explore The World of Fluorescence*” organized by DRIIV & IIT Delhi on 25th April-27th April 2022.
- Rigaku School on “*Practical Crystallography*” from 10th – 21st January 2022.
- “*Single Crystal X-Ray Diffraction Techniques and its Applications*” organized by NECBH IIT Guwahati, India on 22nd - 23rd January, 2021.
- “*Bruker Asia SC-XRD*” online meeting organized by Bruker India Scientific Pvt. Ltd on 11th – 12th November 2021.
- “*Fluorescence and Raman Spectroscopy (FCS 2021)*” organized by Fluorescence society, India on 29th November - 4th December 2021.
- “*Online Workshop on Rietveld Refinement Method*” organized by UGC-DAE consortium for scientific research Mumbai centre in association with Indore Centre, India on 22nd - 24th September 2020.
- “*18th Chem Quiz*” organized by Presidency University, 2014.